29-39 Brunswick Square

London WC1N 1AX

Vat photopolymerisation 3D printing of controlled drug delivery devices

Xiaoyan Xu

Thesis submitted in accordance with the requirements of UCL School of Pharmacy for the

degree of Doctor of Philosophy

October 2022

Department of Pharmaceutics

UCL School of Pharmacy

29-39 Brunswick Square

London WC1N 1AX

Declaration

This thesis describes research conducted in the School of Pharmacy, University College London between 2018 and 2022 under the supervision of Professor Simon Gaisford and Professor Abdul W. Basit. I, Xiaoyan Xu certify that the research described is original and that I have written all the text herein and have clearly indicated by suitable citation any part of this dissertation that has already appeared in publications.

Signature: _____   Date: ____31st October 2022____

                (Xiaoyan Xu)

To my beloved family

Abstract

Pharmaceutical three-dimensional (3D) printing has led to a paradigm shift in the way medicines are designed and manufactured, moving away from the traditional 'one-size-fits-all' approaches and advancing towards personalised medicines. Among different 3D printing techniques, vat photopolymerisation 3D printing affords superior printing resolution, which in turn enables fabrication of micro-structures and smooth finishes.

This thesis aims to investigate different vat photopolymerisation 3D printing techniques for the fabrication of personalised drug delivery devices for different routes of administration. Stereolithography (SLA) and digital light processing (DLP) 3D printing was used to manufacture devices with flexible materials for localised delivery of a single drug in the bladder and at the anterior segment of the eye. *In vitro* release studies demonstrated drug releases from these devices were sustained over weeks. Subsequently, to investigate the feasibility of loading more than one drug in a single dosage form, clinically relevant multi-layer antihypertensive polypills were fabricated using SLA 3D printing. A drug-photopolymer interaction was observed from these polypills, and Michael's addition reaction was confirmed to have occurred. Despite these studies demonstrating the viable use of vat photopolymerization 3D printing for fabricating drug delivery devices, the bulky nature of current printers could be a barrier to clinical integration. As such, a smartphone-enabled DLP 3D printing system was developed to fabricate personalised oral dosage forms and patient-specific drug delivery devices. The portability of this printer could secure exciting opportunities for manufacturing personalised medicines at point-of-care settings. Overall, this thesis showed the potential of vat photopolymerisation 3D printing in preparing different patient-centric drug delivery devices with tuneable and sustained release profiles as well as advancing traditional treatments towards digital healthcare.

Impact statement

The pharmaceutical and healthcare industry is rapidly evolving, with the traditional 'one-size-fits-all' treatment approaches shifting towards patient-centric personalised medicines. 3D printing has been adopted as an innovative technology by enabling the rapid fabrication of bespoke drug delivery therapies. However, current research of 3D printing technologies in formulation development is largely focused on the use of extrusion-based techniques in fabricating oral dosage forms while vat photopolymerisation 3D printing, a technology that has attracted attention in the field of bioprinting is still relatively unexplored in the pharmaceutical research.

This PhD thesis demonstrated the potential of vat photopolymerisation 3D printing in fabricating different controlled drug delivery devices. The current study firstly showed SLA 3D printing could serve as a one-step manufacturing approach for the creation of indwelling intravesical devices for extended and localised drug delivery in the bladder. Subsequent study revealed DLP 3D printing as a promising manufacturing method in the preparation of high-resolution drug-eluting punctal plugs for the treatment of dry eye syndrome. These studies demonstrated vat photopolymerisation 3D printing as a novel platform in preparing implantable controlled-release devices and such potential could be extended for other drug delivery applications. Interestingly, a drug-photopolymer interaction was observed and investigated in this study, highlighting the importance of polymer screening towards the development of drug-loaded delivery systems when using vat photopolymerisation techniques. This study further explores the development of a compact smartphone-enabled 3D printer in preparation of personalised oral dosage forms and by coupling with 3D scanning with mobile apps, the fabrication of patient-specific drug delivery devices. In summary, research in this thesis contributes towards the use of 3D printing technologies for producing personalised medicines i) by highlighting the potential of vat

photopolymerisation 3D printing in the fabrication of controlled drug delivery devices for different routes of administration and; ii) by identifying challenge and limitation of the implementation of vat photopolymerisation to prepare drug-loaded devices and; iii) by advancing the integration of 3D printing in future digital healthcare for point-of-care manufacturing of personalised medicines. This work also aims to inspire researchers to pursue investigations on drug-photopolymer compatibility and to develop novel controlled drug delivery systems which are challenging to produce using conventional pharmaceutical approaches.

Acknowledgements

UCL Research Paper Declaration Forms

UCL Research Paper Declaration Form: referencing the doctoral candidate's own published work(s)

Please use this form to declare if parts of your thesis are already available in another format, e.g. if data, text, or figures:

- have been uploaded to a preprint server;
- are in submission to a peer-reviewed publication;
- have been published in a peer-reviewed publication, e.g. journal, textbook.

This form should be completed as many times as necessary. For instance, if you have seven thesis chapters, two of which containing material that has already been published, you would complete this form twice.

1. **For a research manuscript that has already been published** (if not yet published, please skip to section 2)**:**		
a) **Where was the work published?** (e.g. journal name)	Journal of Controlled Release	
b) **Who published the work?** (e.g. Elsevier/Oxford University Press):	Elsevier	
c) **When was the work published?**	05/10/2020	
d) **Was the work subject to academic peer review?**	Yes	
e) **Have you retained the copyright for the work?**	Yes	
[If no, please seek permission from the relevant publisher and check the box next to the below statement]: ☐ *I acknowledge permission of the publisher named under 1b to include in this thesis portions of the publication named as included in 1a.*		
2. **For a research manuscript prepared for publication but that has not yet been published** (if already published, please skip to section 3)**:**		
a) **Has the manuscript been uploaded to a preprint server?** (e.g. medRxiv):	Please select.	**If yes, which server?** Click or tap here to enter text.

b) Where is the work intended to be published? (e.g. names of journals that you are planning to submit to)	Click or tap here to enter text.	
c) List the manuscript's authors in the intended authorship order:	Click or tap here to enter text.	
d) Stage of publication	Please select.	

3. For multi-authored work, please give a statement of contribution covering all authors (if single-author, please skip to section 4**):**

Xiaoyan Xu: Conceptualization, Writing – Original Draft, Visualization. **Atheer Awad**: Conceptualization, Writing – Review & Editing, Visualization. **Pamela Robles-Martinez**: Conceptualization. **Simon Gaisford**: Writing – Review & Editing, Visualization, Supervision, Funding Acquisition. **Alvaro Goyanes**: Conceptualization, Writing – Review & Editing, Visualization, Supervision, Project Administration. **Abdul W. Basit**: Conceptualization, Writing – Review & Editing, Visualization, Supervision, Project Administration, Funding Acquisition.

4. In which chapter(s) of your thesis can this material be found?

Chapter 1 Introduction

5. e-Signatures confirming that the information above is accurate (this form should be co-signed by the supervisor/ senior author unless this is not appropriate, e.g. if the paper was a single-author work):

Candidate:	Xiaoyan Xu	**Date:**	05/10/2022
Supervisor/ Senior Author (where appropriate)**:**	Professor Simon Gaisford	**Date:**	31/10/2022

UCL Research Paper Declaration Form: referencing the doctoral candidate's own published work(s)

Please use this form to declare if parts of your thesis are already available in another format, e.g. if data, text, or figures:

- have been uploaded to a preprint server;
- are in submission to a peer-reviewed publication;
- have been published in a peer-reviewed publication, e.g. journal, textbook.

This form should be completed as many times as necessary. For instance, if you have seven thesis chapters, two of which containing material that has already been published, you would complete this form twice.

6. For a research manuscript that has already been published (if not yet published, please skip to section 2)**:**	
f) Where was the work published? (e.g. journal name)	Materials Science and Engineering: C
g) Who published the work? (e.g. Elsevier/Oxford University Press):	Elsevier
h) When was the work published?	04/12/2020
i) Was the work subject to academic peer review?	Yes
j) Have you retained the copyright for the work?	Yes
[If no, please seek permission from the relevant publisher and check the box next to the below statement]: ☐ *I acknowledge permission of the publisher named under 1b to include in this thesis portions of the publication named as included in 1a.*	

7. For a research manuscript prepared for publication but that has not yet been published (if already published, please skip to section 3)**:**		
e) Has the manuscript been uploaded to a preprint server? (e.g. medRxiv):	Please select.	**If yes, which server?** Click or tap here to enter text.
f) Where is the work intended to be published? (e.g. names of journals that you are planning to submit to)	Click or tap here to enter text.	
g) List the manuscript's authors in the intended authorship order:	Click or tap here to enter text.	

h) **Stage of publication**	Please select.

8. For multi-authored work, please give a statement of contribution covering all authors (if single-author, please skip to section 4**):**

Xiaoyan Xu: Conceptualization, Methodology, Software, Validation, Formal Analysis, Investigation, Resources, Data Curation, Writing – Original Draft, Visualization. **Alvaro Goyanes**: Conceptualization, Methodology, Writing – Original Draft, Visualization, Supervision, Project Administration. **Sarah J. Trenfield**: Conceptualization, Validation, Investigation, Writing – Original Draft, Visualization. **Luis Diaz-Gomez**: Validation, Investigation, Resources, Writing – Review & Editing. **Carmen Alvarez-Lorenzo**: Validation, Investigation, Resources, Writing – Review & Editing. **Simon Gaisford**: Writing – Review & Editing, Visualization, Supervision, Funding Acquisition. **Abdul W. Basit**: Conceptualization, Writing – Review & Editing, Visualization, Supervision, Project Administration, Funding Acquisition.

9. In which chapter(s) of your thesis can this material be found?

Chapter 2 SLA 3D printing of intravesical devices

10. e-Signatures confirming that the information above is accurate (this form should be co-signed by the supervisor/ senior author unless this is not appropriate, e.g. if the paper was a single-author work):

Candidate:	Xiaoyan Xu	**Date:**	05/10/2022
Supervisor/ Senior Author (where appropriate)**:**	Professor Simon Gaisford	**Date:**	31/10/2022

UCL Research Paper Declaration Form: referencing the doctoral candidate's own published work(s)

Please use this form to declare if parts of your thesis are already available in another format, e.g. if data, text, or figures:

- have been uploaded to a preprint server;
- are in submission to a peer-reviewed publication;
- have been published in a peer-reviewed publication, e.g. journal, textbook.

This form should be completed as many times as necessary. For instance, if you have seven thesis chapters, two of which containing material that has already been published, you would complete this form twice.

11. For a research manuscript that has already been published (if not yet published, please skip to section 2)**:**	
k) Where was the work published? (e.g. journal name)	Pharmaceutics
l) Who published the work? (e.g. Elsevier/Oxford University Press):	MDPI
m) When was the work published?	08/09/2021
n) Was the work subject to academic peer review?	Yes
o) Have you retained the copyright for the work?	Yes
[If no, please seek permission from the relevant publisher and check the box next to the below statement]: ☐ *I acknowledge permission of the publisher named under 1b to include in this thesis portions of the publication named as included in 1a.*	
12. For a research manuscript prepared for publication but that has not yet been published (if already published, please skip to section 3)**:**	

i) Has the manuscript been uploaded to a preprint server? (e.g. medRxiv):	Please select.	**If yes, which server?** Click or tap here to enter text.
j) Where is the work intended to be published? (e.g. names of journals that you are planning to submit to)	Click or tap here to enter text.	
k) List the manuscript's authors in the intended authorship order:	Click or tap here to enter text.	

l) Stage of publication	Please select.

13. For multi-authored work, please give a statement of contribution covering all authors (if single-author, please skip to section 4**):**

Xiaoyan Xu: Conceptualization, Methodology, Software, Validation, Formal Analysis, Investigation, Resources, Data Curation, Writing—original draft preparation, Visualization. **Sahar Awwad**: Conceptualization, Methodology, Software, Validation, Formal Analysis, Investigation, Resources, Data Curation, Writing—original draft preparation, Visualization. **Luis Diaz-Gomez**: Validation, Investigation, Resources, Writing—review and editing, Visualization. **Carmen Alvarez-Lorenzo**: Validation, Investigation, Resources, Writing—review and editing, Visualization. **Steve Brocchini**: Writing—review and editing, Visualization. **Simon Gaisford**: Writing—review and editing, Visualization, Supervision, Funding Acquisition. **Alvaro Goyanes**: Conceptualization, Methodology, Writing—review and editing, Visualization, Supervision, Project Administration, Funding Acquisition. **Abdul W. Basit**: Conceptualization, Writing—review and editing, Visualization, Supervision, Project Administration, Funding Acquisition.

14. In which chapter(s) of your thesis can this material be found?

Chapter 3 DLP 3D printing of punctal plugs

15. e-Signatures confirming that the information above is accurate (this form should be co-signed by the supervisor/ senior author unless this is not appropriate, e.g. if the paper was a single-author work):

Candidate:	Xiaoyan Xu	**Date:**	05/10/2022
Supervisor/ Senior Author (where appropriate)**:**	Professor Simon Gaisford	**Date:**	31/10/2022

UCL Research Paper Declaration Form: referencing the doctoral candidate's own published work(s)

Please use this form to declare if parts of your thesis are already available in another format, e.g. if data, text, or figures:

- have been uploaded to a preprint server;
- are in submission to a peer-reviewed publication;
- have been published in a peer-reviewed publication, e.g. journal, textbook.

This form should be completed as many times as necessary. For instance, if you have seven thesis chapters, two of which containing material that has already been published, you would complete this form twice.

16. For a research manuscript that has already been published (if not yet published, please skip to section 2)**:**		
p) Where was the work published? (e.g. journal name)	Additive Manufacturing	
q) Who published the work? (e.g. Elsevier/Oxford University Press):	Elsevier	
r) When was the work published?	13/01/2020	
s) Was the work subject to academic peer review?	Yes	
t) Have you retained the copyright for the work?	Yes	
[If no, please seek permission from the relevant publisher and check the box next to the below statement]: ☐ *I acknowledge permission of the publisher named under 1b to include in this thesis portions of the publication named as included in 1a.*		
17. For a research manuscript prepared for publication but that has not yet been published (if already published, please skip to section 3)**:**		
m) Has the manuscript been uploaded to a preprint server? (e.g. medRxiv):	Please select.	**If yes, which server?** Click or tap here to enter text.
n) Where is the work intended to be published? (e.g. names of journals that you are planning to submit to)	Click or tap here to enter text.	
o) List the manuscript's authors in the intended authorship order:	Click or tap here to enter text.	

p) Stage of publication	Please select.

18. For multi-authored work, please give a statement of contribution covering all authors (if single-author, please skip to section 4**):**

Xiaoyan Xu: Conceptualization, Methodology, Software, Validation, Formal analysis, Investigation, Resources, Data curation, Writing - original draft, Writing - review & editing. **Pamela Robles-Martinez**: Conceptualization, Methodology, Software, Validation, Formal analysis, Investigation, Resources, Data curation, Writing - review & editing, Visualization. **Christine M. Madla**: Conceptualization, Methodology, Resources, Writing - review & editing. **Fanny Joubert**: Conceptualization, Methodology, Software, Validation, Formal analysis, Investigation, Data curation, Writing - review & editing. **Alvaro Goyanes**: Conceptualization, Methodology, Resources, Writing - review & editing, Supervision, Project administration. **Abdul W. Basit**: Conceptualization, Methodology, Writing - review & editing, Supervision, Project administration. **Simon Gaisford**: Conceptualization, Methodology, Writing - review & editing, Supervision, Project administration.

19. In which chapter(s) of your thesis can this material be found?

Chapter 4 SLA 3D printing of antihypertensive polyprintlets

20. e-Signatures confirming that the information above is accurate (this form should be co-signed by the supervisor/ senior author unless this is not appropriate, e.g. if the paper was a single-author work):

Candidate:	Xiaoyan Xu	**Date:**	05/10/2022
Supervisor/ Senior Author (where appropriate)**:**	Professor Simon Gaisford	**Date:**	31/10/2022

UCL Research Paper Declaration Form: referencing the doctoral candidate's own published work(s)

Please use this form to declare if parts of your thesis are already available in another format, e.g. if data, text, or figures:

- have been uploaded to a preprint server;
- are in submission to a peer-reviewed publication;
- have been published in a peer-reviewed publication, e.g. journal, textbook.

This form should be completed as many times as necessary. For instance, if you have seven thesis chapters, two of which containing material that has already been published, you would complete this form twice.

21. For a research manuscript that has already been published (if not yet published, please skip to section 2)**:**	
u) Where was the work published? (e.g. journal name)	International Journal of Pharmaceutics
v) Who published the work? (e.g. Elsevier/Oxford University Press):	Elsevier
w) When was the work published?	18/10/2021
x) Was the work subject to academic peer review?	Yes
y) Have you retained the copyright for the work?	Yes

[If no, please seek permission from the relevant publisher and check the box next to the below statement]:

☐ *I acknowledge permission of the publisher named under 1b to include in this thesis portions of the publication named as included in 1a.*

22. For a research manuscript prepared for publication but that has not yet been published (if already published, please skip to section 3)**:**		
q) Has the manuscript been uploaded to a preprint server? (e.g. medRxiv):	Please select.	**If yes, which server?** Click or tap here to enter text.
r) Where is the work intended to be published? (e.g. names of journals that you are planning to submit to)	Click or tap here to enter text.	
s) List the manuscript's authors in the intended authorship order:	Click or tap here to enter text.	

t)	**Stage of publication**	Please select.

23. For multi-authored work, please give a statement of contribution covering all authors (if single-author, please skip to section 4**):**
Xiaoyan Xu: Conceptualization, Data curation, Formal analysis, Investigation, Methodology, Validation, Visualization, Writing – original draft, Writing – review & editing. **Alejandro Seijo-Rabina:** Data curation, Investigation, Methodology. **Atheer Awad:** Conceptualization, Visualization, Writing – original draft, Writing – review & editing. **Carlos Rial:** Software, Validation. **Simon Gaisford:** Supervision, Writing – review & editing. **Abdul W. Basit:** Conceptualization, Supervision, Project administration, Writing – review & editing. **Alvaro Goyanes:** Conceptualization, Methodology, Supervision, Project administration, Writing – review & editing.

24. In which chapter(s) of your thesis can this material be found?
Chapter 5 Smartphone-enabled DLP 3D printing of medicines

25. e-Signatures confirming that the information above is accurate (this form should be co-signed by the supervisor/ senior author unless this is not appropriate, e.g. if the paper was a single-author work):

Candidate:	Xiaoyan Xu	**Date:**	05/10/2022
Supervisor/ Senior Author (where appropriate)**:**	Professor Simon Gaisford	**Date:**	31/10/2022

Table of Contents

List of figures

List of tables

Abbreviations

2D	Two-dimensional
2PP	Two-photon polymerisation
3D	Three-dimensional
4D	Four-dimensional
ABS	Acrylonitrile butadiene styrene
ACN	Acetonitrile
AI	Artificial intelligence
API	Active pharmaceutical ingredient
ASTM	American Society for Testing and Materials
CAD	Computer aided design
CLIP	Continuous liquid interface production
CT	Computed tomography
DLP	Digital light processing
DMD	Digital mirror device
DMSO	Dimethyl sulfoxide
DSC	Differential scanning calorimetry
EGDMA	Ethylene glycol dimethacrylate
EOS	Eosin Y disodium salt
FA	Formic acid
FDA	Food and Drug Administration
FDM	Fused deposition modelling
FTIR	Fourier Transform Infrared
GRAS	Generally Recognised as Safe
HEMA	2-hydroxyethyl methacrylate
HMBC	Heteronuclear Multiple-Bond Correlation
HME	Hot melt extrusion
HPLC	High performance liquid chromatography
HPMC	Hydroxypropyl methylcellulose
HSQC	Heteronuclear Single Quantum Correlation
IPA	Isopropyl alcohol
IPN	Interpenetrating network
LAP	Lithium phenyl (2,4,6-trimethylbenzoyl) phosphinate
LCD	Liquid crystal display
LED	Light-emitting diodes

MRI	Magnetic resonance imaging
MW	Molecular weight
NIR	Near-infrared
NMR	Nuclear magnetic resonance
PBS	Phosphate buffered saline
PCL	Polycaprolactone
PEG	Polyethylene glycol
PEGDA	Poly(ethylene glycol) diacrylate
PEGDMA	Poly(ethylene glycol) dimethacrylate
PEGMA	Poly(ethylene glycol) methacrylate
PEO	Polyethylene oxide
PET	Positron emission tomography
PLA	Polylactic acid
Printlet	3D printed tablet
Polyprintlet	3D printed polypill
PVA	Polyvinyl alcohol
RBF	Riboflavin
Ru	Tris (2'2-bipyridyl) dichlororuthenium (II) hexahydrate
SA/V	Surface area/volume
SD	Standard deviation
SEM	Scanning electron microscopy
SLA	Stereolithography
SLS	Selective laser sintering
SP	Sodium persulfate
SSE	Semi-solid extrusion
TEA	Triethanolamine
TFA	Trifluoracetic acid
TPA	Two-photon absorption
TPO	Diphenyl (2,4,6-trimethylbenzoyl) phosphine oxide
USP	United States pharmacopoeia
UV	Ultraviolet
XRPD	X-ray powder diffraction
ZnTPP	Zinc tetraphenylporphyrin

Chapter 1

Introduction

1. Introduction

1.1 Thesis overview

Three-dimensional (3D) printing is a flexible technology that allows the creation of bespoke objects from a computer-aided design (CAD) model in a layer-by-layer manner. In the pharmaceutical field, 3D printing is disrupting the way medicines are designed and manufactured by enabling the fabrication of personalised medicines on demand.

Among different 3D printing techniques, vat photopolymerisation 3D printing is a process that utilises light irradiation to create physical objects from a vat of photocurable materials. This technology offers high flexibility using versatile materials and provides superior printing resolution and accuracy. Vat photopolymerisation 3D printing has attracted attention in healthcare and biomedical applications including patient-specific medical devices and engineered tissues, however, its pharmaceutical applications have remained relatively unexplored.

The overall objective of this thesis is to design a range of drug delivery devices with customisable release profiles by vat photopolymerisation 3D printing. The development of devices for different drug delivery purposes including intravesical devices (Chapter 2), punctal plugs (Chapter 3), and antihypertensive polypills (Chapter 4) has been investigated. In Chapter 5, a vat photopolymerisation-based smartphone-enabled DLP 3D printing system has also been developed for the preparation of personalised medications.

In this chapter, an overview of 3D printing and its recent applications in pharmaceutics will be provided, followed by an introduction to various 3D printing technologies with a more detailed description of vat photopolymerisation 3D printing including the working principles, different printing techniques and their applications in the field of drug delivery.

1.2 Introduction of 3D printing and general applications

Three-dimensional (3D) printing, also known as additive manufacturing or rapid prototyping, is a construction process of physical objects based on a computer-aided design (CAD) model in which material is deposited in a layer-by-layer manner (Basit and Gaisford, 2018). In the 1980s, the first 3D printing technology was first invented by Charles Hull as a rapid prototyping tool to produce aesthetic or functional models (Hull, 1984).

The advancements in its precision, repeatability, and material choice have rapidly expanded applications of 3D printing across countless fields ranging from electronics (Kalkal et al., 2021; Lewis and Ahn, 2015), construction (Kanyilmaz et al., 2021; Tay et al., 2017), food sciences (Varvara et al., 2021), robotics (Wallin et al., 2018), education (Garcia et al., 2018), aerospace industry (Joshi and Sheikh, 2015) as well as healthcare including personalised drug delivery products and biomedical applications such as tissues and organs (**Figure 1.1**) (Awad et al., 2018a; Beg et al., 2020; Prendergast and Burdick, 2020; Trenfield et al., 2019a), dentistry (Khorsandi et al., 2021), biosensors (Elbadawi et al., 2020), and prosthesis (Ghosh et al., 2018).
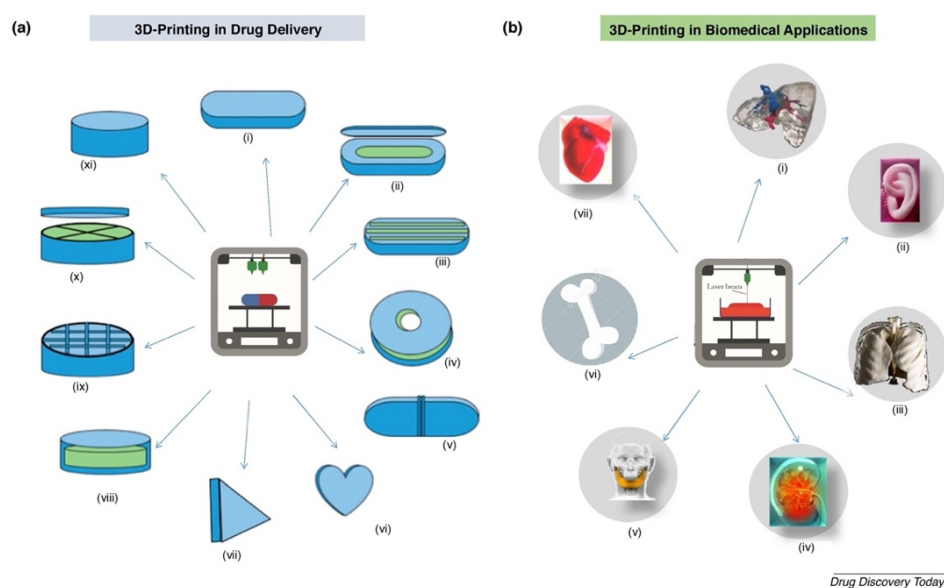
Figure 1.1 Examples of 3D printing technology for drug delivery and biomedical applications: (a) 3D printed tablets in various shapes; (b) development of tissue and organs (Beg et al., 2020).

3D printing has also stepped up and served as an efficient manufacturing option to support healthcare against COVID-19 pandemic (Choong et al., 2020; Radfar et al., 2021). The digital versatility and rapid prototyping of 3D printing allowed decentralised fabrication of personalised protective equipment, medical and testing devices, and isolation wards.

1.3 3D printing of pharmaceuticals

Conventionally, medicines like tablets are mass manufactured in limited discrete strengths which are selected based on the dose required for a safe and therapeutic effect in the majority of the population (Basit and Gaisford, 2018). However, it is evident that one dose might not fit all, and dose requirements could vary based on a patient's genetic profile, disease state, and other factors (age, gender, weight, ethnicity) (Trenfield et al., 2018). Reaction to the same active ingredient and dose can vary significantly among different individuals. Some may experience excessive response associated with adverse drug reactions while others may not feel any significant pharmacological effects due to a weak response (Vaz and Kumar, 2021). This leads to the development of personalised medicine approaches where medications are tailored for the individual rather than the broad patient population (Prendergast and Burdick, 2020). 3D printing could contribute to this transformation by allowing on-demand production of drug products where the dosage, size, shape, release characteristics can be tailored to suit individual patient's need (Trenfield et al., 2019a). In 2016, the U.S. Food and Drug Administration (FDA) approval of the first 3D printed tablet Spritam® by Aprecia Pharmaceutical has established a significant milestone in the pharmaceutical manufacturing history (Trenfield et al., 2021). Using their Zipdose® manufacturing technology, which is based on binder jet printing, high-dose (up to 1000 mg) and fast-dissolving epilepsy medications are produced, benefiting patients with swallowing difficulty or high pill burden. In the last decade, the number of publications on 3D printing in drug delivery has remarkably increased (**Figure 1.2**), confirming the great potential of 3D printing

in developing personalised medications and is expected to continue rapidly evolving in the next decades (Wang et al., 2021a).
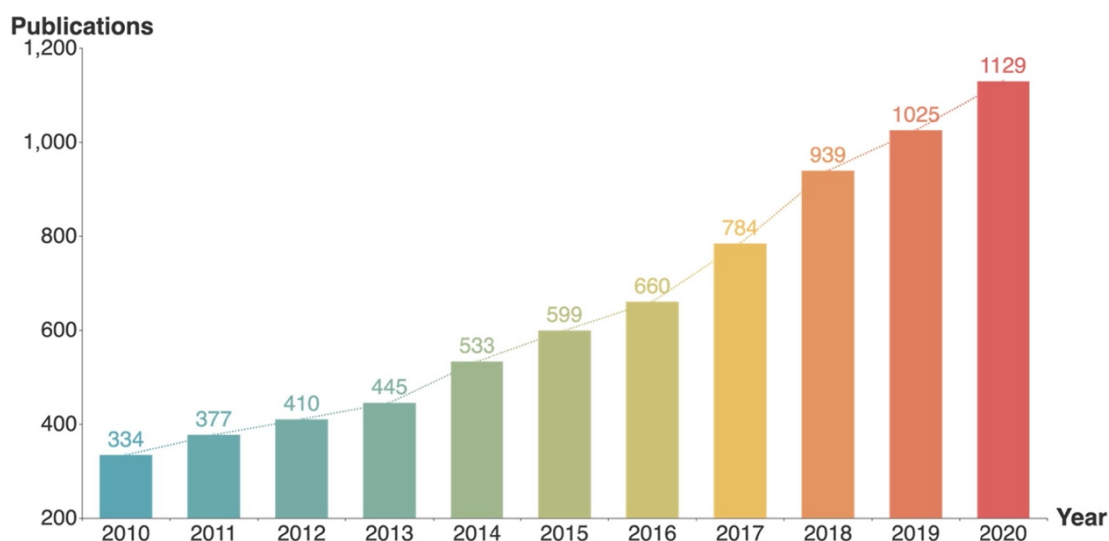
Figure 1.2 Number of publications on 3D printing in drug delivery (2010 - 2020) (Wang et al., 2021a).

1.3.1 Dose flexibility

The dosing requirement can be clearly different for young children and the elderly compared with adults due to physical (age, weight, body surface area) and pharmacokinetics characteristics (metabolic capacity, drug clearance, organ function) (Basit and Gaisford, 2018). Furthermore, narrow therapeutic index drugs such as warfarin (Vuddanda et al., 2018) and theophylline (Okwuosa et al., 2017) require individualised and precise dosing to ensure the therapeutic efficacy and safety. As medicines are formulated in limited discrete strengths, patients or caretakers tend to split tablets or to open the capsules to achieve the desired dose (Trenfield et al., 2018). However, such practices present the risk of inaccurate dosing and dose deviation, which may lead to serious clinical consequences.

To overcome these challenges, 3D printing can be used to fabricate pharmaceuticals with exact doses by changing the dimensions or infill percentage of the dosage forms. The infill percentage could be defined as the

degree to which the 3D printer will fill the hollow object with materials, revealing the porosity of the 3D printed tablets where 0% is a hollow shell and 100% is a solid and nonporous object (**Figure 1.3**) (Goyanes et al., 2014; Pietrzak et al., 2015; Skowyra et al., 2015). In a first single-centre, prospective, crossover study in patients, 3D printed tailored-dose chewable formulations were prepared in a hospital setting for patients with rare metabolic disorder (**Figure 1.3d**) (Goyanes et al., 2019).

The high dose flexibility of 3D printing can also benefit the early phase drug development process (for example, pre-clinical, first-in-human through Phase I/II clinical trials) by enabling inexpensive and rapid small-batch production of formulations (Seoane-Viaňo et al., 2021b).
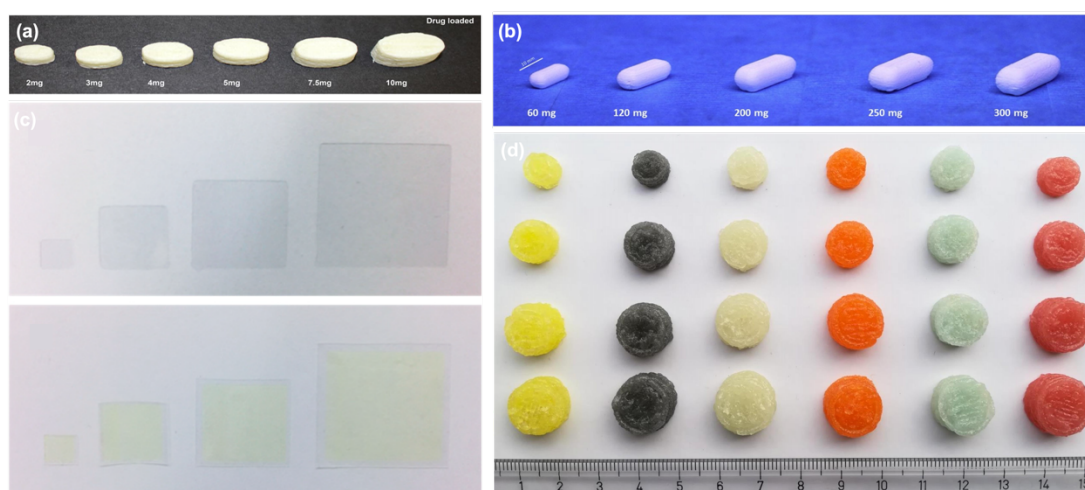
Figure 1.3 (a) 3D printed prednisolone tablets (Skowyra et al., 2015); (b) 3D printed theophylline tablets (Pietrzak et al., 2015) with increasing dose; (c) orodispersible warfarin films prepared by semi-solid extrusion 3D printing and 2D inkjet printing (Öblom et al., 2019); and (d) 3D printed chewable tablets in different colours/favours and doses (Goyanes et al., 2019).

1.3.2 Improved patient acceptability

3D printing can be used to product patient-friendly oral dosage forms, for example, fast-dissolving tablets (Fina et al., 2018c), orodispersible films (Jamróz et al., 2017) and taste-masking chewable formulations (**Figure 1.4a,**

b and c) (Herrada-Manchón et al., 2020; Karavasili et al., 2020a; Tabriz et al., 2021), which could greatly improve patient acceptability, especially among geriatric and paediatric patients. Moreover, a patient acceptability study with regards to ease of swallowability and picking was conducted using a variety of 3D printed tablets (Printlets™) of different sizes and shapes (Goyanes et al., 2017b) (**Figure 1.4d**). The results demonstrated that torus Printlets received the highest score for ease of swallowing and picking and the study highlighted the potential of 3D printed formulations towards tailoring patient's preferences and improving medication adherence.
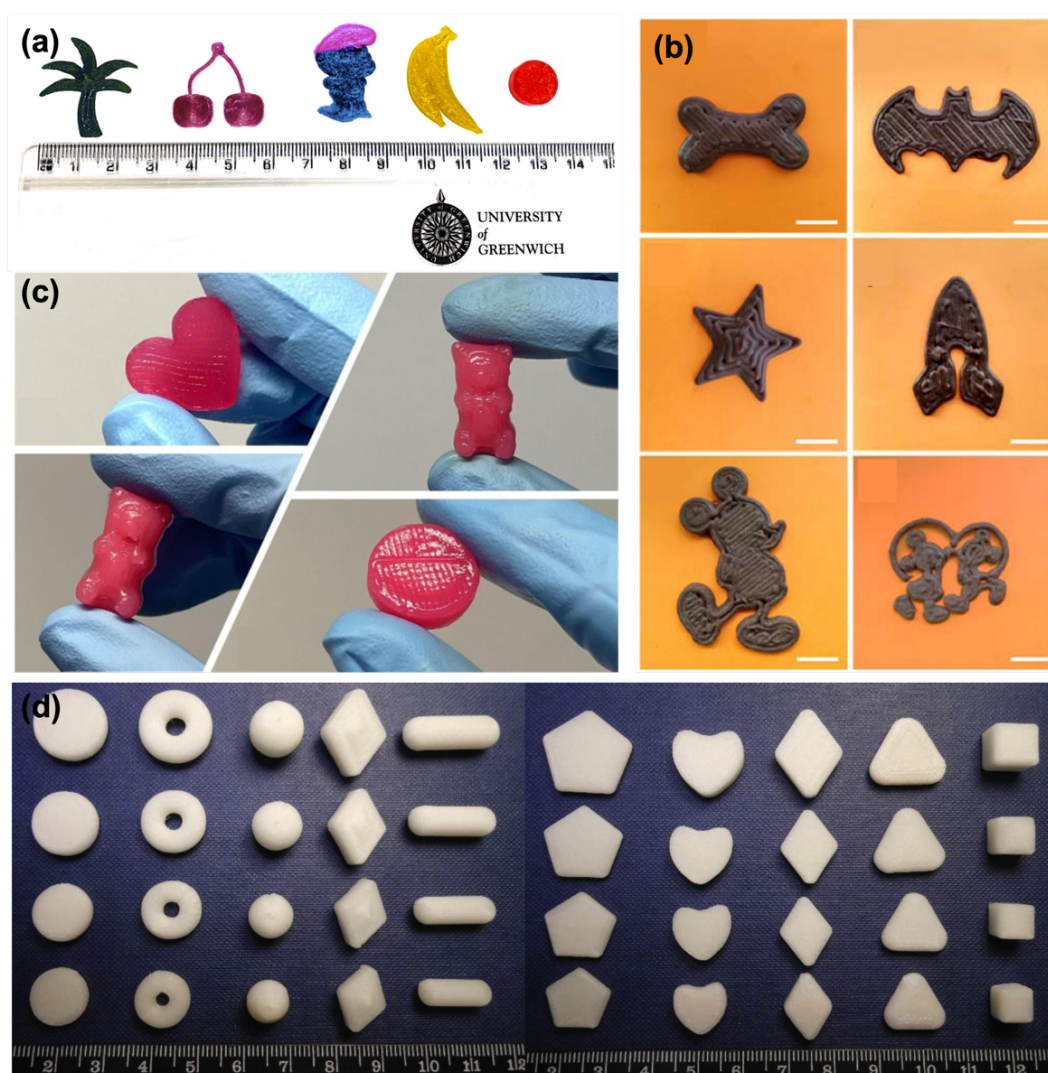
Figure 1.4 (a) 3D printed fruit-chewable formulations (Tabriz et al., 2021); (b) 3D printed chocolate-based dosage forms (Karavasili et al., 2020a); (c) 3D printed gummies in different shapes (Herrada-Manchón et al., 2020); and (d) 3D printed tablets in different sizes and shapes (Goyanes et al., 2017b).

1.3.3 Multi-drug combinations

With an aging population, polypharmacy (commonly defined as the concurrent use of five or more medicines) is a growing concern (Trenfield et al., 2018). Besides, treatment plans of complex diseases such as diabetes, hypertension, and tuberculosis often involve administration of multiple drugs, which could be problematic and lead to medication errors, poor adherence, and increase risk of drug duplication (Charlesworth et al., 2015). In these instances, combining multiple active pharmaceutical ingredients (APIs) into a single dosage form, also referred to as polypills' could simplify a dosing regimen without compromising the treatment plan. However, traditional manufacturing processes such as tableting are limited to produce polypills with a fixed-dose-combinations instead of customised polypills for individual patient's need. Due to its design freedom and capability of accurate distribution of multiple materials, 3D printing is well suited to producing multi-drug formulations (**Figure 1.5**). So far, numerous research has been carried out to demonstrate 3D printing of polypills incorporating 2 (Goyanes et al., 2015c; Haring et al., 2018), 4 (Goh et al., 2021; Pereira et al., 2020), 5 (Khaled et al., 2015a), or 6 different drugs in various designs (Robles-Martinez et al., 2019). More discussions of 3D printing of polypills will be present in the introduction of Chapter 4 SLA 3D printing of antihypertensive polyprintlets.
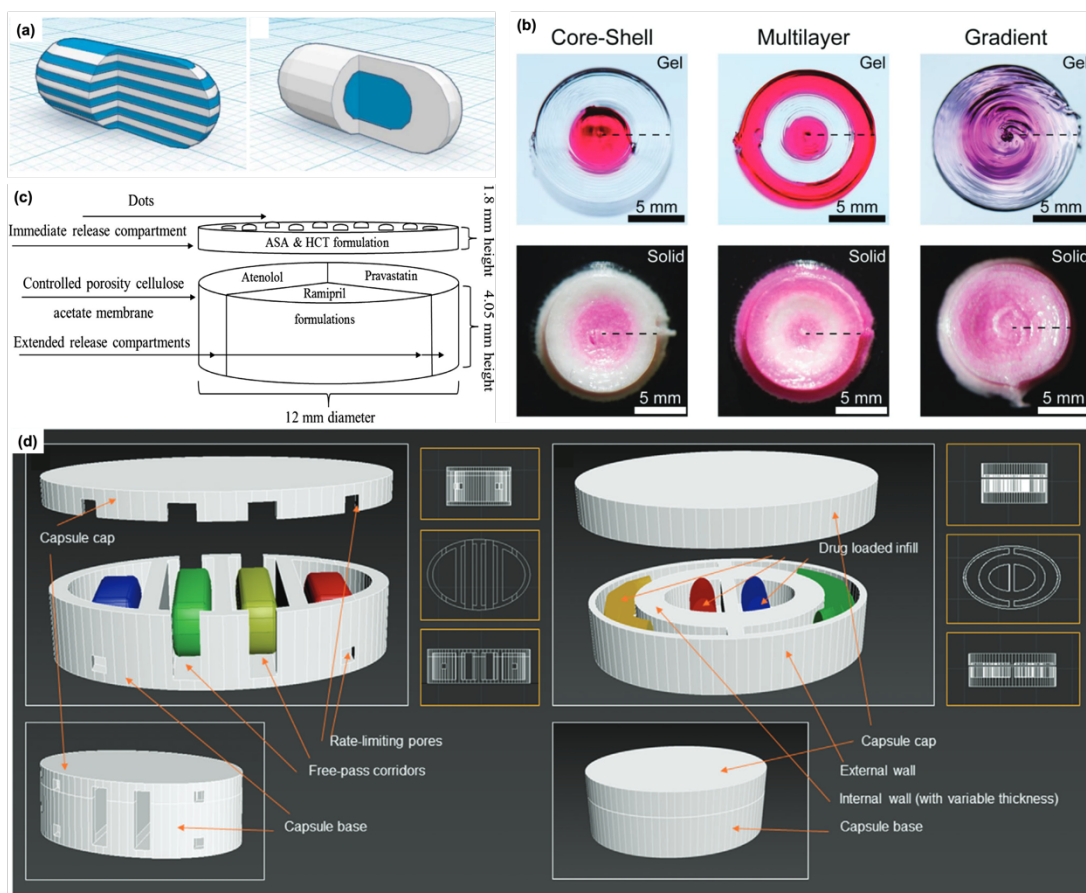
Figure 1.5 (a) 3D representation of the multilayer capsule-shaped tablet (left) and DuoCaplet (right) (Goyanes et al., 2015c); (b) 3D printed polypills containing core-shell, multilayer, and gradient concentration profiles (Haring et al., 2018); (c) Schematic diagram of a five-in-one polypill design (Khaled et al., 2015a); and (d) 3D representation of polypills in two different designs (Pereira et al., 2020).

1.3.4 Tailored release profiles

Importantly, it is necessary to tailor release profiles for patients with different medical and biological conditions (Sun and Soh, 2015). By selecting the suitable excipients and modifying printing parameters, oral dosage forms could be prepared to have defined release characteristics. For example, by changing the surface area to volume ratio of the Printlets, drug release rates were modified and the time to 90% release varied from under 2 h (pyramid) to nearly 12h (sphere and cylinder) (**Figure 1.6a**) (Goyanes et al., 2015b). On the other

hand, modulating printing parameters such as infill percentage in fused deposition modelling (FDM) 3D printing (**Figure 1.6b**) (Thakkar et al., 2020) and laser scanning speeds in selective laser sintering (SLS) 3D printing (Fina et al., 2018c) could also alter the release profiles. Furthermore, release rates can also be fine-tuned by changing the design of the Printlets, for instance, by adding perforated holes (Kadry et al., 2019) and channels (**Figure 1.6d**) (Sadia et al., 2018), and controlling the wall thickness within the capsule (Smith et al., 2018).

By adjusting the concentration of excipients such as hydroxypropyl methylcellulose (HPMC) (Khaled et al., 2014), or using different grade of enteric polymer (Eudragit® L100-55) (Goyanes et al., 2017a), or adding hydrophilic excipients such as polyethylene glycol (PEG), sodium chloride, and mannitol as diluents in the polymeric matrix (Krkobabić et al., 2019; Wang et al., 2016), the release rates could be modified accordingly.

Other than drug release rates, 3D printed oral dosage forms can also be produced with multiple controlled release profiles. Khaled et al. used extrusion 3D printing to develop a five-in-one polypill with two independent controlled release profiles (**Figure 1.6c**) (Khaled et al., 2015a). This dosage form was made of three sustained release compartments which were physically separated by a hydrophobic cellulose acetate shell and covered with an immediate release compartment. Moreover, other important types of release profiles such as zero-order (Fina et al., 2020), increasing, decreasing, and pulsatile (Tan et al., 2020; Xu et al., 2019) could also be customised via 3D printing technologies.
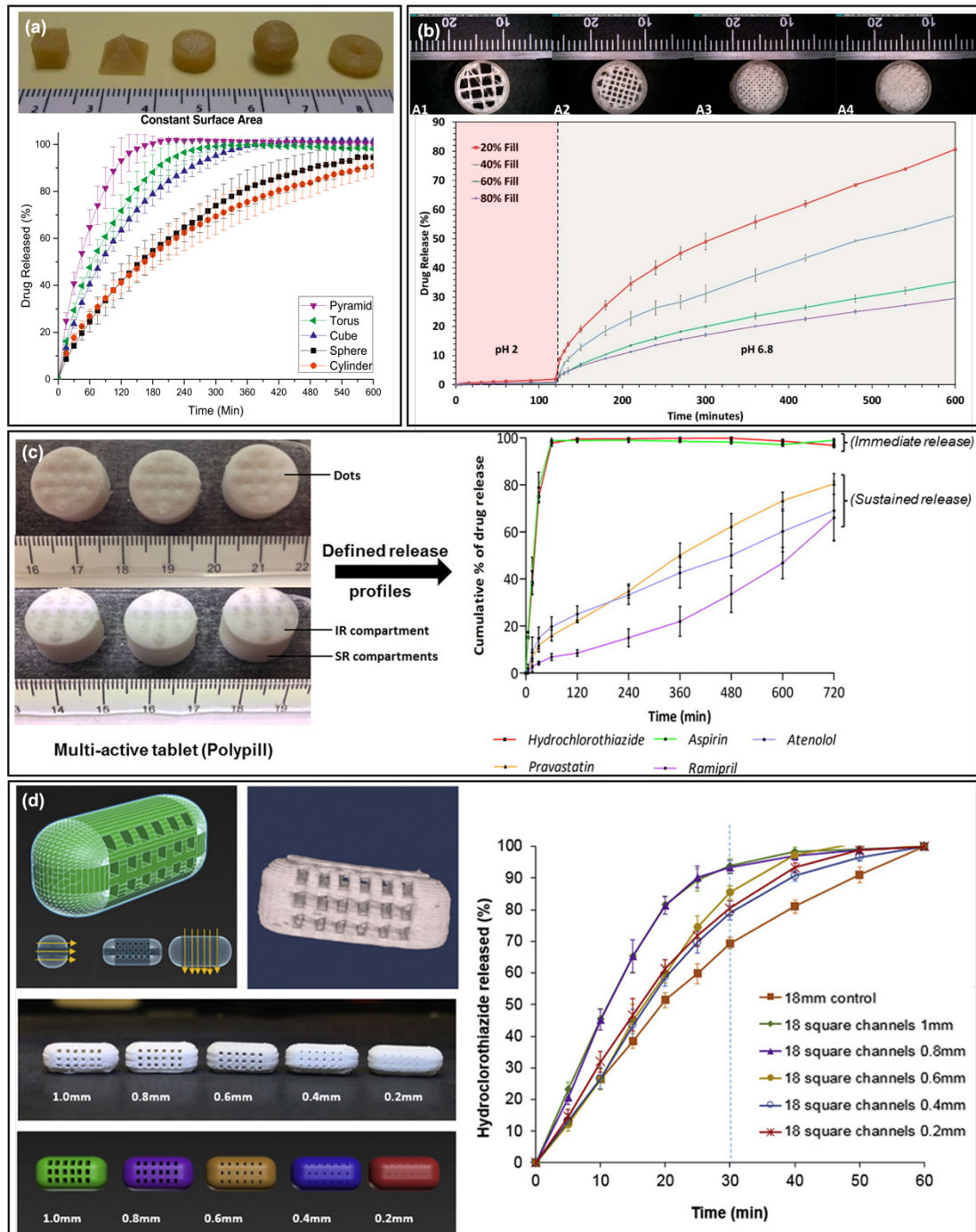
Figure 1.6 (a) 3D printed paracetamol tablets at constant surface area and their drug release profile (Goyanes et al., 2015b); (b) 3D printed ibuprofen tablets with 20%, 40%, 60% and 80% infill density and their drug release profile (Thakkar et al., 2020); (c) 3D printed polypill showing immediate and sustained release profiles (Khaled et al., 2015a); and (d) 3D printed hydrochlorothiazide caplets with 18 channels in decreasing channel size and their drug release profile (Sadia et al., 2018).

1.3.5 Applications with unique functions

Apart from oral dosage forms, 3D printing of pharmaceutical applications with unique functions have also been developed. For instance, 3D printed tramadol Printlets with alcohol-resistant and abuse-deterrent properties were prepared, offering a novel strategy for reducing the prevalence and risks of opioid abuse (**Figure 1.7a**) (Ong et al., 2020). In order to facilitate pre-clinical studies in animals, 3D printed capsular radiolabelled devices have been introduced in rodents for the evaluation of their *in vivo* behaviours by positron emission tomography/computed tomography (PET/CT) imaging (**Figure 1.7b**) (Goyanes et al., 2018). Other examples also include 3D printed oral Printlets with dual track-and-trace (QR code or data matrix) and anti-counterfeit mechanisms (**Figure 1.7c**) (Trenfield et al., 2019b) and 3D printed oral disintegrating Printlets (Awad et al., 2020) and intraoral films (Eleftheriadis and Fatouros, 2021) with Braille patterns suited for patients with visual impairment (**Figure 1.7d**).
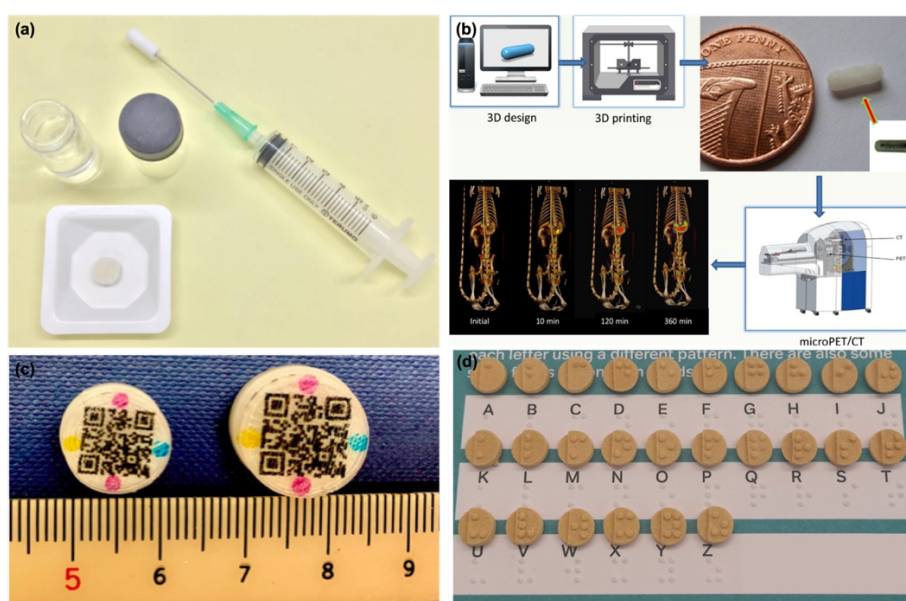
Figure 1.7 (a) Image showing a 3D printed tramadol Printlet designed to deter drug abuse (Ong et al., 2020); (b) PET/CT imaging of 3D printed capsular devices in the gastrointestinal tract of rodents (Goyanes et al., 2018); (c) 3D printed Printlets with anti-counterfeit designs and QR codes (Trenfield et al., 2019b); and (d) 3D printed cylindrical Printlets with Braille patterns (Awad et al., 2020).

1.3.6 Patient-specific drug delivery devices

In recent years, 3D printing has also been combined with 3D scanning to create individualised drug delivery devices. By using handheld 3D scanners or imaging techniques such as magnetic resonance imaging (MRI) or CT scan, patient's unique anatomical features can be captured and 3D printing allows the fabrication of patient-centric devices for different drug delivery purposes. For example, anti-acne nose patch (**Figure 1.8a**) (Goyanes et al., 2016), anti-biofilm hearing aids (**Figure 1.8b**) (Vivero-Lopez et al., 2021b), mouthguards (**Figure 1.8f**) (Liang et al., 2018), devices for topical skin delivery (**Figure 1.8g**) (de Oliveira et al., 2021), and stents (Paunović et al., 2021). Furthermore, lots of drug-eluting devices or implants for local delivery have also been developed to improve patient convenience and compliance by reducing drug administration frequency such as microneedles (Detamornrat et al., 2022), contraceptive devices (**Figure 1.8e**) (Fu et al., 2018), intrauterine devices (**Figure 1.8d**) (Genina et al., 2016), and suppositories (**Figure 1.8c**) (Seoane-Viaño et al., 2020).
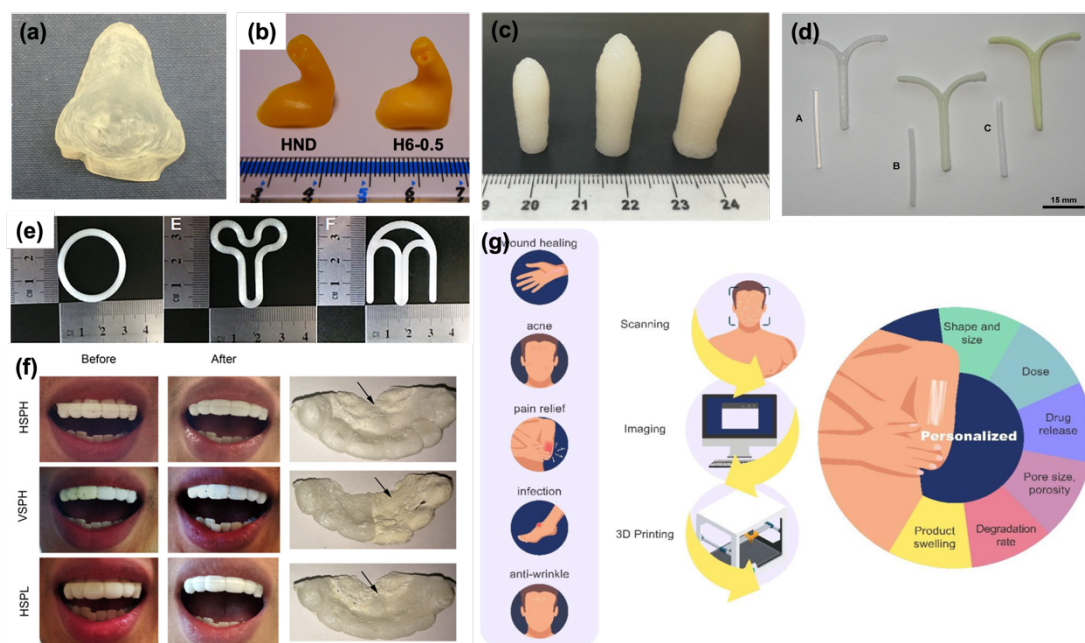
Figure 1.8 (a) 3D printed anti-acne nose patch (Goyanes et al., 2016); (b) 3D printed anti-biofilm hearing aids (Vivero-Lopez et al., 2021b); (c) 3D printed suppositories in different sizes (Seoane-Viaño et al., 2020); (d) The filaments and 3D printed intrauterine prototypes (Genina et al., 2016); (e) 3D printed

vaginal rings with different designs (Fu et al., 2018); (f) Images of different types of 3D printed mouthguards before and after three cycles of wearing by the same volunteer (Liang et al., 2018); and (g) 3D printed products for topical skin delivery (de Oliveira et al., 2021).

1.4   Classification of 3D printing technologies

3D printing is an umbrella term that encompasses a range of different technologies which differ from each other in the feedstock materials (e.g. resins, metals, ceramics, plastics), deposition mechanism, and the characteristics of the final obtained object (Basit and Gaisford, 2018). The American Society for Testing and Materials (ASTM) International classifies 3D printing technologies into seven categories namely binder jetting, powder fusion, direct energy deposition, material extrusion, material jetting, powder bed fusion, sheet lamination, and vat photopolymerisation (ASTM ISO, 2022a) (**Figure 1.9**). This section will provide a general overview of the most used 3D printing technologies in the fabrication of medicines and a summary of their features is shown in **Table 1.1**.
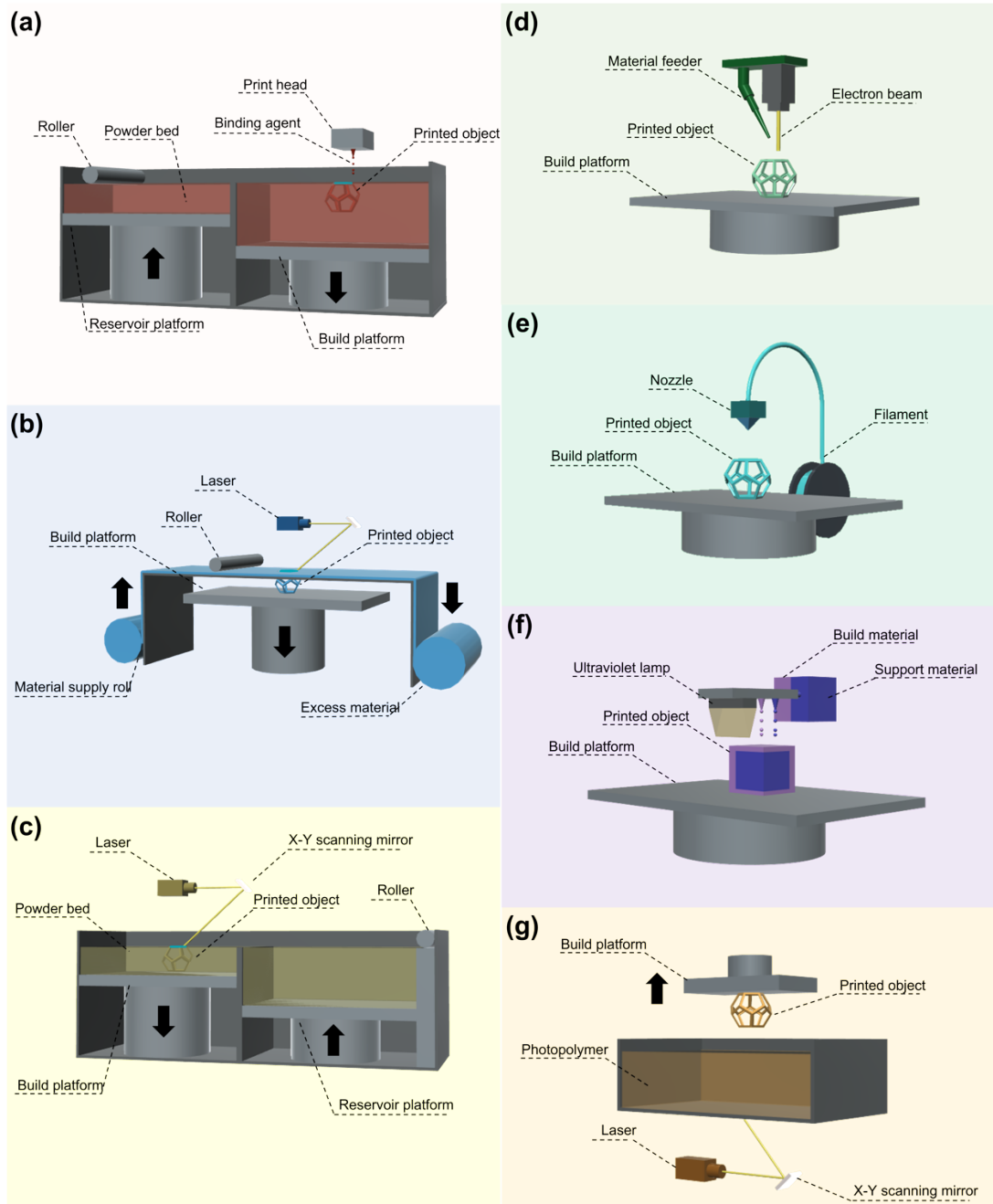
Figure 1.9 Graphical representation of various 3D printing technologies: (a) binding jetting; (b) sheet lamination; (c) powder bed fusion; (d) direct energy deposition; (e) material extrusion; (f) material jetting; and (g) vat photopolymerisation, created with 123D Design (Autodesk Inc., USA).

Table 1.1 A summary of features associated with examples of 3D printing technologies.

3D printing technologies	Technique	Material	Average resolution (mm) (Awad et al., 2018b)
Binder jetting	Binder jetting	Powder and liquid binder	0.089 – 0.12
Powder bed fusion	SLS	Powder	0.1 – 0.12
Material extrusion	FDM	Filaments	0.1 – 0.3
	SSE	Gels and pastes	0.4 – 0.8
Vat photopolymerisation	SLA	Liquid photopolymer	0.025 – 0.125
	DLP		0.012 – 0.2
	CLIP		0.05 – 0.1

1.4.1 Binder jetting

In 1993, binder jetting was introduced at the Massachusetts Institute of Technology (Sachs et al., 1993). In this method, an initial layer of powder is spread onto the build platform by a roller, followed by selective deposition of liquid binding agent from a print head onto the powder bed to form the given cross-section of the CAD model (**Figure 1.9a**) (Ziaee and Crane, 2019). Once the first layer is solidified, the build platform is lowered to allow another layer to be distributed onto the previous one. The process is repeated until the desired object is finished. Similar to powder bed fusion, the fabricated part is physically supported by loose powder in the powder bed, eliminating the requirement for support design (Mirzababaei and Pasebani, 2019). A broad variety of materials including metals, biomaterials, ceramics, and polymers have been processed in binder jetting for various applications in the fields of tissue engineering, electronics, and casting to name a few (Inzana et al., 2014; Le Néel et al., 2018; Rojas-Nastrucci et al., 2017; Shirazi et al., 2015). Since its invention, binder jetting has been widely explored in the pharmaceutical sector (**Figure 1.10**) and the first article was published in 1996, demonstrating the feasibility of fabricating drug delivery devices (Katstra et al., 2000; Wang et al., 2006; Wu et al., 1996).

Figure 1.10 Binder jetting 3D printed solid dosage forms of different formulations (Infanger et al., 2019).

1.4.2 Material extrusion

Material extrusion is one of the most common 3D printing technologies, referring to a process in which the material is selectively dispensed through a nozzle onto the build platform (**Figure 1.9e**). FDM or fused filament fabrication is a material extrusion process whereby a filament is fed through a heated nozzle under controlled temperature and melted. The molten thread-like material is then deposited onto a build platform to create solid geometries layer-by-layer once cooled down (Azad et al., 2020; Basit and Gaisford, 2018). It is currently the most widely used form of 3D printing, mainly owing to its simplicity and low cost. Typical feedstock filaments are made of thermoplastic polymers such as polyvinyl alcohol (PVA), acrylonitrile butadiene styrene (ABS), or polylactic acid (PLA). Recent advances in filament fabrication allows the preparation of composite filaments with hot melt extrusion (HME) by blending different materials such as wood (Tao et al., 2017), metallic particles (Palmero et al., 2019), conductive materials (Gnanasekaran et al., 2017), and drugs (Dumpa et al., 2021; Melocchi et al., 2020; Tan et al., 2018) in the polymers. However, the high extrusion or printing temperature used in FDM 3D printing might be a challenge for formulation of thermolabile drugs (Kollamaram et al., 2018).

Besides FDM, semi-solid extrusion (SSE) 3D printing, also residing under the material extrusion umbrella, is a process that employs pressure-assisted microsyringes to deposit gels or pastes on the build platform to create solid

objects (Azad et al., 2020; Seoane-Viaño et al., 2021a). Benefiting from the nature of the feedstock materials, printing at low temperatures is allowed but post-processing steps, for instance, cooling or drying are required. SSE 3D printing has been adapted for bioprinting using cell-embedded bioinks to fabricate and regenerate tissues and organs (Jiang et al., 2019b; Placone and Engler, 2018). A range of pharmaceutical formulations such as chewable dosage forms (**Figure 1.11**) (Herrada-Manchón et al., 2020; Rycerz et al., 2019), polypills (Khaled et al., 2015a; Rowe et al., 2000), and medical devices (Naseri et al., 2020; Seoane-Viaño et al., 2020) have also been reported.
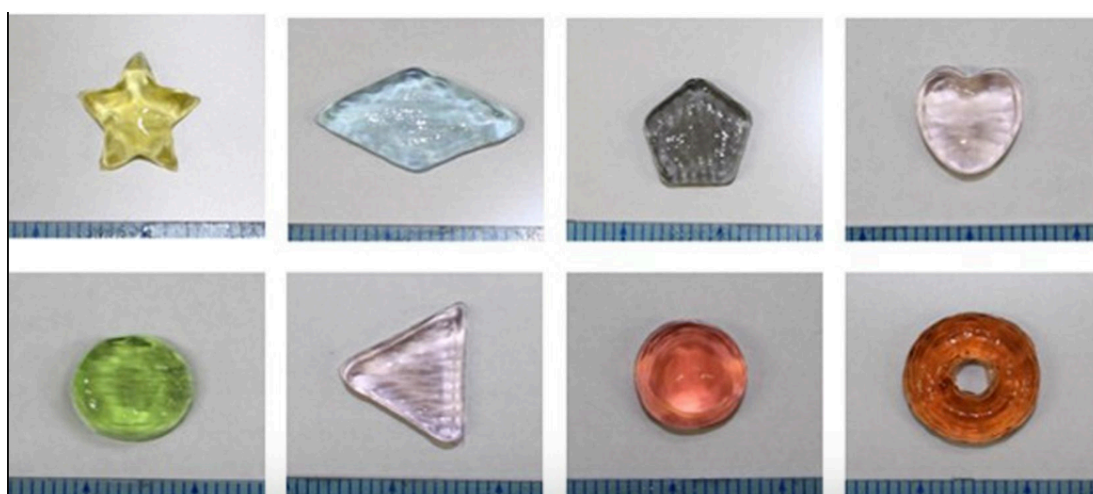
Figure 1.11 SSE 3D printed gummy formulations with various shapes and colours (Tagami et al., 2021a).

1.4.3 Powder bed fusion

Powder bed fusion refers to the selective thermal fusion of powder particles by various sources, such as a laser, into the desired 3D object in a layer-by-layer manner (**Figure 1.9c**) (Fina et al., 2018a). Selective laser sintering (SLS) is a subset of powder bed fusion, and has been recently exploited within the pharmaceutical sector to produce oral dosage forms (Awad et al., 2021a) including orally disintegrating Printlets (**Figure 1.12**) (Allahham et al., 2020; Fina et al., 2018c), pellets (Awad et al., 2019), and drug delivery devices (Salmoria et al., 2018). During the printing process, once the build platform is raised to the highest point, a layer of powder is evenly spread and flattened by

a roller. Upon laser activation, the beam is directed onto the powder bed to create a specific pattern based on the CAD file chosen. After, the build platform is lowered as the reservoir platform is simultaneously elevated to deposit a fresh powder layer above the already sintered material. This process is repeated until completion and the final 3D printed structure is retrieved by the removal of any excess unsintered powder using a brush or compressed air.
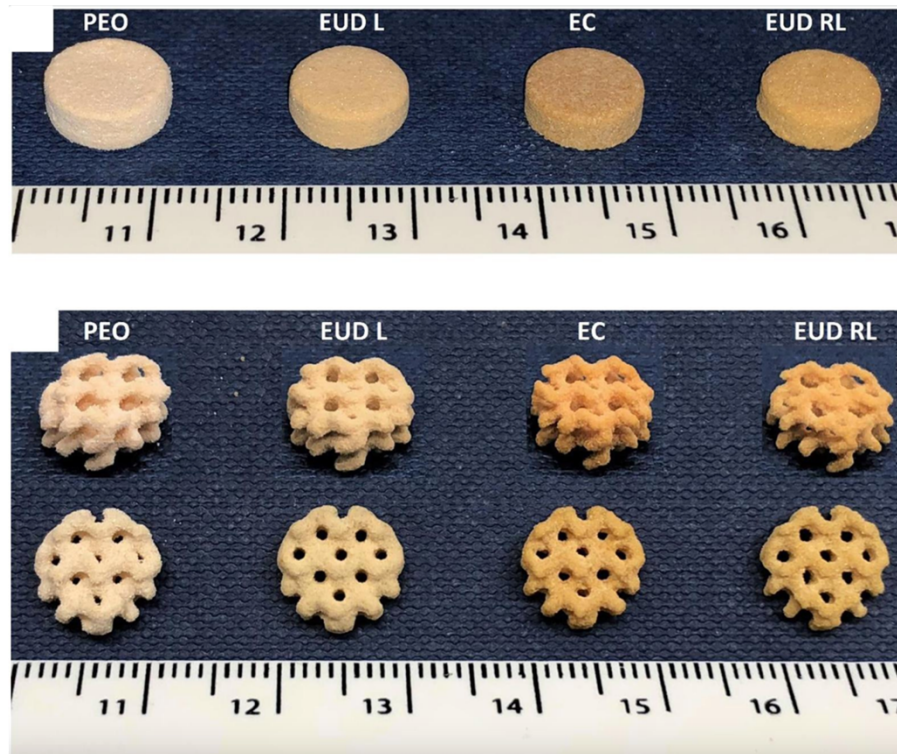
Figure 1.12 SLS 3D printed cylindrical constructs and gyroid lattice solid dosage forms of different polymer formulations (Fina et al., 2018b).

1.4.4 Vat photopolymerisation

Vat photopolymerisation is defined as a liquid to solid process, where computer-spatially-controlled photopolymerisation is used to create solid objects from a vat of liquid resins under light irradiation (**Figure 1.9g**) (Al Rashid et al., 2021; Pagac et al., 2021). This technology offer the benefit of fine details, smooth surface finish, and high accuracy and printing resolution up to the nano-scale region (100 nm) **(Table 1.1)**, enabling the creation of complex microstructures (Kawata et al., 2001; Ng et al., 2020). Compared with

other 3D printing technologies, vat photopolymerisation has a fast-growing journey over the years, from layer-by-layer printing process to continuous production approach, to volumetric printing where the entire object is fabricated at the same time. Benefiting from the room-temperature printing conditions and the use of liquid feedstock material, this type of technology holds enormous potential in biomedical research by allowing incorporation of active biomolecule (e.g., enzymes, antibodies), living materials such as cells or bacteria (Dubbin et al., 2021; Mandon et al., 2016; Ng et al., 2020; Xu et al., 2022), and drug compounds (Krkobabić et al., 2020; Martinez et al., 2017).

1.5   Working principles of vat photopolymerisation 3D printing

Photopolymerisation, also known as photocuring or photocrosslinking, refers to a polymerisation reaction that is induced by light. It requires at least three basic components for the reaction to take place: a photoinitiator, a light source, and a photoreactive monomer or oligomer. Additives such dispersion agents, inhibitors, pigments, and light stabilizers can be incorporated depending on the application (Bártolo, 2011; Fouassier and Lalevée, 2012).

1.5.1   Mechanisms

Depending on the nature of the photoinitiator, photopolymerisation reactions can be radical or ionic (cationic or anionic).

1.5.1.1   Free radical photopolymerisation

One of the most common reactions is the free radical photopolymerisation. The system is well established, and a variety of photoinitiators are available that are activated at different wavelengths. The synthesis of macromolecules by free radical photopolymerisation typically starts with the generation of free radicals from the initiator molecules (Mendes-Felipe et al., 2019). The photopolymerisation process can be broken down into three main steps (Fouassier and Lalevée, 2012):

(I) Initiation

Upon light irradiation, the photoinitiator (PI) decomposes and generates reactive species ($R \cdot$), such as free radicals, which are able to attack the first monomer unit (M) to start the reaction (**Figure 1.13**).

(II) Propagation

Once the photopolymerisation is initiated, the active monomer ($RM \cdot$) then propagates between photoreactive monomers or oligomers to grow the polymeric chains. As the process can occur in 3D, cross-linked networks may be formed.

(III) Termination

The termination step can occur via two types of reaction: recombination or disproportionation. In the case of recombination, two active polymer chains react with each other to terminate the polymerisation. Whereas in the case of disproportionation, a hydrogen atom is transferred from one chain to another, resulting in two polymeric chains.

Initiation	$PI \xrightarrow{hv} R \cdot$
	$R \cdot + M \rightarrow RM \cdot$
Propagation	$RM \cdot + nM \rightarrow RM_{n+1} \cdot$
Termination	$RM_n \cdot + RM_m \cdot \rightarrow RM_nM_mR$ (recombination)
	$RM_n \cdot + RM_m \cdot \rightarrow RM_{n+1} + RM_{m+1}$ (disproportionation)
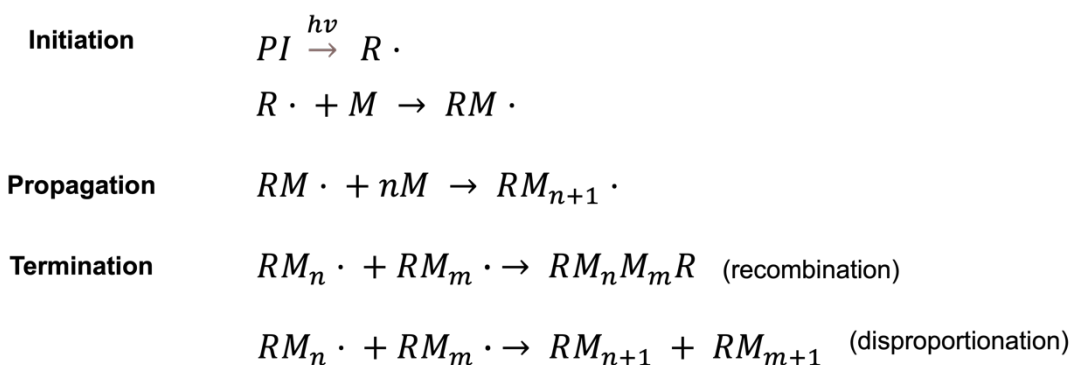
Figure 1.13 General reaction mechanism of free radical photopolymerisation.

Depending upon the way of generating free radicals, there are two types of photoinitiators mainly used in this mechanism. Type I or unimolecular PIs undergo rapid bond cleavage upon light irradiation, resulting in the yielding of a pair of radicals (**Figure 1.14a**). Most of the type I photoinitiators contain

phosphine oxides and acetophenones. On the other hand, type II photoinitiators undergo bimolecular reactions (Schnabel, 2007). After the absorption of light, this photoinitiator forms excited triplet states and is capable of extracting a hydrogen or an electron from suitable co-initiator molecules (e.g., an alcohol or amine) that are deliberately added to the monomer-containing system (**Figure 1.14b**). Common type II PIs include camphorquinones, benzophenones, and thioxanthones.
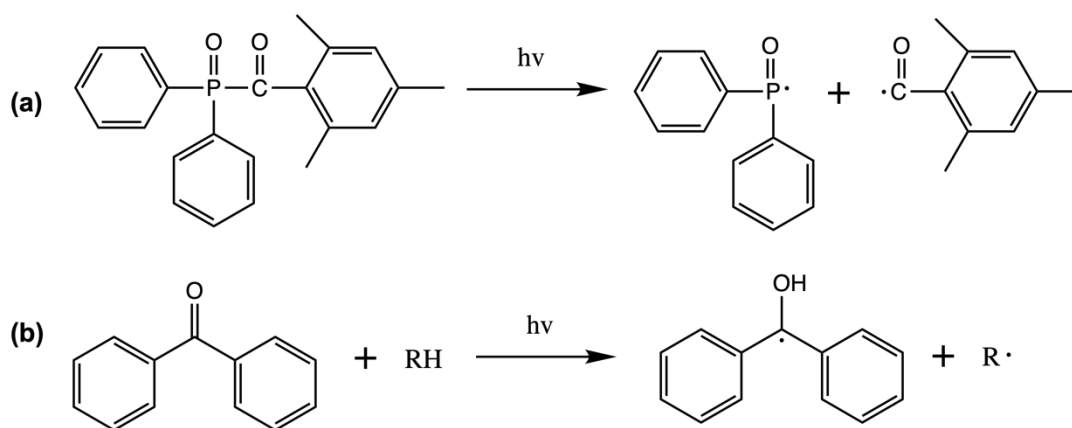
Figure 1.14 (a) Photofragmentation of diphenyl (2,4,6-trimethylbenzoyl) phosphine oxide (TPO); and (b) Generation of free radicals from benzophenone due to hydrogen abstraction.

1.5.1.2 Ionic photopolymerisation

Although free radical photopolymerisations are favorable for broad industrial applications, oxygen inhibition remains a common setback (Ligon et al., 2014). As an alternative, ionic photopolymerisations are gaining increasing interests due to their abundant advantages, including absence oxygen inhibition, minimal sensitivity to water, and their ability to polymerise vinyl ethers, oxiranes (epoxides), and other heterocyclic monomers that do not polymerise by a free radical mechanism (Schnabel, 2007).

Like free radical photopolymerisation, there are also two types of photoinitiators in the ionic mechanism: cationic and anionic. Cationic

photopolymerisation is a type of chain growth involving initiation and propagation steps. However, there is no termination step via neutralisation, and generally it is terminated due to the presence of nucleophilic impurities in the system such as water-, amino-, or hydroxyl-containing compounds (Fouassier and Lalevée, 2012; Schnabel, 2007). Upon light irradiation, reactive cations are generated to initiate the polymerisation reaction. The majority of the cationic photoinitiators are onium salts, such as aryldiazonium and diaryliodonium. Over the years, the anionic photopolymerisations have been considerably less investigated possibly due to the longer reaction time (Dumur, 2021; Fouassier and Lalevée, 2012). Similar to cationic photopolymerisation, the initiation mechanism involves the photoinduced release of a reactive anion, which readily adds to the monomer, leading to the polymer formation through repetitive addition of monomers to the growing anionic chain (Schnabel, 2007).

1.5.2 Light sources

Light is an electromagnetic wave of specific wavelength. One of the main photochemical properties of an electromagnetic wave is that it can transport energy. In order for light to be effective in a photochemical reaction, not only must the photon possess sufficient energy to initiate the reaction, but it must also be absorbed. When a molecule absorbs light, the energy excites it to a higher electronic energy level, where reactions, such as dissociation or interaction, can occur with other molecules.

The range of wavelengths used in vat photopolymerisation typically include (i) ultraviolet (UV) light (λ = 200–400 nm), (ii) visible light (λ = 400–700 nm) and sometimes (iii) near-infrared (NIR) light (λ = 700-1000 nm) (Schnabel, 2007). Typical light sources include conventional artificial (e.g., xenon lamps, mercury arc lamps, doped lamps, microwave lamps, light-emitting diodes (LEDs)), as well as pulsed light and laser sources. The sun is also a natural source of light, which is convenient and inexpensive. However, its intensity is strongly affected by the weather or the location. Sunlight curing presents a green technology which can be of interest, particularly for outdoor applications.

1.5.3 Photoreactive materials

In general, monomers are molecules that can react with each other or with other monomers to form polymers. In photopolymerisation, photoreactive monomers in liquid state are photopolymerised via different mechanisms in the presence of photoinitiators upon exposure to a light source (Bagheri and Jin, 2019). As the main component in the vat photopolymerisation 3D printing, the selection of monomers would impact on the speed of curing, crosslinking density, and the mechanical properties of printed parts (Andreu et al., 2021). The most widely used monomer systems are based on the free radical photopolymerisation of methacrylate- and acrylate-based monomers such as poly(ethylene glycol) diacrylate (PEGDA) and polyethylene glycol methacrylate (PEGMA), which demonstrates fast reaction rates, outstanding storage behaviour and tuneable mechanical properties (Zhang and Xiao, 2018). One major drawback of these monomers is that they exhibit volume shrinkage during the chain growth free radical polymerisation, resulting in high brittleness in the printed parts, which limits their versatility of applications. Naturally-derived materials such as gelatin, hyaluronic acid, alginate have also been modified with methacrylate groups to form photoreactive bio-resins (Ng et al., 2020). In addition, other functional materials also include elastomers, ceramics, hydrogels, conductive, self-healing, biocompatible, and biodegradable resins (Al Rashid et al., 2021; Halloran, 2016; Yu et al., 2020; Zhang et al., 2021).

Smart materials or shape memory materials is a class of polymeric materials that are capable of changing their shapes in a predefined manner when induced by an external stimulus such as heat, pH, moisture or light (Andreu et al., 2021). The 3D printing of shape-memory polymers paved the way for the emergence of four-dimensional (4D) printing, whereby the printed objects display dynamic transformation (e.g., change in shape, property, or functionality) over time. Up to date, a wide range of applications have been developed using 4D printing (**Figure 1.15**). In particular, as vat photopolymerisation offers high resolution and accuracy, complex geometries are easily achievable which is useful for electronics, actuators, and biomedical

applications (Ge et al., 2016; Wang et al., 2021b; Zarek et al., 2016; Zhao et al., 2018). For example, methacrylated polycaprolactone (PCL) was formulated as DLP printable resin with a thermally induced shape-memory behaviour (**Figure 1.15d**) (Zarek et al., 2016). In another recent study, a novel hydrophilic/hydrophobic composite was also developed using poly (ethylene glycol) diacrylate (PEGDA) and poly (propylene glycol) dimethacrylate. The resulting photopolymer was easily patterned using DLP 3D printing to fabricate water-responsive shape-shifting structures (**Figure 1.15b**) (Zhao et al., 2018).
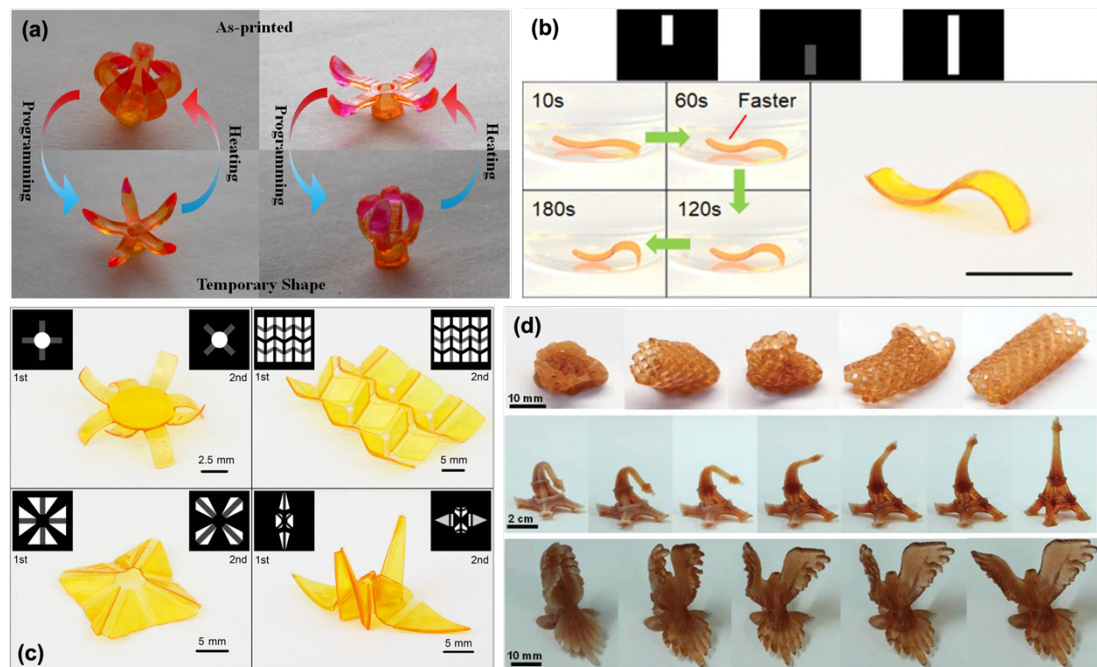
Figure 1.15 (a) Demonstration of the transition between as printed shape and temporary shape of 3D printed multimaterial grippers (Ge et al., 2016); (b) sequential actuation of water-responsive S-shaped strip (Zhao et al., 2018); (c) 3D printed origami structures by two-side illuminations (Zhao et al., 2017); and (d) 3D printed cardiovascular stent, Eiffel Tower, and bird models demonstrating shape changes in response to heat (Zarek et al., 2016).

1.5.4 Photoinitiators

As mentioned above, in addition to light sources and photoreactive monomers, photoinitiators are essential for the initiation step to occur. They play an crucial role in determining the photopolymerisation rate and hence, influence the resulting properties of the printed objects (Pawar et al., 2016). A photoinitiator is a thermally-stable compound that is able to absorb light with a relatively high absorption coefficient within certain wavelength ranges (Schnabel, 2007). The absorption range of a photoinitiator is a decisive factor in the photopolymerisation reaction, wherein the absorbance spectrum has to overlap with the emission spectrum of the light source (Fouassier et al., 2010). As such, based on their absorbance spectrum, photoinitiators can be subclassified.
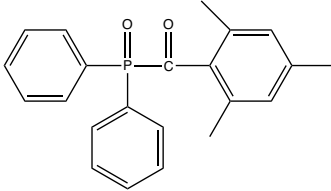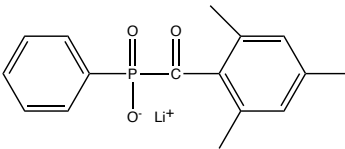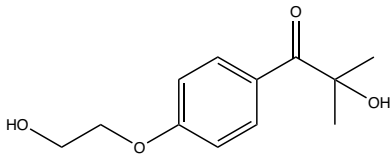
1.5.4.1 UV-sensitive photoinitiators
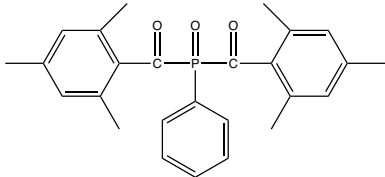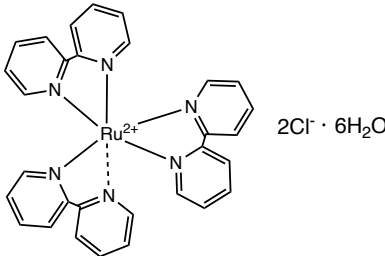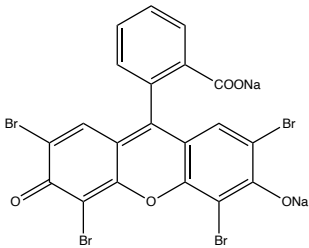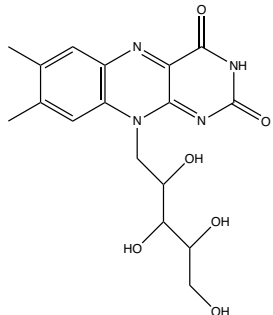
As the name suggests, UV-sensitive photoinitiators are those that absorb within the UV spectrum. TPO remains one of the most commonly used UV-sensitive photoinitiators for pharmaceutical applications (Martinez et al., 2018; Tumbleston et al., 2015; Wang et al., 2016). Other commercially available UV-sensitive photoinitiators are summarised in **Table 1.2**.

In the case where the aim is to fabricate hydrogels, especially those encapsulating live cells, it is necessary for the photoinitiator to be efficient and highly water-soluble (Pawar et al., 2016). Otherwise, substantial heating or mixing with organic solvents is required when using poorly water-soluble photoinitiators. Irgacure 2959 is a well-known, biocompatible photoinitiator used in aqueous systems, exhibiting promising cytocompatibility over a range of cell types (Bryant et al., 2000; Williams et al., 2005). However, it shows low polymerisation efficiency under mild visible light illumination (≥ 365 nm) (Fairbanks et al., 2009). Alternatively, water-soluble lithium phenyl (2,4,6-trimethylbenzoyl) phosphinate (LAP) has been synthesised and evaluated for its effectiveness in initiating the polymerisation of PEGDA monomers (Fairbanks et al., 2009). Lately, TPO was converted into water-dispersible

nanoparticles via the spray drying of volatile microemulsions containing TPO (Pawar et al., 2016). The TPO nanoparticles allowed a much faster photopolymerisation, showing a molar extinction coefficient (ε = 680 M^{-1}cm^{-1}) at 365 nm, which is 300 times larger than that of the commercially available Irgacure 2959 (ε = 2.25 M^{-1}cm^{-1}).

Table 1.2 Examples of commercial photoinitiators used for vat photopolymerisation 3D printing.

Name	Mechanism and type	Chemical Structure	Light absorption (λ_{max})	References
Diphenyl (2,4,6-trimethylbenzoyl) phosphine oxide (TPO)	Free radical (type I)		295 nm, 368 nm, 380 nm, 393 nm	(Martinez et al., 2018; Wang et al., 2016)
Lithium phenyl (2,4,6-trimethylbenzoyl) phosphinate (LAP)	Free radical (type I)		375 nm	(Bagheri and Jin, 2019; Fairbanks et al., 2009)
2-hydroxy-4'-(2-hydroxyethoxy)-2-methylpropiophenone (Irgacure 2959)	Free radical (type I)		274 nm	(Kadry et al., 2019; Park et al., 2018)

Compound	Type		Absorption	Reference
Phenyl bis (2,4,6-trimethylbenzoyl) phosphine oxide (BAPO, Irgacure 819)	Free radical (type I)		295 nm, 370 nm	(Bagheri and Jin, 2019; Schwartz and Boydston, 2019)
Tris (2'2-bipyridyl) dichlororuthenium (II) hexahydrate (Ru)	Free radical (type II)		453 nm	(Bagheri and Jin, 2019; Lim et al., 2016)
Eosin Y	Free radical (type II)		~ 500 nm	(Freire et al., 2014; Shih and Lin, 2013)
Riboflavin (RBF)	Free radical (type II)		365 nm, 444 nm	(Ahmad et al., 2013; Kim and Chu, 2009; Nguyen et al., 2013; Zanetti-Polzi et al., 2017)

1.5.4.2 Visible light-sensitive photoinitiators

The use of visible light has gained much interest due to its safety, convenience, eco-friendliness, and reduced risk of eye damage (Bagheri and Jin, 2019; Park et al., 2018). Examples of commercial visible light-sensitive photoinitiators are listed in **Table 1.2**. Tris (2'2-bipyridyl) dichlororuthenium (II) hexahydrate (Ru) coupled with sodium persulfate was used as a visible-light initiating system to photopolymerise gelatin-methacryloyl-based hydrogel constructs, exhibiting less susceptibility to oxygen inhibition effects (Lim et al., 2016). In addition to the aforementioned examples, a number of visible light photoinitiator systems such as camphorquinone (Bryant et al., 2000), Ivocerin (Oesterreicher et al., 2016), and Eosin Y (Shih and Lin, 2013), have also been investigated to initiate photopolymerisation reactions.

Interestingly, dye molecules can also be utilised as visible light photoinitiators by undergoing electron-transfer reactions with appropriate co-initiators (Schnabel, 2007). In principle, the excited dye molecule can undergo reduction or oxidation, which refer to accepting or transferring an electron from or to the co-initiator. For example, a photocrosslinkable furfurylamine-conjugated gelatin has been previously developed using Rose Bengal (a food dye) as a photoinitiator for visible light (Mazaki et al., 2014). Another example of a natural-based photoinitiator is riboflavin (RBF, vitamin B2), a naturally occurring yellow pigment found in food and plants, which has been broadly used in biomedical applications because of its water solubility and biocompatibility (Kim and Chu, 2009). Moreover, RBF possesses absorbent peaks in both, the UV, and visible light regions, making it usable with both light sources. A number of studies have demonstrated the use of RBF/triethanolamine (TEA) as an efficient photoinitiation system in the polymerisation of 2-hydroxyethyl methacrylate (HEMA) (Ahmad et al., 2013; Bertolotti et al., 1999) and PEGDA (Nguyen et al., 2013). Recently, an RBF/TEA initiating system has been utilised for the direct fabrication of drug-loaded hydrogels (Martinez et al., 2017).

The cytotoxicity information found in the literature of photoinitiators and photoreactive monomers used in this thesis has been summarised in **Table 1.3**. The cell viability of PEGDA is usually measured on the cured PEGDA samples and the results may differ based on the type and amount of photoinitiator used, the light exposure conditions, and the post processing steps.

Table 1.3 Cytotoxicity information of photoinitiators and photoreactive monomers used in this thesis.

Compound name	Concentration and cytotoxicity information	References
Diphenyl (2,4,6-trimethylbenzoyl) phosphine oxide (TPO)	• 1 µM (82.6%) and 50 µM (56.6%) in Chinese hamster lung fibroblasts (24 h) • 1 µM (78.3%) and 50 µM (0%) in human oral keratinocytes (24 h)	(Popal et al., 2018)
	• 1 µM (93.4%) and 50 µM (61.8%) in L-929 mouse fibroblasts (24 h)	(Kim et al., 2022)
Phenyl bis (2,4,6-trimethylbenzoyl) phosphine oxide (BAPO or Irgacure 819)	• 1 µM (73.7%) and 50 µM (19.7%) in Chinese hamster lung fibroblasts (24 h) • 1 µM (63.9%) and 50 µM (0%) in human oral keratinocytes (24 h)	(Popal et al., 2018)
	• 1 µM (93.0%) and 50 µM (56.4%) in L-929 mouse fibroblasts (24 h)	(Kim et al., 2022)
Eosin Y	• 0.01 mM (88.4%) and 0.1 mM (68.8%) in human mesenchymal stem cells (48 h)	(Bahney et al., 2011)
Poly(ethylene glycol) diacrylate (PEGDA)	• 100% in human dermal fibroblast and human adult low calcium high temperature cells (24 h) using 0.5% w/w BAPO	(Lim et al., 2021)
	• 95% and 96% in human neonatal foreskin fibroblasts (24 h) using 0.22 mM and 2.2 mM LAP, respectively	(Fairbanks et al., 2009)

1.5.5 Controlling the printing quality

In photopolymerisation-based techniques, it is fundamental to obtain a working curve of the photocrosslinking network to understand the curing kinetics. To determine the critical exposure and penetration depth, Jacob's equation (Jacobs, 1992), which is adapted from the Beer-Lambert Law, can be used as a kinetic model:

Eq. 1.1
$$C_d = D_p \ln \left(\frac{E}{E_c} \right)$$

Where C_d is the cure depth, D_p is the penetration depth, E is the exposure at the surface, E_c is the critical exposure required to initiate polymerisation.

When $E = E_c$, the resin reaches the so-called "gel point", corresponding to the transition from the liquid phase to the solid phase. In vat photopolymerisation 3D printing, E must exceed E_c to allow a layer of solidified resin to be created on the build platform. Practically, by developing a semi-log plot of C_d versus E, a straight-line working curve can be obtained with a slope of D_p and an x-intercept of E_c (Bennett, 2017). Knowing both D_p and E_c aids the user in selecting the appropriate printing parameters, such as laser power, scan speed and exposure time, needed to optimise the printability and achieve the desired printing resolutions.

1.6 Vat photopolymerisation-based 3D printing techniques

Vat photopolymerisation is a generic term given to a number of 3D printing technologies. In this section, some of the more common vat photopolymerisation processes include SLA, digital light processing (DLP), continuous light interface production (CLIP), two-photon polymerisation (2PP), and more recently, volumetric printing will be briefly discussed.

1.6.1 Stereolithography (SLA)

SLA remains the most commonly used vat photopolymerisation technology. Depending on the setup of the SLA 3D printer, it can be either bottom-up or top-down. In the bottom-up approach (**Figure 1.16a**), the laser beam sits underneath the resin tank and the build platform ascends during printing, whereas in the top-down approach (**Figure 1.16b**), the laser beam is positioned above the resin tank and the platform is lowered into the resin tank. Compared with the top-down approach, the bottom-up setup is more affordable with the advantage of small build volumes, making it easier to swap resins. During the SLA printing process, the laser points at two mirror galvanometers that direct the light in the X and Y axes to cure the first layer of resin on the build platform. Subsequently, the cured layer gets "peeled off" the surface of the resin tank and the platform moves vertically along the z-axis to allow the fresh resin to redistribute. Then the platform descends to recoat, thereby solidifying the second layer on top of the previous one in the same manner. This process is repeated until the final solid object is fabricated.
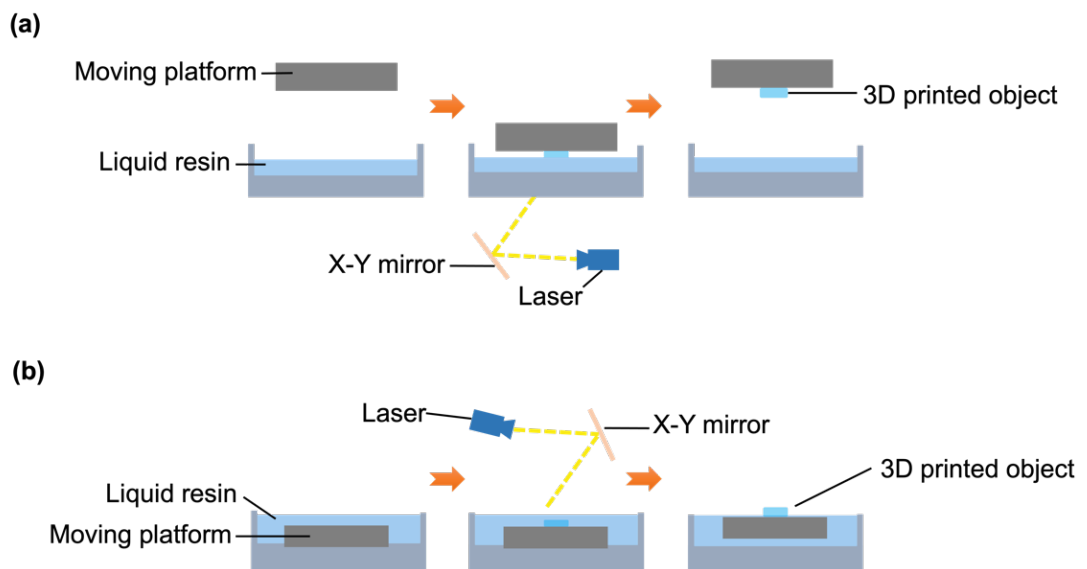
Figure 1.16 Schematic diagram of the (a) bottom-up SLA and (b) top-down SLA 3D printing technology.

1.6.2 Digital light processing (DLP)

Different from SLA where a laser is used to cure the resin in a point-by-point manner, the DLP technology employs a digital light projector to illuminate the image of an entire layer all at once (**Figure 1.17a**). As a result, the printing speed of DLP is considerably faster to print large objects or multiple objects when compared with that of SLA (Bagheri and Jin, 2019). Illumination is achieved by a digital micromirror device (DMD), which is a dynamic mask consisting of thousands of micromirrors that can rotate rapidly and reflect light to create a pattern on the bottom of the resin tank. Since the image of each layer is made up of small square pixels, the resulting layers are composed of rectangular voxels in 3D space. Consequently, the rectangular shape of the voxel creates a stepped effect on the curved edges, also known as the voxel effect. Recently, some DLP printers have replaced the DMD with liquid crystal display (LCD) panels where light coming from the LED lamp shines through the LCD panel (**Figure 1.17b**). In general, LCD printers offer good resolution and are much cheaper, however, the short life of LCD requires regular replacement (Quan et al., 2020).
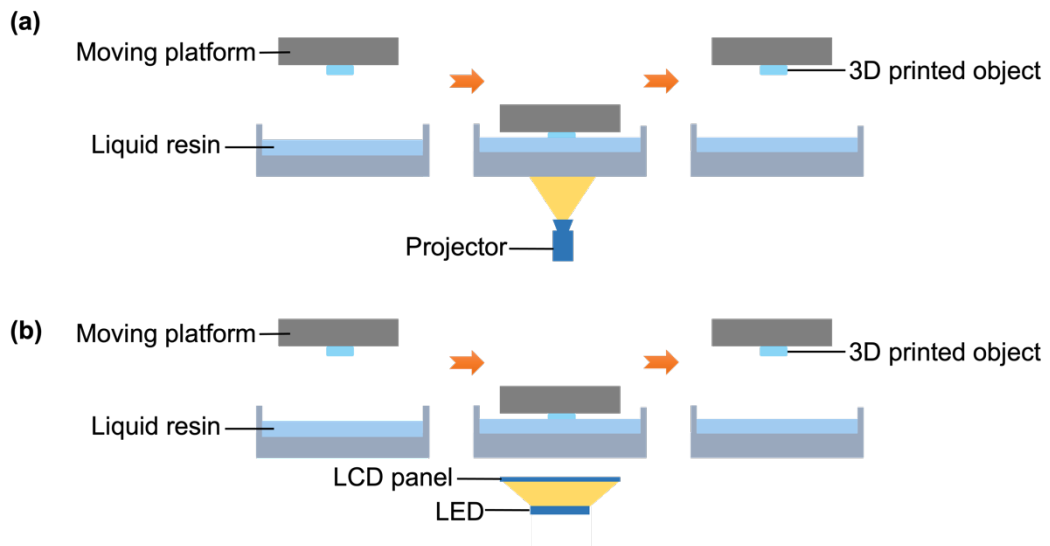
Figure 1.17 Schematic diagram of the (a) DLP and (b) LCD 3D printing technology.

1.6.3 Continuous liquid interface production (CLIP)

The CLIP technology is a relatively newer technique that was developed in 2015 by DeSimone and co-workers (Tumbleston et al., 2015). The fundamental concepts are similar to that of DLP, but it is up to 100 times faster than any other 3D printing technology. In this innovative production method, a "dead zone" is created in the container between the oxygen-permeable window and the surface of the curing part, where photopolymerisation is inhibited (**Figure 1.18**). In this way, the object being cured is continuously pulled out of the resin bath with a production rate of hundreds of millimetres per hour, unlike traditional vat photopolymerisation methods, where a stepwise layer formation is required (exposure and curing, separation, recoating, and repositioning). Additionally, CLIP ultimately yields printed objects with smooth surfaces without slicing artefacts. Recently, novel variations of the CLIP technology have emerged, enabling continuous and rapid printing via the use of a mobile liquid interface (e.g. fluorinated oil) (Walker et al., 2019) and dual-wavelength volumetric photopolymerisation inhibition patterning (De Beer et al., 2019).
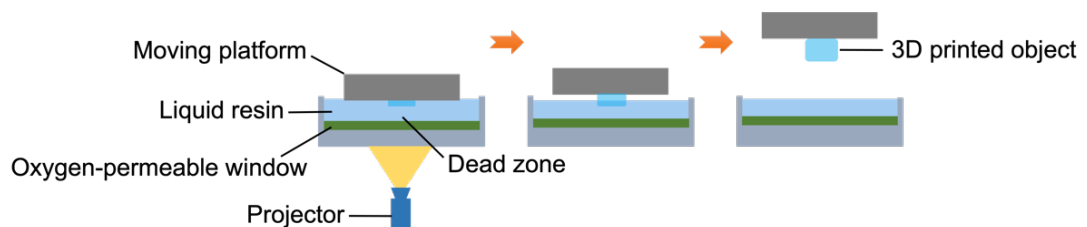
Figure 1.18 Schematic diagram of the CLIP 3D printing technology.

1.6.4 Two-photon polymerisation (2PP)

2PP has gained huge interest for fabricating microstructures with an extremely high resolution (< 100 nm), and has found applications in microdevices, microfluidics, and microphotonics (Xing et al., 2015). Common vat polymerisation techniques use single-photon polymerisation, which is a planar process where only one photon is absorbed by the photoinitiator to initiate polymerisation near the surface of the resin (Wu et al., 2006). Two-photon

absorption (TPA) is a three-order nonlinear optical effect in which the initiator molecule simultaneously absorbs two photons to convert from the ground state to an excited state. The concept was originally proposed by Maria Goeppert-Mayer in 1931 in her doctoral dissertation (Göppert‑Mayer, 1931). The 2PP process is a TPA-based fabrication technique where a titanium sapphire femtosecond laser (λ = 780 nm; repetition rate = 80 MHz) is tightly focused by an objective lens onto the volume of the photosensitive resin (**Figure 1.19**) (Park et al., 2009). When the laser moves in a 3D motion, the solidification is initiated along the trace of the focus, enabling the fabrication of 3D microstructures.
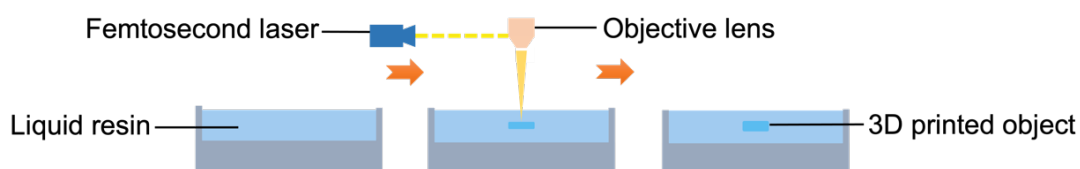
Figure 1.19 Schematic diagram of the 2PP printing technology.

1.6.5 Volumetric printing

Lastly, volumetric printing has created a new fabrication paradigm that enables the fabrication of an entire 3D object within seconds (Bernal et al., 2019; Kelly et al., 2019; Loterie et al., 2020; Shusteff et al., 2017). In contrast to the conventional layer-based printing process, objects are fabricated by irradiating the photocurable resin within a contained volume from multiple angles (**Figure 1.20**). Mainly, there are two different volumetric printing approaches. The first type of volumetric printing is via tomographic reconstruction where a set of 2D images computed by a Radon transform is displayed in synchronisation with the rotating resin container (Kelly et al., 2019; Loterie et al., 2020). The other type is based on a three-beam superposition system. The three orthogonal beams generated from a single light beam by 45° prism mirrors are intersecting in the photosensitive resin where the predefined 3D structure is formed all at once (Shusteff et al., 2017).
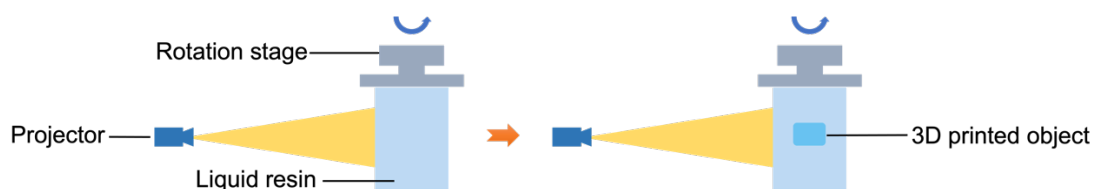
Figure 1.20 Schematic diagram of the tomographic volumetric printing technology.

1.7 Progress of vat photopolymerisation 3D printing within pharmaceutical research

1.7.1 Manufacturing approach

As mentioned earlier, the introduction of 3D printing into the pharmaceutical field has revolutionised the way medications can be made. Various vat photopolymerisation technologies have demonstrated their suitability for the fabrication of drug delivery systems with high printing resolution and accuracy, offering diverse controlled or sustained release profiles. **Figure 1.21** provides a graphical illustration of the way drug-loaded systems can be fabricated via vat photopolymerisation 3D printing. This can be achieved via two different approaches; either by directly incorporating the drug into the liquid resin before printing or by introducing the drug into a blank device after printing (Bloomquist et al., 2018). In the former scenario, the drug is fully dissolved or homogeneously dispersed in a resin, composed of a photoinitiator and a photopolymer, by magnetic stirring at room temperature. Following the printing process, the drug is physically entrapped in the crosslinked polymeric network. Once the device is dispersed into a dissolution medium, the drug is released via diffusion from the swollen matrix. In the case of blank devices, the drug can be incorporated via traditional drug loading techniques based on adsorption, such as dipping and spray coating. Alternatively, the drug can be absorbed into the polymer network by swelling the blank device in a drug concentrated solution. Although post loading adds an additional manufacturing process, it prevents potential drug degradation during pre-printing or printing.
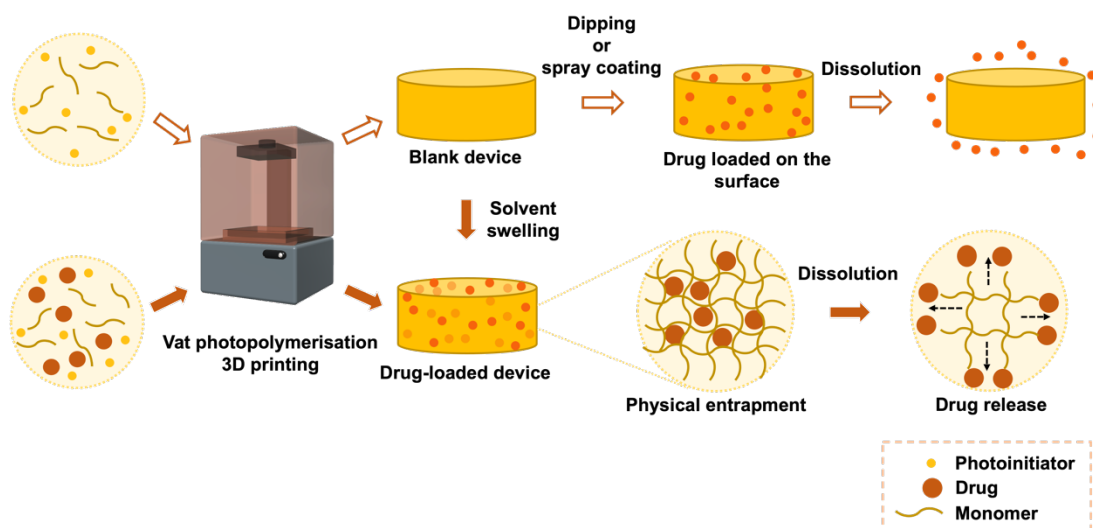
Figure 1.21 Vat photopolymerisation 3D printing for fabrication of drug delivery systems, adapted from (Xu et al., 2021b).

1.7.2 Oral dosage forms

The first study to demonstrate the feasibility of using SLA 3D printing for the preparation of oral dosage forms was reported in 2016 (**Figure 1.22a**) (Wang et al., 2016) where paracetamol and 4-aminosalicylic acid loaded torus Printlets were prepared. By increasing the concentration of PEGDA in the resin formulation, drug release rates were reduced. This was due to a higher degree of crosslinking, resulting in less molecular mobility in the core of the Printlet and slower drug diffusion through the polymer matrix. Later, other excipients such as poly(caprolactone) Triol (Healy et al., 2019), mannitol and sodium chloride (Krkobabić et al., 2019) have been added to manipulate the drug release rates from Printlets. On the other hand, the nature of liquid resins as feedstock materials in vat photopolymerisation 3D printing allows the incorporation of water for preparing swelling and pH responsive hydrogels (**Figure 1.22d**) (Larush et al., 2017; Martinez et al., 2017). The printed hydrogel tablets exhibited high swelling and faster drug release at higher pH, which could be useful for targeted and delayed release in the small intestines. Unlike other oral dosage forms prepared from biodegradable or water-soluble polymers, the structure of Printlets made of photocrosslinkable materials remains intact after the drug release. As such, the Printlets do no degrade and

instead will be eliminated from the body in their solid, intact forms, which may pose risks of intestinal blockage or raise concerns for some patients.

The drug release rate can be fine-tuned by changing the geometry of the Printlets. Printlets with different shapes but similar surface area to volume (SA/V) ratio do not exhibit significant difference in their release properties (**Figure 1.22b top**). On the other hand, increasing the SA/V ratio of a torus Printlet increases the drug release rate (**Figure 1.22b bottom**) (Martinez et al., 2018). Similarly, the drug release rate can also be controlled by adjusting the number of perforations in the Printlets (Kadry et al., 2019; Karakurt et al., 2020).
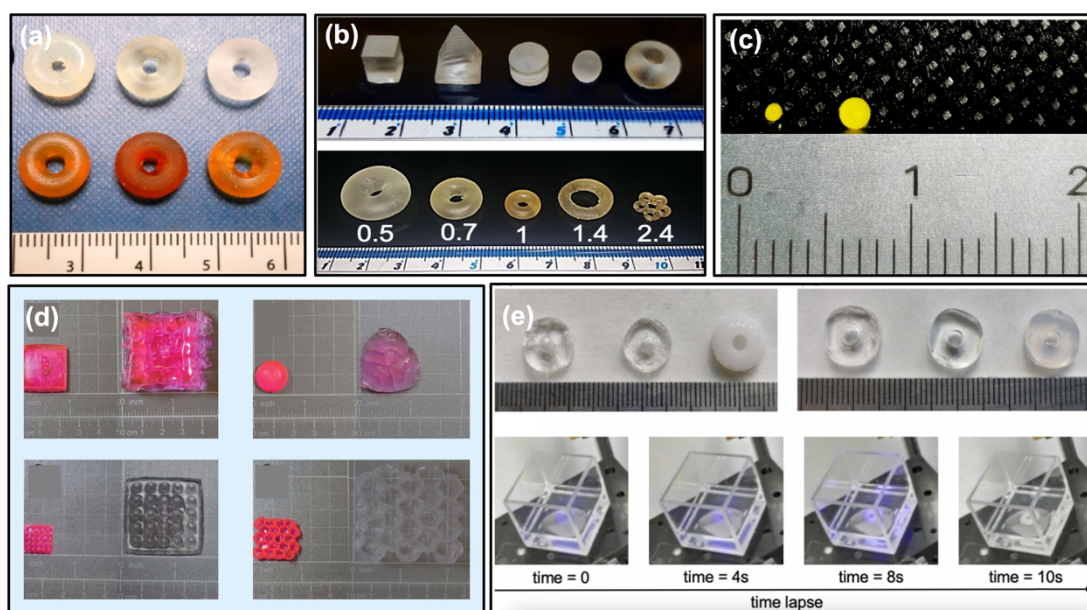
Figure 1.22 (a) SLA torus Printlets containing paracetamol (top) and 4-aminosalicylic acid (bottom) (Wang et al., 2016); (b) SLA Printlets with similar SA/V ratios (top) and SLA torus Printlets with different SA/V ratios (bottom) (Martinez et al., 2018); (c) SLA 3D printed 1 mm and 2 mm pellets (Xu et al., 2021a); (d) DLP 3D printed hydrogels with different shapes before and after 24 h swelling in phosphate buffer (Larush et al., 2017); and (e) Different Printlets produced by volumetric printing and a sequential view of the cuvette during the printing process (Rodríguez-Pombo et al., 2022).

Other oral dosage forms examples include oral pellets in different sizes (**Figure 1.22c**) (Xu et al., 2021a) and nanocomposite pills (Sharma et al.,

2022). More recently, volumetric printing has been successfully used for the fabrication of paracetamol Printlets, enabling on-demand and rapid production of medicines within seconds (**Figure 1.22e**) (Rodríguez-Pombo et al., 2022). Examples of oral dosage forms prepared by vat photopolymerisation 3D printing in recent years are summarised in **Table 1.4.**

It is worth mentioning that in a recently published paediatric visual preferences survey of 3D printed tablets, DLP Printlets were the most visually appealing (61.7%) to 368 children participants regardless of age and gender difference (**Figure 1.23**) (Januskaite et al., 2020). In comparison to the other Printlets, DLP Printlets presented well-defined edges and smooth surface owing to the technology's high resolution, which is highly preferred by the children.
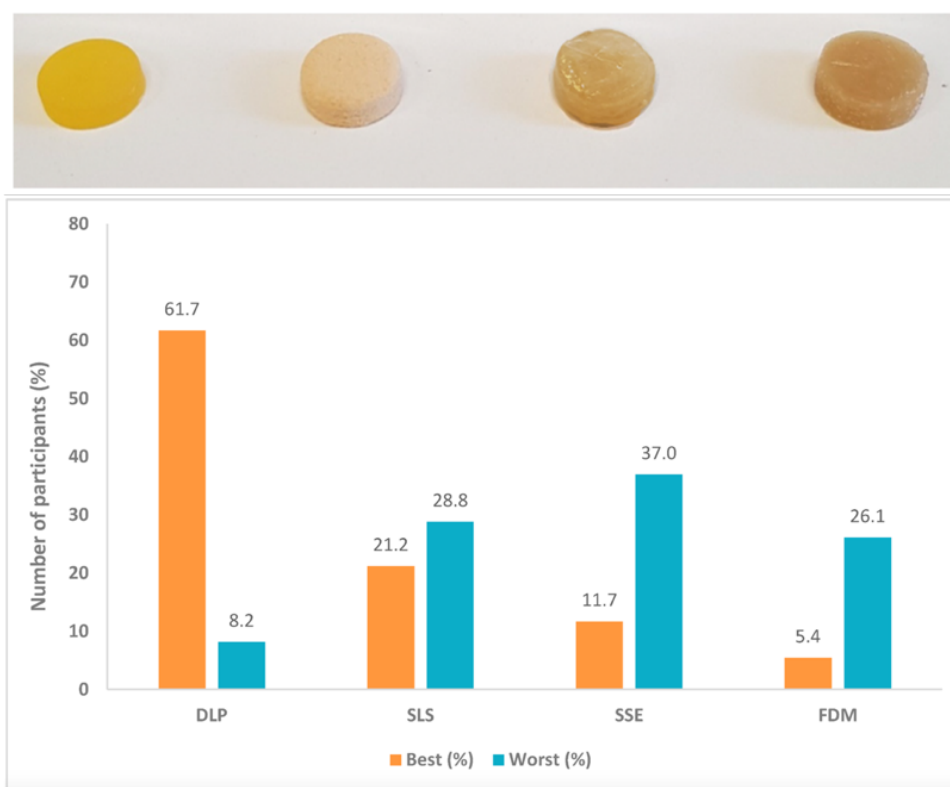
Figure 1.23 Image of 3D printed placebo tablets fabricated with four different 3D printing technologies, from left to right, DLP, SLS, SSE, and FDM and Printlet visual preference results summary (n=368) (Januskaite et al., 2020).

Table 1.4 Examples of oral dosage forms using different vat photopolymerisation 3D printing technologies.

Technology	Drug(s)	Oral dosage form(s)	Material(s)	References
SLA	Paracetamol & Aspirin	Tablets	PEGDA 700, PCL Triol, TPO	(Healy et al., 2019)
	Ibuprofen	Hydrogels	PEGDA 700, PEG 300, TPO, RBF, TEA	(Martinez et al., 2017)
	Ascorbic acid	Hydrogels	PEGDMA 550, RBF, TEA	(Karakurt et al., 2020)
	Naproxen, Aspirin, Paracetamol, Caffeine, Chloramphenicol, Prednisolone	Polypills	PEGDA 575, PEG 300, TPO	(Robles-Martinez et al., 2019)
	Capsaicin	Moulds for capsaicin candies	Commercial LCD-type resins (GODSAID Science and Technology Co., Ltd., China)	(Jiang et al., 2019a)
	Bovine serum albumin	Specimens	PEGDA 700, LAP	(Konasch et al., 2019)

	Berberine chloride	Nanocomposite pills	PEGDA 700, PEO, TPO, SP	(Sharma et al., 2022)
	Ibuprofen	Pellets	PEGDA 700, PEG 400, TPO, tartrazine	(Xu et al., 2021a)
DLP	Theophylline	Tablets	PEGDA 400, PEGDMA 1000, Irgacure 2959	(Kadry et al., 2019)
	Atomoxetine hydrochloride	Tablets	PEGDA 700, PEG 400, TPO	(Krkobabić et al., 2020)
	5-fluorouracil	Tablets	Acrylated hyperbranched polyester	(Chen et al., 2022)
	Sulforhodamine B	Responsive hydrogels	Acrylic acid, PEGDA, TPO nanoparticles	(Larush et al., 2017)
LCD	Ibuprofen	Tablets	PEGDA 700, PEG 400, water, RBF	(Madžarević and Ibrić, 2021)
	Calcein	Tablets	PEGDA 700, PEG 400, water, TPO	(Tagami et al., 2021b)
	Vortioxetine hydrobromide	Moulds	Epoxy acrylate resin (Guangzhou Electronic Technology Co., Ltd., China)	(Li et al., 2022)
Volumetric printing	Paracetamol	Tablets	PEGDA 700, PEGDA 575, water, PEG 300, LAP	(Rodríguez-Pombo et al., 2022)

1.7.3 Medical devices

1.7.3.1 Patient-specific devices

Apart from oral dosage forms, its remarkable resolution and excellent surface finish makes vat photopolymerisation 3D printing attracting interests for the fabrication of medical devices. Examples of medical devices manufactured via vat photopolymerisation in recent years are outlined in **Table 1.5**.

As previously mentioned in **Section 1.3.6**, by coupling 3D printing with imaging techniques (e.g. 3D scanner, CT, MRI) that capture real-time images, patient-specific drug delivery devices can be fabricated, detailing the anatomical features of the patient (Goyanes et al., 2016). Since everyone's ear anatomy is unique and different, hearing aids are a remarkable example of medical devices that benefit from the development of vat photopolymerisation 3D printing. In fact, more than 99% of patient-oriented hearing aids are manufactured using 3D printing nowadays (Banks, 2013). Before 3D printing was introduced into this domain, the production of hearing aids took longer than a week. Today, the whole process, involving scanning, modelling and 3D printing, could take less than a day (Dodziuk, 2016).

Recently, patient-specific hearing devices have been developed using vat photopolymerisation 3D printing for local drug delivery to the ear. A DLP 3D printer was used to prepare personalised hearing aids loaded with combinations of ciprofloxacin and fluocinolone acetonide for patients with ear infections (**Figure 1.8b**) (Vivero-Lopez et al., 2021b). The devices demonstrated constant release of both drugs for up to 7 days and anti-biofilm activity against *Pseudomonas aeruginosa* and *Staphylococcus aureus* by inhibiting bacterial growth, both, on the surface of the device and in the surrounding medium. On the other hand, Triacca et al. developed implants in different designs containing levofloxacin by SLA 3D printing for treating ear infections, which showed antimicrobial activity against *Escherichia coli* and *Staphylococcus aureus* (**Figure 1.24a**) (Triacca et al., 2022).

Other patient-specific devices also include SLA 3D printed personalised anti-acne nose patch containing salicylic acid (**Figure 1.8a**) (Goyanes et al., 2016). Compared to the same devices manufactured by FDM, the SLA devices showed a better printing resolution and higher drug loading, as well as faster drug diffusion rate.
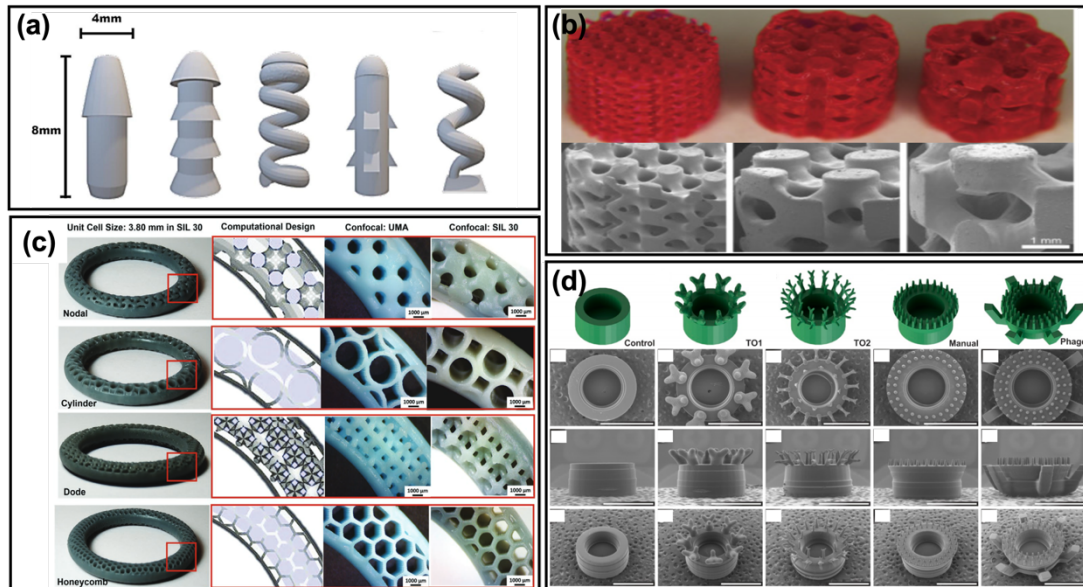
Figure 1.24 (a) SLA 3D printed implants in different designs for local drug delivery to the ear (Triacca et al., 2022); (b) CLIP 3D printed model devices of 1, 2, and 3 mm unit cells (from left to right) loaded with rhodamine B as a surrogate drug (Bloomquist et al., 2018); (c) CLIP 3D printed intravaginal rings with varying unit cell designs (Janusziewicz et al., 2020); and (d) DLP 3D printed microreservoirs with various geometries (Vaut et al., 2020).

Table 1.5 Examples of drug delivery devices using different vat photopolymerisation 3D printing technologies.

Technology	Drug(s)	Device(s)	Material(s)	References
SLA	Insulin	Microneedle arrays	Dental SG Resin (Formlabs, USA)	(Economidou et al., 2019; Pere et al., 2018)
	Rhodamine B	Microneedles with barb	PEGDA 250, Irgacure 819, Sudan I	(Han et al., 2020)
	Salicylic acid	Nose patch	PEGDA 700, PEG 300, TPO	(Goyanes et al., 2016)
	Lidocaine	Scaffolds	PCL macromers, Omnirad TPO-L, Orasol orange G	(Asikainen et al., 2019)
	Ovalbumin	Microjet device	E-Shell 300 Resin (EnvisonTEC Inc., USA)	(Aran et al., 2017)
	Glucagon	Rapid reconstitution packages	VisiJet Clear (3D Systems, Inc.)	(D'hers et al., 2019)
	Levofloxacin	Implants for ear diseases	Flexible 80A (Formlabs, USA)	(Triacca et al., 2022)
	Berberine	Films for topical delivery	PEGDMA 750, PEG 400, TPO	(Choudhury et al., 2021)

DLP	Diclofenac sodium	Microneedle array on finger splints	Castable Resin (Kudo3D Inc., USA)	(Lim et al., 2017)
	Acetyl hexapeptide-3	Microneedle patch	PEGDA 700, BAPO, vinyl pyrrolidone	(Lim et al., 2021)
	Lidocaine, ibuprofen sodium, diclofenac sodium, ketoprofen	Non-dissolving suppository moulds	Castable Resin (Kudo3D Inc., USA)	(Sun et al., 2016)
	Diclofenac sodium, ibuprofen	Implants with various shapes	PEGDA 400, TPO	(Yang et al., 2020)
	Doxycycline, vancomycin, cefazolin	Implants	PEGDA, PEG, diphenyl phosphine oxide	(Ranganathan et al., 2020)
	Fluticasone	Drug-eluting strings and rings	Poly(caprolactone dimethacrylate), TPO, 2-tert-butyl-6(5-chloro-2H-benzo-triazol-2-yl)-4-methylphenol	(Prasher et al., 2021)
	Ciprofloxacin and fluocinolone acetonide	Anti-biofilm hearing aids	Flexible and ENG Hard resin (Kudo3D Inc., USA)	(Vivero-Lopez et al., 2021b)
	Ciprofloxacin and dexamethasone	Ear canal implant	Medical-grade UV silicone	(Matin-Mann et al., 2022)

LCD	Insulin	Microneedle arrays	Nextdent Ortho Rigid resin (Nextdent B.V., Netherlands)	(Xenikakis et al., 2022)
CLIP	Rhodamine B & fluorescein	Microneedle arrays	TMPTA, PEGDMA 500, polycaprolactone trimethacrylate, acrylic acid, TPO	(Johnson et al., 2016)
	Bovine serum albumin	Microneedle arrays	PEGDMA 350, TPO	(Caudill et al., 2018)
2PP	Gentamicin sulphate	Microneedle arrays	PEGDA 600, Irgacure 369	(Gittard et al., 2010)
	Rhodamine B	Drug delivery device	PEGDMA 575, Irgacure 369	(Do et al., 2018)
	Doxorubicin	Microswimmer	Methacrylamide chitosan, LAP	(Bozuyuk et al., 2018)

1.7.3.2 Tuneable devices

Apart from patient-specific devices, vat photopolymerisation 3D printing also represents the opportunity to harness the freedom of design to precisely control and fine tune the drug release properties. For example, CLIP technology was investigated for the fabrication of intravaginal rings (**Figure 1.24c**) (Janusziewicz et al., 2020). This novel approach involved designing and creating complex internal architectures through the incorporation of unit cells using CAD software. Similarly, the fabrication of microreservoir devices for oral drug delivery was reported (**Figure 1.24d**) (Vaut et al., 2020). The surface texture of the microreservoir was found to increase mucoadhesion to the intestinal mucosa by up to two-folds compared to a non-structural control. In addition, design of alternative geometries of microreservoirs featuring anchor-like surface structures has demonstrated to enhance the mucoadhesive performance and potentially, increasing drug uptake.

Although the above-mentioned studies have not demonstrated the drug release characteristics from those devices, they highlighted the potential of vat photopolymerisation 3D printing as the fabrication platform for customising medical devices. CLIP 3D printing has been employed to fabricate biocompatible drug-loaded scaffolds with controlled release properties (**Figure 1.24b**) (Bloomquist et al., 2018). In the study, 0.2% (w/w) rhodamine B was first incorporated as a surrogate drug, where *in vitro* release studies showed that different release rates could be obtained by changing the 3D design of the devices. Essentially, the smaller the unit cell of the device, the higher surface area, and hence, the more rapid the drug release. Subsequently, two clinically relevant small molecules, docetaxel, and dexamethasone-acetate, were loaded in five different resin formulations based on polycaprolactone

dimethacrylate and PEGDMA. The release behaviours of both drugs followed the same trend of rhodamine B, wherein it was demonstrated that a tuneable release can be achieved by changing the crosslinking density and polymer network compositions.

1.7.3.3 High-resolution microneedles

Microneedles have been extensively studied as a minimally invasive approach to enhance transdermal drug delivery. These miniaturised structures are capable of facilitating drug delivery by means of overcoming the stratum corneum barrier without reaching the nerve endings that elicit pain (Rzhevskiy et al., 2018). A wide range of materials have been used for microneedle fabrication, such as silicon, metal, glass, ceramic and various polymers (Donnelly et al., 2010). Polymeric microneedles are gaining attention due to their biocompatibility, biodegradability, strength, and optical clarity. Fabrication of these polymeric microneedles is commonly accomplished by mould-based techniques (e.g. casting, injection moulding), which allows the use of master templates several times (Luzuriaga et al., 2018). However, these approaches are generally complicated, time-consuming, difficult to scale up and could be expensive when it comes to new design screening. Although FDM 3D printing has been previously employed to fabricate microneedles using biocompatible materials, such as polylactic acid, its poor resolution hindered the feasibility of producing sharp microneedles (Luzuriaga et al., 2018). By utilizing vat photopolymerisation 3D printing, the fabrication of microneedles becomes a one-step process, time- and cost-effective without compromising the printing resolution. Bioinspired microneedles with backward-facing curved barbs were created by DLP 3D printing to enhance tissue adhesion (**Figure 1.25a**) (Han et al., 2020). Using the same technology, direct fabrication of personalised

microneedle arrays on curved surfaces has been reported (Lim et al., 2021; Lim et al., 2017). The microneedles fully contoured the undulating surface of the finger and the skin, ensuring complete insertion for effective drug delivery.
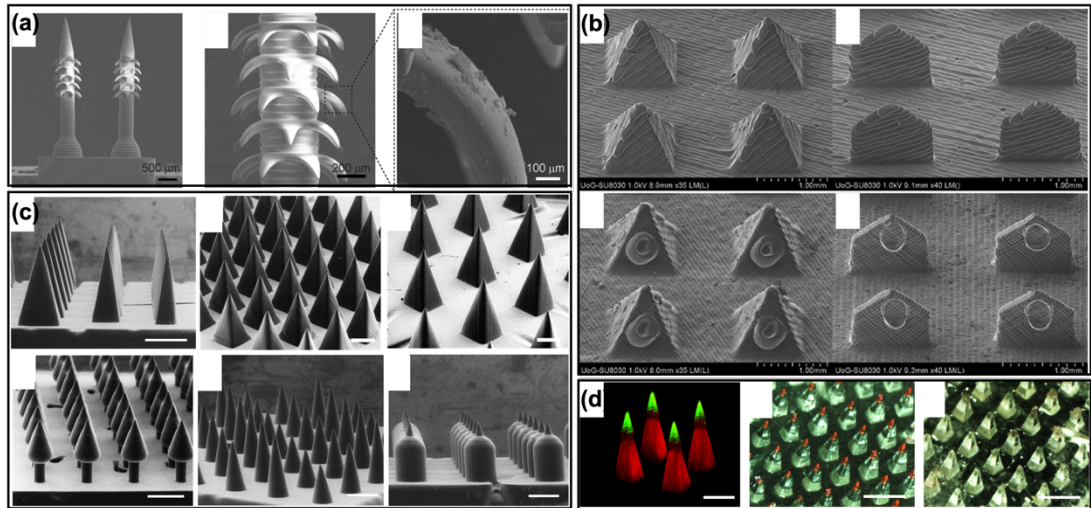
Figure 1.25 (a) SLA 4D printed microneedle array with backward-facing barbs (Han et al., 2020); (b) SLA 3D printed microneedles with pyramid and spear-shaped design uncoated (top) and coated (bottom) with insulin (Detamornrat et al., 2022); (c) CLIP 3D printed microneedles of different shapes (Johnson et al., 2016); and (d) CLIP 3D printed tip loaded microneedles (Johnson et al., 2016).

Pyramid- and spear-shaped microneedle patches were also prepared using an SLA 3D printer, followed by their coating with insulin using ink-jet printing (**Figure 1.25b**) (Pere et al., 2018). All the fabricated microneedle arrays demonstrated successful insertion into porcine skin, with the cone design requiring less force to achieve penetration through the skin. *In vitro* drug release studies showed 90-95% of insulin was released within 30 min. Later on, animal studies also revealed that lower glucose levels was achieved using the insulin-coated SLA 3D printed microneedle arrays compared to subcutaneous injections (Economidou et al., 2019).

In the studies described above, drugs were loaded on the surface of the microneedles following their fabrication. Using a single-step process, high-resolution microneedle arrays in different geometries were developed via CLIP 3D printing within 90 s (**Figure 1.25c**) (Johnson et al., 2016). By exchanging the resin in the middle of the production process, microneedles can be produced with a base that is composed of polycaprolactone encapsulating rhodamine basement (green) and a fluorescein-loaded polyacrylic acid tip (red) (**Figure 1.25d**).

1.7.3.4 Dental applications

Vat photopolymerisation has been extensively explored within the dental industry for the fabrication of prosthetics and orthodontic applications. Dentca™ Denture Base II was the first FDA approved "light-cured resin indicated for the fabrication and repair of full and partial removable dentures and baseplates" in 2015 (FDA, 2015). Similarly, in 2017, NextDent™ Denture was approved by the FDA in as a Class- II 3D printing material for the manufacturing of denture bases (FDA, 2017). Since then, a wide range of biocompatible dental resins have been commercialised for different applications, including trays, drilling templates, dental models, temporary crowns and bridges, and surgical guides (Guttridge et al., 2021). Compared with mouthguards produced using FDM (Liang et al., 2018), those fabricated using vat photopolymerisation have a higher printing resolution, providing an enhanced fitting and more comfort to the patient. Although vat photopolymerisation 3D printing has been a revolutionary manufacturing process in the dental field, it is yet to be explored for drug delivery.

1.7.3.5 Customised moulds

Apart from direct fabrication of devices, vat photopolymerisation 3D printing has also been utilised for the on-demand production of customised moulds, where drug delivery systems can be subsequently produced to meet the individual needs of patients. This method has shown to be more cost-effective in comparison to other manufacturing technologies, such as injection moulding, especially when the production volume is low (Awad et al., 2018b). DLP 3D printing has been used to manufacture personalised moulds for non-dissolving suppositories of drug-laden elastomers aimed at rectal and vaginal drug delivery (Sun et al., 2016). The geometrical features of the suppositories can be designed to meet the needs of female patients, especially those that suffer from different degrees of vaginal relaxation syndrome or posterior prolapse. Other examples also include moulds for preparing microneedles (Krieger et al., 2019), capsaicin candy for treating oral ulcer (Jiang et al., 2019a), and placebo vortioxetine hydrobromide tablets (Li et al., 2022).

1.8   Thesis aims and outline

Evidently, the adoption of 3D printing has paved the way for patient-centric medication, advancing the design and fabrication of oral dosage forms and medical devices. Owing to its high resolution and precision, vat photopolymerisation 3D printing has the capacity to fabricate intricate structures and microdevices with a smooth surface finish. It also allows dose personalisation and drug combination choice, which is otherwise not possible with traditional medicine manufacturing. So far in the literature, numerous efforts have been undertaken to demonstrate the potential of vat photopolymerisation 3D printing in fabricating drug delivery systems and these have mainly focused on oral and transdermal drug delivery. However, the

development of implantable retentive devices for long-term drug delivery remains unexplored. Such devices could be particularly useful for localised drug delivery with sustained or prolonged release, improving patient adherence and reducing systemic exposure. Hence, the principal aim of this thesis is to advance the clinical application of vat photopolymerisation 3D printing through the fabrication of personalised medications to aid the following two areas.

Part 1 – Enhancing medication adherence

The current treatment strategy of some long-term disorders may require repeated administration due to the low local concentration of the therapeutic agent at the disease site. However, the clinical efficacy of conventional medication is often compromised because of patient non-adherence or poor bioavailability. For instance, patients with bladder pain syndrome need installations by urethral catheterisation to achieve pain relief, which is uncomfortable and inconvenient. In the case of dry eye syndrome, topical eye drops are preferred by patients, but ocular bioavailability is very poor due to rapid clearance by blinking and lacrimal drainage. Moreover, polypharmacy is also another common cause of patient non-adherence, wherein many patients with chronic conditions, especially in the older population, struggle to remember how and when to take their medications. To address these clinical unmet needs, SLA and DLP 3D printing will be used to evaluate the possibility of producing the following controlled drug delivery devices:

• Evaluate the possibility of SLA 3D printing to produce indwelling intravesical devices for localised long-term drug delivery in the bladder.

• Study the feasibility of DLP 3D printing to prepare punctal plug for prolonged drug delivery to the anterior segment of the eye.

•   Investigate the viability of employing SLA 3D printing for the fabrication of clinically relevant antihypertensive polypills for alleviating pill burden.

<u>Part 2 – Improving medication accessibility</u>

These drug-eluting systems will demonstrate the versatility of vat photopolymerisation 3D printing for numerous clinical applications. However, the bulk volume of conventional 3D printers limits their deployment in point-of-care clinical settings for on-demand fabrication. A miniaturised and user-friendly printing system would be more accessible for these situations. Therefore, this work will aim to develop a portable DLP 3D printing system using the smartphone's screen as the illumination source. Drug-eluting systems, such as oral dosage forms and medical devices, will be fabricated to demonstrate the versatility of the developed system:

•   Evaluate the possibility of producing oral tablets in various shapes and geometries.

•   Study the feasibility of fabricating anatomically-compliant drug delivery devices utilising 3D scanning mobile apps to obtain patient-specific 3D models.

Chapter 2

SLA 3D printing of intravesical devices

2 SLA 3D printing of intravesical devices

2.1 Overview

Urinary bladder diseases are widespread over the world and have impact on the patient's daily life and social activities. Treatment involves systemic and local drug administration. Intravesical instillation therapy is an approach that offers high drug concentrations at the target site while minimising systemic side effects. However, the short drug residence time in the bladder and the need for repeated catheterisation often limit the therapeutic efficacy. In this chapter, SLA 3D printing was investigated to prepare indwelling intravesical devices using an elastomer to achieve localised and extended drug delivery in the bladder. The devices were designed to be inserted into and retrieved from the bladder using a urethral catheter. Two types of devices (hollow and solid) were prepared incorporating three drug loads of lidocaine hydrochloride (10%, 30%, and 50% w/w). The physical characteristics and mechanical properties of different formulations were assessed, and the *in vitro* drug release profiles were evaluated in simulated urine fluid for up to 14 days.

2.2 Introduction

Disorders of the urinary bladder, such as interstitial cystitis, urinary incontinence, and overactive bladder, affect millions of patients in the world and have a major impact on daily activities, social function, and quality of life. Particularly, bladder cancer is the sixth leading cause of death in the Europe Union with more than 120,000 people diagnosed per year (Leal et al., 2016).

Common therapies for bladder disorders involve systemic administration, mainly by oral medications and transdermal patches. However, these treatments often fail to target the affected tissues and the use of higher doses may lead to undesirable side effects (Palugan et al., 2021). Alternatively, local administration is accomplished by instillation of drug solutions or suspensions directly into the bladder cavity through a catheter inserted into the urethra of the patient (Nickel et al., 2009; Parsons, 2005). Favourably, intravesical installation enables high therapeutic concentrations at the site of interest, thereby improving treatment efficacy and reducing systemic exposure (Lee and Cima, 2011). It should be taking consideration that the maximum residence time of instilled drug solution in the bladder is approximately 2 h before it is voided by urination. Therefore, repeated catheterisation procedure is required which is associated with patient inconvenience and discomfort, as well as increasing risk of inflammation and bacterial infection (Fraser et al., 2002; Lee and Choy, 2016; Palugan et al., 2021).

Innovative indwelling drug delivery systems have been designed to be administered by transurethral catheterisation and remained in the bladder for prolonged drug delivery (Zacchè et al., 2015). These systems can either be biodegradable and will be eliminated by urination, or they are made with nondegradable materials, which require physical removal of the device at the end of the treatment by urethral cystoscopy. The former avoids the removal procedure but could provoke debris that might lead to voiding difficulties while the latter unavoidably reduces patient compliance (Von Walter et al., 2009).

2.2.1 Biodegradable intravesical devices

The use of shape memory polymers was proposed for preparing novel indwelling devices for intravesical drug delivery (Melocchi et al., 2019). Utilising hot melt extrusion (HME) and fused deposition modelling (FDM) 3D printing, caffeine-loaded intravesical retentive systems in various shapes were prepared using the pharmaceutical grade poly(vinyl alcohol) (PVA) **(Figure 2.1a).** To assist insertion, the device is deformed to a temporary shape suitable for administration via catheter. Upon exposure to body temperature, the device exhibits shape recovery and controlled release of the drug.

Another semi-biodegradable system was developed for treating overactive bladder syndrome (Hopmann et al., 2015). The device is composed of multiple carriers (spheres or pills) that consist of foamed absorbable matrix made from poly-D, L-lactide-*co*-glycolide-co-polyethylene glycol di-block copolymer (PLGA-PEG) embedding trospium chloride-loaded microspheres. The spherical carriers are connected flexibly with each other by means of an absorbable suture thread **(Figure 2.1b).** The device is designed to be expanded in the bladder through pulling the threads, and the subsequent change in shape allows retention of the device in the bladder. After degradation of the PLGA-PEG matrix, the non-absorbable microspheres are eliminated in the urine.

A reservoir-based device constructed of biodegradable elastomer has been presented for localised urological therapies (Tobias et al., 2010). The device made of poly(glycerol-*co*-sebacic acid) is casted in tubular geometry with ciprofloxacin hydrochloride powder packed into its core and laser-drilled orifices on its wall to allow osmotic drug release **(Figure 2.1c)**.
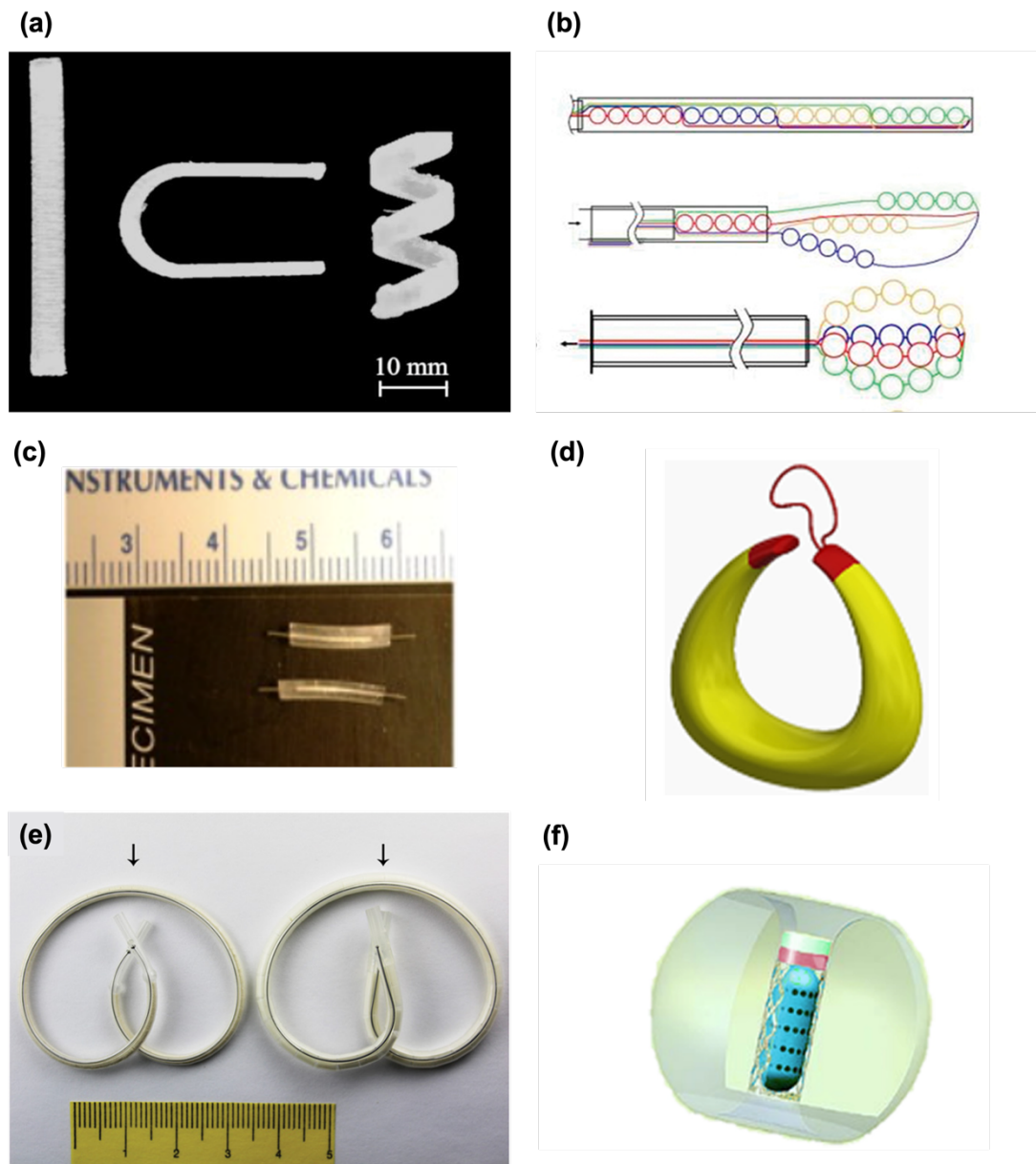
Figure 2.1 Images of different intravesical devices including (a) PVA-based specimens in different shapes (Melocchi et al., 2019); (b) the multiple carriers system (Hopmann et al., 2015); (c) the reservoir-based elastomeric device (Tobias et al., 2010); (d) the UROS infuser (Palugan et al., 2021); (e) the LiRIS™ devices (Nickel et al., 2012); and (f) the intravesical balloon (Palugan et al., 2021).

2.2.2 Nondegradable intravesical devices

One nonbiodegradable example is the UROS infusion pump developed by Situs Corporation Ltd. **(Figure 2.1d)** (Fraser et al., 2002). The device involves a drug reservoir that can be easily inserted empty as a straight tube (10 mm length × 6 mm outer diameter) into the bladder and filled with oxybutynin solution from the outside. After the device is filled, it transforms into a crescent shape and maintains a constant drug release at 10 mL/day over time (Cima et al., 2014). The size of the reservoir is large enough not be voided out accidentally but not too large to cause bladder irritation or obstruction. In Phase I clinical trials, the UROS infusers were tested in healthy volunteers and the results showed clinical benefits, although they failed to progress beyond Phase II (Nickel et al., 2012).

LiRIS™ (lidocaine-releasing system) and GemRIS™ (gemcitabine-releasing system) were intravesical drug delivery devices developed by TARIS Biomedical **(Figure 2.1e)** (Nickel et al., 2012; Tan and Kelly, 2018). The dual-lumen pretzel-shaped devices include a water-permeable silicon tube containing either lidocaine or gemcitabine minitablets and a laser-drilled orifice as an osmotic pump (Lee and Cima, 2011). The second lumen is for the nitinol wire to retain the shape of the device and provide retention. To administer this system, the device is uncurled inside a catheter and inserted into the bladder. Once the device is positioned, the superelastic nitinol regains the initial shape, and the device is retained in the target area.

Yachia and Hirszowicz patented a floating system for monitoring bladder function or in the treatment of urinary incontinence **(Figure 2.1f)** (Innoventions Ltd; Yachia and Hirszowicz, 2001). The system comprises an expandable

balloon to be filled and compressed prior to insertion, or to be inserted into the bladder and filled afterwards so that it is inflated in the bladder for sustained drug delivery. The balloon contains a magnetic portion to displace the device into a sealing position within the bladder. A self-sealing valve located in the wall of the balloon is used to fill the lumen and prevents leakage after the needle used for filling is withdrawn.

Although the above-mentioned approaches are novel, the manufacturing processes of these devices seem to be complex and require multiple steps, which makes them inherently time consuming and cost intensive. Therefore, development of an easy-to-manufacture intravesical device that is able to provide sustained drug release in the bladder for a desired time frame appears needed. Such a device could potentially reduce the requirement of repeated catheterisation at the hospital, benefiting both the patients and the involved healthcare personnel as well as lowering the incidence of secondary infections (Palugan et al., 2021).

2.2.3 Model drug and photopolymer

Lidocaine hydrochloride **(Figure 2.2)** was chosen to be the model compound in this chapter. It is a local anaesthetic, and it acts by blocking sensory fibres (Digesu et al., 2020). It is frequently used for interstitial cystitis or bladder pain syndrome by instillations.
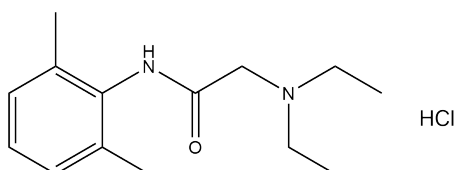
Figure 2.2 Chemical structure of lidocaine hydrochloride.

Elastomers (elastic polymers or rubbery polymers) are a class of polymers with viscoelasticity that are characterised by having weak intermolecular forces and low Young's modulus. They are capable of resuming their original shape after removal of the deforming force (such as stretching or compression). These characteristics are desirable for manufacturing drug delivery devices that require different conformations for insertion and for retention. Previously, various elastomers have been considered for preparing biomedical devices with drug delivery purposes including vaginal rings and pessaries (Bashi et al., 2021; McCoy et al., 2018; Spoerk et al., 2021), gastric-resident dosage forms (Bellinger et al., 2016; Kirtane et al., 2018), wearable films (Di et al., 2015), and transdermal patches (Gennari et al., 2020). In this chapter, Elastic Resin (Formlabs Inc., USA) (Formlabs, 2019) was selected as the photopolymer for SLA 3D printing.

2.3 Aim

- To explore the feasibility of using SLA 3D printing in the development of elastomer-based intravesical devices.
- To design and develop two types of intravesical devices (hollow and solid) using lidocaine hydrochloride with three different drug loadings, (10%, 30%, and 50% w/w).
- To assess the physical and mechanical characteristics of different drug-loaded formulations.
- To evaluate the drug release profiles of different intravesical devices in relevant media.

2.4   Materials

Lidocaine hydrochloride monohydrate (MW 288.81 g/mol, logP <0 (Sawant et al., 2010), water solubility 50 mg/mL (Alfa Aesar, 2022)), magnesium chloride anhydrous ($MgCl_2$, ≥98%, MW 95.21 g/mol), urea (≥99%, MW 60.06 g/mol), and acetonitrile (≥99.9%, HPLC grade) were obtained from Sigma-Aldrich (Dorset, UK). The printing polymer, Elastic Resin (a thermoset material), was purchased from Formlabs Inc. (USA). Gelucire® 48/16 was obtained from Gattefosse (Saint-Priest, Lyon, France). Potassium dihydrogen phosphate (KH_2PO_4, 99.5-100.5%, MW 136.09 g/mol), magnesium sulphate ($MgSO_4$, 99.7%, MW 120.37 g/mol), potassium chloride (KCl, 99.5-101.0%, MW 74.55 g/mol) and calcium chloride dihydrate ($Cacl_2 \cdot H_2O$, 99.0-103.0%, MW 147.01 g/mol) were acquired from VWR International Ltd. (Leicestershire, UK). Phosphoric acid (for HPLC, 85-90%, MW 97.99 g/mol) was purchased from Honeywell (Seelze, Germany). Sodium chloride (NaCl, ≥99.5%, MW 58.44 g/mol) was obtained from Fisher Scientific (Loughborough, UK). All materials were used as received.

2.5   Methods

2.5.1   3D design

3D models of the devices were designed using 123D Design (Autodesk Inc., USA) with an S-shape, allowing their retention in the bladder. The designs could be elongated in a straight tube shape with a length of approximately 130 mm and an outer diameter of 3 mm, allowing insertion in the bladder with a urethral catheter (size ranges from 4.6 to 5.3 mm outer diameter for adults). Two types of intravesical device (hollow and solid) were designed. The hollow devices (**Figure 2.3** left, size 1.0) comprised a drug reservoir (0.5 mm shell

thickness) and two holes (1 mm diameter) at the ends to allow loading of the drug as a melted solution into the devices and control the drug release. The solid devices (**Figure 2.3** right, size 1.0) were designed without any voids and were directly fabricated from the drug-loaded printing resin. The solid devices were also prepared in various sizes by applying a scale factor of 0.5, 0.6, 0.7, 0.8, 0.9 on the 3D design.
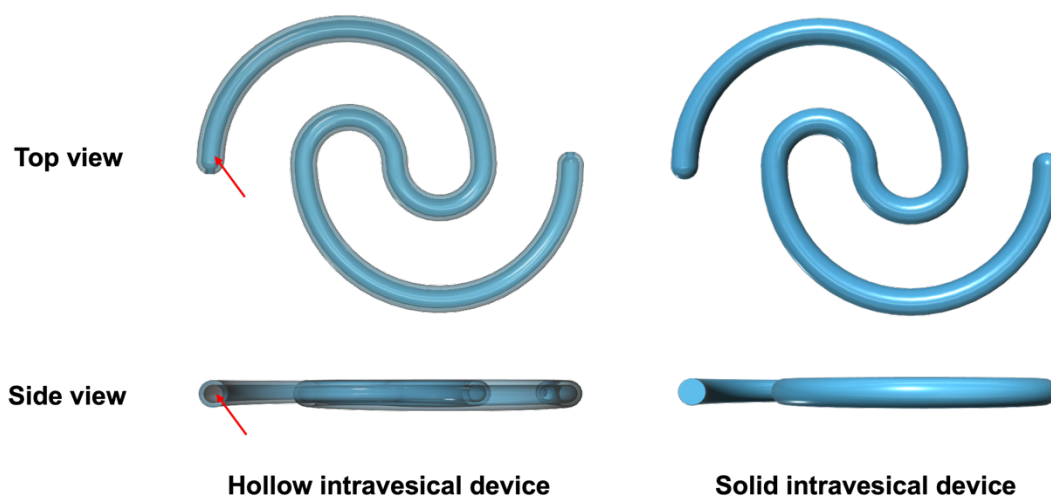
Figure 2.3 3D designs of the hollow (left) and solid (right) intravesical devices size 1.0 (red arrows indicate the hollow cavity).

Tensile bars were prepared for performing tensile test (section 2.5.11) to understand the mechanical properties (strength and ductility) of different drug-loaded formulations. The 3D model of the tensile bar was designed using 123D Design based on the guidelines from the ASTM D638-14 Standard Test Method for Tensile Properties of Plastics, Type IV specimen (ASTM ISO, 2022b) at a scale factor of 0.5 (**Figure 2.4**).
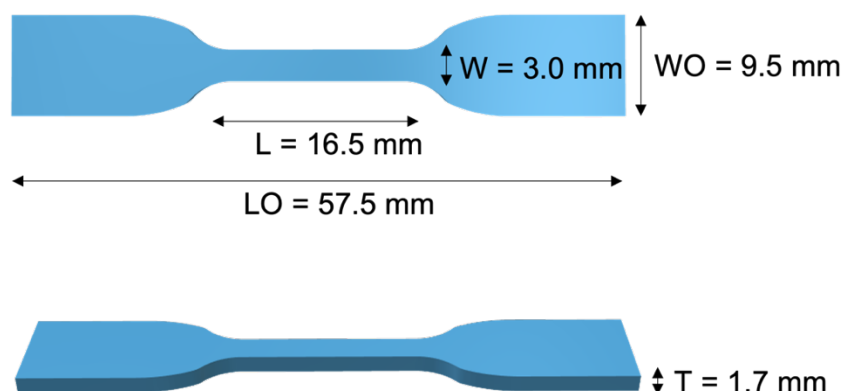
Figure 2.4 3D model of the tensile bar (W – Width of narrow section; WO – Width overall; L – length of narrow section; LO – length overall; T– thickness).

2.5.2 Preparation of drug-loaded resin formulations

The drug-loaded resins formulations were prepared by adding 10%, 30%, and 50% w/w of lidocaine hydrochloride into the Elastic Resin under stirring at room temperature until the drug was homogenously dispersed within the resin (**Table 2.1**). Then the drug-loaded resins were directly loaded into the tray of the 3D printer. A control formulation IVS-0 (solid, with 0% drug load) was prepared for comparison in the X-ray micro computed tomography and mechanical testing.

Table 2.1 Compositions (% w/w) of the drug-loaded resin formulations used to print solid intravesical devices.

Formulations	Lidocaine hydrochloride (% w/w)	Elastic Resin (% w/w)
IVS-0	0	100
IVS-10	10	90
IVS-30	30	70
IVS-50	50	50

2.5.3   3D printing process

A commercial Form 2 SLA 3D printer (Formlabs Inc., USA) equipped with a 405 nm laser was used to prepare the intravesical devices (**Figure 2.5**). The 3D models of the intravesical devices were exported as a stereolithography (.stl) file to the Preform Software (Formlabs Inc., USA). "Elastic" was selected as the material setting with a layer thickness of 50 µm. For the hollow devices, the drug reservoirs were printed with supports (mini rafts, density 1.00, touchpoint size 0.50 mm) on the build platform using the Elastic Resin. For printing of the solid devices, the Open Mode was enabled to allow the use of with third-party resins. All the solid devices were printed with supports (mini rafts, density 1.00, touchpoint size 0.50 mm) using the lidocaine hydrochloride-loaded resin formulations. After printing, all the SLA printed devices were washed with isopropyl alcohol (1 min for solid devices and 20 min for hollow devices) in Form Wash (Formlabs Inc., USA) to remove any uncured resin on the surface of the devices. Additionally, a post curing process was performed in a Form Cure (Formlabs Inc., USA) at 60 °C for 20 min under a source of light (λ= 405 nm) for all the devices. A side cutter was used to remove the supports carefully.
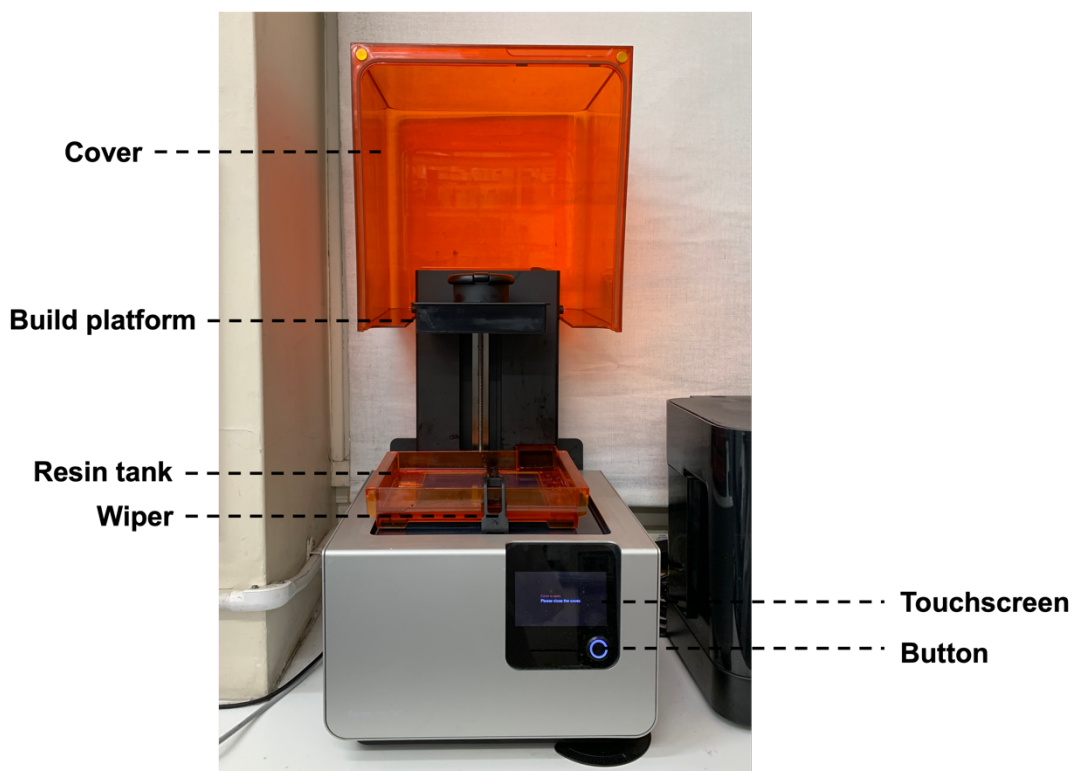
Figure 2.5 Picture of a Form 2 SLA 3D printer with the cover lifted.

2.5.4 Preparation of drug-loaded Gelucire® mixture

The filling of the hollow intravesical device contained a mixture of 10%, 30%, and 50% w/w of lidocaine hydrochloride and Gelucire® 48/16 **(Table 2.2)**. Gelucire® 48/16 is a non-ionic water-dispersible surfactant with hydrophilic-lipophilic balance values of 12, comprising polyethylene glycol (PEG) -32 (M_W 1500) mono- and diesters of palmitic (C_{16}) and stearic (C_{18}) acids and was chosen as a carrier due to its low melting point (48 °C), water solubility and ease of manipulation for injection into the medical device (Gattefosse). The mixtures were prepared in a glass beaker by heating at 80 °C under magnetic stirring to ensure complete dissolution of drug in the melted Gelucire® 48/16. The mixtures were then transferred to a 2 mL syringe (maintained at 80 °C to

avoid solidification) and were subsequently injected into the void cavity of the hollow devices.

Table 2.2 Compositions (% w/w) of the drug-loaded formulations used for the hollow intravesical devices.

Formulations	Lidocaine hydrochloride (% w/w)	Gelucire® (% w/w)
IVH-10	10	90
IVH-30	30	70
IVH-50	50	50

2.5.5 X-ray powder diffraction (XRPD)

Discs (23 mm diameter x 1 mm height) were SLA 3D printed using drug-loaded formulations (IVS-10, IVS-30, IVS-50) for the solid device characterisation. For the hollow device characterisation, drug-loaded fillings (IVH-10, IVH-30, and IVH-50) were prepared as in section 2.5.4 in 2 mL syringes and moulded into the metallic disc holder to obtain the discs (23 mm diameter x 1 mm height). The XRPD patterns were obtained in a Rigaku MiniFlex 600 (Rigaku, USA) equipped with a Cu Kα X-ray source (λ=1.5418Å). Samples of lidocaine hydrochloride, Gelucire® 48/16, and all the drug-loaded discs were analysed. The intensity and voltage applied were 15 mA and 40 kV. The angular range of data acquisition was 3–60° 2θ with a stepwise size of 0.02° at a speed of 5°/min.

2.5.6 Thermal analysis

Differential scanning calorimetry (DSC) was used to characterise lidocaine hydrochloride, Gelucire® 48/16, the SLA printed drug-loaded formulations

(IVS-10, IVS-30, IVS-50), and the drug-loaded fillings for the hollow devices (IVH-10, IVH-30, and IVH-50). The measurements were performed with a Q2000 DSC (TA instruments, Waters, LLC, USA) from 0 °C to 150 °C at a heating rate of 10 °C/min. Calibration for cell constant and enthalpy was performed with indium (T_m = 156.6 °C, Δ Hf = 28.71 J/g) according to the manufacturer's instructions. Nitrogen was used as a purge gas at 50 mL/min for all the experiments. TA aluminium pans and Tzero hermetic lids (pin hole made with a tweezer) were used with an average sample mass of 3 – 5 mg. Data were collected with TA Advantage software for Q series (version 2.8.394) and analysed using TA Instruments Universal Analysis 2000. All melting temperatures are reported as extrapolated onset unless otherwise stated.

2.5.7 X-ray micro computed tomography (Micro-CT)

A high-resolution X-ray micro computed tomography (Micro-CT) scanner (SkyScan1172, Bruker-microCT, Kontich, Belgium) was used to visualise the internal structures and density of small sections of the intravesical devices. The samples were scanned using no filter with a resolution of 2000 × 1048 pixels. 3D imaging was performed by rotating the object through 360° with steps of 0.4° and four images were recorded for each of those. NRecon software (Version 1.7.0.4, Bruker-microCT) was used to reconstruct the images and the collected data were analysed using the software CT Analyzer (CTan version 1.16.4.1), where maps of different colours were used to represent the atomic density of the devices.

2.5.8 Scanning electron microscopy (SEM)

Sections of the intravesical devices were attached to a self-adhesive carbon disc mounted on a 25 mm aluminium stub, which was coated with 25 nm of gold using a sputter coater. The stub was then placed into a FEI Quanta 200 FEG Scanning Electron Microscope (FEI, UK) at 5 kV accelerating voltage using secondary electron detection to obtain the cross-section SEM images.

2.5.9 Determination of drug loading

For the solid intravesical devices, drug loading was determined by cutting the devices into small pieces and stirring them in 100 mL of isopropyl alcohol to allow extraction of the drug. In the case of the hollow intravesical devices, the filling mixtures were dissolved in 100 mL of distilled water. Samples of solutions were filtered through 0.45 µm filters (Millipore Ltd., Ireland) and the concentration of drug was determined with HPLC (Hewlett Packard 1260 Series HPLC system, Agilent Technologies, Cheadle, UK). The stationary phase was an Eclipse plus C18 column, 100 mm × 4.6 mm (Zorbax, Agilent technologies, Cheshire, UK) and the mobile phase consisted of 0.01 M potassium dihydrogen phosphate (pH 2.1 adjusted with phosphoric acid) (80% v/v) and acetonitrile (20% v/v) at 30 °C. The injection volume was 30 µL and the flow rate was kept at 1 mL/min. The eluent was screened at a wavelength of 214 nm and the retention time of lidocaine hydrochloride was at 3.5 – 3.6 min.

2.5.10 *In vitro* drug release study

Drug release from the SLA printed intravesical devices was determined using a shaking water bath (DMS360, Fisher Scientific, UK), maintained at a speed of 60 oscillations/min at 37 ± 0.5 °C under sink conditions (n=3). The intravesical devices were incubated in 500 mL of simulated urine fluid (composed of NaCl 13.75, $MgSO_4$ 1.69, $MgCl_2$, 0.83, $CaCl_2$ 0.67, KCl 0.38, and urea 17.40 g/mL, pH 7.50) (Sherif et al., 2018) in glass bottles. 2 mL of fluid samples were withdrawn at predetermined time intervals and an equal volume of medium was replaced. After the release study, the devices were retrieved to extract any residual drugs, and this was be taken into consideration in the calculation of percentage of drug released. The concentration of drug was determined using HPLC (as per the method in section 2.5.9).

To determine the drug release kinetics and mechanism, various mathematical models (zero-order model, first-order model, Higuchi model, and Korsmeyer-Peppas model) were tested to fit the data obtained from *in vitro* release study into the following equations (Bruschi, 2015):

Zero-order model $$Q_t = Q_0 + k_0 \times t$$ (Eq. 2.1)

Where Q_t is the amount of drug released over time t, Q_0 is the initial amount of drug in the solution, and k_0 is the zero-order release constant.

First-order model $$logQ_t = logQ_0 + \frac{k_1 \times t}{2.303}$$ (Eq. 2.2)

Where Q_t is the amount of drug released over time t, Q_0 is the initial amount of drug in the solution, and k_1 is the first-order release constant.

Higuchi model $$Q_t = k_H \times t^{\frac{1}{2}}$$ (Eq. 2.3)

Where Q_t is the amount of drug released over time t and k_H is the Higuchi release constant.

Korsmeyer-Peppas model $$\frac{M_t}{M_\infty} = k \times t^n$$ (Eq. 2.4)

Where M_t/M_∞ is the fraction of drug released over time t, k is the constant of incorporation of structural modifications and geometrical characteristics of the system, and n is the exponent of release.

2.5.11 Tensile testing

To determine the effect of lidocaine on the mechanical properties of the formulation, a tensile test was carried out using an Instron 5567 Universal Testing Machine at room temperature (n=6). The dimensions (length, width, and thickness) of each tensile bar were measured using a digital calliper and recorded in the software. Following the guidelines from the ASTM standard D638-2014, the speed of testing was chosen as 50 mm/min for non-rigid specimens to give ruptures within 0.5 min to 5 min testing time. Five tensile bars were tested in each group and the failure at the narrow section of the tensile bar was expected.

2.5.12 Statistical analysis

Drug dissolution tests and mechanical tests were performed in triplicate and sextuplicate, respectively. All numerical results are presented as mean ± standard deviation (SD), unless otherwise specified. Error bars represent standard deviation. Data from the mechanical tests were statistically analysed by performing one-way ANOVA with Tukey's post-hoc test executed (OriginPro 2017, OriginLab corporation, Northampton, MA, USA). $P < 0.05$ was considered statistically significant. Significance level notation was

expressed as * for p < 0.05, ** for p < 0.01, *** for p < 0.001, and **** for p < 0.0001.

2.6   Results and discussion

2.6.1   Hollow intravesical devices

2.6.1.1   3D printing

Hollow intravesical devices were successfully fabricated in two steps; first, SLA 3D printing was used to produce the drug reservoir of the device using the Elastic Resin **(Figure 2.6a);** then after removing the supports, melted lidocaine-loaded Gelucire® mixtures were filled into the hollow cavity using syringes **(Figure 2.6b)**. The drug reservoirs were fabricated the same as the 3D model design with high resolution and smooth surface finish. The devices were transparent before loading of the mixture of drug and excipient and showed an opaque and cream-coloured aspect after loading of the mixture. The average weight of the drug reservoir was 774.4 ± 20.4 mg. Approximately 254.4 ± 24.2 mg of lidocaine-loaded Gelucire® mixtures were fitted into the hollow cavity, correlating to 25 mg, 75 mg, and 125 mg of lidocaine being loaded into the IVH-10, IVH-30, and IVH-50 intravesical devices.

The flexibility of the hollow intravesical devices was tested under external force **(Figure 2.6c).** The devices could be stretched into a straight tube shape, and they recovered their original shape when no force was applied. This feature is crucial to ensure the device is able to be retained in the bladder without being expelled or causing harm to the bladder wall while releasing the drug. Intravesical devices without a retention frame have been reported to be voided from the bladder of rabbits (Lee and Cima, 2011).

Figure 2.6 Picture of (a) an SLA 3D printed drug reservoir with supports (size 1.0); (b) hollow intravesical device (size 1.0) before (left) and after (right) filling with 10% lidocaine-loaded Gelucire® mixture; and (c) the IVH-10 device (size 1.0) under stretching. Scale in cm.

In general, the catheter size for adults ranges from 4.6 to 5.3 mm (outer diameter). The average outer diameter of the SLA printed hollow intravesical devices was 3.0 ± 0.02 mm, which potentially was thin enough to be fitted into the catheter to be implanted into the bladder.

2.6.1.2 Physical characterisation

XRPD and DSC analyses were conducted to evaluate the physical characteristics of the IVH-10, IVH-30, and IVH-50 drug-loaded Gelucire® mixtures. The XRPD data **(Figure 2.7)** showed that Gelucire® 48/16 exhibited partial crystallinity indicated by the two peaks at 19.1° and 23.4° 2θ. When the

Gelucire® 48/16 content decreases from 90% to 50% w/w, the intensity of the Gelucire peaks decrease. No crystalline peaks of lidocaine (12.4°, 13.7°, 24.6°, and 25.5° 2θ) were observed by XRPD in any of the hollow formulations. This could be due to the fact that only a small portion of the drug remains in a crystalline form and does not dissolve within the melted Gelucire carrier, and this is not observed using XRPD because of the detection limit (>5%) of the method.
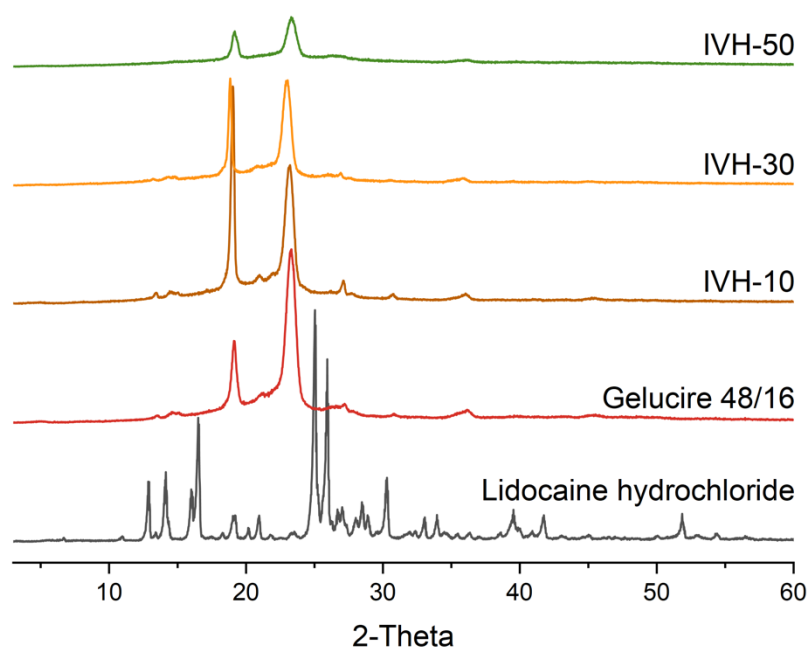
Figure 2.7 X-ray powder diffractograms of lidocaine hydrochloride, Gelucire® 48/16, and drug-loaded Gelucire® mixtures.

Similarly, the DSC results **(Figure 2.8)** show the endothermic peak of the melting of lidocaine at 80 °C, which was visible only in the IVH-30 and IVH-50 mixtures. The melting of Gelucire® 48/16 at around 45-50 °C was less visible with the amount of Gelucire® 48/16 decreasing from 90% to 70% then to 50% w/w.
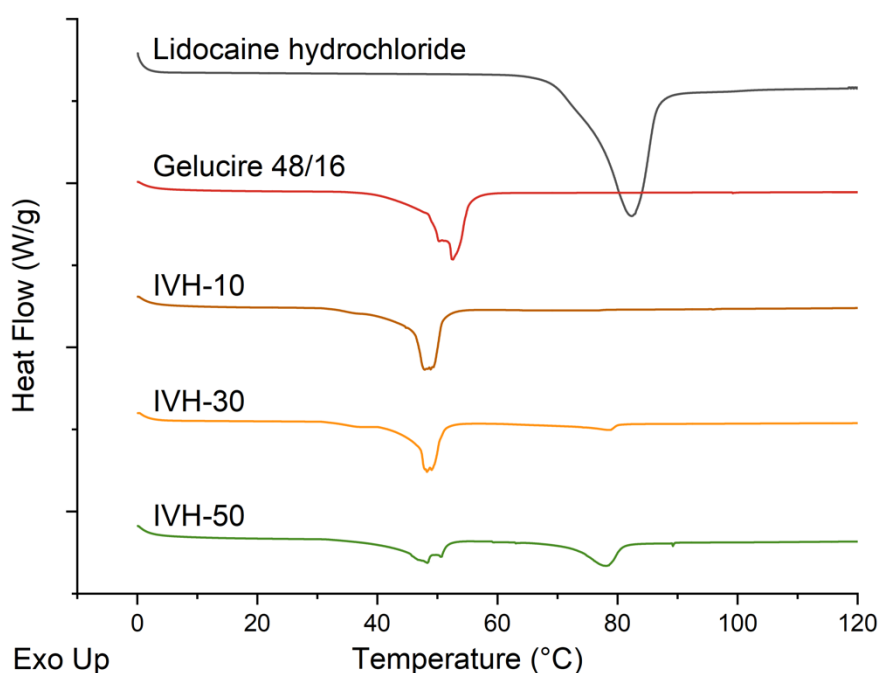
Figure 2.8 DSC thermograms of lidocaine hydrochloride, Gelucire® 48/16, and drug-loaded Gelucire® mixtures.

X-ray micro-CT imaging was used to visualise the internal structure of the hollow intravesical devices **(Figure 2.9, Top)**. A clear distinction between the reservoir (red colour) and the drug-loaded Gelucire® mixtures (mainly white colour) was observed in the images. By increasing the loading of lidocaine in the Gelucire formulations, an increased amount of white colour can be visualised, indicating that the drug has a higher atomic density compared with the Elastic Resin and Gelucire. The SEM images **(Figure 2.9, Bottom)** also confirmed that when the lidocaine loading increases, more drug particles are observed on the surface of the drug-loaded Gelucire® mixtures.
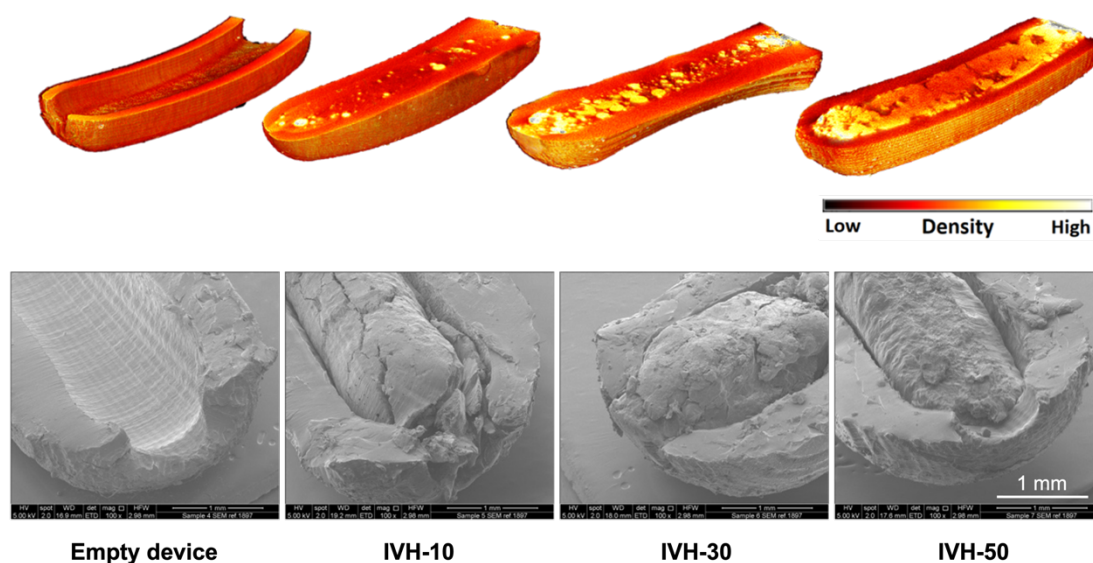
Figure 2.9 X-ray micro-CT images (top) and SEM images (bottom) of sections of the hollow intravesical devices (size 1.0). From left to right, empty device, IVH-10, IVH-30, and IVH-50 devices. The scale bar in the micro-CT image is representative of atomic density.

2.6.1.3 *In vitro* drug release

Drug loading of the lidocaine-loaded Gelucire® mixtures was evaluated before loading into the hollow cavity. The lidocaine contents were 10.4% ± 0.6, 31.3% ± 0.9 and 48.7% ± 3.0 for IVH-10, IVH-30, and IVH-50 devices, respectively, which are in broad agreement with theoretical drug loadings, confirming that little drug loss occurred during the preparation process. Drug dissolution profiles from the hollow intravesical devices over a 7-day period **(Figure 2.10)** were obtained in 500 mL of simulated urine fluid to simulate the dissolution conditions in the bladder. Within the first 10 h, 46% lidocaine was released from the IVH-50 devices, whereas 31% and 19% were released from the hollow IVH-30 and IVH-10 devices, respectively. During the dissolution test, water entered into the hollow device through both holes on the sides of the

devices and the mechanism of drug release was through erosion of the lidocaine-loaded Gelucire® mixtures. In the IVH-50 devices, all the lidocaine was released in 3 days. For the hollow IVH-10 and IVH-30 devices, lidocaine was completely released after 4 days.
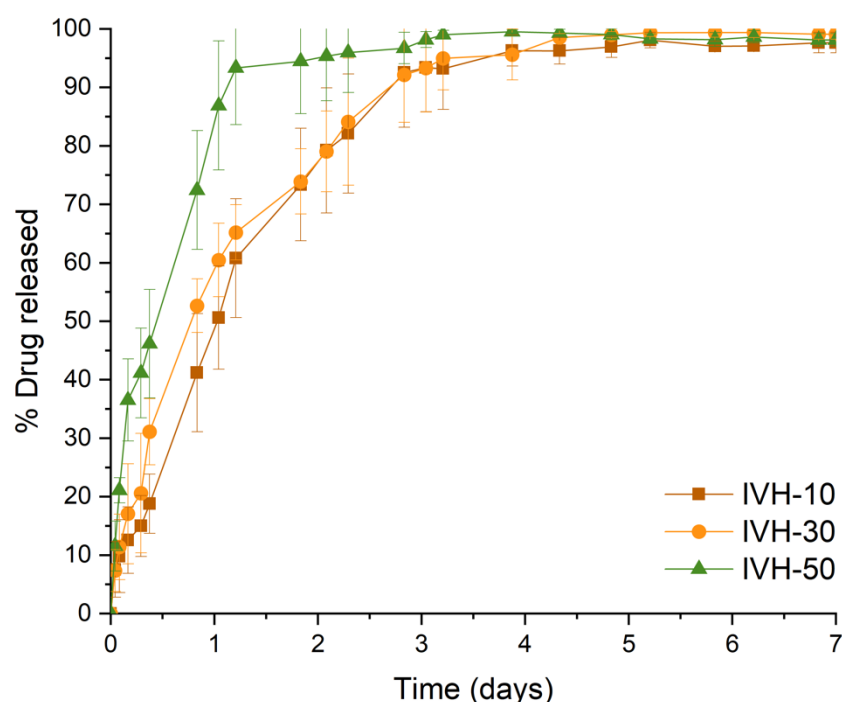
Figure 2.10 Cumulative release profiles of lidocaine hydrochloride from the SLA 3D printed IVH-10, IVH-30, and IVH-50 devices (size 1.0). Data values represent mean ± SD, which are not seen in some data points as they are smaller than the symbols (n=3).

Furthermore, the *in vitro* dug release data were fitted into various kinetic models. Since the release from the hollow devices is directional though two holes on the side, it does not follow one of the assumptions to use the Higuchi model, which is the diffusion is unidirectional, because the edge effects are negligible (Bruschi, 2015). Therefore, only zero-order, first-order, and

Korsmeyer-Peppas kinetic models were used to determine the drug release kinetics. As shown in **Table 2.3**, the first-order model was found to be the best-fit model for all the hollow devices with the highest correlation coefficient R^2, meaning the drug release rate is concentration-dependent. The IVH device presents a reservoir system which means with higher drug loading, the drug dissolution within the hollow cavity is faster compared to drug diffusion through the holes considering the drug having a higher solubility than the Gelucire. However, the IVH-10 and IVH-30 devices displayed similar release profiles, showing the same value of first-order release constant k_1. This could be due to the drug loading was relatively low (< 50%), the drug dissolution rate within the reservoir was not necessarily faster than the rate of diffusion, hence no different between the drug release rates. When the drug loading was high as in the IVH-50 devices, more than 2-fold of increase was shown in the release rate. By fitting the data in the Korsmeyer-Peppas model, it shows that all the hollow devices also exhibited n values higher than 0.45 but less than 0.89 (considered as cylinders), which suggested the model was anomalous transport and the mechanism of drug release was governed by diffusion and swelling (Bruschi, 2015).

Table 2.3 Release kinetic data of the SLA 3D printed hollow intravesical devices containing lidocaine hydrochloride.

Release kinetics model	Parameters	IVH-10	IVH-30	IVH-50
Zero-order	R^2	0.973	0.929	0.933
	k_0 (h^{-1})	1.502	1.465	3.076
First-order	R^2	0.993	0.990	0.965
	k_1 (h^{-1})	0.031	0.031	0.072
Korsmeyer-Peppas	R^2	0.929	0.981	0.956
	k (h^{-n})	3.855	7.083	12.814
	n	0.795	0.644	0.625

The hollow intravesical devices demonstrated prolonged lidocaine release over 4 days, which is an improvement in comparison to previously fabricated 3D printed drug loaded retentive devices, in which caffeine was completely released within 2 h (Melocchi et al., 2019). It is worthy to note that whilst drug release over 4 days could improve the short-term compliance of patients with bladder pain syndrome or interstitial cystitis, a longer release profile would be more suitable for patients suffering from the condition chronically and reduce the number of catheterisation procedures.

2.6.2 Solid intravesical devices

2.6.2.1 3D printing

In order to prolong the release of lidocaine hence increasing drug residence time at the target site, solid intravesical devices were designed and evaluated. Prior to printing, when mixing the drug with the Elastic Resin, lidocaine was observed as needle-shape particles suspended in the resin and the number of

particles increased as the drug loading increased from 10% to 30% w/w **(Figure 2.11).**

(a) (b)
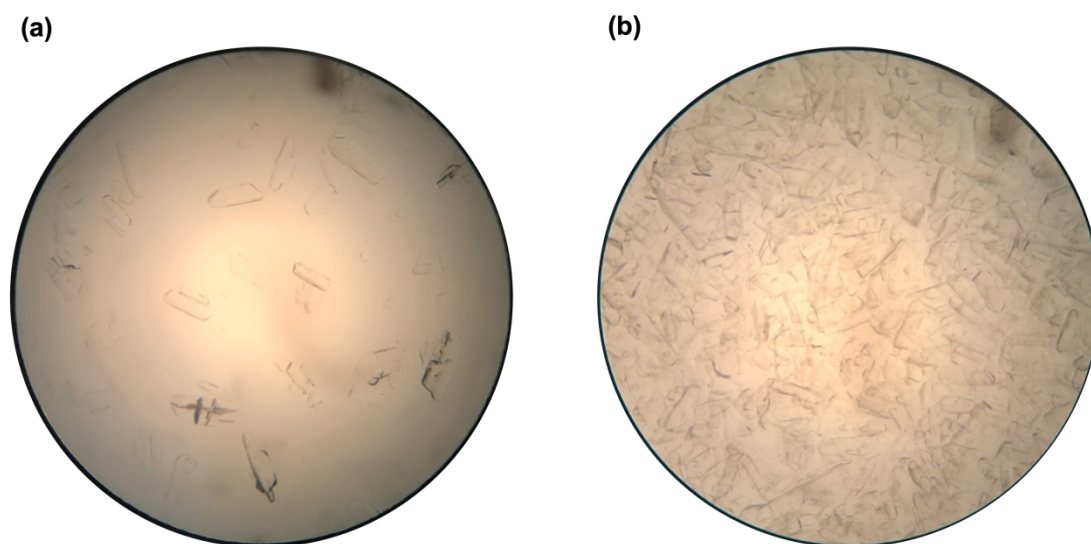
Figure 2.11 Light microscope image of (a) IVS-10 and (b) IVS-30 resin formulations.

Favourably, all the solid intravesical devices were successfully printed, regardless of the drug loading **(Figure 2.12a)**. The colour of the IVS-10 device was transparent with visible white particles of lidocaine whereas the IVS-30 and IVS-50 devices exhibited in fully white colour. The surface texture of IVS-10 was smoother than IVS-30 and IVS-50 due to lower drug loading of lidocaine. Some support marks could be observed. The average weights of the solid devices were 1411.7 ± 15.1 mg, 1564.7 ± 5.7 mg, and 2549.2 ± 28.9 mg, corresponding with approximately 150 mg, 450 mg, and 1250 mg of lidocaine loaded in the IVS-10, IVS-30, and IVS-50 devices, respectively. The outer diameters of the solid device were 3.1 ± 0.02 mm, 3.7 ± 0.06 mm, and 5.1 ± 0.17 mm, which were suitable for insertion via a catheter. It is worth mentioning that the commercial Form2 SLA 3D printer used in this chapter is not designed to print with third-party resins, which means the printing parameters (e.g., laser

power, laser speed, the number of laser passes) are not optimal to print other resin formulations. Therefore, the drug particles suspended in the resin may affect the layer thickness, resulting in much wider outer diameters (IVS-30 and IVS-50 devices) compared with the 3D model. Moreover, increasing the drug loading has increased the viscosity, causing the resin formulation not able to flow back into the gap between the surface of the resin tank and the previous cured layer. Hence, pausing was required during printing to manually distribute the resin, resulting in longer printing time. In a similar manner to the hollow intravesical device, the solid intravesical device could withstand elongation and could instantaneously return to its initial design once the external force was removed **(Figure 2.12b).**
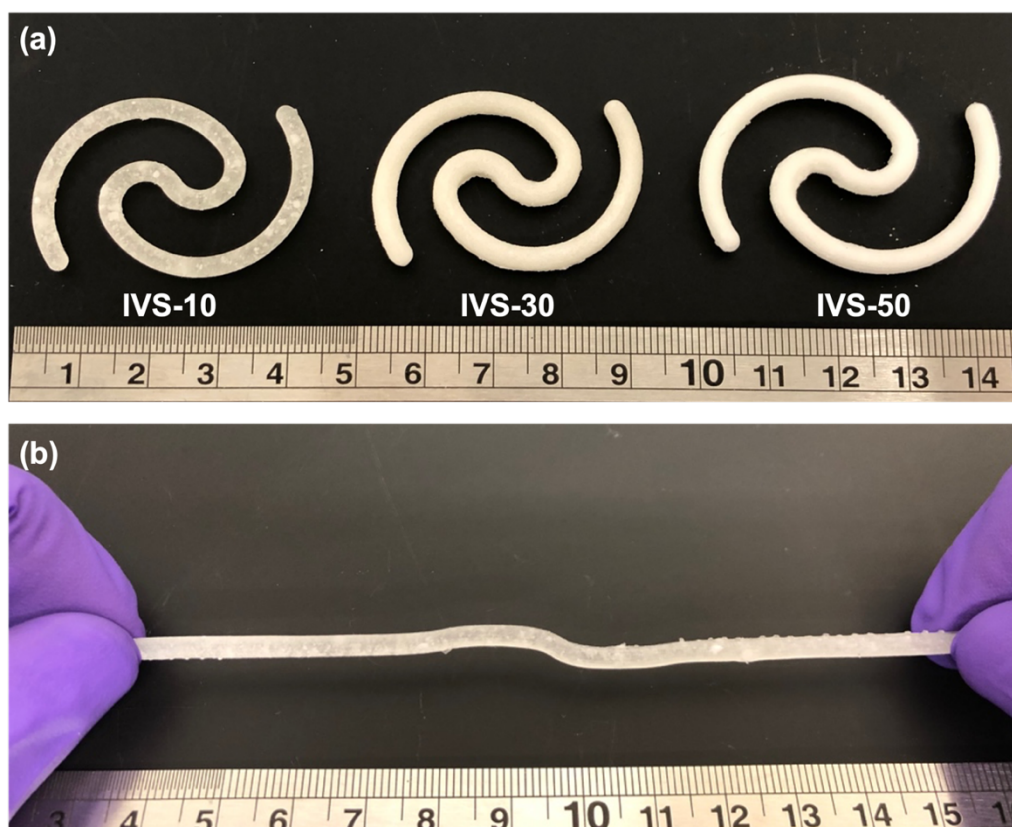
Figure 2.12 Picture of (a) SLA 3D printed IVS-10, IVS-30, and IVS-50 intravesical devices (size 1.0) and (b) the IVS-10 device (size 1.0) under stretching (bottom). Scale in cm.

In addition, SLA 3D printing is capable of preparing solid devices in a wide range of sizes to provide personalised therapies to individual patients by scaling the dimensions of the 3D design **(Figure 2.13)**, highlighting the flexibility and reproducibility of the technology in producing drug delivery devices. This could also be particularly beneficial during early drug development whereby smaller devices with a tailored dose could be easily designed and manufactured to suit an animal study (Goyanes et al., 2018; Trenfield et al., 2019a). This single-step manufacturing approach is easy and cost effective when compared with alternative 3D printing methods, such as FDM, which requires the preparation of drug-loaded filaments via hot melt extrusion that may cause thermal degradation of the drug (Kollamaram, Croker et al. 2018).
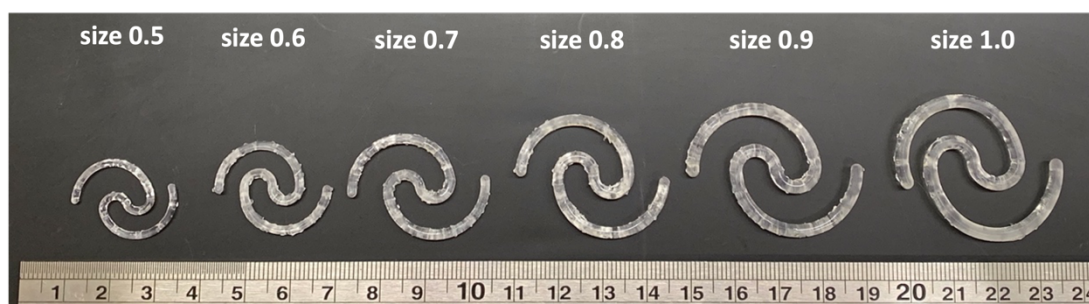
Figure 2.13 Picture of the SLA 3D printed solid intravesical devices in range of sizes. From left to right, IVS-0 devices prepared with a scale factor of 0.5, 0.6, 0.7, 0.8, 0.9, and 1.0. Scale in cm.

2.6.2.2 Physical characterisation

XRPD and DSC analyses were used to evaluate how the drug was incorporated into the solid intravesical devices. XRPD results **(Figure 2.14)** showed the characteristic peaks of lidocaine hydrochloride at 16.6°, 25.0°, and 25.9° 2θ in the IVS-10 and IVS-30 devices, suggesting that lidocaine was

present, to some extent, in the crystalline form. When the drug content was increased to 50%, almost all the crystalline peaks of lidocaine hydrochloride were visible.
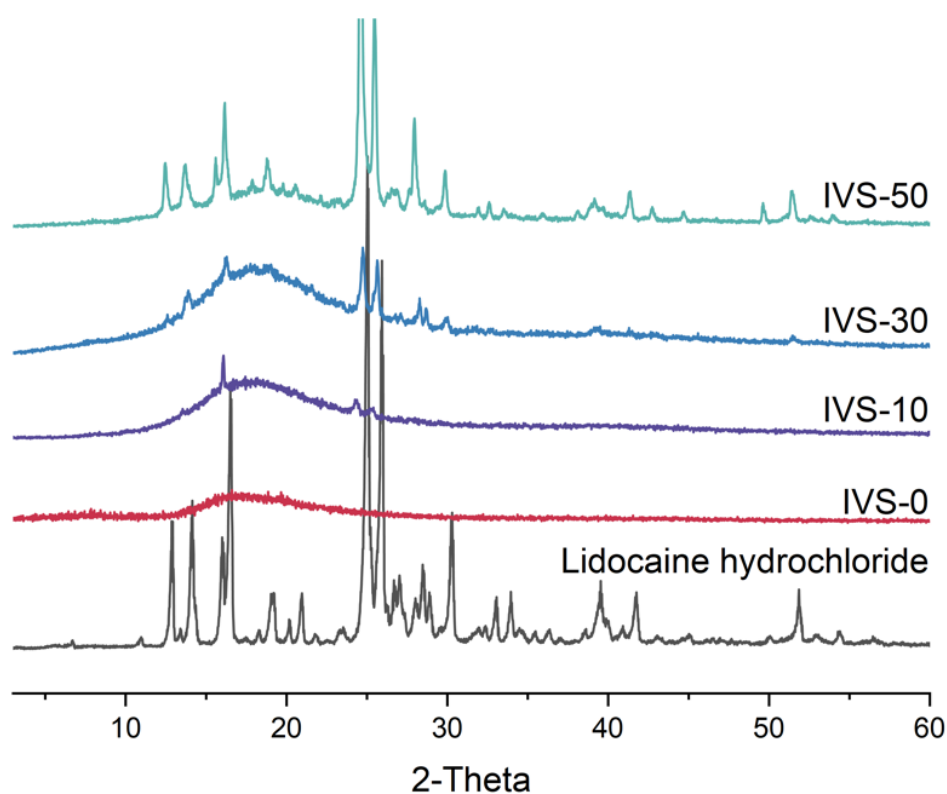
Figure 2.14 X-ray powder diffractograms of lidocaine hydrochloride and SLA 3D printed drug-loaded formulations.

The DSC thermograms **(Figure 2.15)** showed melting endotherms for lidocaine at 80 °C. Evidence of melting was observed in all the SLA printed formulations and was more visible with increasing loading of lidocaine, again indicating that the drug was present in the crystalline form. These results were consistent with the XRPD findings.
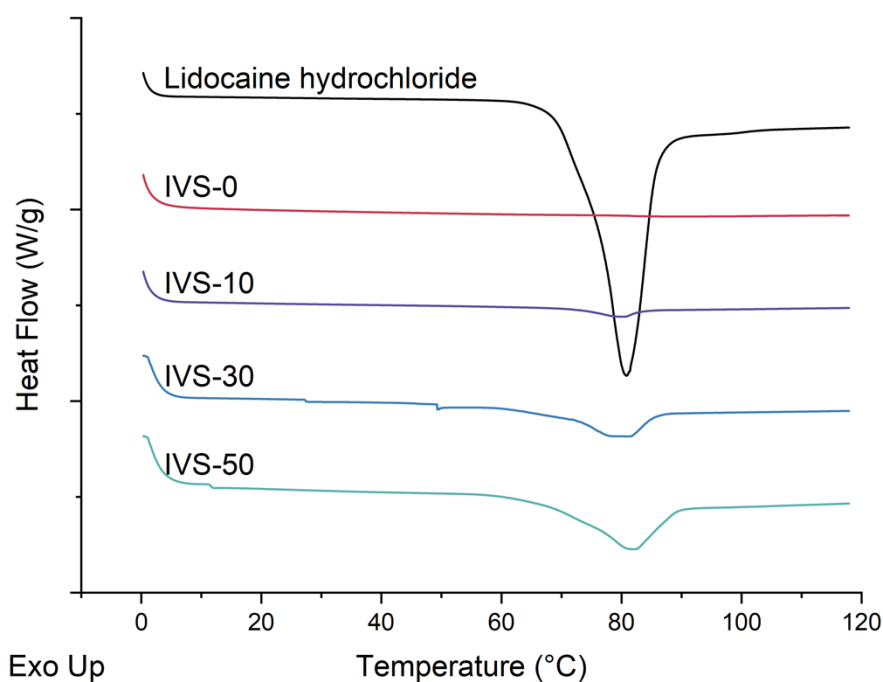
Figure 2.15 DSC thermograms of lidocaine hydrochloride and SLA 3D printed drug-loaded formulations.

X-ray micro-CT imaging was employed to visualise the internal structures of the solid intravesical devices **(Figure 2.16, Top).** Compared with the control device without drug (IVS-0), lidocaine particles are clearly observed in the white colour; the number of white regions increased as a function of lidocaine concentration. Additionally, devices with higher drug loadings showed a lighter and brighter colour on the surface, due to the constructs having increased atomic density. SEM images of the solid intravesical devices **(Figure 2.16, Bottom)** were consistent with the micro-CT results, with the cross-sectional surfaces of the IVS-30 and IVS-50 devices showing a rougher surface with an increased number of drug particles compared with the IVS-0 and IVS-10 devices that exhibited a smooth surface morphology.

| IVS-0 | IVS-10 | IVS-30 | IVS-50 |
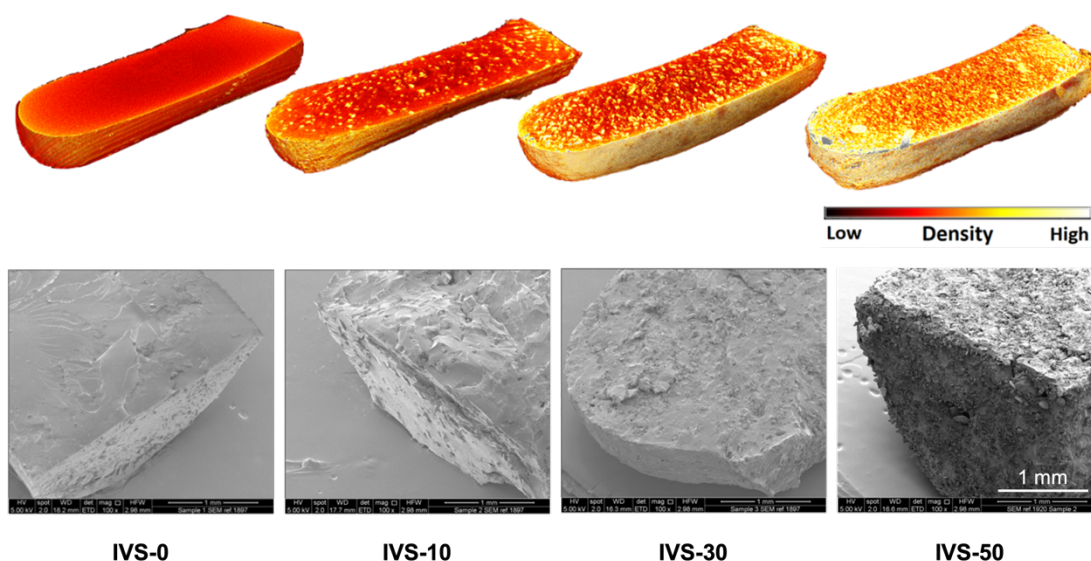
Figure 2.16 X-ray micro-CT images (top) and SEM images (bottom) of the sections of solid intravesical devices (size 1.0). From left to right, IVS-0, IVS-10, IVS-30, and IVS-50 devices. The scale bar in the micro-CT images is representative of atomic density.

2.6.2.3 Mechanical characterisation

Mechanical properties of the solid intravesical devices were evaluated by tensile mechanical testing using the standard dog-bone shaped tensile bars. Six tensile bars of the same thickness were printed for each formulation **(Figure 2.17).** Same as the solid devices, the white colour of the tensile bars was more visible when the loading of lidocaine was increased.
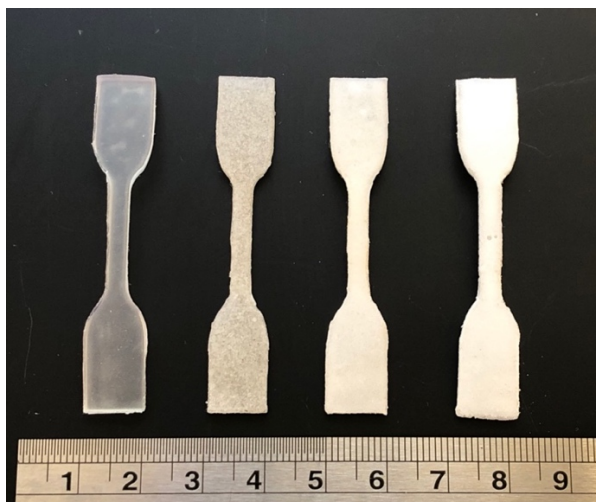
Figure 2.17 Picture of the SLA 3D printed IVS-0, IVS-10, IVS-30, and IVS-50 (from left to right) tensile bars. Scale in cm.

As shown in **Figure 2.18**, the tensile stress of IVS-10 (1.19 ± 0.12 MPa) is slightly lower than that of the control IVS-0 (1.38 ± 0.07 Mpa) ($p<0.05$). The stress of IVS-30 (0.92 ± 0.02 Mpa) and IVS-50 (0.89 ± 0.04 Mpa) are very similar but significantly lower (by almost 30%) compared with IVS-0. These results suggested that the introduction of drug particles in the resins led to a decrease in mechanical strength. A similar decreasing trend could also be seen in the case of elongation at break, displaying values of 85.56 ± 5.29%, 69.36 ± 5.39%, and 58.05 ± 7.43% for IVS-10, IVS-30, and IVS-50, respectively ($p<0.05$). These results further demonstrate the impact of increased lidocaine content causing a reduction in the crosslinking density during printing, compromising the elasticity as well as the stiffness of the devices. Statistical analysis revealed that the groups showed significant differences between each other, with the exception of the tensile stress values of IVS-30 and IVS-50 ($p > 0.05$).
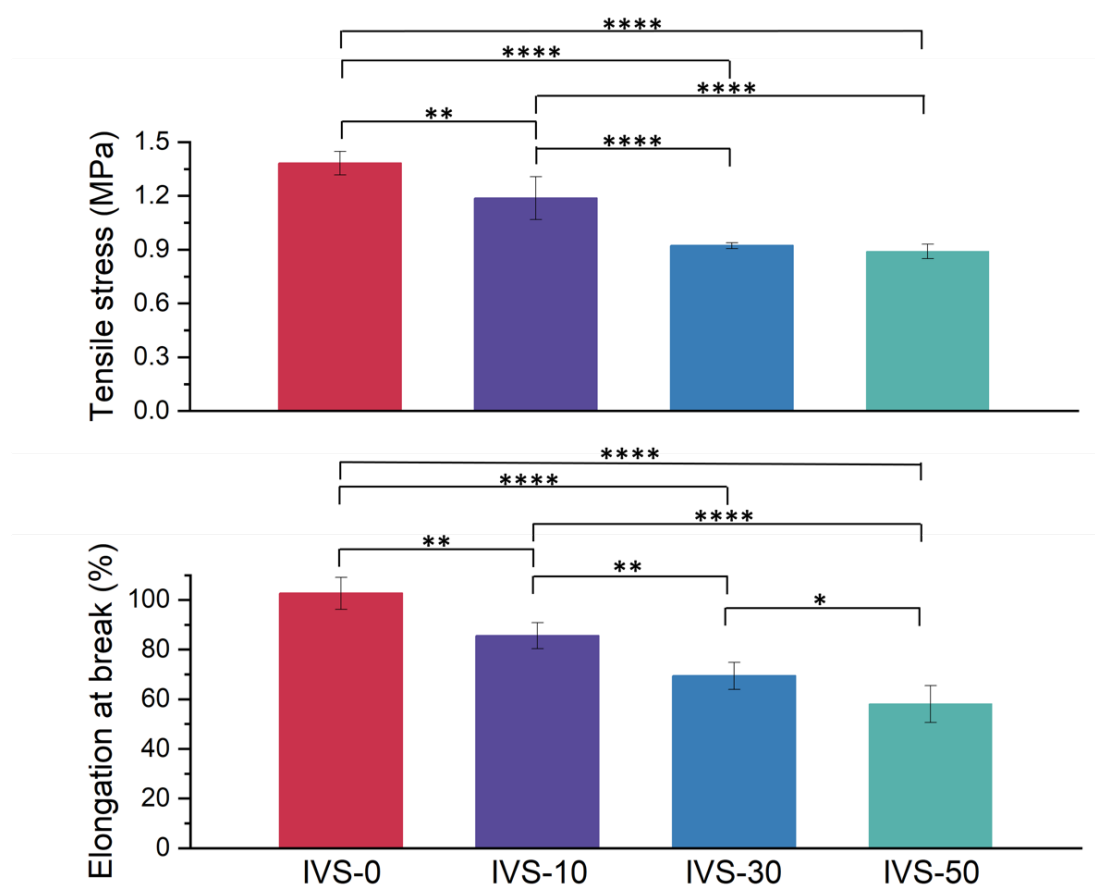
Figure 2.18 Mechanical properties of the SLA 3D printed tensile bars as a function of different drug loading of lidocaine (n=6). Columns and error bars represent means ± SD (* for $p < 0.05$, ** for $p < 0.01$, *** for $p < 0.001$, and **** for $p < 0.0001$).

2.6.2.4 *In vitro* drug release

Drug loading of the solid intravesical devices was evaluated and the lidocaine percentages of the IVS-10, IVS-30, and IVS-50 devices were 101.1% ± 6.9, 86.3% ± 3.3 and 97.7% ± 0.8, respectively. Drug release profiles for the solid devices were obtained using the same conditions as for the hollow devices, but over a 14-day period **(Figure 2.19).** In the initial 24 h, drug release of 17.8%, 28.8% and 74.1% were observed from the IVS-10, IVS-30, and IVS-50 devices

respectively. Decreasing the relative concentration of Elastic Resin was found to significantly increase the drug release rate, because of a lower degree of crosslinking density in the polymeric matrix, enabling an accelerated diffusion of drug from the matrix. As expected, the devices with the highest percentage of lidocaine (IVS-50) displayed the fastest release rate with 90% of lidocaine released in 3 days. Conversely, the IVS-30 devices demonstrated slower release rates across 14 days, reaching 88% (247 mg) total release. Approximately 3-4% lidocaine content was released per day from the IVS-10 devices, reaching a total of 61% (78 mg) after 14 days. The drug release from the solid devices was comparable to the LiRIS devices where 66% (131 mg) and 62% (400 mg) of lidocaine was released from the 200 mg and 650 mg formulations after 14 days (Nickel et al., 2012).
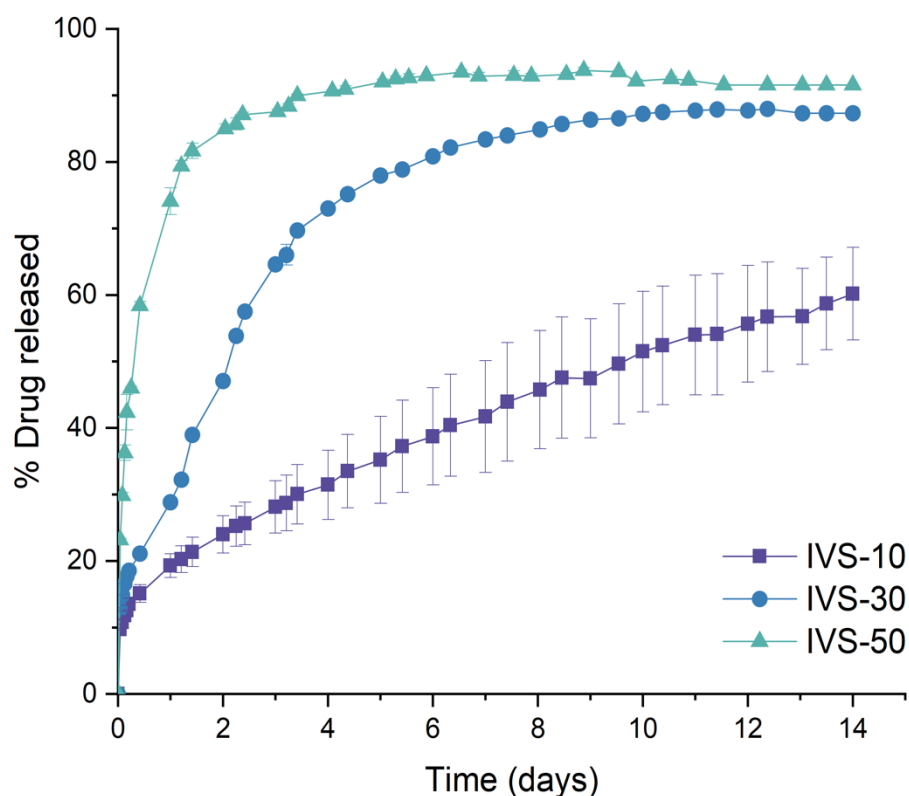
Figure 2.19 Cumulative release profile of lidocaine hydrochloride from the SLA 3D printed solid intravesical devices (size 1.0). Data values represent mean ± SD, which are not seen in some data points as they are smaller than the symbols (n=3).

The *in vitro* drug release data were fitted into zero-order, first-order, Higuchi and Korsmeyer-Peppas drug release kinetic models as presented in **Table 2.4**. Based on the results, the IVS-10 and IVS-30 release data were best fitted with first-order release with R^2 values being 0.995 and 0.992, respectively. On the other hand, the Korsmeyer-Peppas model was found to be the best-fit model for IVS-50 devices with an n value of 0.402, indicating the drug release mechanism was similar to Fickian diffusion (Bruschi, 2015). IVS-10 and IVS-30 devices also exhibited n values less than 0.45, which suggested drug release was governed by diffusion.

Table 2.4 Release kinetic data of the SLA 3D printed solid intravesical devices containing lidocaine hydrochloride.

Release kinetics model	Parameters	IVS-10	IVS-30	IVS-50
Zero-order	R^2	0.953	0.944	0.797
	k_0 (h^{-1})	0.147	0.590	2.116
First-order	R^2	0.995	0.992	0.980
	k_1 (h^{-1})	0.002	0.012	0.044
Higuchi	R^2	0.992	0.984	0.962
	k_H ($h^{-0.5}$)	2.976	7.052	13.858
Korsmeyer-Peppas	R^2	0.964	0.950	0.993
	k (h^{-n})	7.638	11.066	23.131
	n	0.332	0.363	0.402

After the 14-day period, the solid devices were retrieved, dried and pictures were taken using SEM **(Figure 2.20).** Compared with the SEM images of the solid devices before the dissolution test, all the devices exhibited porous surfaces, contributing to the release of lidocaine particles from the devices. An increased number of pores could be seen for devices with higher drug loading.

IVS-10
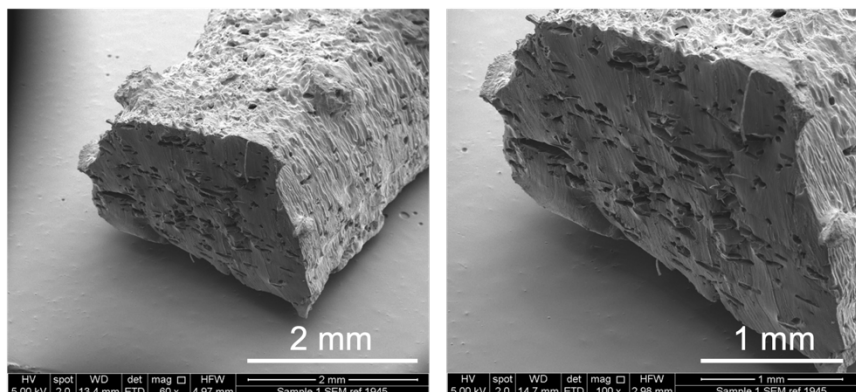
IVS-30
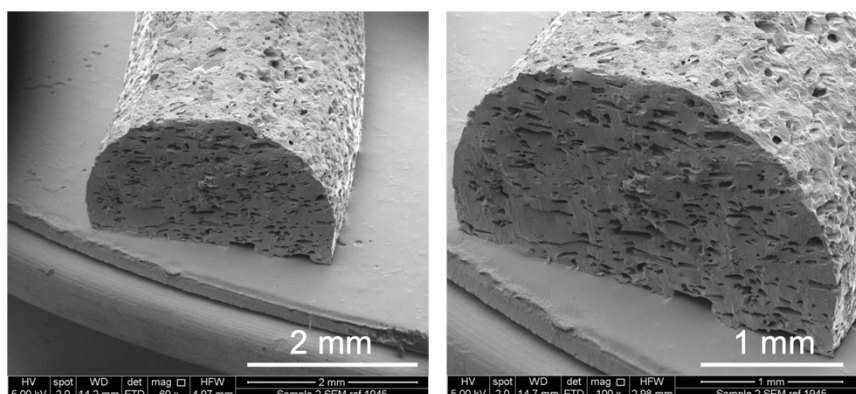
IVS-50
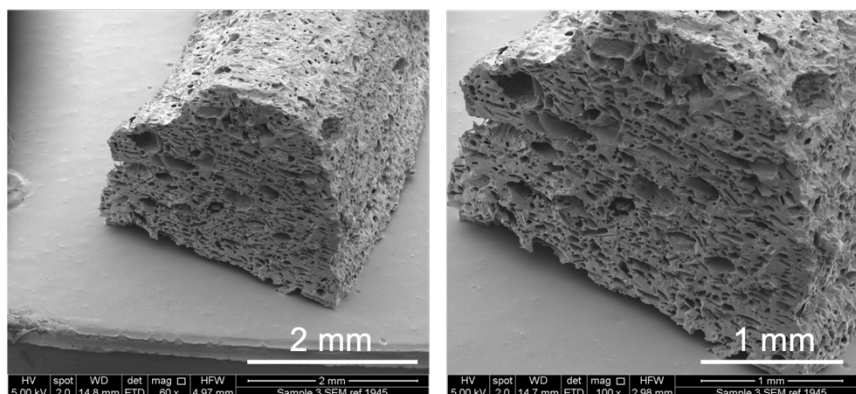
Figure 2.20 SEM images of sections of the solid intravesical devices (size 1.0) after dissolution studies. From top to bottom, IVS-10, IVS-30, and IVS-50 devices.

The feasibility of fabricating novel, implantable bladder drug delivery systems with SLA 3D printing has been demonstrated. The use of two configurations (hollow and solid) were found to change the dissolution rates and profiles. The hollow and solid intravesical devices both presented excellent retentive features and were capable of recovering their original S-shape conformation

automatically and immediately; this compares favourably with the shape memory behaviour of the previously manufactured devices (Melocchi et al., 2019), which required body temperature (37 °C) and water contact to achieve conformational changes. The intravesical devices could also provide a versatile platform for the inclusion of other therapeutic agents for the treatment of other bladder disorders. Such a concept would be beneficial for increasing the drug indwelling time in the bladder and overcoming the discomfort of repeated instillations through catheters.

Favourably, the Elastic Resin used here is an elastic polymer, which is lighter, cheaper, easier to process, exhibits a higher extent of elastic deformation and excellent biocompatibility and potential biodegradability compared to the shape memory alloy used for LiRIS (Nitinol) (Jani et al., 2014; Liu et al., 2007; Sokolowski et al., 2007). This study highlights the potential of using innovative SLA 3D printing technologies for the manufacture of personalised and retentive drug delivery devices.

However, there are limitations associated with the use of SLA 3D printing in fabrication of these intravesical devices. Firstly, the SLA 3D printer used in this chapter is a commercial 3D printer and it is not designed to print with third-party resins including blending pharmaceutical compounds in commercial resins. Hence, the limited choice of printing parameters was not ideal and was affecting the printing resolution (thickness and diameter) of the devices, for example, the IVS-50 devices was printed much thicker than the designed dimension. On the other hand, increasing the concentration of drug has increased the viscosity of the formulation, which led to poor flowability. As a result, pausing was needed during the manufacturing process which was time-consuming and could possibly affect reproducibility. A strategy to solve this

problem could be a wiper that could equally distribute the resin between the surface of the resin tank and the previous cured layer. Challenge has also occurred when printing the hollow devices since uncured resin was trapped in the hollow cavity during and extensive rinsing was required to remove it, otherwise any resin left cured during the post curing process and blocked the device. Moreover, the material used in this chapter is a commercial resin. It is not a medical-grade material approved for direct body contact. Continuations of this work could involve the use of biocompatible elastomers and possibly biodegradable materials to eliminate the need to retrieve the device after treatment. In addition, investigation on the mechanical properties of the devices could be further explored including compressibility and resistance to rupture of the device when passing through the catheter with external force applies.

2.7   Conclusion

In this chapter, SLA 3D printing was employed to demonstrate the feasibility of preparing novel indwelling intravesical devices, providing sustained and localised lidocaine delivery to the bladder. Two types of intravesical devices (hollow and solid) were successfully prepared using elastomers with different lidocaine content (10%, 30% and 50%), highlighting that SLA 3D printing is a highly flexible process, allowing easy modification of dosages to facilitate personalisation. The printed devices exhibited excellent flexibility under stretching could immediately recover their original shape. Mechanical tests revealed that increasing lidocaine content decreased the strength and elongation at break of the tensile bars. *In vitro* drug release studies showed that the hollow devices enabled a complete release of lidocaine within 4 days, compared with up to 14 days for the solid devices, which is beneficial for

improving patient compliance. These proof-of-concept intravesical devices showed drug release profiles comparable to other retentive intravesical devices found in the literature, yet the manufacturing process was simpler, more personalised and cost effective. This research presents a new opportunity for SLA 3D printing in the manufacture of retentive drug delivery systems, allowing for a controlled delivery of lidocaine at the local site to avoid systemic side effects and improve patient compliance. By changing the selected drug, these devices could be easily adapted for the treatment of other bladder disorders, including overactive bladder disorder and bladder cancers, revolutionising intravesical treatment outcomes for patients.

Chapter 3

DLP 3D printing of punctal plugs

3 DLP 3D printing of punctal plugs

3.1 Overview

Dry eye disease is a common ocular disorder that is characterised by tear deficiency or excessive tear evaporation. Current treatment involves the use of eye drops; however, therapeutic efficacy is limited because of poor ocular bioavailability of topically applied formulations. In this chapter, DLP 3D printing was employed to develop paracetamol- and dexamethasone-loaded punctal plugs. Punctal plugs with different drug loadings were fabricated using poly(ethylene glycol) diacrylate (PEGDA) and polyethylene glycol 400 (PEG 400) to create a semi-interpenetrating network. Drug-loaded punctal plugs were characterised in terms of physical characteristics (XRPD and DSC), potential drug-photopolymer interactions (FTIR), and drug release profile. *In vitro* release kinetics of the punctal plugs were evaluated using an in-house flow rig model that mimics the subconjunctival space for more than 21 days.

3.2 Introduction

Vision is considered one of the most important senses (Awwad et al., 2017b). Dry eye is a common chronic disorder that affects millions of people worldwide and represents a growing public health concern (Rouen and White, 2018; Uchino and Schaumberg, 2013). It occurs due to deficient tear production and/or increased evaporation of the tear film and can lead to corneal inflammation and conjunctiva if left untreated. Ocular drug delivery has always been a challenging task because of the static and dynamic barriers that provide protection against external agents reaching the eye, such as pathogens and therapeutic molecules (Gote et al., 2019; Patel et al., 2013).

Topical administration (e.g., eye drops) is the preferred route for the delivery of therapeutic agents to the anterior segment of the eye because it minimises systemic side effects, is non-invasive, and is easily accessible. However, ocular bioavailability from topically applied formulations is usually poor (< 5%),

a result of numerous factors including short drug residence time, blinking, high tear turnover rate and naso-lacrimal drainage (Gote et al., 2019).

Novel formulation approaches to improve ocular bioavailability include extending the drug residence time or promoting corneal penetration with the use of liposomes, nanoparticles, penetration enhancers, mucoadhesive polymers and/or *in situ* gelling components- although maintaining stability could be challenging (Alvarez-Lorenzo et al., 2019; Jumelle et al., 2020; Yellepeddi et al., 2015). Physical force-based methods, such as iontophoresis and sonophoresis, represent promising strategies to enhance penetration efficiency by temporarily disrupting the barrier structures in a minimally or non-invasive fashion (Huang et al., 2018). Concerns about temporary tissue damage from these strategies are present (Alvarez-Lorenzo et al., 2019; Jung et al., 2018). A variety of state-of-the-art drug-eluting systems have been developed for effective and extended delivery of ocular therapeutics release including microneedles (**Figure 3.1a**) (Thakur Singh et al., 2017; Than et al., 2018), drug-eluting contact lenses (**Figure 3.1b**) (Alvarez-Lorenzo et al., 2019; Xu et al., 2018), and nanowafers (**Figure 3.1c**) (Coursey et al., 2015; Yuan et al., 2015). Nonetheless, the prolonged wear of hydrogel lens may reduce oxygen permeability especially during overnight, which could lead to corneal edema.
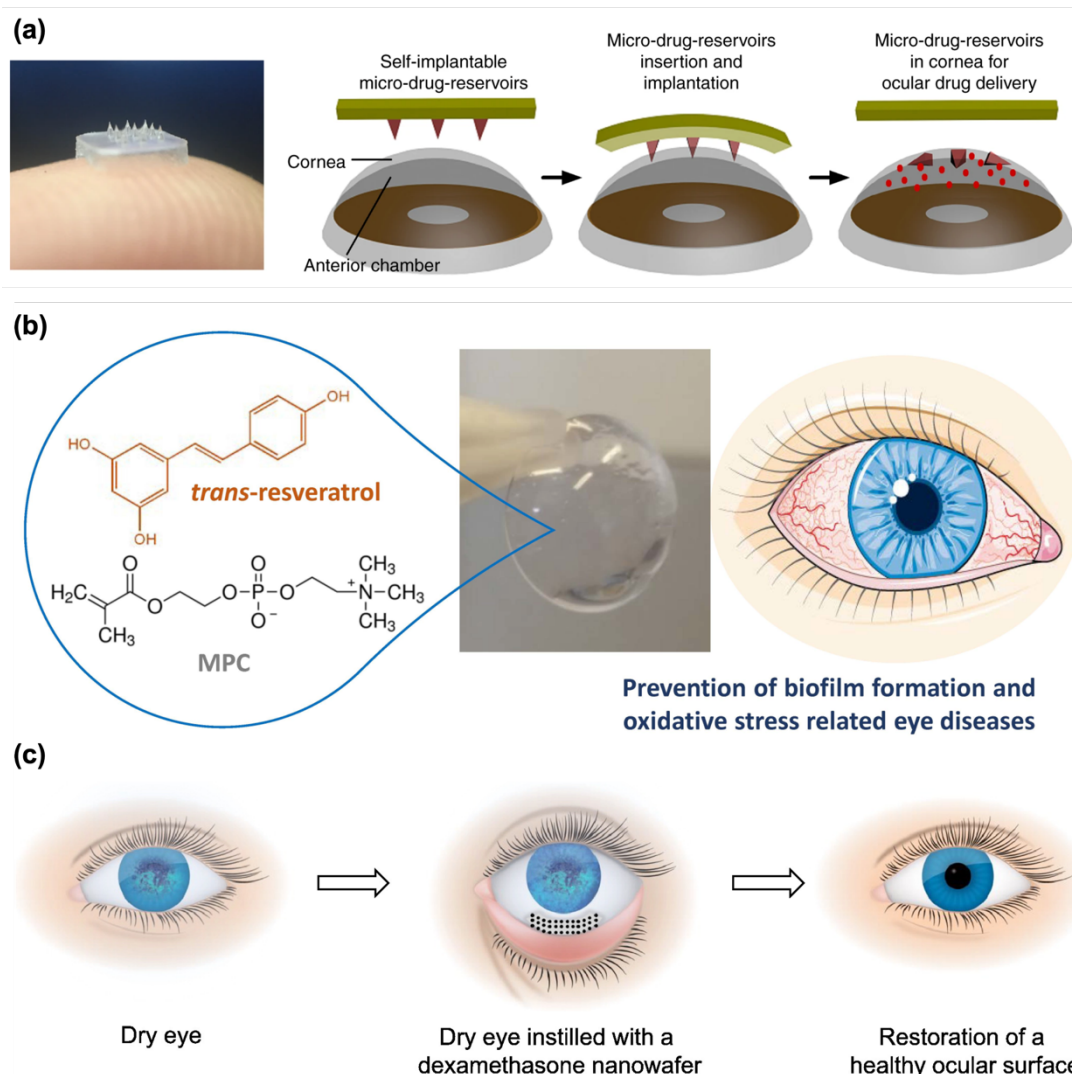
Figure 3.1 Images of novel drug-eluting systems for ocular drug delivery including (a) microneedles (Than et al., 2018); (b) contact lenses (Vivero-Lopez et al., 2021a); and (c) nanowafers (Coursey et al., 2015).

3.2.1 Punctal plugs

Punctal plugs are common and non-invasive medical devices for the treatment of dry eye syndromes (Gupta and Chauhan, 2011; Xie et al., 2017). They work by blocking the canaliculi, which connects the eyes to the nose, preventing tear drainage (Ervin et al., 2017; Jehangir et al., 2016; Yellepeddi et al., 2015). Punctal occlusion by means of plugs has been reported to improve tear film stability, tear osmolarity, and functional visual acuity of dry eye patients (Goto et al., 2003).

The first punctal plug was introduced by Foulds in 1961 where fine water-soluble gelatin rods were inserted for temporary obstruction of the canaliculi (Foulds, 1961). In 1975, Freeman developed the design of a dumbbell-shaped punctal plug made of silicone and this concept is still in use (**Figure 3.2a and b**) (Jehangir et al., 2016). More recently, modern designs of the punctal plugs have been developed for easier insertion, better retention, and greater patient comfort (Yellepeddi et al., 2015) (**Figure 3.2c and d)**. Punctal plugs that are inserted at the opening of the puncta are visible and easily removable after treatment. In contrast, canalicular plugs are invisible as they are placed in the horizontal or vertical canaliculus, which makes removal difficult.

Based on the material used, punctal plugs can be either temporary or semi-permanent. Temporary punctal plugs are normally made from collagen and last for up to 14 days, whereas semi-permanent plugs are usually made of medical grade silicone, polydioxanone, and polycaprolactone (PCL) and could be effective for 2-6 months (Jehangir et al., 2016).
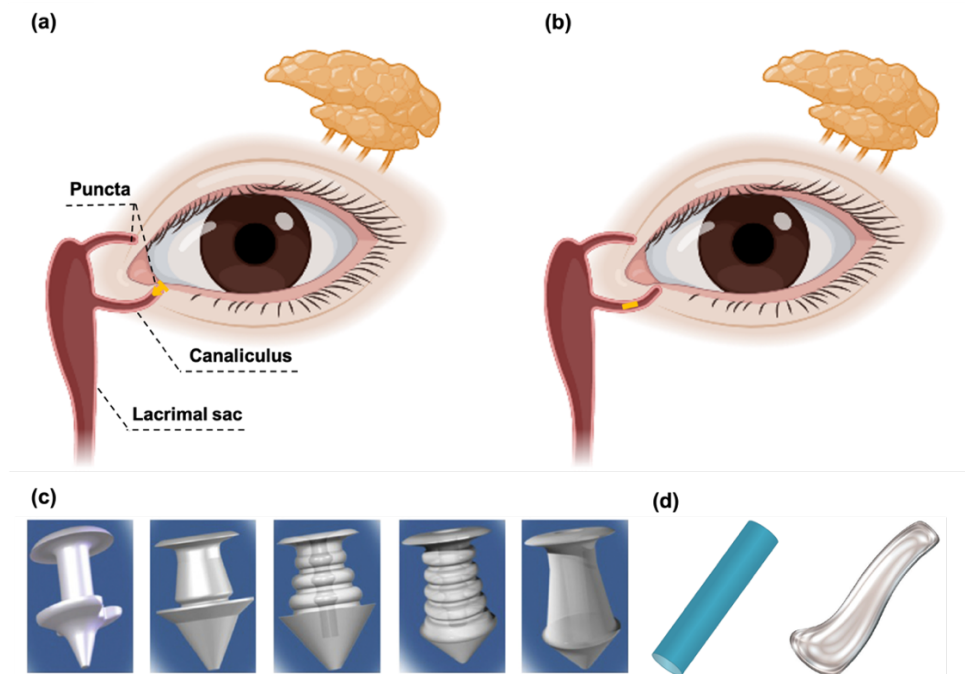
Figure 3.2 Schematic illustration of punctal plug (a) in the punctum and (b) in the caliculus of the eye; (c) schematic representation of assorted designs of (c) punctal and (d) canalicular plugs (Jehangir et al., 2016; Yellepeddi et al., 2015).

Although initially developed for blocking the tear drainage, punctal plugs have been recently engineered for controlled drug delivery. Previously, a few studies reported the combination use of eye drops and punctal plugs could provide an additive effect, indicating the evident advantages of developing drug-loaded punctal plugs (Roberts et al., 2007; Yellepeddi et al., 2015). Gupta and Chauhan reported their study of developing punctal plugs that can release cyclosporine A for treating dry eyes (Gupta and Chauhan, 2011). The core of the punctal plug made of hydroxy ethyl methacrylate (HEMA) crosslinked with ethylene glycol dimethacrylate (EGDMA) containing cyclosporine A microparticles. For making the core, the HEMA, EGDMA, and cyclosporine A solution was firstly prepared and filled into silicone tubing which was sealed with office clamps followed by submerged into a water bath at 80 °C for 20 min. Polymerisation of the monomers within the tubing results in the formation of a rod surrounded by a silicone annulus. Subsequently, the rod was divided into sections of desired length and portion of the silicone annulus was cut off to produce the design as illustrated in **Figure 3.3.** The results show zero-order release of cyclosporine A for about 3 months. In another study, moxifloxacin-loaded punctal plugs have been developed for the treatment of bacterial conjunctivitis (Chee, 2012). The plug was a dried polyethylene glycol hydrogel rod embedded with moxifloxacin-encapsulated microspheres and was designed to provide sustained delivery for over 10 days.
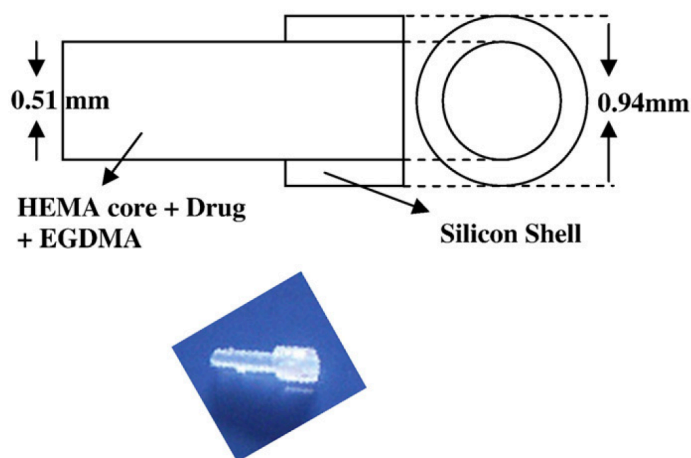
Figure 3.3 Schematic and image of the drug-loaded punctal plug (Gupta and Chauhan, 2011).

Nevertheless, the manufacturing methods of drug-loaded punctal plugs in the above-mentioned studies were not straight forward and may require multiple steps. Moreover, spontaneous extrusion of punctal plugs has been previously reported by patients due to the use of non-optimal plug size (Tai et al., 2002), Therefore, the need to customise punctal plugs presents an opportunity.

3.2.2 Model drugs and photopolymer

Paracetamol **(Figure 3.4a)** was used as the preliminary model drug to evaluate printability because it is stable and generally inexpensive and has been tested in previous studies using vat photopolymerisation 3D printing technologies in preparing drug delivery systems (Martinez et al., 2018; Wang et al., 2016). Dexamethasone **(Figure 3.4b)**, a corticosteroid, was selected because of its anti-inflammatory properties and wide applications in corneal disease treatment, including dry eye symptoms (Patane et al., 2011; Zidan et al., 2021).
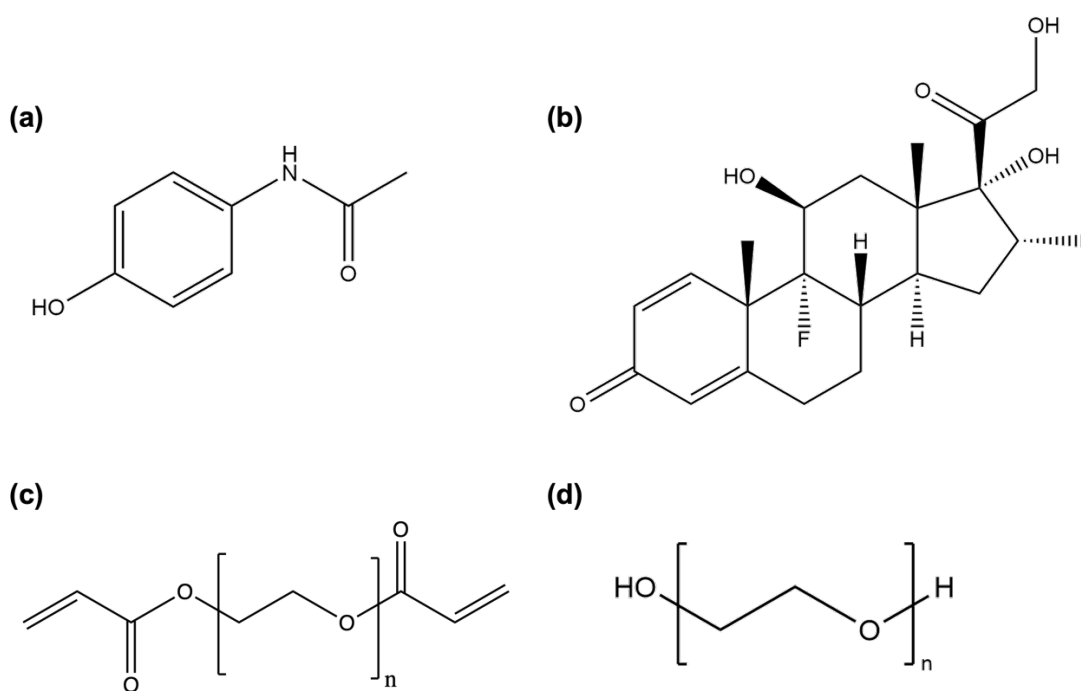
Figure 3.4 Chemical structures of (a) paracetamol, (b) dexamethasone, (c) PEGDA, and (d) PEG 400.

PEGDA **(Figure 3.4c)**, one of the most commonly used photocurable material for biomedical applications, was chosen due to its flexibility, biocompatibility, ease of crosslinking, and uniform pore size (Blanchette et al., 2016; Steier et al., 2020; Urrios et al., 2016). PEG 400 **(Figure 3.4d)**, a hydrophilic excipient, was added because PEG 400 is not photocrosslinkable. The addition of it in the formulation was previously reported to result in lower degree of crosslinking density within the polymeric matrix, increasing the molecular mobility of the drug and consequently the drug release rate (Krkobabić et al., 2019; Wang et al., 2016).

3.3　Aim

In this chapter, DLP 3D printing was investigated to prepare drug-loaded punctal plugs for controlled drug delivery to the front of the eye. This technology can be particularly advantageous since it is possible to prepare various sizes, shapes, and doses of the punctal plugs in a single step. The aims of Chapter 3 include:

- To design and develop drug-eluting punctal plugs for dry eye disease using DLP 3D printing.
- To use paracetamol as the preliminary model compound and a commercial Flexible resin to assess feasibility of drug-loaded punctal plugs.
- To develop different types of dexamethasone-loaded punctal plugs with two different drug loadings (10% and 20% w/w) using PEGDA and PEG 400.
- To assess the physical characteristics of different drug-loaded formulations.
- To evaluate the drug release profiles of different punctal plugs using an in-house flow rig model that mimics the subconjunctival space.

3.4 Materials

Paracetamol (MW 151.2 g/mol, logP 0.46, water solubility 14 mg/mL at 25 °C (PubChem, 2023a)), dexamethasone (MW 392.46 g/mol, Pharmaceutical Secondary Standard, logP 1.83, water solubility 0.089 mg/mL at 25 °C (PubChem, 2023d)), phenylbis (2,4,6-trimethylbenzoyl) phosphine oxide (Irgacure 819, MW 418.46 g/mol), β-carotene (MW 536.87 g/mol, ≥ 93% UV), polyethylene glycol 400 (PEG 400, MW 400 g/mol), and poly(ethylene glycol) diacrylate (PEGDA, Mn 575), Dulbecco's phosphate buffered saline (PBS), trifluoroacetic acid (TFA, ≥99.0%, HPLC grade), and acetonitrile (ACN, ≥ 99.9 %, HPLC grade) were obtained from Sigma-Aldrich (Dorset, UK). Flexible resin was supplied by Kudo3D Inc. (USA). All materials were used as received.

3.5 Methods

3.5.1 3D design

The punctal plug was designed to be inserted in the punctum of the eye with the configuration similar to those of commercially available punctal plugs, which range from 1 – 2 mm in length and from 0.2 – 1.0 mm in diameter. The dimension of the punctal plug was 1.9 mm in length and 1.0 mm in diameter with a cylindrical core diameter of 0.5 mm (**Figure 3.5a**).
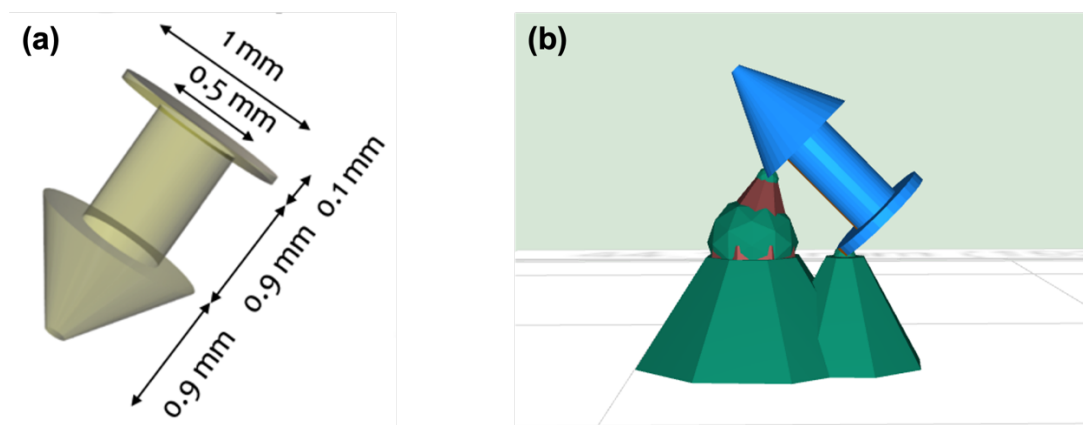
Figure 3.5 (a) 3D design of the punctal plug and (b) the punctal plug with the generated supports from the Kudo software at a 45° angle.

3.5.2 Preparation of drug-loaded resin formulations

3.5.2.1 Paracetamol-loaded resin formulations

10% (w/w) paracetamol was blended into the Flexible resin to a total mass of 2 g (formulation P10), followed by fully stirring until the drug was homogenously dispersed within the resin. Then the formulation was poured into the resin tank before 3D printing.

3.5.2.2 Dexamethasone-loaded resin formulations

Drug-loaded resin formulations were prepared with 2% (w/w) photoinitiator (Irgacure 819) and 1% (w/w) photoabsorber (β-carotene) to a total mass of 2 g. Dexamethasone, PEGDA, and PEG 400 were added to each resin according to the compositions shown in **Table 3.1**. In formulation D10 and D20, only PEGDA was used as polymeric component, while in the formulation D10PEG and D20PEG, PEG 400 was added to form the semi-interpenetrating network and facilitate drug release rates (PEGDA:PEG 400 4:1 w/w ratio). The resins were kept in amber containers and continuously stirred overnight at room temperature (~25 °C) until the drug was homogeneously dispersed within the resin. The suspension was then added into the resin tank of the DLP 3D printing.

Table 3.1 Compositions (% w/w) of the drug-loaded resin formulations used to print punctal plugs.

Formulations	Dexamethasone (%)	Irgacure 819 (%)	β-carotene (%)	PEGDA (%)	PEG 400 (%)
D10	10	2	1	87	-
D20	20	2	1	77	-
D10PEG	10	2	1	69.6	17.4
D20PEG	20	2	1	61.6	15.4

3.5.3   3D printing process

All the punctal plugs were printed with a commercial DLP 3D printer (Titan2 HR, Kudo3D Inc., CA, USA) equipped with an HD DLP projector, which has a visible light source (400-700 nm) **(Figure 3.6)**. The printer XY resolution was set to 23 μm. The punctal plugs were designed with 123D Design (Autodesk Inc. CA, USA) and exported as a stereolithographic file (.stl) into the Kudo3D Print Job software for slicing into layers with a thickness of 25 μm and sent for printing. All punctal plugs were printed with generated supports (tip diameter 0.10 mm, pole diameter 0.80 mm, height of the foot 0.50 mm) from the Kudo software at a 45° angle on the build platform (**Figure 3.5b**). The printing time was 6 s per layer for the P10 punctal plugs, 2 s per layer for the D10 and D10PEG punctal plugs, and 5s per layer for D20 and D20PEG punctal plugs (10 s for the first layer). After printing, the plugs were rinsed for 1 min in isopropyl alcohol (IPA) in the sonicator, followed by a post cure process at 405 nm for 30 min in a Form Cure (Formlabs Inc., MA, USA). The total printing time was 20 min for printing 20 punctal plugs.
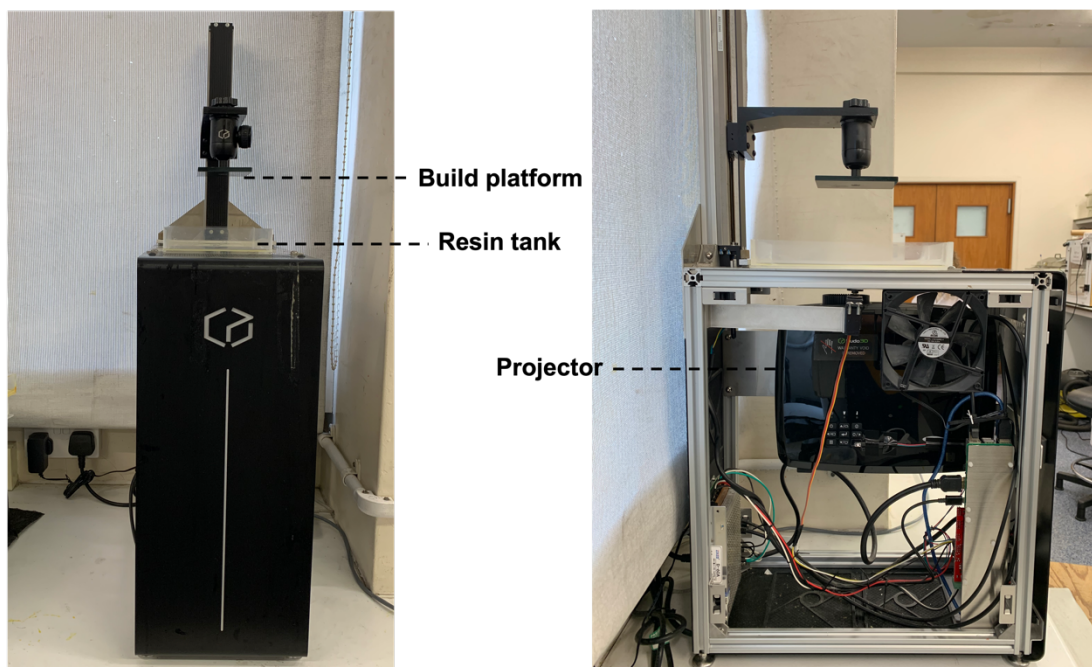
Figure 3.6 Pictures of a Titan2 HR DLP 3D printer from the front and side view.

3.5.4 UV-visible spectrophotometry

Photoinitiator (Irgacure 819) and photoabsorber (β-carotene) solutions were prepared at concentration of 0.025% (w/v) and 0.0025% (w/v) in ethanol respectively. The UV-visible spectra were analysed on a Cary 100 UV-vis spectrophotometer (Agilent Technologies, UK) between 200-800 nm at a scan rate of 600 nm/min.

3.5.5 Determination of device morphology

Images of the DLP 3D printed punctal plugs (P10, D10, D20, D10PEG, D20PEG) were captured with a Leica Galen III optical microscope (Leica, USA) and pictures were taken with an iPhone (Apple, CA, USA) through the eyepiece. The length of the punctal plugs were measured using ImageJ (NIH, MD, USA) (n=3).

3.5.6 X-ray powder diffraction (XRPD)

Discs (23 mm diameter x 1 mm height) were specifically prepared for XRPD analysis for different formulations (P10, D10, D20, D10PEG, D20PEG) using the same printing conditions as the drug-loaded punctal plugs. Powdered samples of pure paracetamol and dexamethasone were analysed by XRPD. XRPD patterns were obtained with a Rigaku MiniFlex 600 (Rigaku, USA) equipped with a Cu Kα X199 ray source (λ=1.5418Å). The intensity and voltage applied were 15 mA and 40 kV. Samples were scanned between 2θ = 3-60° with a stepwise size of 0.02° at a speed of 5°/min.

3.5.7 Thermal analysis

Differential scanning calorimetry (DSC) measurements were performed with a Q2000 DSC (TA instruments, Waters, LLC, USA) at a heating rate of 10 °C/min from 0 to 300 °C to characterise paracetamol powder, dexamethasone powder and different punctal plugs (P10, D10, D20, D10PEG, D20PEG). Nitrogen was used as a purge gas with a flow rate of 50 mL/min for all the experiments. Data

were collected with TA Advantage software for Q series (version 2.8.394) and analysed using TA Instruments Universal Analysis 2000. TA aluminium pans and Tzero hermetic lids (pin hole made with a tweezer) were used with an average sample size of 3 – 5 mg.

3.5.8   Scanning electron microscopy (SEM)

DLP 3D printed punctal plugs (P10, D10, D20, D10PEG, D20PEG) were attached to a self-adhesive carbon disc mounted on a 25 mm aluminium stub, which was sputter coated with 25 nm of gold. The images were captured with an FEI Quanta 200 FEG SEM (FEI, UK) at 5 kV accelerating voltage using secondary electron detection to obtain the images.

3.5.9   Attenuated Total Reflection Fourier-Transform infrared spectroscopy (ATR-FTIR)

The infrared spectra of formulations (D10, D20, D10PEG, D20PEG) before and after DLP 3D printing were collected using a Spectrum 100 FTIR spectrometer (PerkinElmer, Waltham, MA). All samples were scanned over a range of $4000 - 650$ cm^{-1} at a resolution of 1 cm^{-1} for 6 scans. The spectra of pure dexamethasone drug powder and PEGDA were collected as the references.

3.5.10 Determination of drug loading

The concentration of drug in the DLP 3D printed punctal plugs was determined by cutting the plugs into small pieces and stirring them in 5 mL ethanol at room temperature overnight to allow extraction of the drug. The solutions were filtered through 0.45 µm filter (Millipore Ltd., Ireland) and drug concentration was determined with HPLC (Hewlett Packard 1260 Series HPLC system, Agilent Technologies, Cheadle, UK) using the following methods.

3.5.10.1   Paracetamol

The mobile phase consisted of methanol (15% v/v) and water (85% v/v), which was pumped at a flow rate of 1 mL/min through an Eclipse plus C18 column, 100 × 4.6 mm (Zorbax, Agilent technologies, Cheshire, UK). The sample injection volume was 20 µL, and measurements were made at room temperature with a detection wavelength of 247 nm.

3.5.10.2   Dexamethasone

An Eclipse plus C18 column, 100 × 4.6 mm (Zorbax, Agilent technologies, Cheshire, UK) was employed with a flowrate of 1 mL/min, and a mobile phase gradient consisting of ACN and 0.1% v/v TFA water. The gradient was: 20% ACN increased to 70% in 10 min and decreased to 20% in 1 min and held for 4 min prior to the next injection. The sample injection volume was 100 µL, and measurement were made at 30 °C with a detection wavelength of 240 nm.

3.5.11 *In vitro* drug release study

Drug release rates from the punctal plugs were measured using an in-house *in vitro* dynamic flow cell model (**Figure 3.7**) (Angkawinitwong et al., 2017) under non-sink conditions. A sample chamber (8.8 mm diameter × 3.27 mm height) with a capacity of 200 µL was employed for the study and the punctal plug was placed in the chamber. In order to simulate the condition in the front of the eye, fresh PBS (pH 7.4, with 0.05% sodium azide, 37 °C) was used as the medium, which was continuously supplied by a peristaltic pump (Michael Smith Engineers Ltd, UK) at a flow-rate of 1.6-2.0 µL/min via the inlet port into the chamber. Samples were collected from the outlet port for a period of 21 days. After the release study, the devices were retrieved to extract any residual drugs, and this was be taken into consideration in the calculation of percentage of drug released. The drug concentration in the sample solutions was evaluated using HPLC (as described in Section 3.5.10).
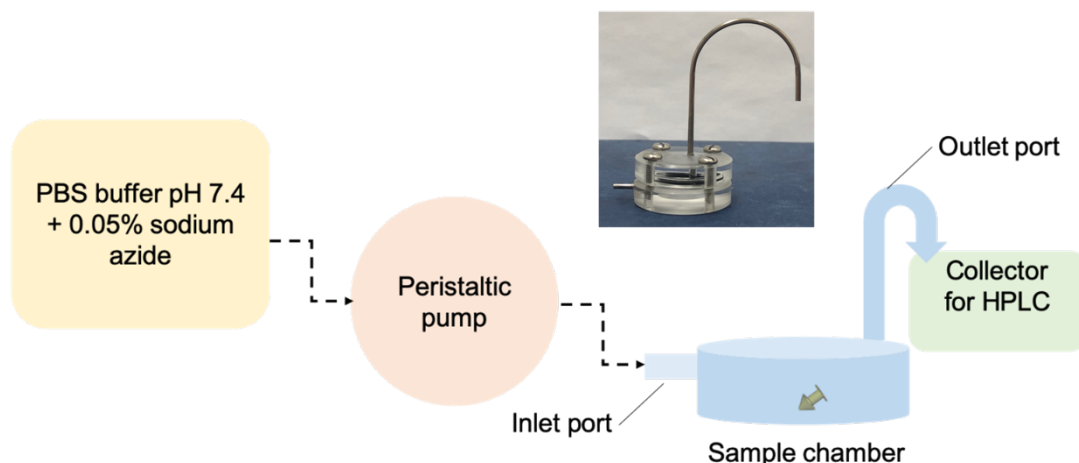
Figure 3.7 Schematic diagram illustrating the in-house flow rig model for *in vitro* dissolution studies.

To determine the drug release kinetics and mechanism, various mathematical models (zero-order model, first-order model, Higuchi model, and Korsmeyer-Peppas model) were tested to fit the data obtained from *in vitro* release study into the following equations (Bruschi, 2015):

Zero-order model
$$Q_t = Q_0 + k_0 \times t \qquad \text{(Eq. 3.1)}$$

Where Q_t is the amount of drug released over time t, Q_0 is the initial amount of drug in the solution, and k_0 is the zero-order release constant.

First-order model
$$logQ_t = logQ_0 + \frac{k_1 \times t}{2.303} \qquad \text{(Eq. 3.2)}$$

Where Q_t is the amount of drug released over time t, Q_0 is the initial amount of drug in the solution, and k_1 is the first-order release constant.

Higuchi model
$$Q_t = k_H \times t^{\frac{1}{2}} \qquad \text{(Eq. 3.3)}$$

Where Q_t is the amount of drug released over time t and k_H is the Higuchi release constant.

Korsmeyer-Peppas model
$$\frac{M_t}{M_\infty} = k \times t^n \qquad \text{(Eq. 3.4)}$$

Where M_t/M_∞ is the fraction of drug released over time t, k is the constant of incorporation of structural modifications and geometrical characteristics of the system, and n is the exponent of release.

3.6   Results and discussion

3.6.1   Paracetamol-loaded punctal plugs

3.6.1.1 3D printing

First, printing of paracetamol-loaded punctal plugs was attempted to be directly printed on the platform. However, due to the bottom-up setup of the DLP 3D printer and the overhanging design of the punctal plug, the resulting punctal plug demonstrated poor resolution as shown in **Figure 3.8**.
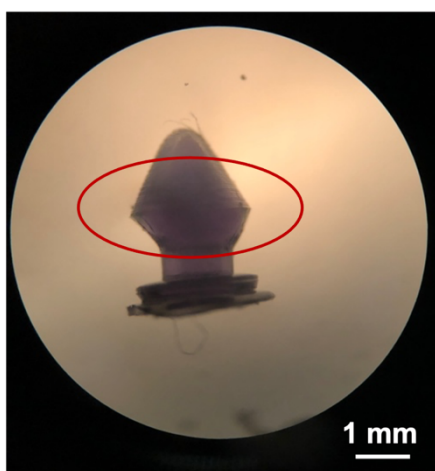
Figure 3.8 Light microscope image of the DLP 3D printed P10 punctal plug printed without supports.

Therefore, supports were generated so that the punctal plugs could be printed at a 45 °C angle on the build platform. With this approach, paracetamol-loaded punctal plugs were successfully fabricated using the Flexible resin (printing time: 50 min). The average weight of the printed device was 1.1 mg ± 0.02 mg, and the average length was measured to be 2.0 mm ± 0.02 mm. Images of the

devices **(Figure 3.9)** were taken with light microscope, and they showed great resolution and uniformity in shape.
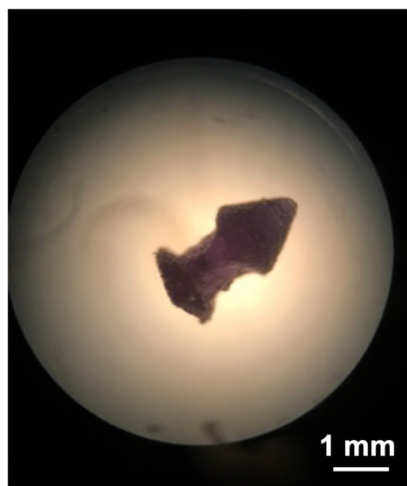
Figure 3.9 Light microscope image of the DLP 3D printed P10 punctal plug printed with supports.

SEM imaging of the blank punctal plugs (**Figure 3.10**) showed a smoother surface finish compared with that of the P10 punctal plugs. Pores can be observed on the surface of the P10 punctal plugs, indicating a lower photocrosslinking density.
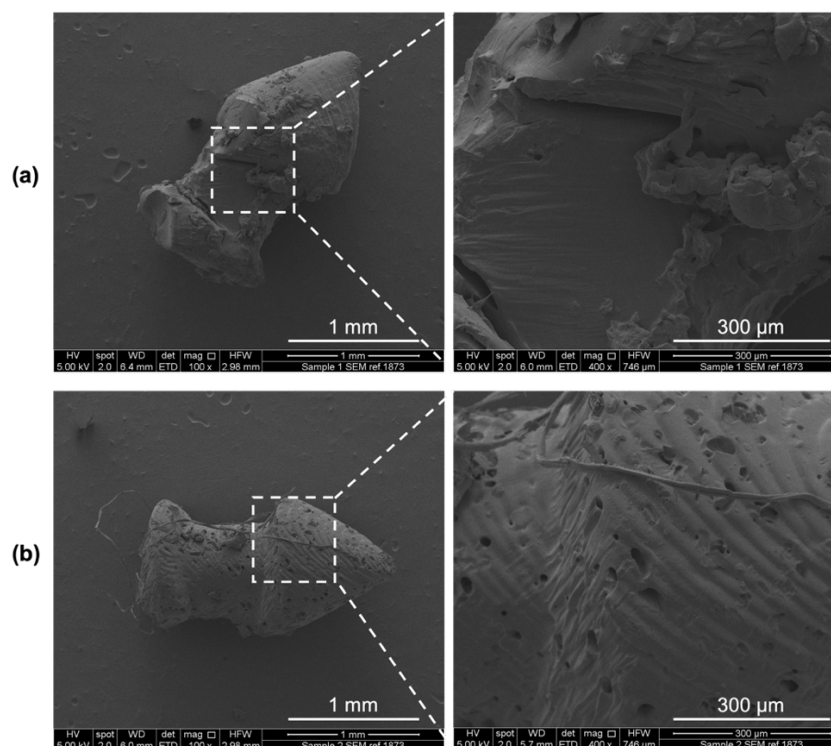
Figure 3.10 SEM images of the DLP 3D printed (a) blank and (b) P10 punctal plugs.

3.6.1.2 Physical characterisation

XRPD and DSC were performed to evaluate how paracetamol was incorporated in the printed formulation. The XRPD results (**Figure 3.11**) demonstrated characteristic peaks of paracetamol at 16.0°, 18.7°, 24.9°, and 27.1° 2θ and the presence of some of these peaks in the P10 diffractogram suggested paracetamol was present in the partially crystalline phase in the DLP 3D printed P10 formulation. However, in the DSC traces (**Figure 3.12**), no melting endotherm of paracetamol at 169 °C could be found in the P10 thermogram, indicating that the amount of undissolved paracetamol in the printed formulation was very low.
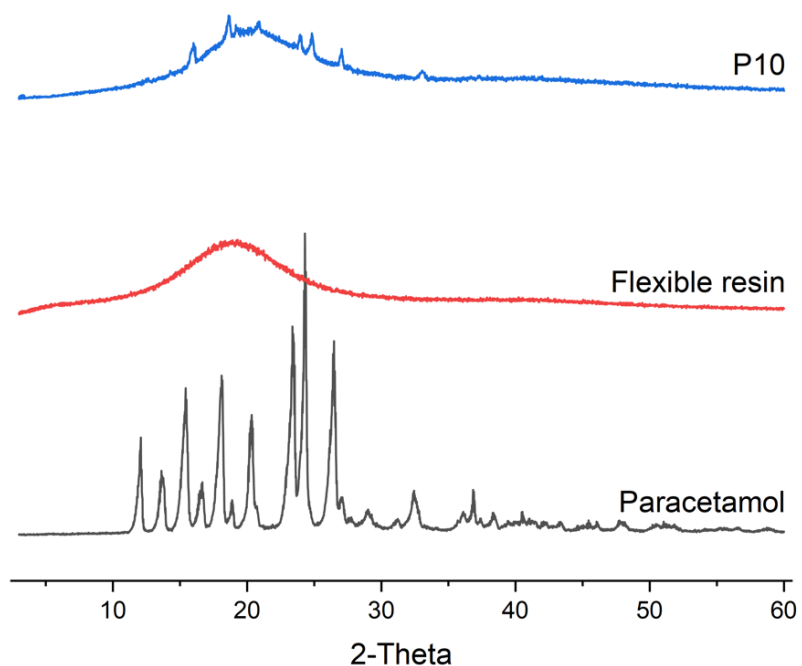
Figure 3.11 X-ray powder diffractograms of paracetamol and DLP 3D printed Flexible resin (blank) and P10 formulation.
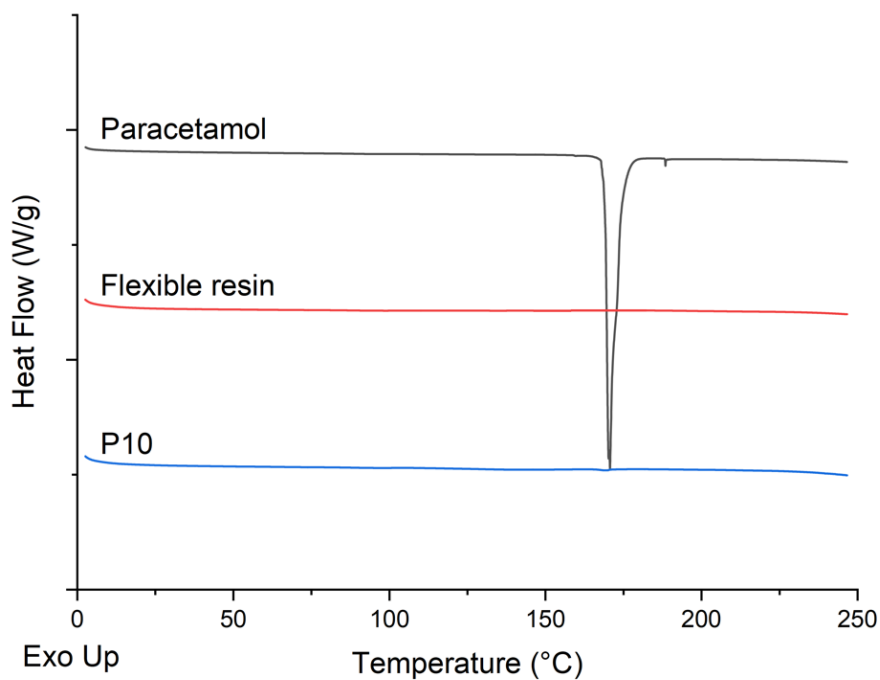
Figure 3.12 DSC thermograms of paracetamol and DLP 3D printed Flexible resin (blank) and P10 formulation.

3.6.1.3 *In vitro* drug release

Dissolution studies were conducted using an in-house *in vitro* model, which mimics the aqueous mass transfer through the anterior route (Angkawinitwong et al., 2017; Awwad et al., 2015). Fresh PBS was constantly flowed into the sample chamber at a rate of 1.6 μL/min to mimic the aqueous turnover rate of the human eye. Paracetamol powder was used as control and was cleared within 24 h (data not shown). A sustained drug release profile was observed throughout the 30-day period (**Figure 3.13**) with a cumulative release of 62.6 ± 13.5% paracetamol of the actual loading. The concentration profile of paracetamol exhibited a biphasic release beginning with a burst release over the first day (5.4 μg/mL), which could be due to the drug on the surface of the devices. A decrease in paracetamol concentration was observed in the next 10 days and subsequently a constant rate of release with the concentration ranging from 0.4 to 0.65 μg/mL was displayed in the remaining study period.
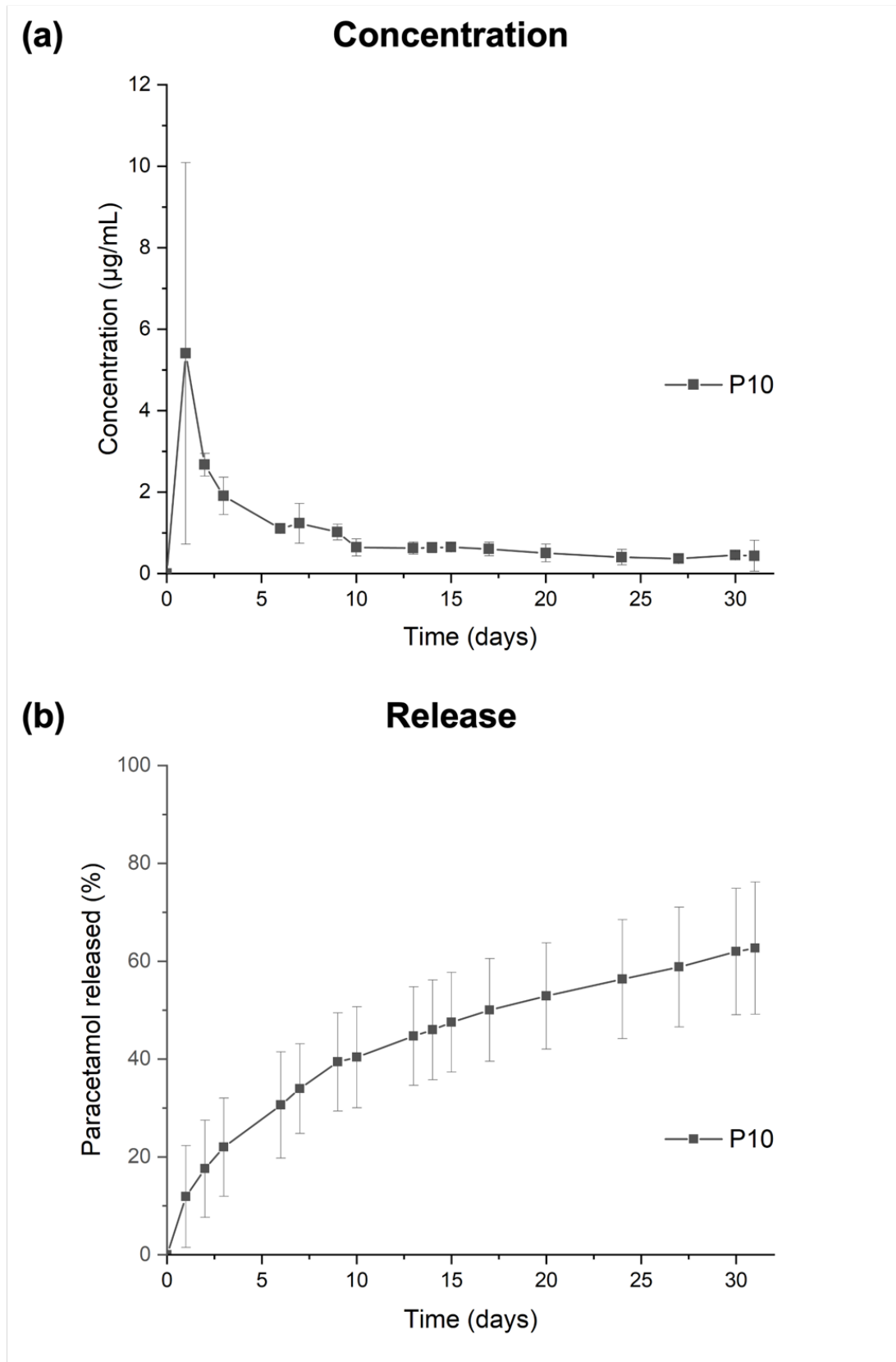
Figure 3.13 (a) Concentration and (b) cumulative release profile of paracetamol from the DLP 3D printed punctal plugs in a rig model mimicking the subconjunctival space. Data are shown as mean ± SD (n=3).

3.6.2 Dexamethasone-loaded punctal plugs

3.6.2.1 3D printing

Following the successful incorporation of paracetamol in the 3D printed punctal plugs using a commercial Flexible resin, which demonstrated a sustained release profile over 30 days, a more clinically relevant drug for treating dry eye syndrome (dexamethasone) was used to prepare punctal plugs using PEGDA. Since the DLP 3D printer used in this study was equipped with a visible-light source (400 – 800 nm), which offers numerous benefits over ultraviolet UV light, such as being energy efficient with reduced risks of eye damage and improved biocompatibility and functional group tolerance (Ahn et al., 2020; Madžarević and Ibrić, 2021; Park et al., 2018), it is important to use a suitable photoinitiator that works within the same spectral range. In this chapter, a commercially available photoinitiator, phenylbis (2,4,6-trimethylbenzoyl) phosphine oxide or (Irgacure 819) was selected due to its absorbance between 400 – 450 nm and its applicability in biomedical research (Bagheri and Jin, 2019). In the resins, β-carotene was incorporated as a photoabsorber due to its absorbance in the visible light range (400 – 500 nm) (**Figure 3.14**) in order to decay the light intensity, helping to achieve high printing resolution of the punctal plugs. Unlike the commonly used light absorbers, such as Sudan I which has been reported to be genotoxic and carcinogenic (Grigoryan et al., 2019), β-carotene is a natural pigment found in plants and fruits and acts as an antioxidant, and thus represents a suitable choice as a biocompatible photoabsorber (Breloy et al., 2019; Field et al., 2021).
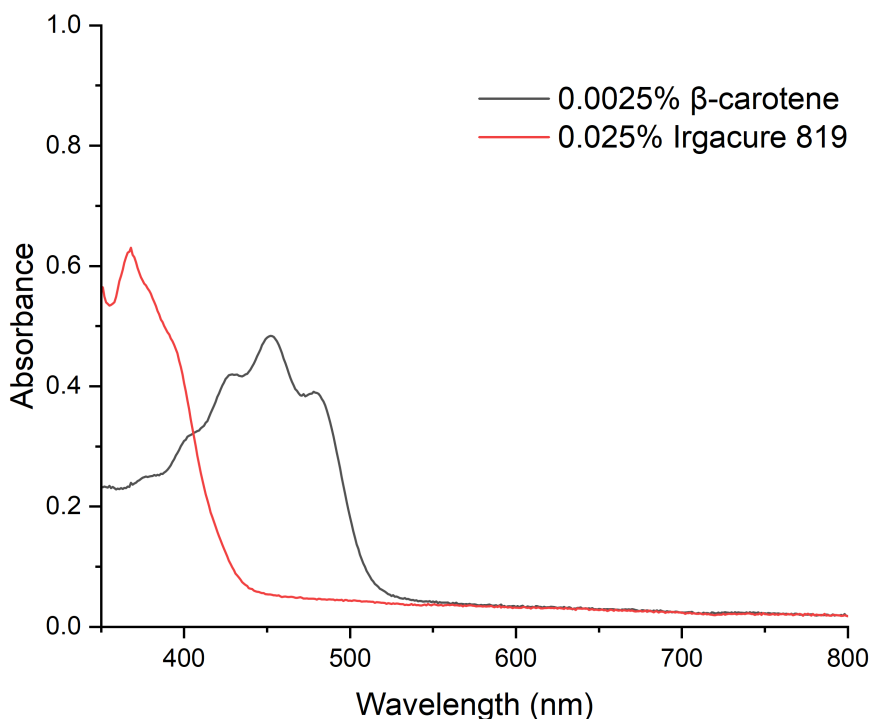
Figure 3.14 UV-vis spectra of light absorbance for 0.025% (w/v) Irgacure 819 and 0.0025% (w/v) β-carotene.

Different dexamethasone-loaded punctal plugs were successfully fabricated via DLP 3D printing with good resolution and reproducibility. The punctal plug was designed to possess a tapered shaft, which exerts horizontal force to keep it in place for easy insertion and removal (Jehangir et al., 2016). The total printing time was only 20 min and more than 20 punctal plugs could be fabricated in one print, highlighting the capability of 3D printing in the preparation of small-batch personalised drug delivery devices. The punctal plugs showed an orange colour due to the addition of β-carotene (**Figure 3.15**). All the devices were fabricated with uniform weights and lengths (**Table 3.2**).
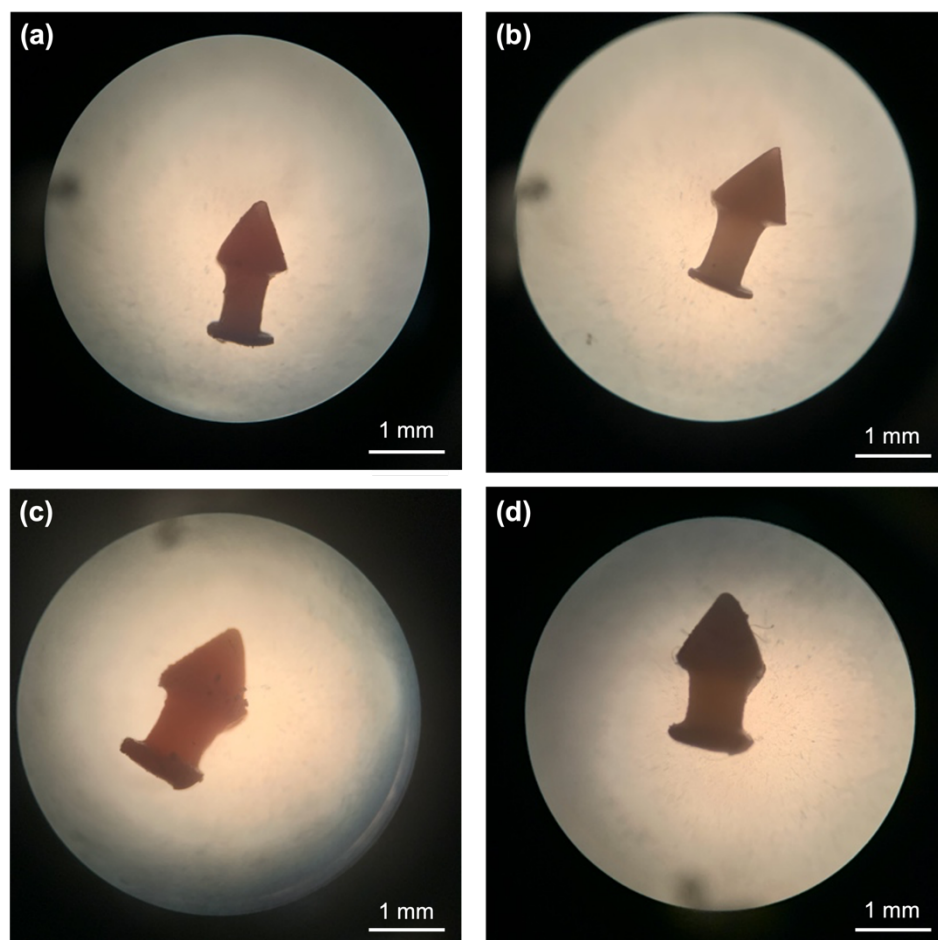
Figure 3.15 Light microscope images of the DLP 3D printed (a) D10, (b) D10PEG, (c) D20, and (d) D20PEG punctal plugs.

Table 3.2 Weights and dimensions of different DLP 3D printed punctal plugs.

Formulations	Weight (mg ± SD)	Length (mm ± SD)
D10	0.9 ± 0.03	1.9 ± 0.03
D20	1.5 ± 0.03	2.0 ± 0.02
D10PEG	0.6 ± 0.05	1.8 ± 0.05
D20PEG	1.4 ± 0.03	2.0 ± 0.01

SEM images showed the surface morphologies of the different punctal plugs (**Figure 3.16**). A minor increase in roughness was seen with an increase in drug loading from 10 to 20%. Although the removal of supports after printing was easily achieved using tweezers, minor damage was visualised on the surface (**Figure 3.16a and 3.16c**).
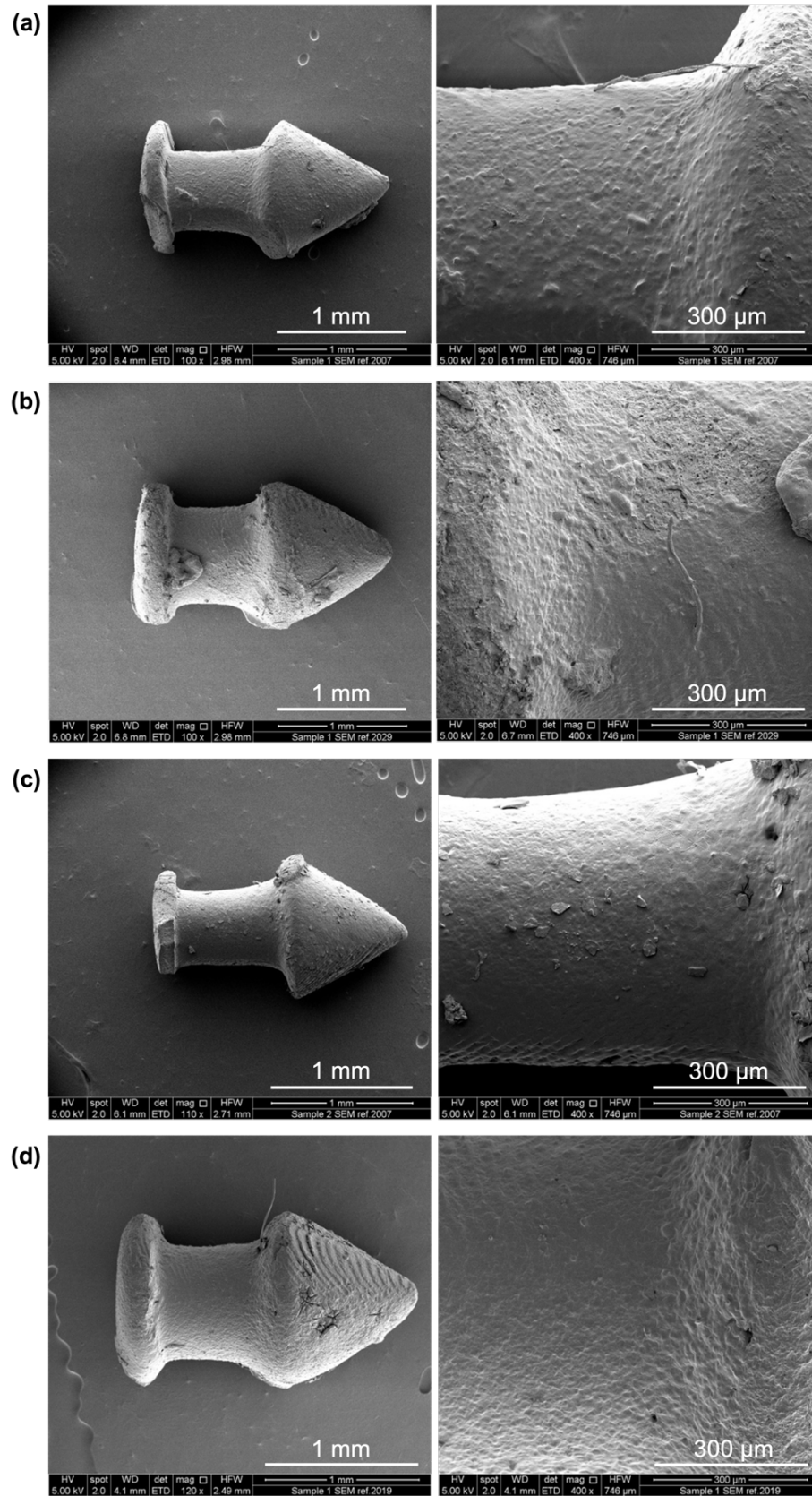
Figure 3.16 SEM images of the DLP 3D printed (a) D10, (b) D20, (c) D10PEG and (d) D20PEG punctal plugs.

3.6.2.2 Physical characterisation

Dexamethasone and DLP 3D printed drug-loaded discs (23 mm diameter x 1 mm height) for different formulations (D10, D20, D10PEG, D20PEG) were analysed by XRPD to evaluate the physical state of the drug and the degree of its incorporation in the polymer matrices. The diffraction patterns (**Figure 3.17**) show characteristic peaks of dexamethasone at 12.92° 2θ, 15.50° 2θ, and 17.08° 2θ in the printed formulations, suggesting part of the drug remained in a crystalline state. Peaks were more intense in the D20 and D20PEG 3D printed formulations when the drug content was increased from 10 to 20% (w/w), indicating a greater proportion of drug was crystalline.
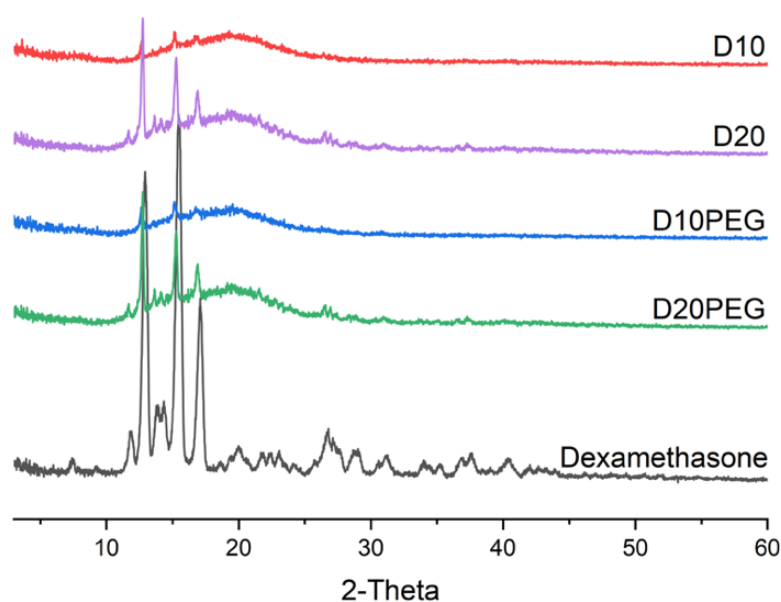
Figure 3.17 X-ray powder diffractograms of dexamethasone and DLP 3D printed formulations.

DSC thermograms were also obtained for the dexamethasone powder and different punctal plugs (D10, D20, D10PEG, D20PEG), showing the melting peak of dexamethasone at 266 °C (**Figure 3.18**), in agreement with literature (Li et al., 2013). No evidence of melting was observed in the D10 or D10PEG 3D printed formulations. Both D20 and D20PEG showed a small endothermic

peak at 258 °C, consistent with there being a small fraction of drug in the crystalline state, as also noted in the XRPD data.
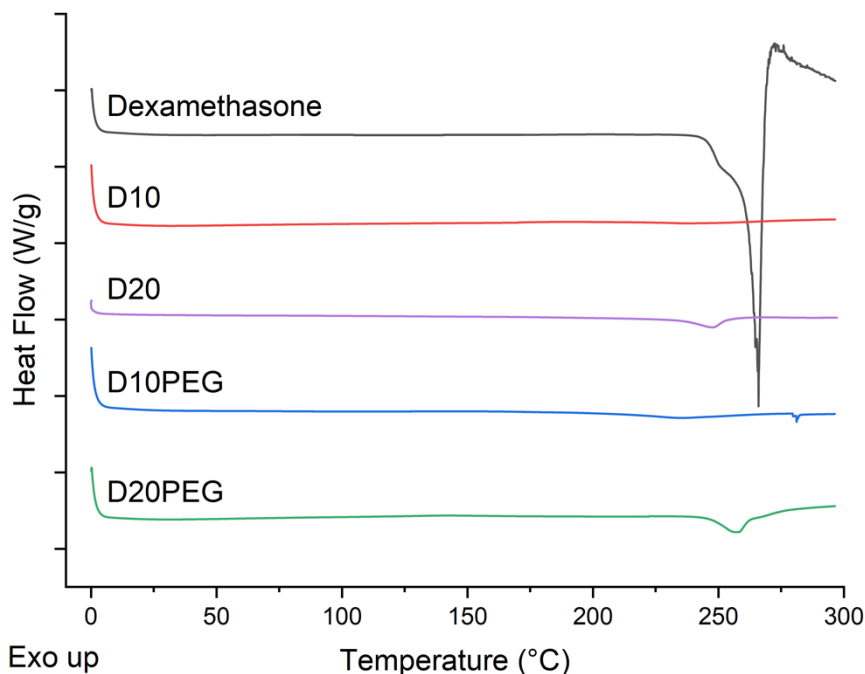
Figure 3.18 DSC thermograms of dexamethasone and DLP 3D printed formulations.

ATR-FTIR was performed to investigate potential interactions between dexamethasone and the photopolymer before and after DLP 3D printing. Previously, drug-photopolymer reaction has been reported in oral dosage forms prepared using SLA 3D printing (Xu et al., 2020). Therefore, it is important to ensure the drug-photopolymer compatibility of the fabricated drug-loaded punctal plugs in order to maintain therapeutic efficacy. Characteristic peaks of dexamethasone (**Figure 3.19**) (wavenumber highlighted in black) were recorded at 3464 cm^{-1} (O-H stretching), 1660 cm^{-1} (C=O stretching), and 891 cm^{-1} (axial deformation of C-F group) (da Silva et al., 2011). These absorption bands were clearly observed in the spectra of all the formulations before and after 3D printing, indicating the presence of drug, and no interactions were seen between dexamethasone and the photopolymers. For comparison, the spectrum of PEGDA is also included, showing its distinct

peaks (wavenumber highlighted in red) at 1722 cm^{-1} (C=O stretching), 1633 cm^{-1} (C=C stretching), 1408 cm^{-1} and 810 cm^{-1} (CH$_2$=CH) (Clark et al., 2017; Visentin et al., 2014). After 3D printing, these peaks at 1633 cm^{-1}, 1408 cm^{-1} and 810 cm^{-1} disappeared, because of the conversion of C=C bonds to C-C bonds of PEGDA via photocrosslinking (Kadry et al., 2019; Krkobabić et al., 2019; Lin et al., 2005).
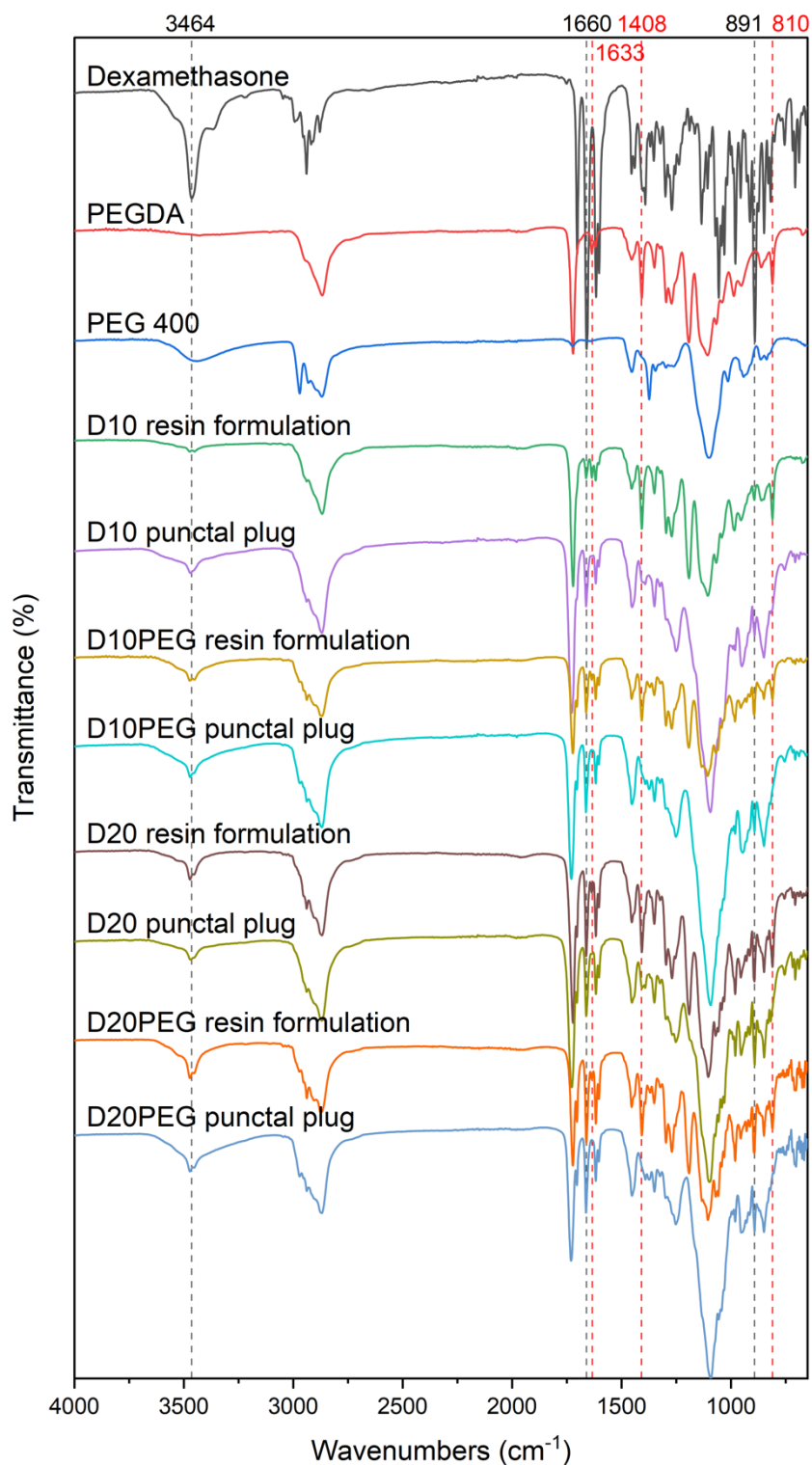
Figure 3.19 FTIR spectra of dexamethasone, PEGDA, PEG 400, different resin formulations and punctal plugs.

3.6.2.3 *In vitro* drug release

Drug loadings of the different DLP 3D printed punctal plugs were determined using HPLC. The loading of dexamethasone in various DLP 3D printed punctal plugs was consistent with that in the resin formulation (**Table 3.3**). Dissolution studies were conducted using the same in-house *in vitro* model that mimics the subconjunctival space of the eye (Angkawinitwong et al., 2017). A burst release of dexamethasone with a C_{max} value of 12.4 ± 5.3 µg/mL (57.6 ± 8.4% of total drug released) was observed by day 1 from the D10PEG punctal plugs (**Figure 3.20**). Complete drug release was achieved in 4 days. On the other hand, the D20PEG punctal plugs exhibited a polyphasic release profile with a burst concentration at 16.1 – 17.6 µg/mL in the first 2 days, followed by a constant rate of release at 8.5 – 10.5 µg/mL in the next 5 days (accounting for 80.4 ± 5.0% of release in 1 week). The concentration was maintained at approximately 3.0 µg/mL per day in the remaining period. Although the reduced PEGDA concentration in the D20PEG punctal plugs was expected to lower the polymer density in the crosslinked network (and increase the drug release rate), the observed slower dissolution rate from D20PEG was mainly attributed to the poor aqueous solubility of dexamethasone (0.1 mg/mL) (Awwad et al., 2017a).

Table 3.3 Drug loading in resin formulations and DLP 3D printed punctal plugs.

Formulations	Drug loading (% w/w ± SD)		Dose (µg)
	Resin formulations	DLP 3D printed punctal plugs	
D10	11.9 ± 0.3	9.8 ± 0.5	84.4
D20	20.2 ± 1.6	20.3 ± 2.1	305.6
D10PEG	10.6 ± 0.1	10.0 ± 0.6	59.0
D20PEG	19.4 ± 2.1	21.2 ± 1.4	294.4

Conversely, prolonged release profiles were observed for the D10 and D20 punctal plugs. Despite the C_{max} reaching 4.0 ± 1.3 µg/mL in the first day, D10 displayed a release rate ranging from 2.6 – 1.7 µg/mL in the first 7 days, reaching 64.1 ± 2.4% of dexamethasone release. D20 demonstrated a

continuous and monophasic release profile over 21 days with a close-to-constant release rate between 2-1 – 5.1 µg/mL, where only 51.1 ± 6.5% of total release has been achieved within 11 days. As expected, the incorporation of PEG 400 as a hydrophilic diluent in D10PEG and D20PEG lowered the polymer density in the matrix, facilitating the drug release rates (Krkobabić et al., 2019; Wang et al., 2016). Recently, dexamethasone-loaded nanowafers (Coursey et al., 2015) were proposed for treating dry eye disease, however, drug release only continued for 24 h.

(a)

(b)
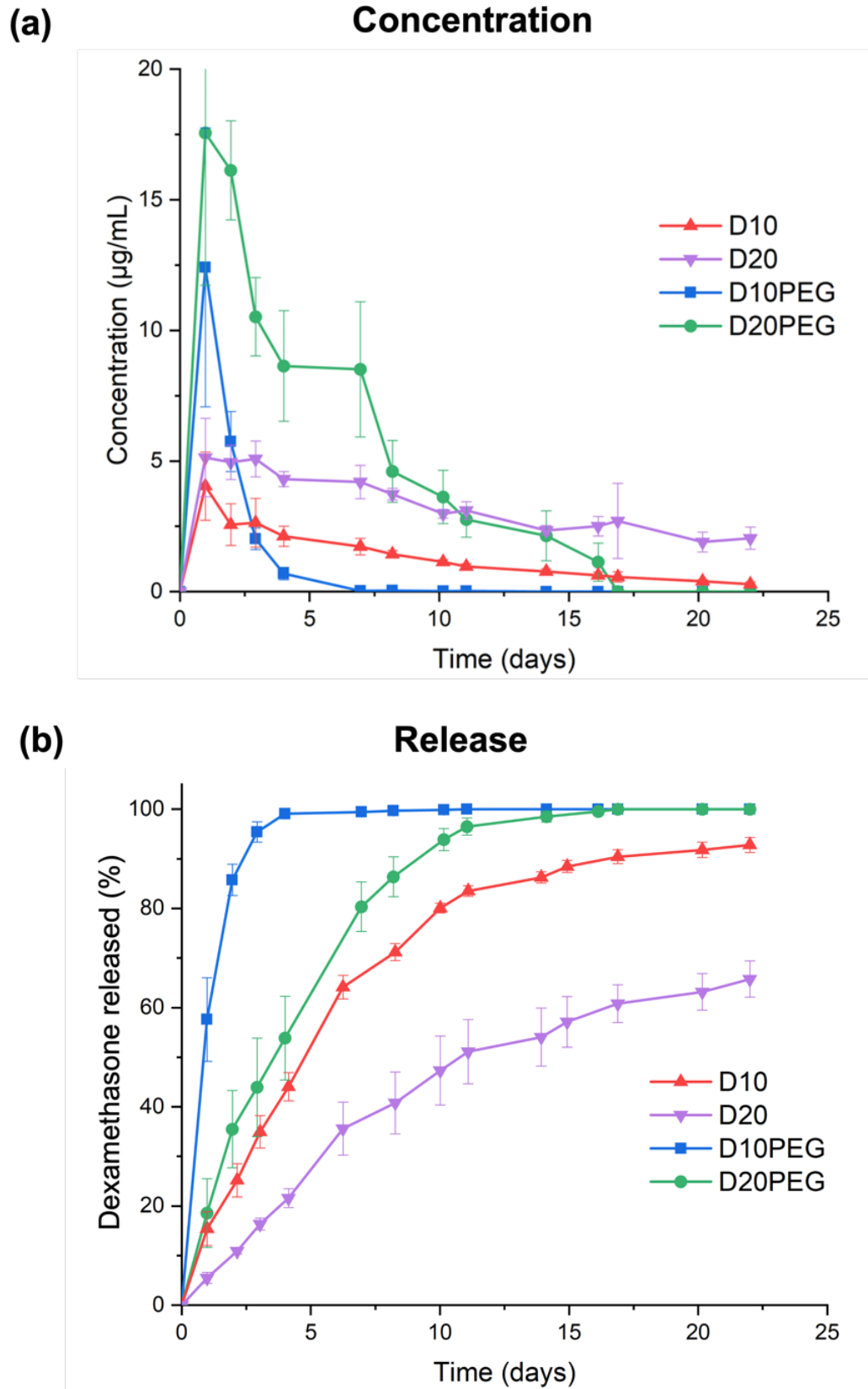
Figure 3.20 (a) Concentration and (b) cumulative release profile of dexamethasone from the DLP 3D printed punctal plugs in a rig model mimicking the subconjunctival space. Data are shown as mean ± SD (n=4).

Since the release environment was not under sink conditions, it did not follow one of the assumptions to use the Higuchi model (Bruschi, 2015). The in vitro release data of the DLP 3D printed punctal plugs were fitted into different kinetic models (zero-order, first-order, and Korsmeyer-Peppas model) to better understand the release kinetics. As shown in **Table 3.4**, the release of dexamethasone from D10PEG and D20PEG punctal plugs was best fitted in first-order kinetics, with an R^2 of 0.994 and 0.991, showing the release rates were dependent on the concentration. On the other hand, the release of dexamethasone from D10 and D20 punctal plugs was best fitted in Korsmeyer-Peppas model, with R^2 of 0.993 and 0.987. The n values of all punctal plugs were between 0.45 and 0.89 (for cylinders), which indicated non-Fickian diffusion model and suggested their mechanisms of drug release were governed by diffusion and swelling, which attributed to the swelling nature of PEGDA in aqueous solution (Bruschi, 2015).

Table 3.4 Release kinetic data of the DLP 3D printed punctal plugs containing dexamethasone.

Release kinetics model	Parameters	D10	D20	D10PEG	D20PEG
Zero-order	R^2	0.973	0.919	0.813	0.967
	k_0 (h^{-1})	0.360	0.127	0.983	0.556
First-order	R^2	0.989	0.969	0.994	0.991
	k_1 (h^{-1})	0.006	0.002	0.053	0.008
Korsmeyer-Peppas	R^2	0.993	0.987	0.973	0.984
	k (h^{-n})	1.478	0.359	13.104	1.791
	n	0.734	0.883	0.475	0.754

After the 21-day release study, the punctal plugs were collected, dried, and imaged with SEM (**Figure 3.21**). Compared with the SEM images before dissolution (**Figure 3.16**), porous surfaces can be observed in all the plugs, contributing to the release of dexamethasone from the devices. The punctal

plugs with higher drug loading (D20 and D20PEG) showed an increased number of pores than the D10 and D10PEG plugs.
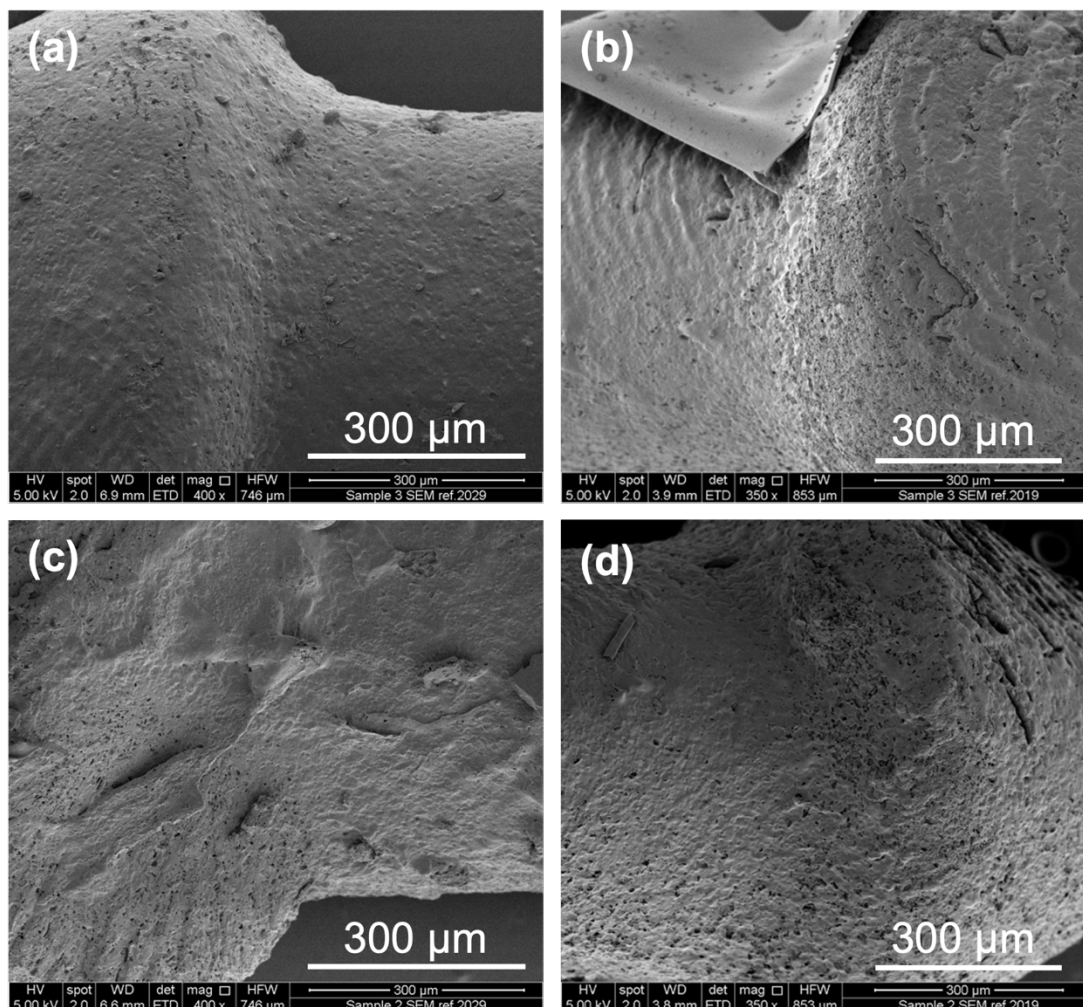
Figure 3.21 SEM images of DLP 3D printed (a) D10, (b) D10PEG, (c) D20, and (d) D20PEG punctal plugs after dissolution.

Overall, this study highlights the potential of drug-releasing punctal plugs, which are not limited to dry eye disease, but could vastly benefit a range of ocular diseases including open-angle glaucoma, ocular hypertension, and bacterial conjunctivitis (Chee, 2012; Singh et al., 2020). With the use of DLP 3D printing, small batches of drug-loaded punctal plugs (more than 20) could be fabricated at the same time within 20 minutes. However, challenges and limitations need to be considered regarding printing such small objects. Since objects are fabricated upside down in DLP 3D printers, supports are necessary

when printing objects with overhanging features like the punctal plugs. As a result, removing the support may lead to damage to the surface of the device, and potentially loss of drug contents. In addition, since dexamethasone suspensions were used for printing in this chapter due to its low solubility in PEGDA, homogeneity of the formulation could be not consistent during the printing process with the up-and-down movement of the platform. A simple wiper would be a helpful tool, which not only could distribute the resin across the printing area between each layer but could also ensure the drug particles are homogeneous suspended.

3.7   Conclusion

Here, DLP 3D printing was explored as a manufacturing method for the direct preparation of drug-loaded punctal plugs with prolonged drug delivery to the front of the eye for patients with dry eye disease. Using paracetamol as a model compound and the commercial Flexible resin, the drug-loaded punctal plugs were successfully prepared and sustained release of paracetamol was demonstrated over 30 days using an *in vitro* ocular model. Subsequently, dexamethasone-loaded punctal plugs were fabricated with two loadings of dexamethasone (10% w/w and 20% w/w) using different compositions of PEGDA and PEG 400. All punctal plugs were successfully prepared with high resolution and uniformity in size, demonstrating the flexibility and precision of 3D printing. FTIR spectra confirmed the absence of drug-photopolymer interactions. *In vitro* drug release results showed that drug release from D10PEG and D20PEG plugs can be sustained for 1 week while D10 and D20 plugs can prolong the release with 50% of dexamethasone released in 5 and 11 days, respectively.

Compared with the traditional method of preparing punctal plugs, such as moulding, DLP 3D printing offers high flexibility in personalising the dosage, size, shape, and material of the plug to suit different patients' needs. Overall, the results presented in this chapter highlights the potential of fabricating personalised drug-loaded punctal plugs via DLP 3D printing, which is not

limited to dry eye disease, but could vastly benefit a range of ocular diseases by adapting other ocular therapeutics for drug delivery to the front eye.

Chapter 4

SLA 3D printing of antihypertensive

polyprintlets

4 SLA 3D printing of antihypertensive polyprintlets

4.1 Overview

Combination therapy has gained momentum with the aim of improving treatment outcomes currently achieved by polypharmacy. Otherwise challenging to produce via conventional large-scale manufacturing techniques, 3D printing has been explored to fabricate personalised multi-component dosage forms for individuals. In this chapter, SLA 3D printing was used to develop a multi-layer 3D printed oral dosage form (polyprintlet) incorporating four antihypertensive drugs including irbesartan, atenolol, hydrochlorothiazide and amlodipine using poly(ethylene glycol) diacrylate (PEGDA) and polyethylene glycol 300 (PEG 300). Physical characteristics of different 3D printed drug-loaded layers were evaluated using XRPD and DSC. Although successful in its fabrication, a chemical reaction between a photopolymer and one of the drugs was observed and further investigated using Fourier Transform Infrared (FTIR) spectroscopy and Nuclear Magnetic Resonance (NMR) spectroscopy. The *in vitro* drug release profiles of each drug from the polyprintlet were assessed.

4.2 Introduction

4.2.1 Hypertension

High blood pressure, or hypertension is a leading global risk factor for increasing the chance of developing cardiovascular disease, stroke, and other serious conditions. It is defined as having systolic blood pressure of 140 mmHg or higher or diastolic blood pressure of 90 mmHg or higher (Zhou et al., 2017). In 2010, 31.1% of adults (1.38 billion people) worldwide had hypertension (Mills et al., 2020). Hypertension prevalence is rising globally due to population growth and ageing as well as increased exposure to lifestyle risk factors such as unhealthy diets and lack of physical activity.

Beyond lifestyle changes, most patients are usually treated with monotherapy as the initial therapy, however, this does not typically yield sufficient blood pressure control as monotherapy only reduces blood pressure by around 9/5 mmHg on average (Chow et al., 2017). Consequently, there is a pressing need for new antihypertensive treatment strategies with improved efficacy and reduced adverse effects. A study analysed 354 randomised double blind placebo controlled trials of the five main categories of blood pressure lowering drugs (thiazides, beta blockers, angiotensin converting enzyme inhibitors, angiotensin II receptor antagonists, and calcium channel blockers). The results demonstrated that all five categories of drug produced similar reductions in blood pressure. Although the average blood pressure reductions using half standard dose (7.1/4.4 mmHg) was 20% lower than those using standard dose (9.1/5.5 mmHg), the adverse effects were much less common (Law et al., 2003). The study also showed the reductions in blood pressure using drugs in combination are additive, especially using three drugs in combination at low dose would reduce the risk of stroke by two thirds and heart disease by half.

Mahmud and Feely reported that a combination of four drugs (amlodipine, atenolol, bendroflumethiazide, and captopril) from four classes of standard antihypertensive agents each at one-quarter dose was able to achieve a greater reduction (60%) in mean arterial pressure than each agent at standard dose individually (15% to 40%) (Mahmud and Feely, 2007). In addition, a recently published study provided the results of the first placebo-controlled trial on another use of quarter-dose quadruple combination therapy (amlodipine, atenolol, hydrochlorothiazide, and irbesartan), showing that 24 h ambulatory blood pressure was reduced by 19/14 mmHg (Chow et al., 2017). The findings in this study showed that administration of a single quarter-dose quadruple combination therapy daily is likely to provide blood pressure control with minimised adverse effects compared to up-titrating monotherapy.

4.2.2 Polypills

Combination therapy has gained momentum with the aim of improving therapeutic outcomes currently achieved by polypharmacy. The concurrent use of multiple medications by a patient, however, is an ongoing concern due to the high pill burden, patient non-adherence and increasing risk of medication errors (Maher et al., 2014; Trenfield et al., 2018). To overcome such limitations, "polypills", the concept of incorporating more than one active pharmaceutical ingredient in a single dosage form, was devised as an optimised therapeutic approach for treatments such as cardiovascular disease (Wald and Law, 2003). Nevertheless, the polypills used in both studies were prepared by cutting medicines in quarters with a pill splitting device and encapsulated them in gelatin capsules, which may lead to the unequal distribution of doses (Chow et al., 2017; Mahmud and Feely, 2007).

4.2.3 3D printing of polypills

As discussed in Chapter 1.3.3, 3D printing is gaining increasing attention as a manufacturing platform for the development of polypills due to its low cost, high flexibility, and adaptability. Previous attempts towards patient-centric polypills have been achieved via different 3D printing technologies including SLS 3D printed pellets combining paracetamol and ibuprofen with modified release properties (**Figure 4.1a**) (Awad et al., 2019), SSE 3D printed polypill containing an osmotic pump and a sustained release compartment (**Figure 4.1b**) (Khaled et al., 2015b), FDM 3D printed cardiovascular polypill (rosuvastatin, amlodipine, lisinopril, and indapamide) (**Figure 4.1c**) (Pereira et al., 2019), and SLA 3D printed polypills in two designs incorporating six different drugs (naproxen, aspirin, paracetamol, caffeine, chloramphenicol, and prednisolone) (**Figure 4.1d**) (Robles-Martinez et al., 2019).
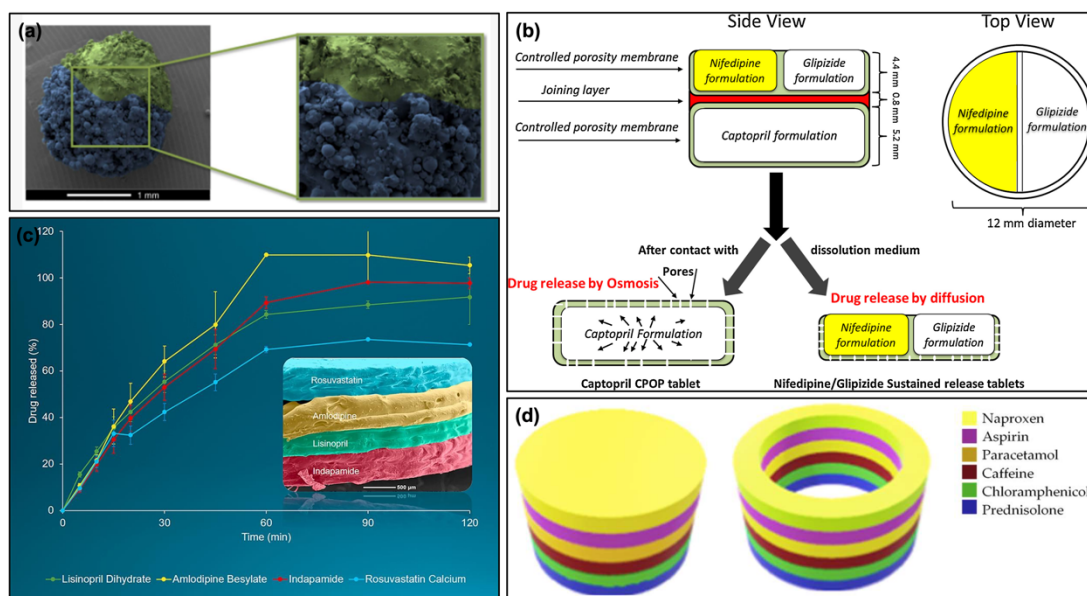
Figure 4.1 (a) SEM image of a 3D printed miniprintlet (Awad et al., 2019); (b) schematic structural diagram of a 3D printed polypill (Khaled et al., 2015b); (c) SEM image of the surface of a cardiovascular polypill (Pereira et al., 2019); (d) 3D design of polypills containing six drugs (Robles-Martinez et al., 2019).

4.2.4 Multi-material vat photopolymerisation 3D printing

Within vat photopolymerisation 3D printing, there are different approaches to achieve objects fabricated with multiple materials, which will be briefly described in the following section.

4.2.4.1 Manual approach

The most common and simplest approach is by pausing the printing process at a certain point, then manually switching the resins or the resin tanks (**Figure 4.2a**) (Zhou et al., 2013). This approach may require a washing step whereby the printed part needs to be rinsed and dried to avoid cross-contamination between different materials.
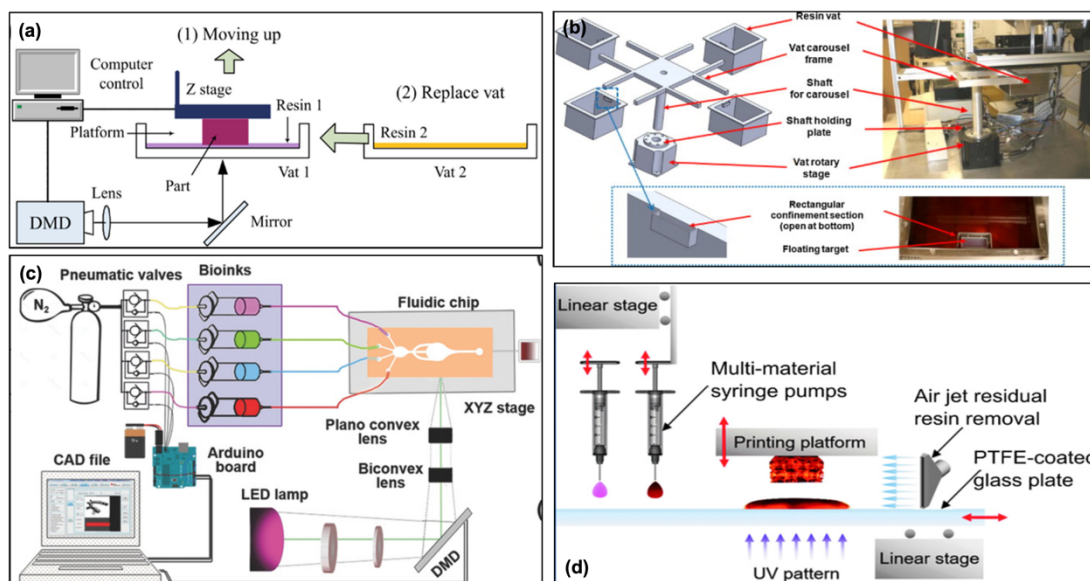
Figure 4.2 Examples of multi-material vat photopolymerisation 3D printing via (a) manual approach (Sampson et al., 2021; Zhou et al., 2013); (b) mechanical approach, the rotating carousal system (Choi et al., 2011); (c) mechanical approach, the microfluidic system (Miri et al., 2018); and (d) the automated material exchange system (Kowsari et al., 2018; Sampson et al., 2021).

4.2.4.2 Mechanical approach

On the other hand, customisation of the printers can be done to include supplementary mechanical components that are capable of switching one material to another, hence enabling multi-material printing. For example, the rotating vat carousel system (**Figure 4.2b**) which contains four stainless steel resin vats mounted on a rotary stage (Choi et al., 2011), the microfluidic system (**Figure 4.2c**) (Han et al., 2019; Miri et al., 2018), and the automated material exchange system (**Figure 4.2d**) where puddles of resins on a glass plate are horizontally translated and cleaned with an air jet (Kowsari et al., 2018).

4.2.4.3 Multi-layer approach

Following the advancement of volumetric printing, multi-material printing becomes possible via the multi-layer approach, meaning a second material can be printed around the pre-existing solid objects (Kelly et al., 2019). Since

this approach is fairly new technique, future challenges include overprinting around complex geometries as well as regions with different mechanical properties for biomedical applications such as biological tissues (Sampson et al., 2021).

4.2.4.4 Chemistry approach

More recently, the development of orthogonal chemistry mechanisms enables dual-wavelength method of photopolymerisation where different wavelengths of light source can be used to selectively induce radical and cationic photopolymerisation. This ability to control curing reactions would allow multi-material printing with diverse chemical and mechanical responses (Dolinski et al., 2018). For example, Schwartz and Boydston used the combination of 365 nm UV and visible light projector sources to produce multi-material objects with hard (acrylate and epoxide) and soft (acrylate) networks (Schwartz and Boydston, 2019).

4.2.5 Model drugs and photopolymer

The four drugs selected in this chapter were antihypertensive drugs from different classes used in the study of Chow et al. being atenolol (beta blockers), hydrochlorothiazide (thiazide diuretics), irbesartan (angiotensin receptor II blockers), and amlodipine (calcium-channel blockers) (**Figure 4.3**).
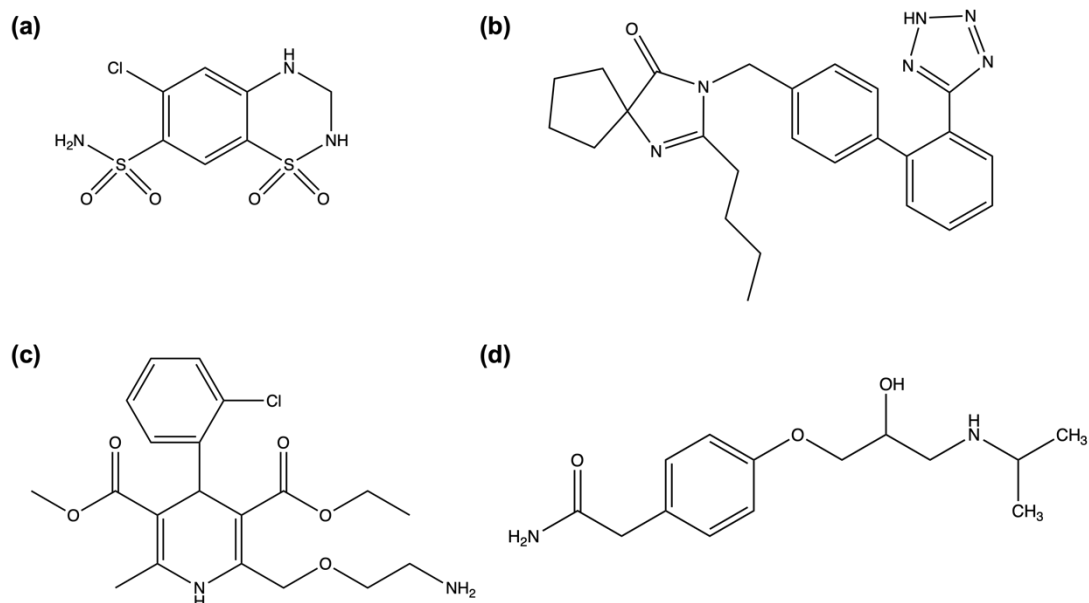
Figure 4.3 Chemical structures of (a) hydrochlorothiazide, (b) irbesartan, (c) amlodipine, and (d) atenolol.

The same as Chapter 2 and 3, PEGDA was chosen as the main photocurable materials and PEG 300 was selected as the diluent to decrease the crosslinking density, hence increase the drug release rate.

4.3 Aim

This chapter aimed to explore the amenability of SLA 3D printing to fabricate multi-layer antihypertensive polypills (herein coined as polyprintlets) of four antihypertensive drugs (irbesartan, atenolol, hydrochlorothiazide, and amlodipine). The aims of Chapter 4 include:

- To design and develop polyprintlets incorporating four antihypertensive drugs at specific doses using SLA 3D printing.
- To assess the physical characteristics of different drug-loaded formulations.
- To evaluate the *in vitro* drug release profiles of different drugs from the polyprintlets.
- To study the chemical reaction between the photopolymers and drugs.

4.4 Materials

Hydrochlorothiazide (MW 297.74 g/mol, logP -0.07, water solubility 0.722 mg/mL at 25 °C (PubChem, 2023e)), poly(ethylene glycol) diacrylate (PEGDA, Mn 575), diphenyl(2, 4, 6-trimethyl-benzoyl) phosphine oxide (TPO), and acetonitrile (ACN, ≥99.9%, HPLC grade) were purchased from Sigma-Aldrich (Dorset, UK). Irbesartan (MW 428.53 g/mol, logP 4.5, water solubility 0.00884 mg/mL (PubChem, 2023f)) was obtained from Sun Pharmaceutical Industries Ltd., India. Amlodipine (MW 408.88 g/mol, logP 3.0, water solubility 0.0753 mg/mL at 25 °C (PubChem, 2023b)) and atenolol (MW 266.34 g/mol, logP 0.16, water solubility 13.3 mg/mL at 25 °C (PubChem, 2023c)) were purchased from LKT Laboratories Inc., USA. Polyethylene glycol 300 (PEG 300, MW 300 g/mol) was acquired from Acros Organics, UK. Formic acid (FA, Optima, LC-MS grade) was purchased from Fisher Scientific, UK. The salts for the preparation of the buffer dissolution media were purchased from VWR International Ltd., UK. Dimethyl sulfoxide-d6 (99.9%) was obtained from Cambridge Isotope Laboratories, Inc., USA. All materials were used as received.

4.5 Methods

4.5.1 3D design

Four antihypertensive drugs were incorporated in different regions of the polyprintlet (**Figure 4.4**) and explored in two orientations. The selected dimension of the polyprintlet was 10 mm diameter × 5 mm height with a 1 mm layer thickness for each drug, except for irbesartan. The thickness of irbesartan layer was doubled (2 mm) to allow a lower concentration of drug in the layer (20.9% w/w) to obtain the desired dose (**Table 4.1**). If the thickness of irbesartan layer was 1 mm the required drug concentration would be 41.8% w/w, which was not printable. To investigate how surface area to volume (SA/V) ratio of a specific layer changes drug release rate, the polyprintlets were designed in 2 configurations; Type 1 and Type 2. The Type 1 polyprintlet was designed to incorporate the drugs with higher doses (irbesartan and atenolol) on the outer layers and lower dosed drugs (hydrochlorothiazide and

amlodipine) in the inner layers. The order of drugs in the Type 2 polyprintlet was changed.
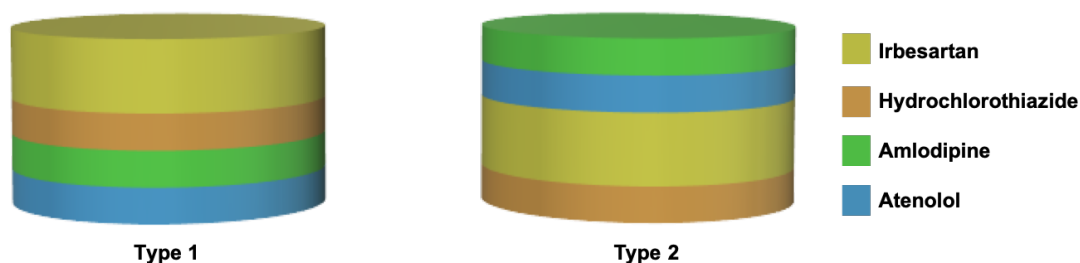
Figure 4.4 3D designs of the polyprintlets.

4.5.2 Preparation of drug-loaded resin formulations

The resin formulations were prepared with 1% (w/w) of TPO added to a total mass of 5 g. The model drugs were added to each solution according to previously calculated concentrations (**Table 4.1**). PEG 300 was added as a diluent to decrease the crosslinking density at a ratio of 35% (w/w) PEGDA to 65% (w/w) PEG 300. The resin formulations were kept in amber vials and stirred thoroughly overnight at room temperature until the drugs and photoinitiator were fully dissolved.

Table 4.1 Compositions (% w/w) of material used for each layer.

Layer	Drug (%)	PEG 300 (%)	PEGDA (%)
Irbesartan	20.8	50.8	27.4
Atenolol	13.9	55.3	29.8
Hydrochlorothiazide	6.9	59.9	32.2
Amlodipine	1.4	63.4	34.2

*Each formulation included 1% (w/w) TPO

4.5.3 3D printing process

The resin formulation was loaded into a commercial Form 1+ SLA 3D printer (Formlabs Inc., USA) equipped with a 405 nm laser (**Figure 4.5**). The geometry

of the polyprintlet was designed with AutoCAD 2015 (Autodesk Inc., USA) and exported as a stereolithography file (.stl) in the 3D printer software (Preform Software v. 2.3.3 OpenFL, Formlabs, USA). The Form 1+ SLA 3D printer is designed to print uniform objects with only one material. In order to allow the use of different materials in a single object, the operation of the printer was conducted using OpenFL. This application programming interface was developed by Formlabs for the Form 1 and Form 1+ SLA 3D printers and has previously been described in the literature (Robles-Martinez et al., 2019). The OpenFL software allows the user to pause the printing process and raise the build platform to change the material on the resin tank. After changing the material, the build platform was lowered to its previous position and printing was resumed. Deionised water was used to rinse the printed layer between materials to avoid cross contamination. In the material print setting, the customised number of laser passes was selected as 10 for the first layer and 2 for the remaining layers with a layer thickness of 100 μm to achieve high resolution. The polyprintlets were printed directly on the platform without the need of any supports.
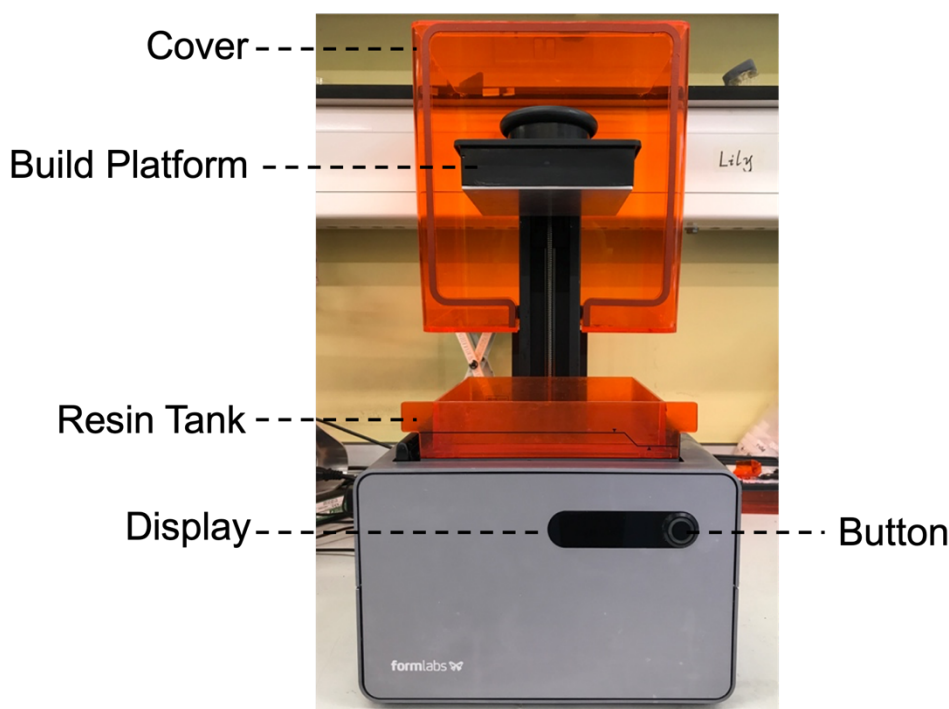
Figure 4.5 Picture of a Form 1+ SLA 3D printer with the cover lifted.

4.5.4 Determination of polyprintlet morphology

The dimensions (diameter and height) of the polyprintlets were measured using a digital calliper (0.150 mm PRO-MAX, Fowler, mod S 235 PAT). Pictures of the polyprintlets were taken with an iPhone (Apple, USA).

4.5.5 X-ray powder diffraction (XRPD)

Single drug-loaded discs (23 mm diameter × 1 mm height) and discs without drugs (control) were printed via SLA and analysed together with the four drugs individually. X-ray powder diffraction patterns were obtained in a Rigaku MiniFlex 600 (Rigaku, USA) using a Cu Kα X-ray source (λ=1.5418Å). The angular range of data acquisition was 3-60° 2θ with a stepwise size of 0.02° at a speed of 5°/min. The intensity and voltage applied were 15 mA and 40 kV.

4.5.6 Thermal analysis

Differential scanning calorimetry (DSC) was used to characterise the single drug-loaded 3D printed formulations, the control and the pure drug samples. DSC measurements were performed with a Q2000 DSC (TA instruments, Waters, LLC, USA) at a heating rate of 10 °C/min. Calibrations for cell constant and enthalpy were performed with indium (T_m = 156.6 °C, ΔH_f = 28.71 J/g) according to the manufacturer instructions. Nitrogen was used as a purge gas with a flow rate of 50 mL/min for all the experiments. Data were collected with TA Advantage software for Q series (version 2.8.394) and analysed using TA Instruments Universal Analysis 2000. All melting temperatures are reported as extrapolated onset unless otherwise stated. TA aluminium pans and Tzero hermetic lids (pin hole made with a tweezer) were used with an average sample mass of 8 – 10 mg.

4.5.7 Scanning electron microscopy (SEM)

The polyprintlet samples were previously cut in half and attached to a self-adhesive carbon disc mounted on a 25 mm aluminium stub, which was coated with 25 nm of gold using a sputter coater. The stub was then placed into a FEI Quanta 200 FEG Scanning Electron Microscope (FEI, UK) at 5 kV accelerating voltage using secondary electron detection to obtain the cross-section images of the SLA 3D printed polyprintlets.

4.5.8 Attenuated Total Reflection Fourier-Transform infrared spectroscopy (ATR-FTIR)

The infrared spectra were collected using a Spectrum 100 FTIR spectrometer (PerkinElmer, Waltham, MA). Amlodipine, hydrochlorothiazide drug powders and PEGDA were measured as the references. Physical mixtures containing 1.39%, 10%, 20%, 30% and 50% (w/w) of amlodipine in PEGDA and 50% (w/w) hydrochlorothiazide in PEGDA were prepared by thoroughly stirring. All samples were scanned over a range of $4000 - 650 cm^{-1}$ at a resolution of $1 cm^{-1}$ for 64 scans.

4.5.9 Nuclear Magnetic Resonance (NMR) spectroscopy

All NMR spectra were recorded in 99.9% dimethyl sulfoxide-d6 (DMSO-d6, Cambridge Isotope Laboratories, Inc., USA). ^{1}H-NMR spectra of amlodipine and PEGDA were obtained separately. In order to investigate the reaction between amlodipine and PEGDA, sample solution of amlodipine mixed with PEGDA (molar ratio of 2:1) was prepared. ^{1}H and ^{13}C NMR spectra of the solutions were obtained using a Bruker AVANCE 400 spectrometer. Data acquisition and processing were performed using standard TopSpin software (Bruker, UK).

4.5.10 Determination of drug loading

To quantify the drug content of the resins, aliquots of each resin formulation loaded with drug were weighed and diluted together with 70% (v/v) methanol and 30% (v/v) water in volumetric flasks (10 mL). The solutions were left under magnetic stirring overnight and filtered through 0.45 μm filter (Merck Millipore Ltd., Ireland). The concentration of drug was then determined by HPLC (Agilent 1260 Infinity Quaternary LC System). For determination of drug loading in the polyprintlet, single drug-loaded layers were crushed and stirred with 70% (v/v) methanol and 30% (v/v) water in volumetric flasks (25 mL). Samples of the solutions were left under magnetic stirring overnight then filtered through 0.45 μm syringe filter (Merck Millipore Ltd., Ireland) and the concentration of drug was determined by HPLC.

The gradient mobile phase consisted of (A) 0.1% v/v FA in water, (B) methanol and (C) ACN which was pumped at a flowrate of 1 mL/min through a Luna 5u Phenyl-Hexyl 5 μm column, 250 mm × 4.6 mm (Phenomenex) under the gradient program shown in **Table 4.2**. The sample injection volume was 30 μL and the total run time was 13 min. Experiments were performed at room temperature with a wavelength of 215 nm.

Table 4.2 HPLC gradient programme.

Time (min)	0.1% FA in water (A) (% v/v)	Methanol (B) (% v/v)	ACN (C) (% v/v)
0.0	95	0	5
5.5 – 6.0	50	0	50
6.5	87	0	13
9.0 – 10.0	77	10	13
11.0	95	0	5

4.5.11 Dissolution testing conditions

Dissolution profiles for each 3D printed polyprintlet were obtained using USP-II apparatus (Model PTWS, Pharmatest, Germany) under sink conditions for atenolol, hydrochlorothiazide, and amlodipine and non-sink conditions for irbesartan. Polyprintlets were first placed in 750 mL of 0.1 M HCl for 2 h to simulate gastric residence time and then transferred into 950 mL of physiological bicarbonate buffer (Hanks buffer) (pH 5.6 to 7) for 35 min followed by 1000 mL of modified Krebs buffer (pH 7 to 7.4 and then to 6.5). Hanks buffer (0.441 mM KH_2PO_4, 0.337 mM $Na_2HPO_4 \cdot 2H_2O$, 136.9 mM NaCl, 5.37 mM KCl, 0.812 mM $MgSO_4 \cdot 7H_2O$, 1.26 mM $CaCl_2 \cdot 2H_2O$, 4.17 mM $NaHCO_3$) was modified to form an in-situ modified Kreb's buffer by the addition of 50 mL of pre-Krebs solution (6.9 mM KH_2PO_4 and 400.7 mM $NaHCO_3$) to every dissolution vessel (Fadda and Basit, 2005; Goyanes et al., 2015a).

The polyprintlets were tested in the small intestinal environment for 3.5 h with a pH value of 5.6 to 7.4, followed by pH 6.5 representing the colonic environment (Fadda and Basit, 2005; Goyanes et al., 2015a). The dissolution medium is primarily a bicarbonate buffer system in which both bicarbonate (HCO_3^-) and carbonic acid (H_2CO_3) exist in an equilibrium together with CO_2 (aq) resulting from the dissociation of the carbonic acid (Goyanes et al., 2015a). The pH of the bicarbonate buffer is modulated and controlled by an Auto pH System^{TM} which incorporates a pH probe connected to a supply of CO_2 (pH reducing gas), as well as to a supply of helium (pH increasing gas) (Merchant et al., 2014). During dissolution testing, the control unit monitors the pH changes and adjusts the pH by feeding CO_2 or helium into the dissolution vessel. The paddle speed of the USP-II was fixed at 50 rpm and the dissolution media was maintained at 37 ± 0.5 °C. 1 mL samples of the dissolution media were withdrawn every half an hour in the first 3 hours, followed by every hour. The concentration of the drugs was determined by HPLC (previously described in section 4.5.10). After the dissolution test, the polyprintlets were retrieved to extract any residual drugs, and this was be taken into consideration in the calculation of percentage of drug released.

To determine the drug release kinetics and mechanism, various mathematical models (zero-order model, first-order model, Higuchi model, and Korsmeyer-Peppas model) were tested to fit the data obtained from *in vitro* release study into the following equations (Bruschi, 2015):

Zero-order model $$Q_t = Q_0 + k_0 \times t$$ (Eq. 4.1)

Where Q_t is the amount of drug released over time t, Q_0 is the initial amount of drug in the solution, and k_0 is the zero-order release constant.

First-order model $$logQ_t = logQ_0 + \frac{k_1 \times t}{2.303}$$ (Eq. 4.2)

Where Q_t is the amount of drug released over time t, Q_0 is the initial amount of drug in the solution, and k_1 is the first-order release constant.

Higuchi model $$Q_t = k_H \times t^{\frac{1}{2}}$$ (Eq. 4.3)

Where Q_t is the amount of drug released over time t and k_H is the Higuchi release constant.

Korsmeyer-Peppas model $$\frac{M_t}{M_\infty} = k \times t^n$$ (Eq. 4.4)

Where M_t/M_∞ is the fraction of drug released over time t, k is the constant of incorporation of structural modifications and geometrical characteristics of the system, and n is the exponent of release.

4.6   Results and discussion

4.6.1   3D printing

Prior to SLA 3D printing, pure amlodipine and hydrochlorothiazide powders were readily dissolved in the resin although a longer time was required to completely dissolve atenolol and irbesartan. Hydrochlorothiazide and amlodipine solutions were clear, although both printed layers appeared off white. A white solution was achieved following the homogenous dispersion of pure atenolol in the resin. However, after completely dissolving, the atenolol

solution became clear. The irbesartan suspension was creamy and viscous as it contained a high concentration of drug (20.8% w/w).

Drug loaded polyprintlets were successfully fabricated as shown in (**Figure 4.6**). The printing settings were customised and optimised for the different formulations using the OpenFL software. Compared with the designed dimension of the polyprintlet (10 mm diameter x 5 mm diameter), the Type 1 polyprintlet (diameter 11.2 mm ± 0.3 mm, height 5.4 mm ± 0.3 mm) was printed slightly wider in diameter and thicker in height whereas the Type 2 polyprintlet (diameter 10.4 mm ± 0.2 mm, height 6.7 mm ± 0.3 mm) was fabricated with a good diameter but much thicker in height.
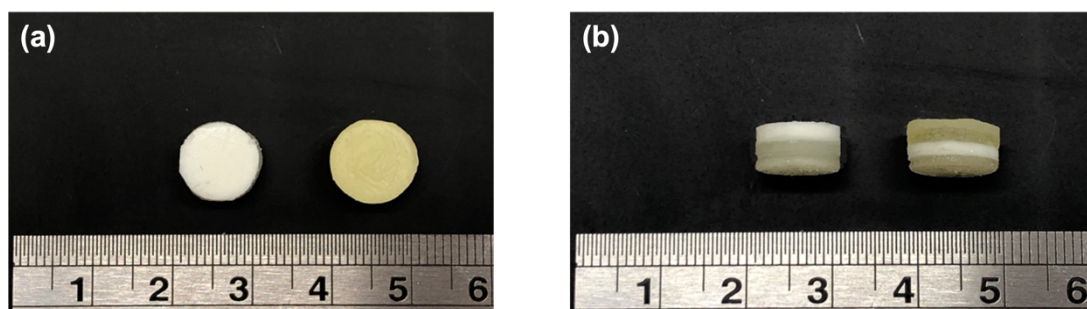
Figure 4.6 Top view (a) and lateral view (b) of Type 1 (left) and Type 2 (right) polyprintlets. Type 1 was loaded with (from top to bottom) irbesartan, amlodipine, hydrochlorothiazide, and atenolol. Type 2 was loaded with (from top to bottom) amlodipine, atenolol, irbesartan and hydrochlorothiazide. The scale is in cm.

SEM imaging was used to visualise the surface and cross-sections of the polyprintlets (**Figure 4.7**). Visible signs of separation between the four printed layers can be observed from both types of polyprintlets, indicating that the individual drug and resin did not mix during the printing process.
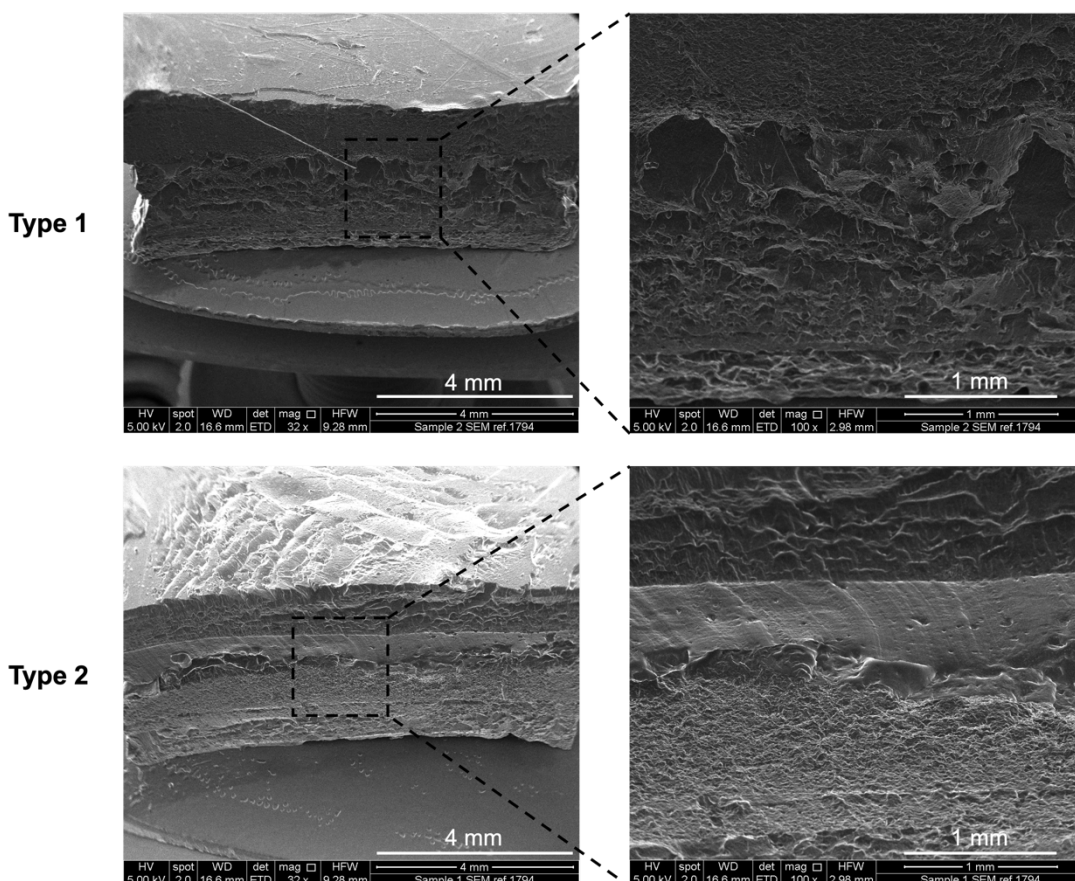
Figure 4.7 SEM image of cross section of the Type 1 (top) loaded with (from top to bottom) irbesartan, amlodipine, hydrochlorothiazide, and atenolol and Type 2 (bottom) polyprintlet loaded with (from top to bottom) amlodipine, atenolol, irbesartan and hydrochlorothiazide.

4.6.2 Physical characterisation

Pure drug powders and SLA 3D printed discs were analysed by XRPD to evaluate the incorporation of drugs in the drug-polymer matrices. The diffractogram shows peaks of pure atenolol at around 20° 2θ (**Figure 4.8**). Characteristic peaks at 9.5°, 19.5°, and 23.8° 2θ were observed for pure amlodipine and peaks at 18.6° and 28.3° 2θ were shown for pure hydrochlorothiazide. The absence of these peaks in the atenolol, amlodipine and hydrochlorothiazide 3D printed formulations indicated that these drugs existed in the amorphous form. Conversely, typical peaks of irbesartan at around 4.4° and 12.1° 2θ were still visible in the printed formulation indicating

that irbesartan was existing in its partially crystalline form in the printed formulation. This suggests that the irbesartan drug powder may not have fully dissolved in the resin prior to printing.
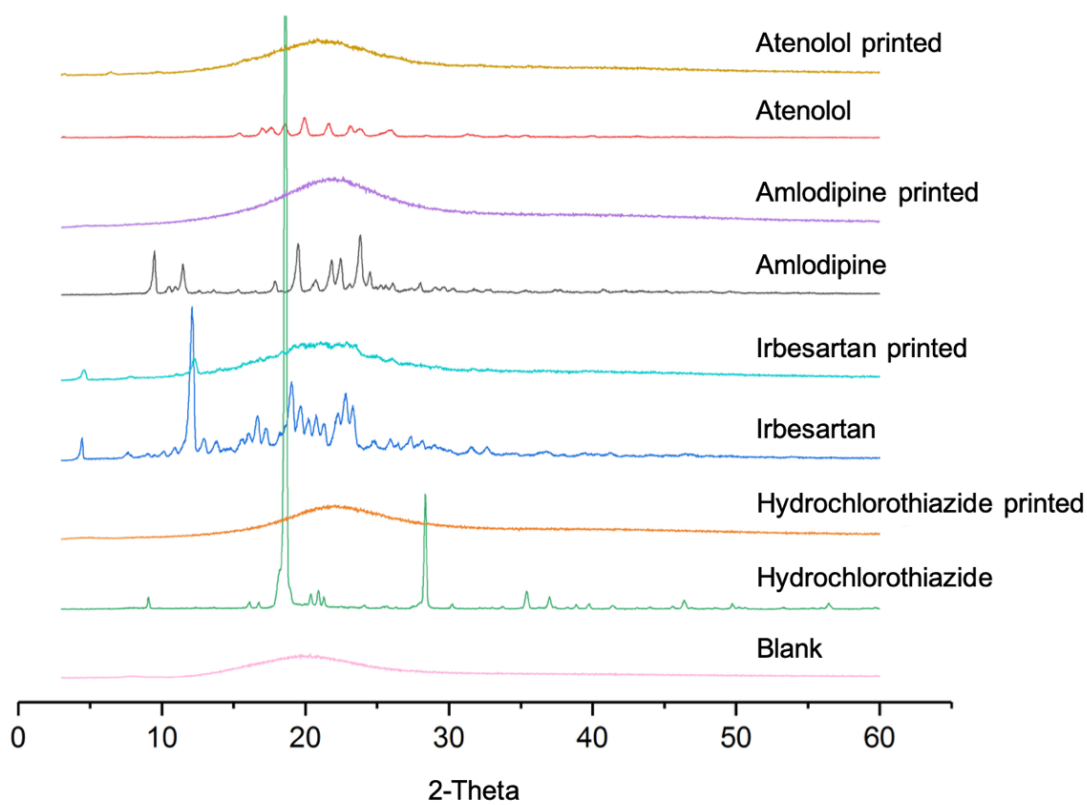
Figure 4.8 X-ray powder diffractograms of model drugs and SLA 3D printed formulations.

DSC analysis of drugs and the 3D printed formulations were performed in order to determine the physical state of drugs in the resin formulations before and after printing. The blank was a printed formulation consists of TPO, PEG 300 and PEGDA and it was used as a reference to distinguish the signals happened between 0 – 300 °C in the DSC data. TPO has a melting point at around 90 °C and the crosslinked PEGDA has a glass transition temperature at -40 °C (He and Kyu, 2016; Li et al., 2018; Saimani and Kumar, 2008). No evidence of melting of TPO was observed in the printed blank or any drug-loaded formulations indicated that the small amount (1% w/w) of photoinitiator has been completely dissolved before 3D printing. DSC results showed melting peaks at 154 °C, 140 °C and 273 °C for pure atenolol, amlodipine, and

hydrochlorothiazide respectively (**Figure 4.9**). The exothermic peak at 317 °C was corresponded to thermal degradation of hydrochlorothiazide (Gioumouxouzis et al., 2017). No evidence of melting was observed in the atenolol, amlodipine and hydrochlorothiazide 3D printed formulations which indicated that the drugs were completely dissolved in the resin formulations before printing which was further corroborated by the XRPD findings. The DSC of pure irbesartan showed a sharp endothermic peak at around 187 °C which corresponded to the melting point of irbesartan, followed by an exotherm at 243 °C due to thermal decomposition (Darwish et al., 2021). A small exothermic peak was also observed in the irbesartan printed formulation which suggests that the irbesartan powder was not completely dissolved in the resin formulations.
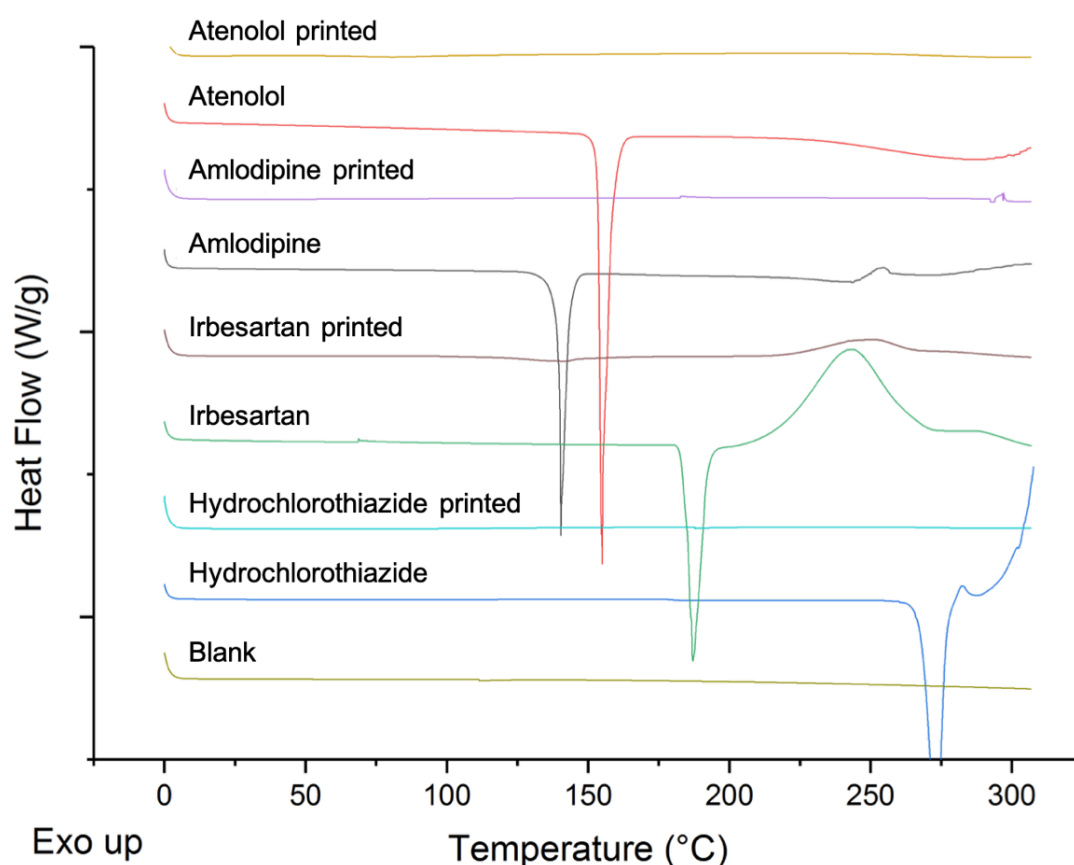
Figure 4.9 DSC thermograms of model drugs and SLA 3D printed formulations.

Drug loading of irbesartan, atenolol and hydrochlorothiazide in the 3D printed layers were slightly lower than that in the resin formulations which may be due to incomplete drug extraction from the crosslinked network (**Table 4.3**). Noticeably, amlodipine was not detected in either the resin formulation or the printed layer which suggests a possible reaction between amlodipine and PEGDA during the mixing process.

Table 4.3 Drug loading in resin formulations and SLA 3D printed individual layers.

Drug	Theoretical drug loading (% w/w)	Drug loading in resin formulations (% w/w)	Drug loading in SLA 3D printed layers (% w/w)
Irbesartan	20.85	20.9 ± 0.1	18.7 ± 0.8
Atenolol	13.90	13.9 ± 1.6	12.7 ± 0.4
Hydrochlorothiazide	6.95	7.1 ± 0.2	6.1 ± 0.0
Amlodipine	1.39	-	-

ATR-FTIR was firstly employed to investigate the potential cause of drug and photopolymer reaction. Different masses of amlodipine were mixed with PEGDA until the drug was fully dissolved accompanied with continuous magnetic stirring. Results from FTIR showed that the typical peak of amlodipine at 3390 cm^{-1} (N-H bond stretching) was not observed in any of the spectra of amlodipine-PEGDA physical mixtures regardless of the concentration which could indicate a possible effect on the N-H bonds of amlodipine (**Figure 4.10**).
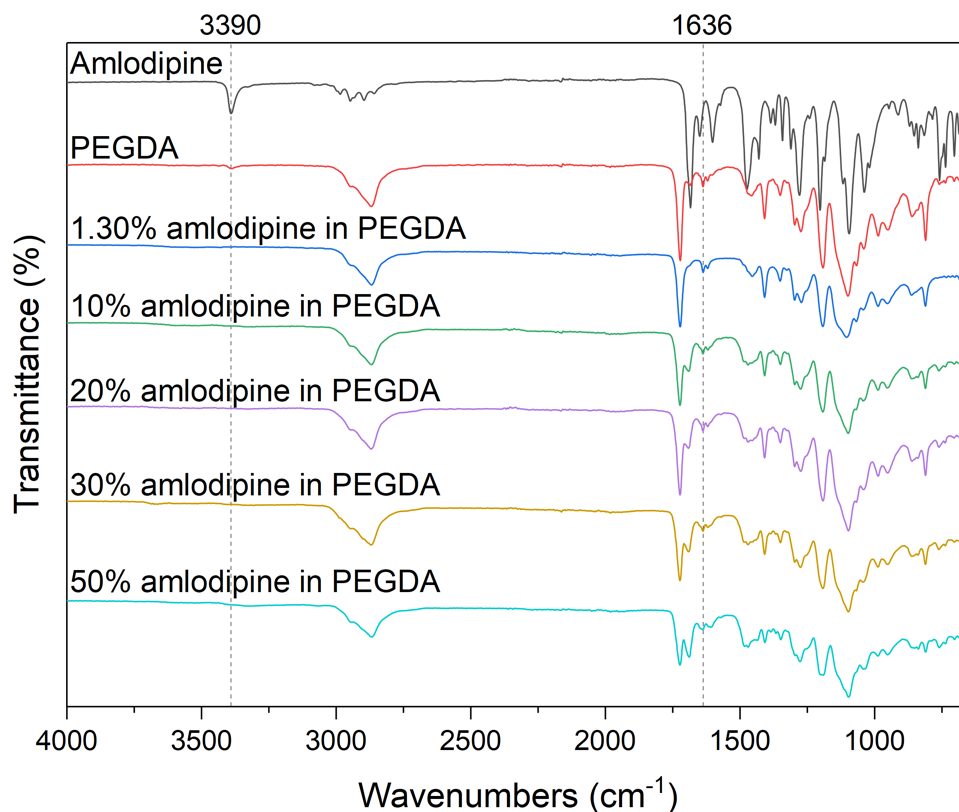
Figure 4.10 FTIR spectra of amlodipine, PEGDA and physical mixtures of amlodipine-PEGDA.

Different from amlodipine, the other model drugs such as hydrochlorothiazide clearly demonstrated its typical bands at 3359 to 3162 cm^{-1} corresponding to N-H stretching in the FTIR spectrum of hydrochlorothiazide-PEGDA physical mixture (**Figure 4.11**) (Chikukwa et al., 2020; Pires et al., 2011). The spectrum also revealed characteristics peaks at 1604 and 1519 cm^{-1} representing C=C stretching, along with S=O asymmetric (1315 cm^{-1}) and symmetric (1148 and 1057 cm^{-1}) stretching, and 771 cm^{-1} corresponding to C-Cl stretching (El-Gizawy et al., 2015).
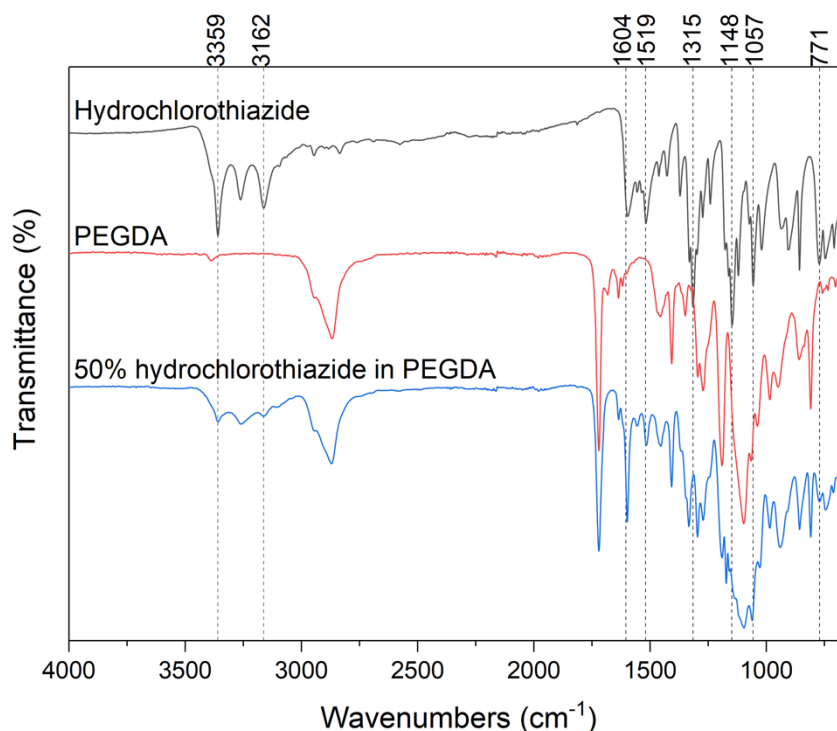
Figure 4.11 FTIR spectra of hydrochlorothiazide, PEGDA and physical mixtures of hydrochlorothiazide-PEGDA.

NMR spectroscopy was performed to confirm the reaction between amlodipine and PEGDA. As the polyprintlets were designed to deliver a low-dose combination therapy, the photocrosslinkable monomer PEGDA was used in a large excess when compared with amlodipine (1.39% w/w). The use of this formulation for NMR study, however, did not allow the observation of drug peaks. As such, the characteristic peaks of the combination of amlodipine to PEGDA were not detected due to the predominant signals of the distinct PEGDA peaks. Consequently, the molar ratio of amlodipine to PEGDA was increased to 2:1 for the ease in amlodipine peak detection and the covalent bond between amlodipine and PEGDA respectively. **Figure 4.12** shows the ^{1}H NMR spectra of amlodipine, PEGDA and amlodipine-PEGDA physical mixture and **Figure 4.13** shows the ^{13}C NMR spectra of amlodipine-PEGDA physical mixture. 2D NMR experiments, Heteronuclear Single Quantum Correlation (HSQC) (**Figure 4.14a**) and Heteronuclear Multiple-Bond Correlation (HMBC) (**Figure 4.14b**) facilitated the full assignment of the ^{1}H and ^{13}C NMR spectrum (**Figure 4.12** and **Figure 4.13** respectively). Each characteristic peak of

PEGDA and amlodipine was detected in both 1D spectrum. However, an additional set of signals at 4.16, 3.62, 2.84 and 2.51 ppm (peaks labelled in green) was detected in the ^{1}H NMR spectrum which were assigned to the methylene groups of PEGDA after interacting with amlodipine. Additionally, the intensity of the signals of the diacrylate group at 6.34, 6.20 and 5.91 ppm were much lower than expected from a molar ratio of amlodipine to PEGDA of 2:1.
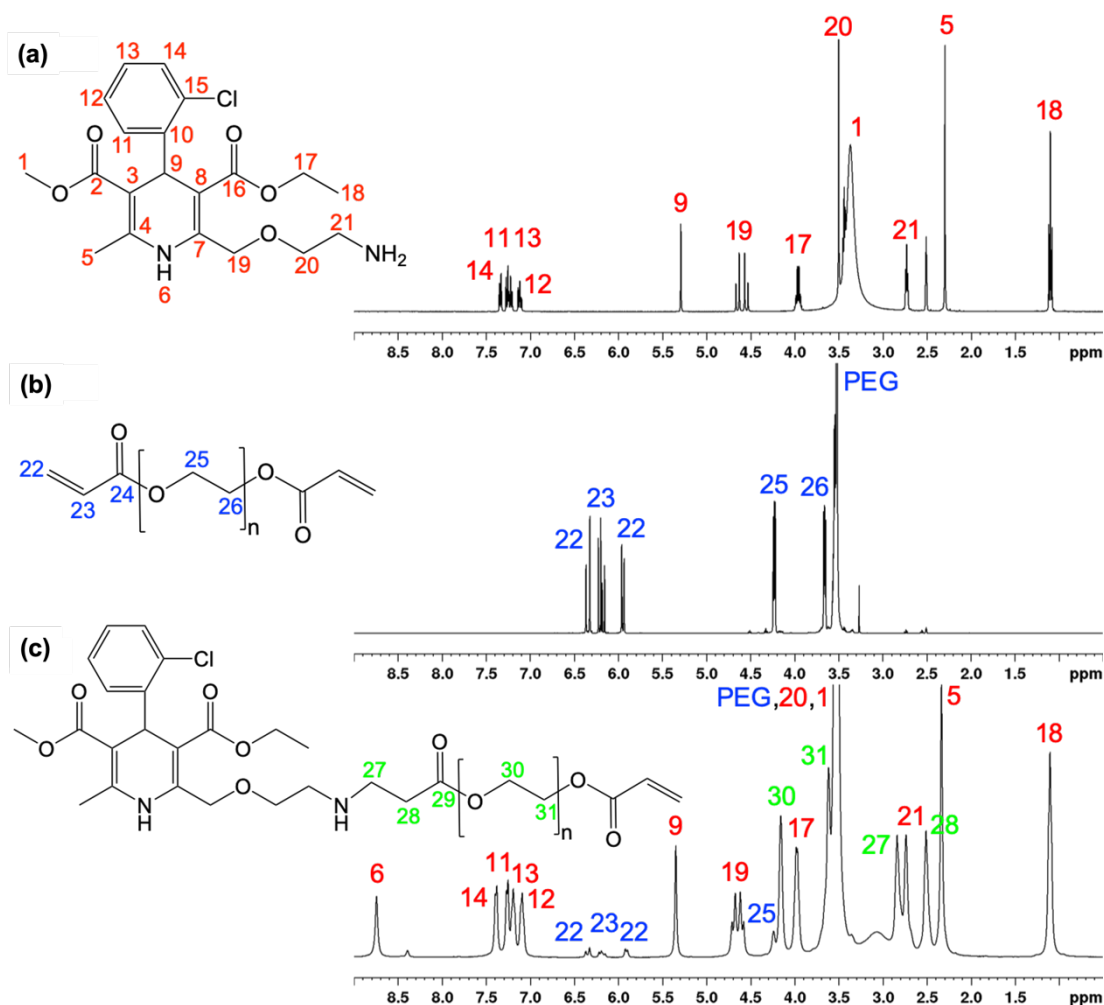
Figure 4.12 ^{1}H NMR spectra (DMSO-d6) of (a) amlodipine, (b) PEGDA, and (c) amlodipine-PEGDA physical mixture.

When compared with the spectra of amlodipine and PEGDA, the integral peak areas for the -NH- group of amlodipine and CH$_2$=CH- of PEGDA were found to be only 0.83 and 0.10 in the amlodipine-PEGDA physical mixture. In other words, an integrated ratio of peak area of amlodipine to PEGDA of 2:0.24 was

calculated, thus indicating a loss of approximately 80% of PEGDA due to its reaction with amlodipine. It is proposed that the primary amine of amlodipine and the diacrylate of PEGDA could undergo a Michael addition in mild conditions without the use of catalysts or solvents (Read et al., 2010). The proton at the position 27 has only three carbon correlations in the HMBC spectrum (**Figure 4.14b**) indicating the formation of a secondary amine via the single functionalisation of the primary amine with PEGDA. Akyol *et al*. described the synthesis of novel poly(beta amino ester) macromonomers through Michael addition of various diacrylates including PEGDA and a phosphonate that contains primary amine, as well as propyl amine (Akyol et al., 2018). In their 1H-NMR spectra, a change of peaks was observed due to methylene groups attaching to a carbonyl group, nitrogen, and oxygen. In addition, in an article where an example was given for a diacrylate and an amine, the NMR results illustrated the disappearance of the amine protons as well as the weak intensity of the acrylate peaks after they were interacting with each other (Anderson et al., 2006).
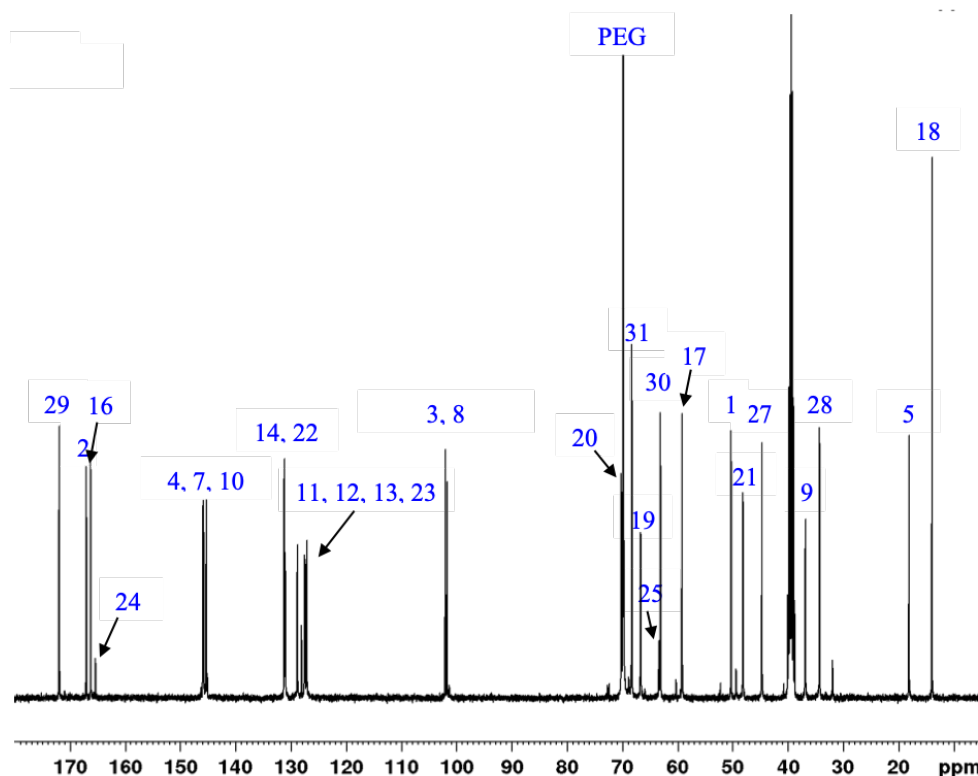
Figure 4.13 ^{13}C NMR spectrum (DMSO-d6) of amlodipine-PEGDA physical mixture.
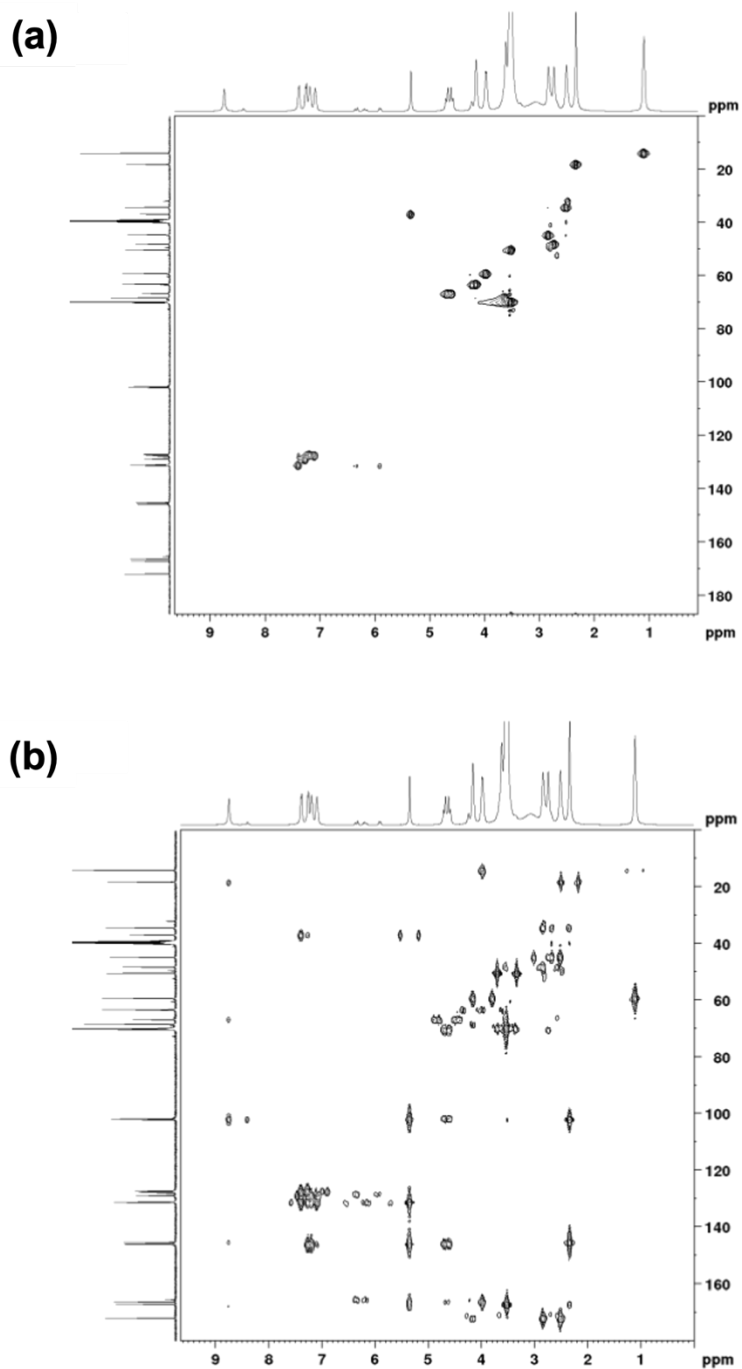
Figure 4.14 HSQC (a) and HMBC (b) of amlodipine-PEGDA physical mixture in (DMSO-d6).

4.6.3 *In vitro* drug release

The SLA 3D printed polyprintlets were tested in the dynamic *in vitro* dissolution model that mimics the physiological conditions of the gastrointestinal tract. The drug release of atenolol, hydrochlorothiazide and irbesartan from both formulations commenced in the gastric phase and continued in the intestinal phase over a period of 24 h (**Figure 4.15**). The polyprintlets were designed and formulated to evaluate the effect of geometry on the dissolution profiles. Over 75% of atenolol was released in the first 120 min in Type 1 polyprintlets while 55% drug release was achieved in the Type 2 polyprintlets at the same time. This coincided with the fact that atenolol was located on the outer layer in the Type 1 polyprintlets (atenolol SA/V = 1.8; irbesartan SA/V = 1.3; hydrochlorothiazide and amlodipine SA/V = 1.0) where SA/V ratio was higher than where it was in the Type 2 polyprintlets (atenolol SA/V=1.0; irbesartan SA/V = 1.0; hydrochlorothiazide and amlodipine SA/V = 1.8) (Goyanes et al., 2015b). For hydrochlorothiazide and irbesartan, minimal changes in drug release were observed on the different surface to volume ratio of Types 1 and 2 polyprintlet. On the other hand, it was observed that atenolol was the only formulation to reach 100% drug release in both polyprintlets while 48% and 17% of hydrochlorothiazide and irbesartan were released in total after 24 h. This could be attributed to their poor aqueous solubilities (0.70 mg/mL for hydrochlorothiazide and 0.00884 mg/mL for irbesartan) and the non-sink release environment for irbesartan (Khan et al., 2015; Patel et al., 2011). Otherwise, strong affinity of the drug to the polymetric matrix could also affect drug dissolution rates. No release of amlodipine was detected in any type of polyprintlet which confirm the complete degradation of the drug via its reaction with PEGDA.
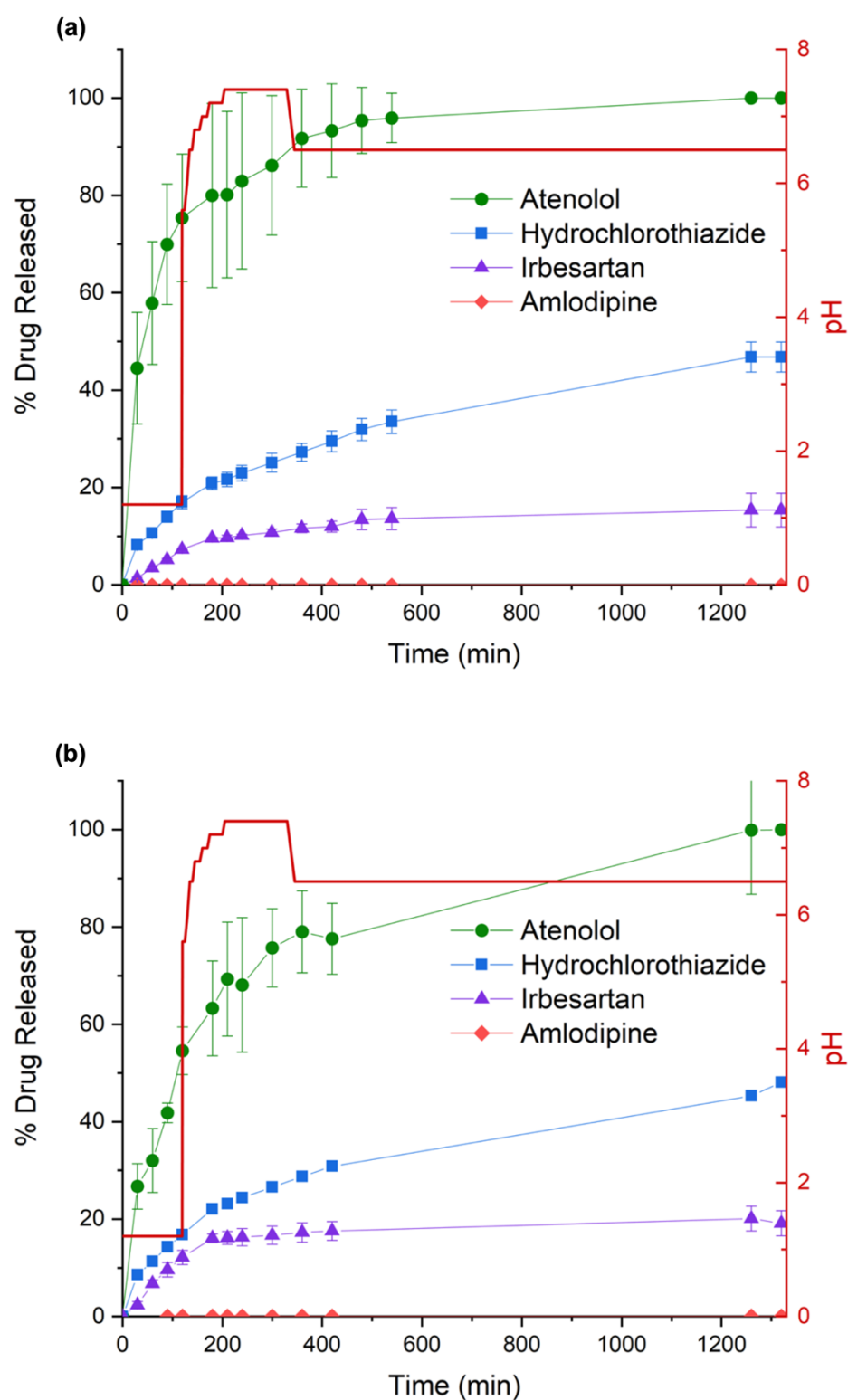
Figure 4.15 Drug dissolution profiles from SLA 3D printed (a) Type 1 and (b) Type 2 polyprintlets. Red line shows the pH values of the dissolution media. Data values represent mean ± SD (n=3).

The in vitro dissolution test data were subjected to various kinetic models to better understanding the release kinetics. Since the release environment for irbesartan was not under sink conditions, it did not follow one of the assumptions to use the Higuchi model (Bruschi, 2015). As shown in **Table 4.4**, release of atenolol, hydrochlorothiazide, and irbesartan from both Type 1 and Type 2 polyprintlets were found best fitted with the Korsmeyer-Peppas model with highest R^2 values and n values between 0.45 and 0.89 (for cylinders), suggesting the model was anomalous transport and the mechanism of drug release was governed by diffusion and swelling (Bruschi, 2015; Siepmann and Peppas, 2012). By comparing the release constant k, atenolol had an obvious faster release rate in Type 1 polyprintlet than in Type 2 whereas irbesartan, although with incomplete release, exhibited faster release rate in Type 2 polyprintlet than in Type 1. No distinct difference was observed from the release rate of hydrochlorothiazide.

Crucially, undesirable reactions between the photoreactive monomer and the API should be avoided when using the SLA 3D printing approach in drug delivery, otherwise the active drug molecule could undergo possible degradation or iteration which can consequently deplete therapeutic effects. Previously, studies involving SLA 3D printing of oral dosage forms have demonstrated at least more than 90% of drug contents in the printed tablets suggesting the absence of drug-photopolymer reactions (Robles-Martinez et al., 2019; Wang et al., 2016). A recent article that utilised the DLP 3D printing technology to fabricate oral tablets also employed FTIR to assess possible drug-polymer reactions. No detectable chemical reactions, however, were found in the oral formulations (Kadry et al., 2019). This could be due to the study design of proof of concept studies; researchers tend to select common drugs such as paracetamol, 4-aminosalicylic acid (Wang et al., 2016), theophylline (Kadry et al., 2019), and ibuprofen (Madzarevic et al., 2019; Martinez et al., 2017) to demonstrate the feasibility of using vat photopolymerisation 3D printing for printing drug-loaded oral dosage forms.

Table 4.4 Release kinetic data of the SLA 3D printed Type 1 and Type 2 polyprintlets.

Release kinetics model	Parameters	Type 1 polyprintlet		
		Atenolol	Hydrochlorothiazide	Irbesartan
Zero-order	R^2	0.750	0.828	0.617
	k_0 (min^{-1})	0.397	0.034	0.012
First-order	R^2	0.938	0.937	0.638
	k_1 (min^{-1})	0.007	0.0005	0.0001
Higuchi	R^2	0.958	0.992	-
	k_H (min$^{-0.5}$)	6.179	1.347	-
Korsmeyer-Peppas	R^2	0.997	0.993	0.861
	k (min^{-n})	11.041	1.619	0.270
	n	0.408	0.481	0.632
Release kinetics model	Parameters	Type 2 polyprintlet		
		Atenolol	Hydrochlorothiazide	Irbesartan
Zero-order	R^2	0.814	0.833	0.427
	k_0 (h^{-1})	0.167	0.029	0.013
First-order	R^2	0.929	0.939	0.444
	k_1 (h^{-1})	0.003	0.0005	0.0001
Higuchi	R^2	0.964	0.982	-
	k_H (h$^{-0.5}$)	4.043	1.278	-
Korsmeyer-Peppas	R^2	0.969	0.988	0.713
	k (h^{-n})	4.571	1.882	1.049
	n	0.502	0.458	0.460

In this chapter, however, reported the reaction between drug and polymer could be possibly due to a Michael addition reaction under a solvent-free and catalyst-free conditions. This therefore may represent a limitation for the advancement of the vat photopolymerisation 3D printing in the development of drug delivery devices when the drug is directly mixed with photoreactive

monomers. Michael addition is a versatile polymer synthesis reaction that allows the biocompatible preparation of polymers including poly(amido amines), poly(amino esters) and poly(ester sulfides) with different chain lengths (Read et al., 2010). Beyond primary amines, nucleophiles such as secondary amines, thiols and phosphines could perform as Michael donors to undergo Michael addition with numerous Michael acceptors including ester acrylates and acrylamides, for example (Mather et al., 2006).

Active compounds which could serve as a Michael donor can react with a Michael acceptor (in this case the PEGDA or other monomers with diacrylate groups) even during the physical mixing procedure. To resolve this issue, other biocompatible photocrosslinkable monomers without acrylate groups should be considered to replace PEGDA. Alternative novel biomaterials have recently been developed for photopolymerisation-based 3D printing like alkyne carbonate based monomers which showed considerably lower cytotoxicity and higher conversion rates when compared with methacrylates (Oesterreicher et al., 2016). Moreover, mixtures of poly(propylene fumarate) (PPF)/diethyl fumarate (DEF) (Lu et al., 2015) and vegetable oil-derived epoxy monomers (Branciforti et al., 2019) have also been exploited as photopolymerisable materials for SLA 3D printing.

Apart from the drug-photopolymer interaction challenge presented in this chapter, challenge in multi-material printing was also worth mentioning. As discussed in Chapter 2, commercial SLA 3D printers do not support the use of third-party photopolymer resins. Peeling effect and delamination was observed due to insufficient exposure between different drug layers within the polyprintlet. This could be due to the pausing during printing and the cleaning in between the drug layers to avoid cross contamination. To solve this issue, a thin binding layer could be added to enhance the adhesion between the drug layers.

4.7   Conclusion

In this chapter, multi-layer antihypertensive polyprintlets that could potentially deliver a low-dose combination therapy were fabricated utilising a novel SLA 3D printing approach. Although successful in its fabrication, interaction between the photocrosslinkable monomers (PEGDA) and one of the model drugs (amlodipine) was observed and investigated using FTIR and NMR spectroscopy. The results suggested the primary amine of amlodipine and the diacrylate of PEGDA could undergo a Michael addition reaction during the mixing process. *In vitro* drug release study showed the effect of surface area to volume ratio on release rate of atenolol only, possibly due to the low aqueous solubility of the other drugs.

The findings from this chapter have not only demonstrated the suitability of SLA 3D printing in preparation of low-dose antihypertensive polyprintlets, but also highlighted the need to screen for photoreactive monomers to ensure the compatibility of drug-loaded oral dosage forms. This work presents the vast opportunities and consequently the challenges that need to be addressed towards the advancement of novel and versatile photocurable biomaterials in vat photopolymerisation 3D printing for drug delivery.

Chapter 5

Smartphone-enabled DLP 3D printing of medicines

5   Smartphone-enabled DLP 3D printing of medicines

5.1   Overview

Vat photopolymerisation 3D printing is empowering the small-scale development of personalised medicines that are tailored to the individual needs of patients within healthcare. However, the current research is focused on employing conventional 3D printers that are designed to operate with large volumes of resins, which could be inconvenient for healthcare professionals in specialised clinical settings. There is a need for integrating novel digital solutions that allow for rapid, safe, and remote medical interventions directly at the point-of-care. In this chapter, a portable smartphone-activated 3D printer, operated with a custom mobile app is proposed to prepare personalised medicines. The printer uses the light from the smartphone's screen to photopolymerise liquid resins and create solid structures. Personalised Printlets (3D printed tablets) in various geometries and patient-specific drug delivery devices were successfully printed using different photosensitive resins. The phone printed drug-loaded formulations were subsequently subjected to physical characterisation tests (XRPD, DSC, FTIR) and *in vitro* studies (dissolution studies and diffusion studies) in biorelevant media.

5.2   Introduction

In recent years, the pharmaceutical and healthcare industries have been embracing the rapidly evolving technologies of Industry 4.0, such as 3D printing, artificial intelligence (AI) (Hirschberg et al., 2020), machine learning (Muniz Castro et al., 2021), finite element analysis (Karavasili et al., 2020b), robotics (Awad et al., 2021b), and mobile applications (Arden et al., 2021). The combination of these digital approaches offers a potential future of smart healthcare.

Nowadays, smartphones have become essential for daily life activities with their ability to provide access to the internet. Therefore, the smartphone platform has emerged as a promising and cost-effective alternative for

providing affordable and accessible healthcare. Although smartphone-based point-of-care applications are increasingly reported, most of them utilise the smartphone's camera for diagnostic and monitoring purposes, or for data collection and analysis through smartphone apps (Kühnemund et al., 2017; Laksanasopin et al., 2015; Mannino et al., 2018). A method for directly fabricating pharmaceuticals using one's own mobile phone could be advantageous for printing medications at home, on the move or even in resource-limited areas. On the other hand, smartphones are equipped with high resolution cameras that are capable to be used for scanning and creating 3D models directly. This could be particularly useful for acquiring 3D models of a patient's unique anatomical features (face, hands, and feet) and generate patient-specific medical devices for drug delivery purposes.

In recent years, vat photopolymerisation 3D printers based on mobile devices, such as smartphones and tablets, have emerged (e.g., ONO, T3D, LumiBee, Lumifold TB) (Kickstarter, 2021a, b; Lumi Industries, 2021a, b). Like LCD 3D printers, the light from the device's screen is utilised to harden photosensitive resins. In the pharmaceutical field, mobile-based systems may provide a clear benefit to patients who live remotely, improving their accessibility to healthcare by allowing them to obtain their medications directly. Moreover, the interconnectivity of such devices could allow healthcare professionals to monitor the whole preparation process remotely, ensuring patient safety. Recently, Li and co-workers reported a smartphone-enabled DLP 3D printer (**Figure 5.1**) (Li et al., 2021). This system is controlled directly by the smartphone and is based on a smartphone-powered pocket projector, which is used as the light source and pattern-generator.
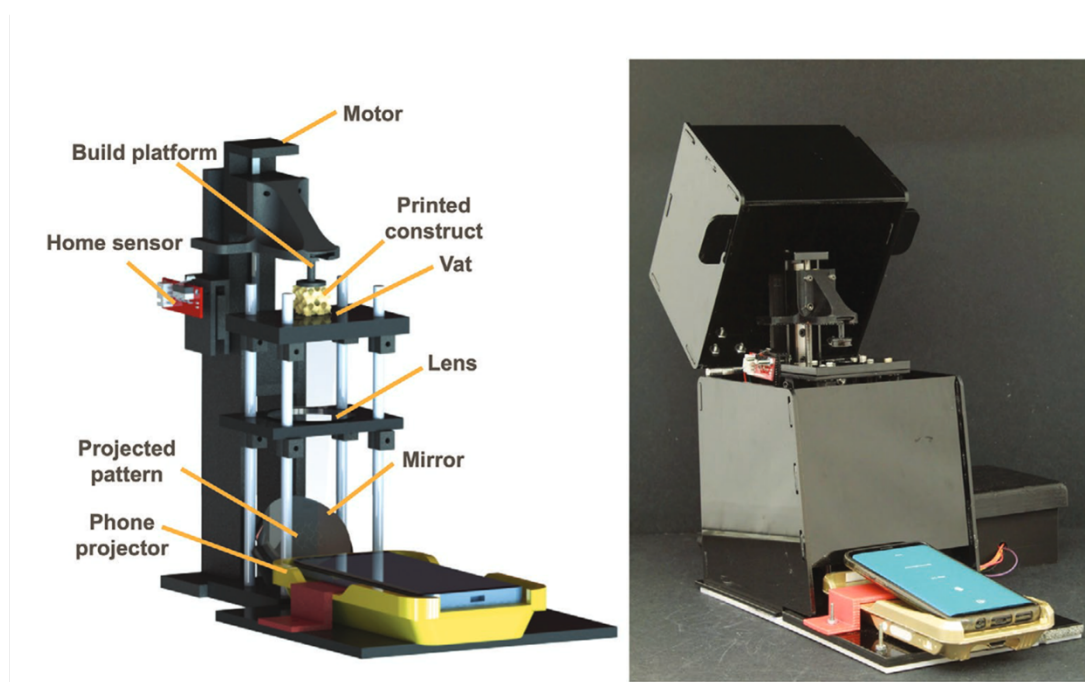
Figure 5.1 Schematic and photograph of a smartphone-enabled DLP printer (Li et al., 2021).

In this chapter, a smartphone-enabled DLP 3D printer was proposed where the smartphone itself was directly used as the light source to generate curing patterns as well as controlling the printer via a custom-written mobile app. The printer is portable and easy to operate, and the design of the custom printing app is simple, making it suitable for use, even in the absence of professional knowledge on 3D printer operation or 3D model design.

5.2.1 Model drugs and photopolymer

Warfarin sodium (**Figure 5.2a**) is a widely prescribed oral anticoagulant for the treatment and prevention of thromboembolic disorders. Due to its narrow therapeutic index and large variability in interpatient response, the safe use of warfarin sodium is challenging (Kimmel, 2008; Reynolds et al., 2007). In particular, because it is commercially available in limited doses (0.5, 1, 3, 4, and 5 mg) (BNF, 2021), acquiring specific doses entails the intake of a combination of dose strengths or splitting large-dose tablets. However, this increases the risk of medication non-adherence and errors, leading to

unwanted adverse events and subsequent hospitalisations (Vuddanda et al., 2018). Therefore, the use of warfarin sodium could be safeguarded by defining individualised dosing for the patient (Niese et al., 2019). As such, it is chosen as the model compound in this chapter, and the smartphone-enabled DLP 3D printer could potentially be used where on-demand oral dosage forms need to be tailored with flexible warfarin dosing, matching the individual needs and disease state of each patient.
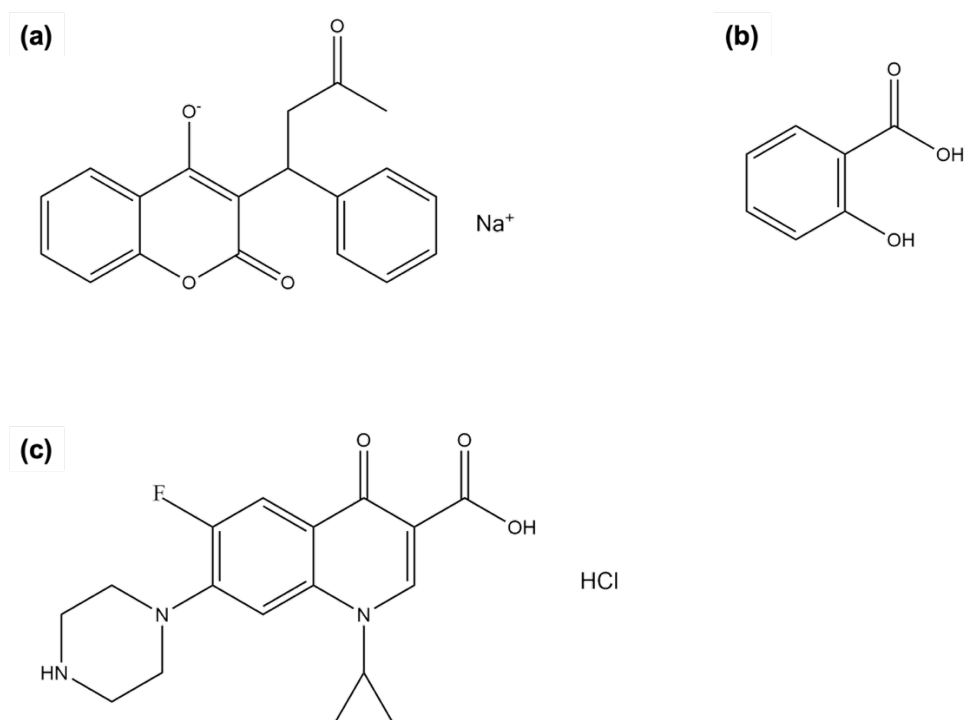
Figure 5.2 Chemical structures of (a) warfarin sodium, (b) salicylic acid, and (c) ciprofloxacin hydrochloride.

Salicylic acid (**Figure 5.2b**) is a commonly used peeling agent in the treatment of acne (Arif, 2015; Lu et al., 2019). It works by softening the stratum corneum and rapidly dissolving desmosomes, causing cells to shed and leading to exfoliation. In this chapter, it was selected as a model compound for the preparation of patient-specific anti-acne nose patch (Goyanes et al., 2016).

Ciprofloxacin hydrochloride (**Figure 5.2c**) belongs to a group of antibiotics called fluoroquinolones and it is commonly used to treat bacterial infections. In the case of ear infections such as chronic otitis media, ciprofloxacin ear drops

are commonly used as the treatment (Lorente et al., 2014). In this chapter, it was chosen as a model drug for preparing patient-specific hearing aids. Previously, Vivero-Lopez et al. has shown 3D printed hearing aids with antibiotics, ciprofloxacin hydrochloride and fluocinolone acetonide, demonstrated anti-biofilm activities against *Pseudomonas aeruginosa* and *Staphylococcus aureus* (Vivero-Lopez et al., 2021b).

5.3 Aim

In this chapter, a smartphone-enabled DLP 3D printer was investigated to prepare medicines including personalised Printlets and two patient-specific drug delivery devices, nose patches and hearing aids. The development of this portable and compact platform using one's mobile phone could be particularly advantageous, allowing printing medications at home, on the move or even in resource-limiting areas.

The aims of Chapter 5 include:

- To screen different visible-light photoinitiator systems and select the optimal one for the fabrication of personalised Printlets.
- To develop warfarin sodium Printlets in various geometries.
- To use the smartphone to directly scan and obtain the 3D models of the volunteer.
- To design and develop patient-specific drug delivery devices using the smartphone-enabled DLP 3D printer.
- To assess the physical characteristics of different phone printed drug-loaded formulations.
- To evaluate the *in vitro* drug release profiles of different Printlets in biorelevant media.
- To perform diffusion study to estimate the diffusion rates of drugs from the phone printed devices using Franz cells.

5.4 Materials

Poly(ethylene glycol) diacrylate (PEGDA, average Mn 575 g/mol), Eosin Y disodium salt (EOS, MW 691.85 g/mol), triethanolamine (TEA, MW 149.19 g/mol, ≥ 99.0% (GC),) Tris(2,2′-bipyridyl)dichlororuthenium(II) hexahydrate (Ru), sodium Persulfate (SP), trifluoroacetic acid (TFA, MW 114.02 g/mol, ≥ 99.0 %), acetonitrile (ACN, ≥ 99.9 %, HPLC grade), and Dulbecco's phosphate buffered saline were purchased from Sigma-Aldrich (Dorset, UK). Riboflavin (RBF, MW 376.37 g/mol, > 98.0%) was obtained from Bio Basic (Toronto, Canada). Warfarin sodium (MW 330.31 g/mol, ⩾ 98.0%, logP 2.90, water solubility 1000 mg/mL (Kasim et al., 2004)) was acquired from LKT Laboratories Inc. (St. Paul MN, USA). Daylight resin (red, hard) was acquired from RS Components Ltd (Northants, UK). Salicylic acid (MW 138.12 g/mol, ⩾ 98.0%, logP 2.26, water solubility 2.24 mg/mL at 25 °C (PubChem, 2023g)) was obtained from VWR International Ltd. (Lutterworth, UK). Ciprofloxacin hydrochloride (MW 367.80 g/mol, logP -0.94 at 37 °C in n-octanol/pH 7.0 buffered solution, water solubility 0.16 mg/mL in pH 7.5 phosphate buffer at 37 °C (Olivera et al., 2011)) was acquired from MP Biomedicals (Solon, USA). Phosphoric acid (MW 97.99 g/mol, for HPLC 85-90%) was supplied from Honeywell (Seelze, Germany). 3DSR ENG Hard resin was purchased from Kudo 3D Inc. (USA). Clear resin and BioMed Clear resin were acquired from Formlabs Inc. (USA). All materials were used as received.

5.5 Methods

5.5.1 Emission spectra of the smartphone screen

For best selection of photoinitiators, the emission spectra of the phones were measured using an Agilent 8453 UV-Vis spectrophotometer (Agilent Technologies, UK) between 200-800 nm. The emission spectrum of a Huawei P10 mobile phone (Android 7.0) was collected while the screen displayed a white picture at maximum brightness. The emission spectra of the smartphones were plotted by inverting the absorbance spectra.

5.5.2 Preparation of drug-loaded resin formulations

An initial screen of different visible-light photoinitiators found in the literature was performed to select the most suitable photoinitiator system. Three formulations were prepared with different compositions of photoinitiator, and co-initiator, as shown in **Table 5.1**.

Table 5.1 Composition (% w/w) of different formulations for initial screening.

Formulation	EOS 1% (w/v) solution (%)	TEA (%)	Ru 1% (w/v) solution (%)	SP 1% (w/v) solution (%)	RBF (%)	PEGDA (%)
RU1	-	-	15	47.6	-	37.4
RBF1	-	3	-	-	0.1	96.9
EOS1	6.92	7.5	-	-	-	85.58

After selection of the formulation with the best printability, 5% (w/w) of warfarin sodium was added as model compound for the preparation of Printlets. For the preparation of patient-specific drug delivery devices, 2% (w/w) of salicylic acid was used as the model compound for the preparation of personalised nose patches (Goyanes et al., 2016) and 2% (w/w) of ciprofloxacin hydrochloride was used for fabricating hearing aids (Vivero-Lopez et al., 2021b). The resin formulations were prepared in amber vials as shown in **Table 5.2** and were magnetically stirred thoroughly at room temperature for at least 12 h.

Table 5.2 Composition (% w/w) of different drug-loaded formulations used to prepare Printlets and drug delivery devices.

Formulation	EOS 1% (w/v) solution (%)	TEA (%)	Warfarin sodium (%)	Salicylic acid (%)	Ciprofloxacin hydrochloride (%)	PEGDA (%)
EOS2	6.92	7.5	5	-	-	80.58
FSA2	6.92	7.5	-	2	-	83.58
FCH2	6.92	7.5	-	-	2	83.58

5.5.3 3D design of Printlets

Printlets (cylindrical) were printed in three sizes: size-8 (8 mm diameter x 2.5 mm height), size-11 (11 mm diameter x 2.5 mm height) and size-16 (16 mm diameter x 2.5 mm height). Dimensions of Printlets in other geometries were designed as caplet (8 mm length x 2.5 mm width x 1.5 mm height), triangle (4 mm radius x 2.5 mm height), diamond (9 mm length x 6.76 mm width x 2.5 mm height), square (8 mm side length x 2.5 mm height), pentagon (4 mm radius x 2.5 mm height), and torus (10 mm outer diameter x 6 mm inner diameter x 2.4 mm height). All were created with 123D Design (Autodesk Inc., USA). The dimension of the gyroid lattice Printlets was the same as previously reported with a scale factor of 1.5 (Fina et al., 2018b).

5.5.4 3D scanning and design of devices

5.5.4.1 Hearing aids

Mould of volunteer's ears were taken using reusable silicone ear plugs, which were then scanned using a smartphone application (*Qlone 3D Scanner,* Version 3.14.0 (Premium), EyeCue Vision Tech Ltd., Israel). The scanned model (raw 3D model) was exported as an stl. file and processed with Meshmixer (Autodesk Inc., USA) for hollowing and with 123D Design (Autodesk Inc., USA) to create 2 holes on the model (**Figure 5.3**).
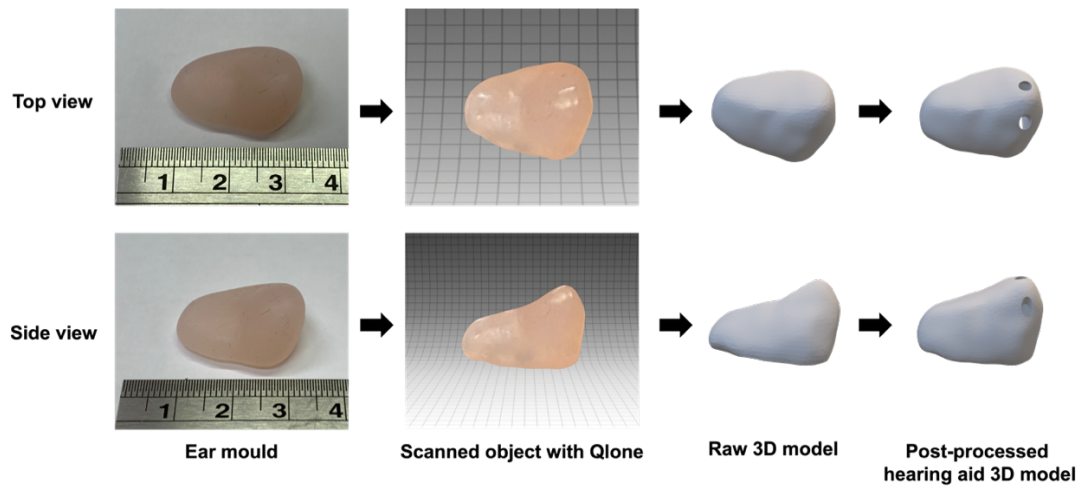
Figure 5.3 Workflow of preparing a patient-specific hearing aid.

5.5.4.2 Nose patch

The face of a volunteer was scanned using a smartphone application (*SCANN3D*, version 3.1.0, SmartMobileVision, Hungary) by taking multiple pictures. The generated raw 3D nose model from the app was then post-processed with Meshmixer (Autodesk Inc., USA) for hollowing and thickening in order to create the personalised nose patch (**Figure 5.4**).
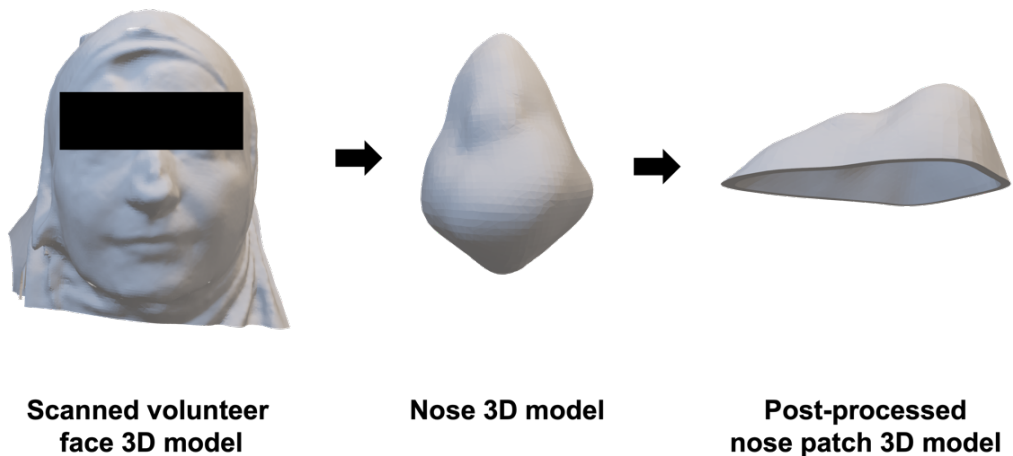
Figure 5.4 Workflow of preparing a personalised nose patch.

5.5.5 3D Printing process

All the post-processed 3D models were exported as stereolithography (.stl) files and loaded into the Chitubox software (China) to slice the 3D models and generate 2D images. The resolution of the projected images was adjusted according to the smartphone specifications including the screen size and display resolution to reflect the original designed dimensions.

The smartphone-based printer (M3DIMAKER LUX, FabRx Ltd., UK) (19.5 cm x 19.5 cm x 15 cm) contains a build platform, a resin tank, and a container underneath the resin tank for the smartphone (**Figure 5.5**). The previously generated 2D images in **Section 5.5.3 and 5.5.4** were selected, copied, and pasted into the specific folder on the smartphone for displaying while printing. Then, the prepared resin was loaded into the resin tank.
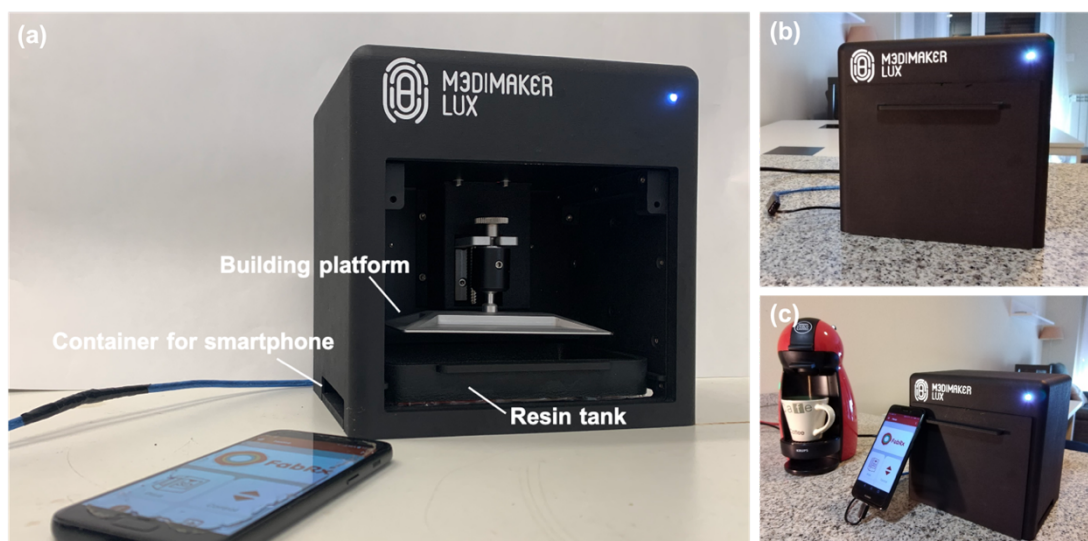
Figure 5.5 Pictures of the (a) smartphone-based 3D printer alongside a smartphone; (b) the printer with the smartphone inside it during the printing process; and (c) comparison of the size of printer with a coffee machine.

A custom printing mobile app was developed to control the printing process of this smartphone-enabled 3D printer. Once connected to a smartphone via a cable, and with the app running, the main menu displays three options, "Print",

"Control", and "Configuration" (**Figure 5.6**). The "Control" page allows control of the build platform movement.
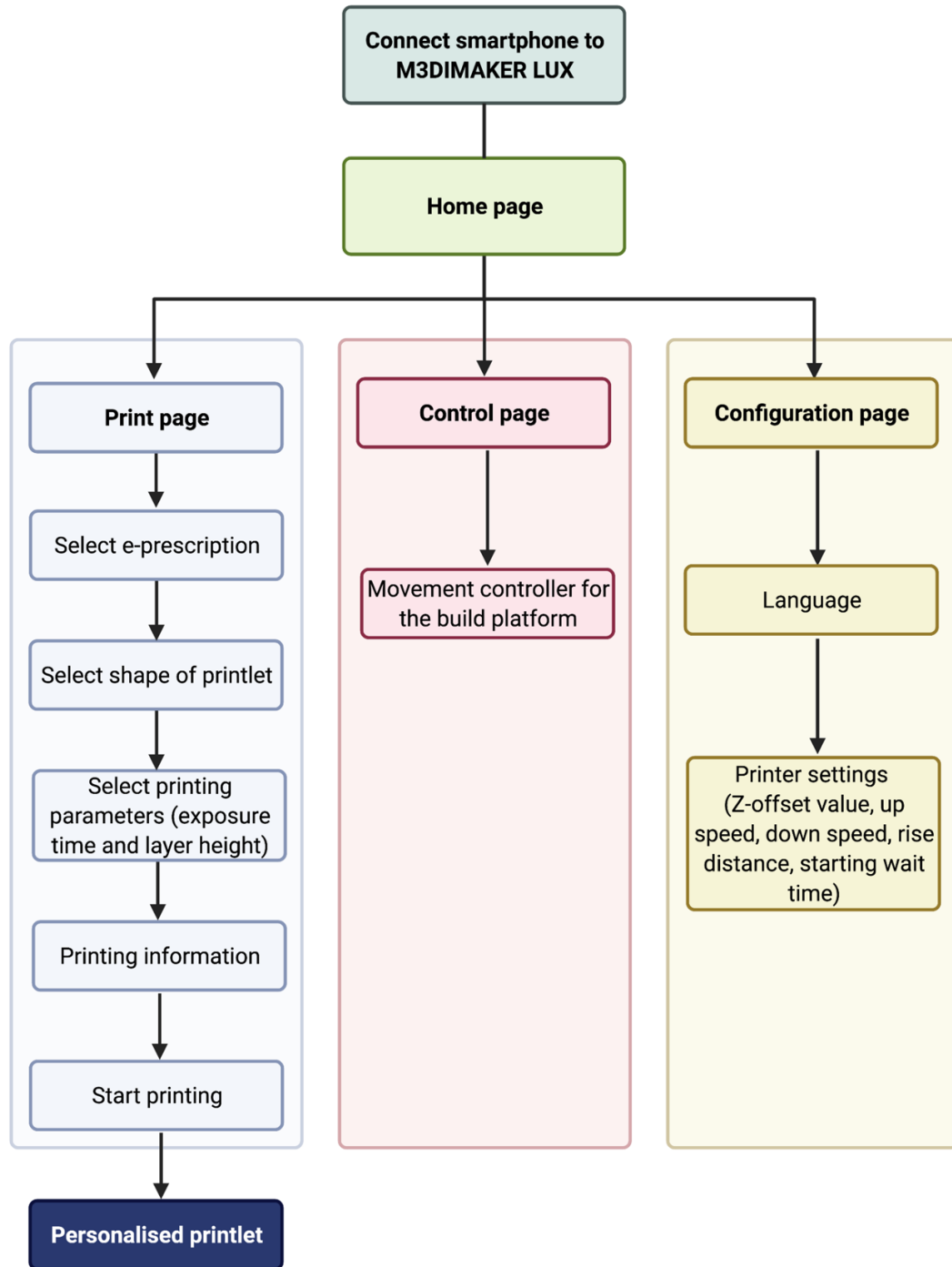
Figure 5.6 Flow chart of a smartphone-enabled DLP 3D printing process using the custom mobile printing app.

By clicking the "Configuration" page (**Figure 5.7a**), different printer settings, including language, z-offset value, up speed, down speed, rise distance, and starting wait time can be specified. The fabrication of Printlets was initiated by selecting the "Print" page (**Figure 5.7b**) where two printing parameters (exposure time (s) and the layer height (mm)) can be modified. In this work, the layer height was selected as 0.05 mm and the exposure time used for different formulations was summarised in **Table 5.3**. After clicking PRINT, a summary of the printing information with all the selected parameters is displayed for double checking; then the START PRINTING command is selected and the smartphone is returned to the container for the printing process.
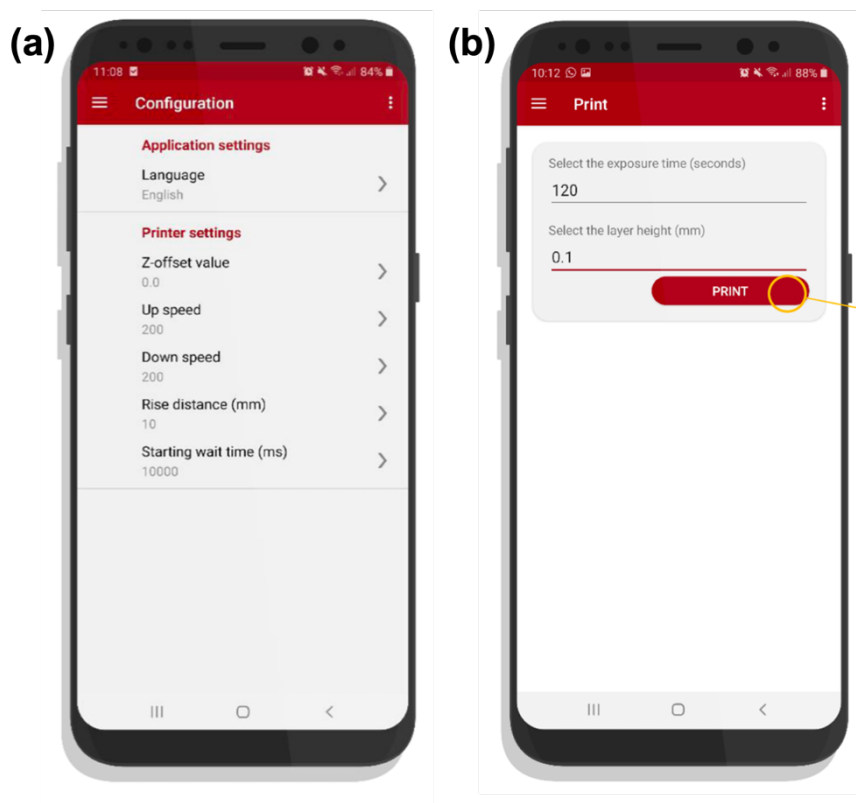
Figure 5.7 Screenshot images of the 'Print' page and 'Configuration' page shown on the custom app.

Table 5.3 Exposure time used for different formulations.

Formulation	Exposure time (s)
EOS1	150
EOS2	150
FSA2	210
FCH2	150
Daylight resin	60

During the printing process, a series of 2D images were directly projected on the smartphone (**Figure 5.8**). After printing, all the Printlets and devices were rinsed with isopropyl alcohol for 1 min to remove any uncured resin on the surface and post cure for 30 min in a Form Cure (Formlabs Inc., USA).

For the comparison of printing resolution, the hearing aid and nose patch 3D models were also printed using commercial SLA and DLP 3D printers. 3DSR ENG Hard Resin was used in the Kudo 3D Titan2 HR DLP 3D printer (Kudo3D Inc., USA) with 5 s per layer (60 s for the first layer) as exposure time and a layer thickness of 0.025 mm. Clear resin and BioMed Clear resin were used in the Form2 SLA 3D printer (Formlabs Inc., USA) with a layer thickness of 0.025 mm.
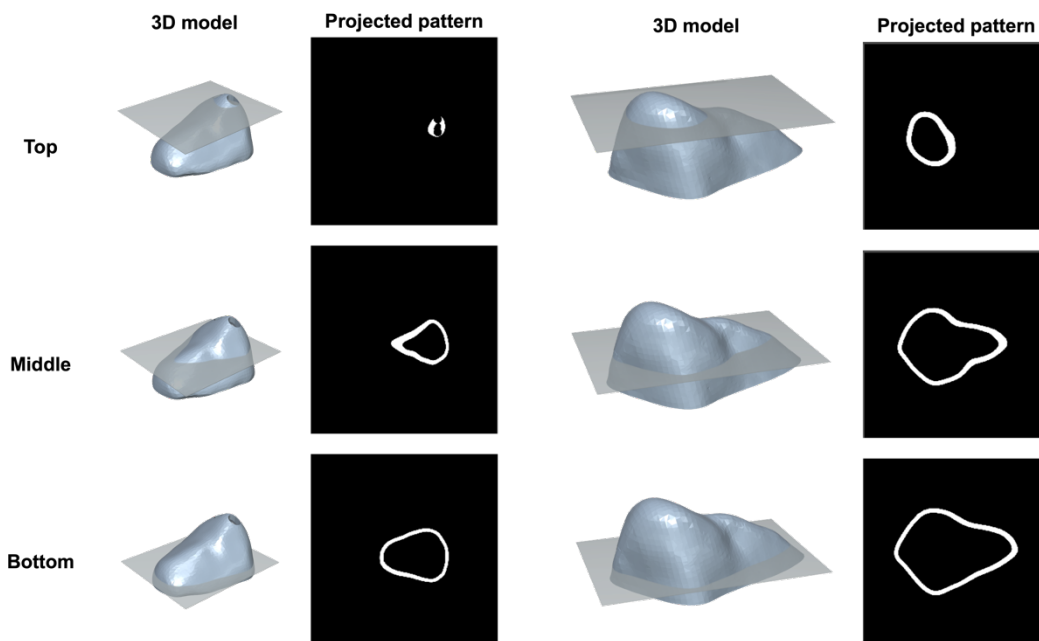
Figure 5.8 Projected patterns from the top, middle, and bottom of the patient-specific hearing aid (left) and nose patch (right) 3D models shown on the smartphone.

5.5.6 UV-visible spectrometry

The visible-light photoinitiators including EOS, Ru, and RBF were prepared at concentrations of 0.001% (w/v) for EOS and Ru and 0.004% (w/v) for RBF, in distilled water respectively. UV-visible spectra were collected on a Cary 100 UV-Vis spectrophotometer (Agilent Technologies, UK) between 200-800 nm at a scan rate of 600 nm/min.

5.5.7 Determination of Printlet and device morphology

Pictures of the Printlets and devices were taken with an iPhone XS (Apple, USA). The dimension of the Printlets (diameter and thickness, n=3) and the devices (length in the X, Y, and Z axes of the device, n=2) were measured using a digital calliper (**Figure 5.9**). The dimensions of the 3D models were generated from 123D Design (Autodesk Inc., USA).

(a)

(b)
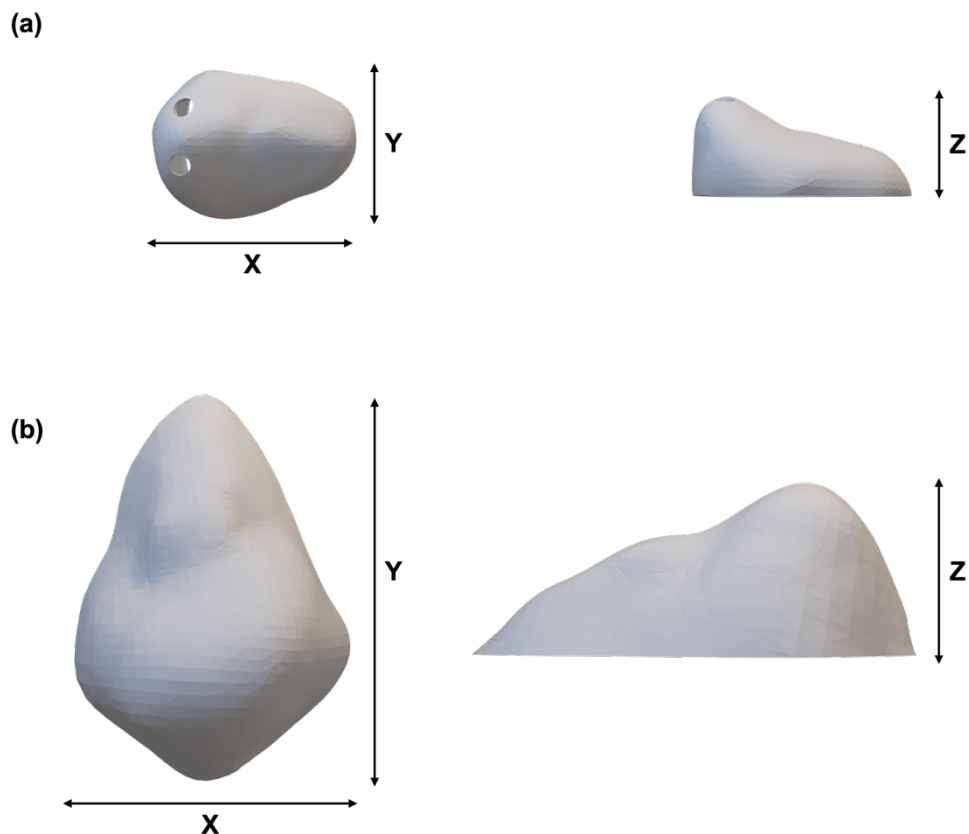
Figure 5.9 Dimension of the (a) hearing aid and (b) nose patch measured in the X, Y, Z axes.

5.5.8 X-ray powder diffraction (XRPD)

The model drugs (warfarin sodium, salicylic acid, and ciprofloxacin hydrochloride) and phone printed drug-loaded discs (23 mm diameter × 1 mm height) were analysed. X-ray powder diffraction patterns were obtained in a Rigaku MiniFlex 600 (Rigaku, USA) using a Cu K α X-ray source (λ =1.5418 Å). The angular range of data acquisition was 3–60° 2 θ with a stepwise size of 0.02° at a speed of 5°/min. The intensity and voltage applied were 15 mA and 40 kV, respectively.

5.5.9 Thermal Analysis

Differential scanning calorimetry (DSC) was used to characterise the model drugs and the phone printed drug-loaded formulations. DSC measurements were performed with a Q2000 DSC (TA instruments, Waters, LLC, USA) at a heating rate of 10 °C/min. Calibrations for cell constant and enthalpy were performed with indium (Tm=156.6 °C, Δ Hf=28.71 J/g) according to the manufacturer instructions. Nitrogen was used as a purge gas with a flow rate of 50 mL/ min for all the experiments. Data were collected with TA Advantage software for Q series (version 2.8.394) and analysed using TA Instruments Universal Analysis 2000. All melting temperatures are reported as extrapolated onset unless otherwise stated. TA aluminium pans and Tzero hermetic lids (pin hole made with a tweezer) were used with an average sample mass of 3 – 5 mg.

5.5.10 Scanning electron microscopy (SEM)

The phone printed samples were cut in small sections, attached to a self-adhesive carbon disc mounted on a 25 mm aluminium stub and coated with 25 nm of gold using a sputter coater. The stub was then placed into a FEI Quanta 200 FEG Scanning Electron Microscope (FEI, UK) at 5 kV accelerating voltage using secondary electron detection to obtain the cross-section images.

5.5.11 Attenuated Total Reflection Fourier-Transform infrared spectroscopy (ATR-FTIR)

Infrared spectra were collected using a Spectrum 100 FTIR spectrometer (PerkinElmer, Waltham, MA). Pure drug powders and PEGDA were measured as the references. Resin formulations and phone printed drug-loaded formulations were scanned over a range of $4000 – 650$ cm^{-1} at a resolution of 4 cm^{-1} for 16 scans.

5.5.12 Determination of drug loading

Printlets were crushed into fine particles using a mortar and a pestle and stirred in 100 mL water to allow extraction of the drug (n=3). The solutions were filtered through a 0.45 µm filter (Merck Millipore Ltd., Ireland) and the concentration of drug was then determined by HPLC (Hewlett Packard 1260 Series HPLC system, Agilent Technologies, Cheadle, UK). An Eclipse plus C18 column, 150 mm × 4.6 mm (Zorbax, Agilent Technologies, Cheshire, UK) was used as the stationary phase.

For the determination of warfarin sodium concentration, the mobile phase consisted of 50 mM acetate buffer (pH 5.5) and ACN which was pumped at a flowrate of 1 mL/ min under the gradient program as follows: 15 % (v/v) ACN increased to 60 %(v/v) in 5 min and decreased to 15 %(v/v) in 1 min and held for 4 min prior to the next injection. The sample injection volume was 10 µL and the total run time was 10 min. Experiments were performed at 30 °C and a wavelength of 300 nm.

For the determination of salicylic acid concentration, the method used was adapted from previous work (Goyanes et al., 2016). The mobile phase consisted of 0.1% TFA in water (30% v/v) and methanol (70% v/v) was pumped at a flow rate of 1 mL/min. The sample injection volume was 20 µL with a column temperature of 25 °C. The eluent was screened at the wavelength of 234 nm. The total run time was 15min and the retention time of salicylic acid was at 2.8 min.

For the determination of ciprofloxacin hydrochloride content, the flowrate was set to 0.8 mL/min and mobile phase consisting of 0.1% phosphoric acid and ACN was pumped under a gradient programme at 40 °C as follows: 20% (v/v) ACN increased to 70% (v/v) in 8 min and decreased to 20% (v/v) in 1 min and held for 6 min prior to the next injection. The injection volume was 20 µL with eluents detected at a wavelength of 275 nm and the retention time of ciprofloxacin hydrochloride was 3.6 min.

5.5.13 Dissolution testing conditions

Dissolution profiles for each type of Printlets were obtained using USP-II apparatus (Model PTWS, Pharmatest, Germany) under sink conditions (n=3). Printlets were first placed in 750 mL of 0.1M HCl for 2 h to simulate gastric residence time and then transferred into 950 mL of physiological bicarbonate buffer (Hanks buffer) (pH 5.6–7) for 35 min followed by 1000 mL of modified Krebs buffer (pH 7–7.4 and then to 6.5). Hanks buffer (0.441 mM KH_2PO_4, 0.337 mM $Na_2HPO_4 \cdot 2H_2O$, 136.9 mM NaCl, 5.37 mM KCl, 0.812 mM $MgSO_4 \cdot 7H_2O$, 1.26 mM $CaCl_2 \cdot 2H_2O$, 4.17 mM $NaHCO_3$) was modified to form an in-situ modified Kreb's buffer by the addition of 50 mL of pre-Krebs solution (6.9 mM KH_2PO_4 and 400.7 mM $NaHCO_3$) to every dissolution vessel (Fadda and Basit, 2005; Goyanes et al., 2015a).

The Printlets were tested in the small intestinal environment for 3.5 h with a pH value of 5.6–7.4, followed by pH 6.5 representing the colonic environment (Fadda and Basit, 2005; Goyanes et al., 2015a). The dissolution medium is primarily a bicarbonate buffer system in which both bicarbonate (HCO_3^-) and carbonic acid (H_2CO_3) exist in an equilibrium together with CO_2 (aq) resulting from the dissociation of the carbonic acid (Goyanes et al., 2015a). The pH of the bicarbonate buffer is modulated and controlled by an Auto pH System™ which incorporates a pH probe connected to a supply of CO_2 (pH reducing gas), as well as to a supply of helium (pH increasing gas) (Merchant et al., 2014). During dissolution testing, the control unit monitors the pH changes and adjusts the pH by feeding CO_2 or helium into the dissolution vessel.

The paddle speed of the USP-II was fixed at 50 rpm and the dissolution medium was maintained at 37 ± 0.5 °C. 1 mL samples of the dissolution medium were withdrawn every half an hour in the first 3 h, followed by every hour. The concentration of the drugs was determined by HPLC (previously described in section 5.5.12). After the dissolution test, the Printlets were retrieved to extract any residual drugs, and this was be taken into consideration in the calculation of percentage of drug released.

To determine the drug release kinetics and mechanism, various mathematical models (zero-order model, first-order model, Higuchi model, and Korsmeyer-Peppas model) were tested to fit the data obtained from *in vitro* release study into the following equations (Bruschi, 2015):

Zero-order model $$Q_t = Q_0 + k_0 \times t$$ (Eq. 5.1)

Where Q_t is the amount of drug released over time t, Q_0 is the initial amount of drug in the solution, and k_0 is the zero-order release constant.

First-order model $$log Q_t = log Q_0 + \frac{k_1 \times t}{2.303}$$ (Eq. 5.2)

Where Q_t is the amount of drug released over time t, Q_0 is the initial amount of drug in the solution, and k_1 is the first-order release constant.

Higuchi model $$Q_t = k_H \times t^{\frac{1}{2}}$$ (Eq. 5.3)

Where Q_t is the amount of drug released over time t and k_H is the Higuchi release constant.

Korsmeyer-Peppas model $$\frac{M_t}{M_\infty} = k \times t^n$$ (Eq. 5.4)

Where M_t/M_∞ is the fraction of drug released over time t, k is the constant of incorporation of structural modifications and geometrical characteristics of the system, and n is the exponent of release.

5.5.14 Diffusion studies

Drug diffusion experiments from phone printed circular-shaped discs (16 mm diameter x 1 mm height) were conducted as previously reported (Goyanes et al., 2016) in vertical glass Franz cells with an effective diffusion area of 98.5 ± 4.8 mm^2 and a receptor volume of 4.6 mL (n = 3). The phone printed discs were mounted between the donor and receptor compartments, separated from the receptor by a cellulose nitrate membrane (pore size 0.45 µm, cat no. 7184-002, Whatman, UK) previously soaked in receptor fluid

for at least 12 h before the test was started. The receptor compartment of the diffusion cell was filled with Dulbecco's phosphate buffered saline. The whole assembly was incubated at 32 ± 0.5 °C in a water bath to mimic the skin temperature and the solution in the receptor compartment was constantly stirred at 400 rpm using a magnetic stirrer. Parafilm was used to cover the donor compound and the sampling port to prevent evaporation. 50 µL samples were withdrawn from each cell at different time intervals and replaced with an equal amount of phosphate buffered saline. The drug concentration was then determined by HPLC (as described in Section 5.5.12). The cumulative percentages of drug permeated per square centimetre from the 3D printed discs were plotted against time.

5.6   Results and discussion

5.6.1   Personalised Printlets

5.6.1.1 3D printing

In the first part of this chapter, a smartphone-enabled DLP 3D printer was tested for the fabrication of personalised medications. Using this system, the light from the smartphone screen is utilised as the illumination source to irradiate the designed patterns and generate physical objects by solidifying the photoreactive materials above the smartphone in the resin tank. The printing process can be easily activated and directly controlled via a built-in custom mobile app including the exposure time and layer resolution. Besides, the use of visible light is considered a safer fabrication process over UV light used in some of the commercial SLA or DLP 3D printers, offering the benefits of reduced risk of eye damage and improved biocompatibility and functional group tolerance (Ahn et al., 2020; Park et al., 2018).

To enable the selection of the most suitable photoinitiator, the spectral power distribution of the smartphone display was measured (**Figure 5.10**). The smartphone showed its emission spectrum within the visible spectrum with spikes showing at the blue, green, and red regions.
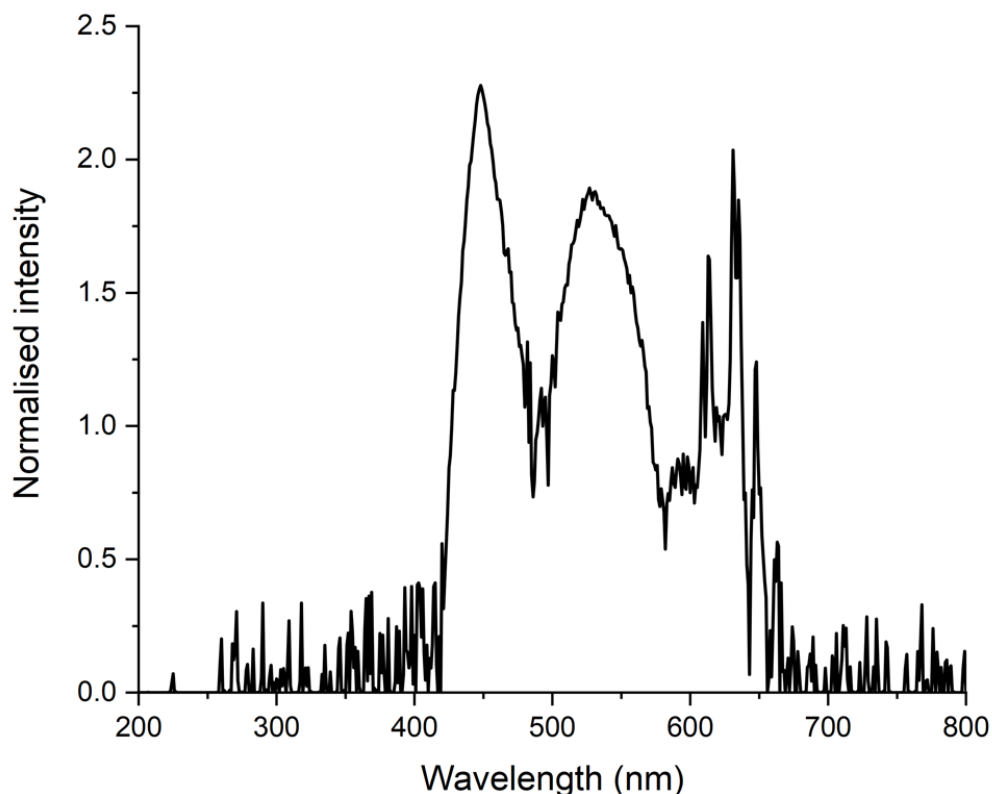
Figure 5.10 Emission spectra of the smartphone screen showing a white background with 100% screen brightness (Huawei P10, Android 7.0).

Several visible-light photoinitiators found in the literature were examined by measuring their absorption spectra in the visible light range (**Figure 5.11**). Eosin Y (EOS) is a xanthene dye commonly used for histological staining, which shows absorbance at 500-520 nm (Freire et al., 2014; Shih and Lin, 2013). Recently, a new visible-light photoinitiating system containing tris (2'2-bipyridyl) dichlororuthenium (II) hexahydrate (Ru) and sodium persulfate (SPS) has been developed for radical polymerisation (350-450 nm) (Lim et al., 2016). Likewise, riboflavin (RBF) also known as vitamin B2, has been widely applied as a visible-light non-toxic photoinitiator, possessing absorbance maxima between 350-450 nm (Ahmad et al., 2013; Madžarević and Ibrić, 2021).
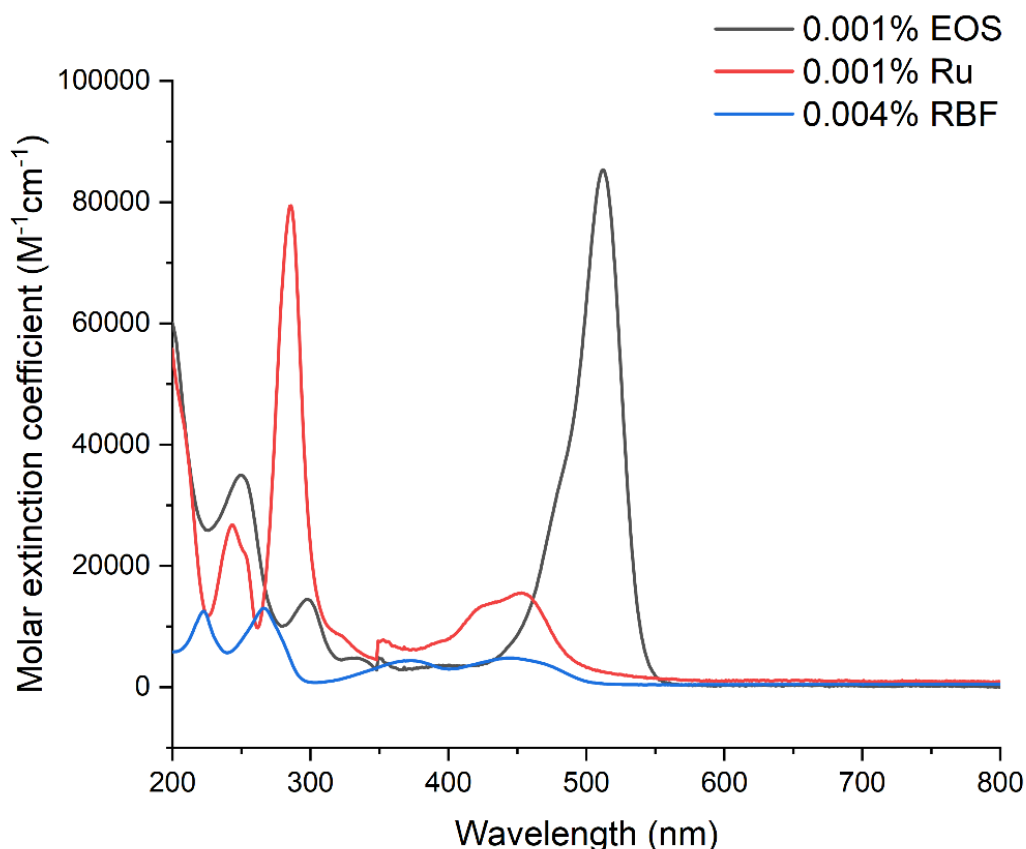
Figure 5.11 UV-vis spectra for 0.001% (w/v) EOS, 0.001% (w/v) Ru, and 0.004% (w/v) RBF in distilled water.

In the initial screening, each of the visible-light photoinitiators and their co-initiators were incorporated in the resin formulation containing PEGDA and loaded into the printer. Under an exposure time of 120 s per layer, RU1 (**Figure 5.12a**) and EOS1 (**Figure 5.12b**) Printlets were successfully obtained. EOS1 Printlets exhibited better printability and higher dimensional accuracy than RU1. All the Printlets exhibited an orange colour attributed to the presence of Eosin Y. Unfortunately, no Printlets could be obtained from the riboflavin-based formulation (RBF1) even with a longer exposure time of up to 350 s per layer. Therefore, EOS1 was selected as the base formulation to move forward to the next stage of printing with the model drug, warfarin sodium.
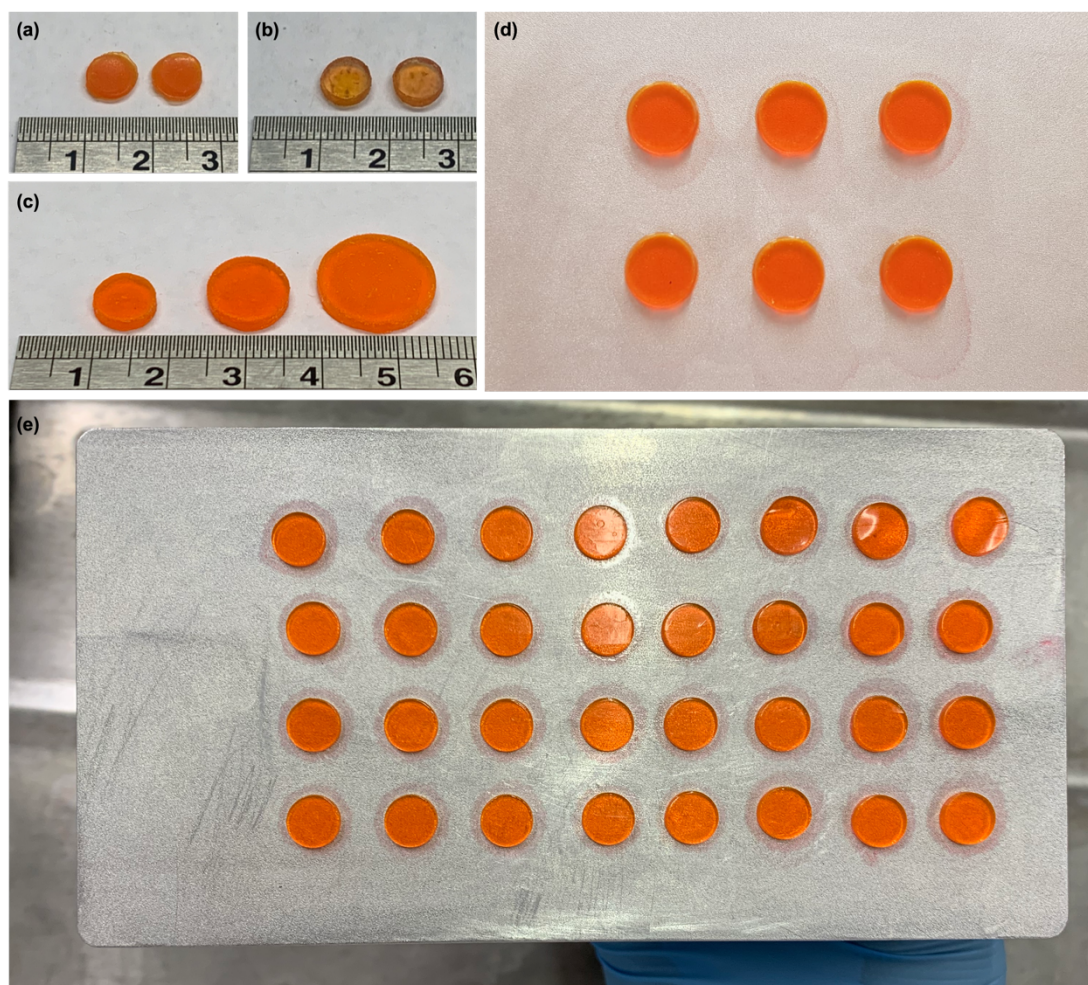
Figure 5.12 Pictures of (a) RU1 size-8 Printlets, (b) EOS1 size-8 Printlets, (c) EOS2 size-8, size-11, and size-16 Printlets, (d) multiple EOS2 size-11 Printlets and (e) multiple EOS2 mini Printlets (6mm diameter x 1mm) printed on the build platform. Scale shown in cm.

Warfarin-loaded Printlets (EOS2) in three different sizes were designed and successfully prepared (**Figure 5.12c**). Similar to the EOS1 Printlets, all EOS2 Printlets had the same orange colour. SEM images showed that all Printlets were fabricated with flat and smooth outer surfaces (**Figure 5.13**) and the layer-by-layer feature of 3D printing was also seen. Additionally, the size of the resin tank (14.5 cm x 8.5 cm x 2 cm) and the build platform (12.5 cm x 6.5 cm) were made relatively smaller than commercial DLP 3D printers which could be advantageous for cost and material savings. As can be observed from **Figure 5.12d and e**, multiple Printlets could be prepared at the same time, suggesting the potential and convenience of this novel platform in preparing small batches

of personalised medicines overnight. The average diameter, thickness, and weight of different EOS2 Printlets are shown in **Table 5.4**. All the Printlets were fabricated with uniform diameter and thickness as designed, highlighting the high resolution and precision of this printing system.
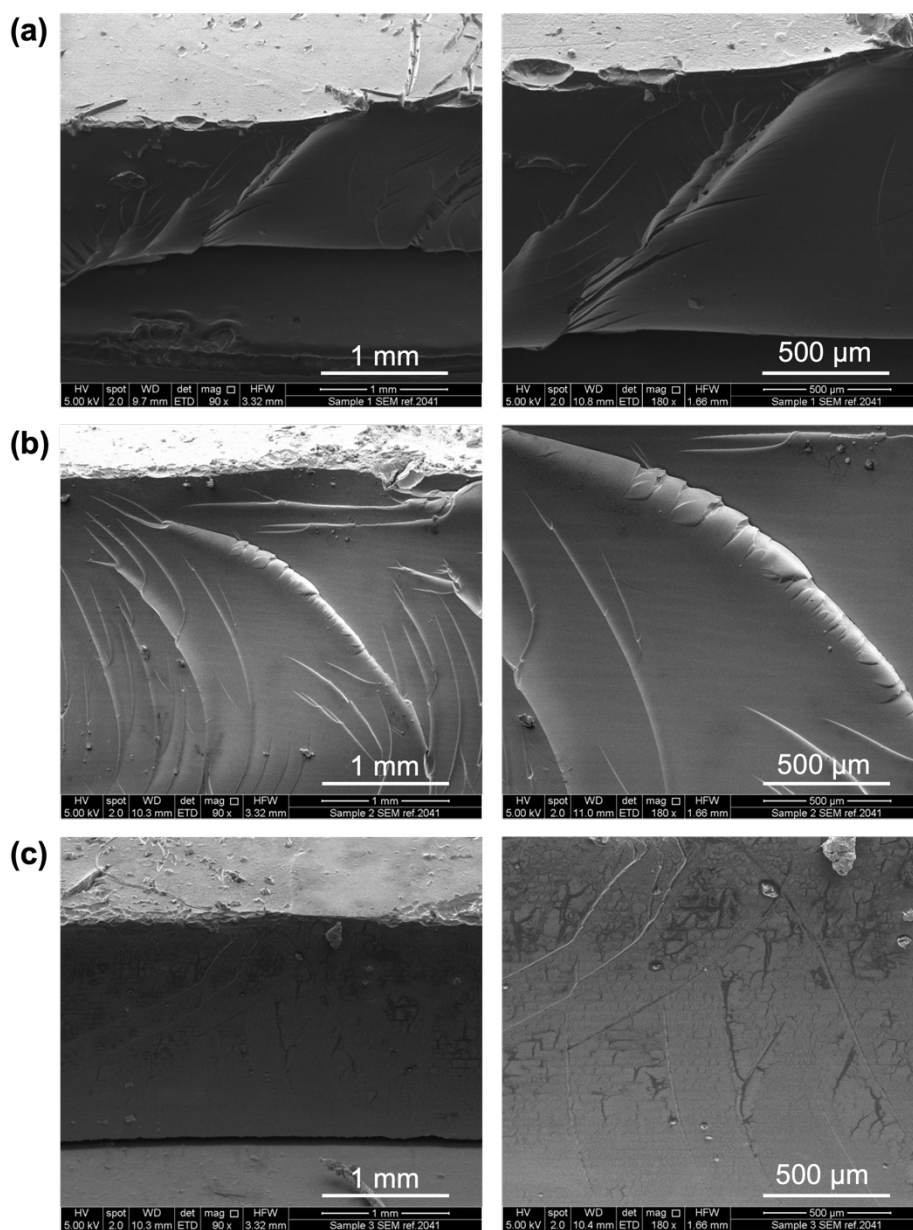
Figure 5.13 SEM images of cross-sections of (a) EOS2 size-8 Printlet, (b) EOS2 size-11 Printlet, and (c) EOS2 size-16 Printlet.

Table 5.4 Dimensions and drug loading of the EOS2 Printlets.

EOS2 Printlets	Diameter (mm)	Deviation in diameter (%)	Thickness (mm)	Deviation in thickness (%)	Weight (mg)	Drug loading (%)	Dose (mg)
Size-8	8.1 ± 0.06	1.0	2.5 ± 0.03	-2.0	148.4 ± 5.45	5.1 ± 0.04	7.5
Size-11	11.1 ± 0.07	0.6	2.5 ± 0.04	-0.8	283.2 ± 1.29	5.1 ± 0.02	14.3
Size-16	16.1 ± 0.10	0.3	2.4 ± 0.03	-2.4	594.4 ± 11.65	4.9 ± 0.04	29.3

To demonstrate the flexibility of this smartphone-enabled platform, Printlets with various geometries (**Figure 5.14a**) were fabricated using the EOS1 formulations providing benefits for developing patient-centric medicines. Gyroid lattice Printlets (**Figure 5.14b**) were prepared using EOS1 formulations as well as commercial Daylight resin in high resolutions, illustrating the adaptability of this 3D printer to versatile materials.
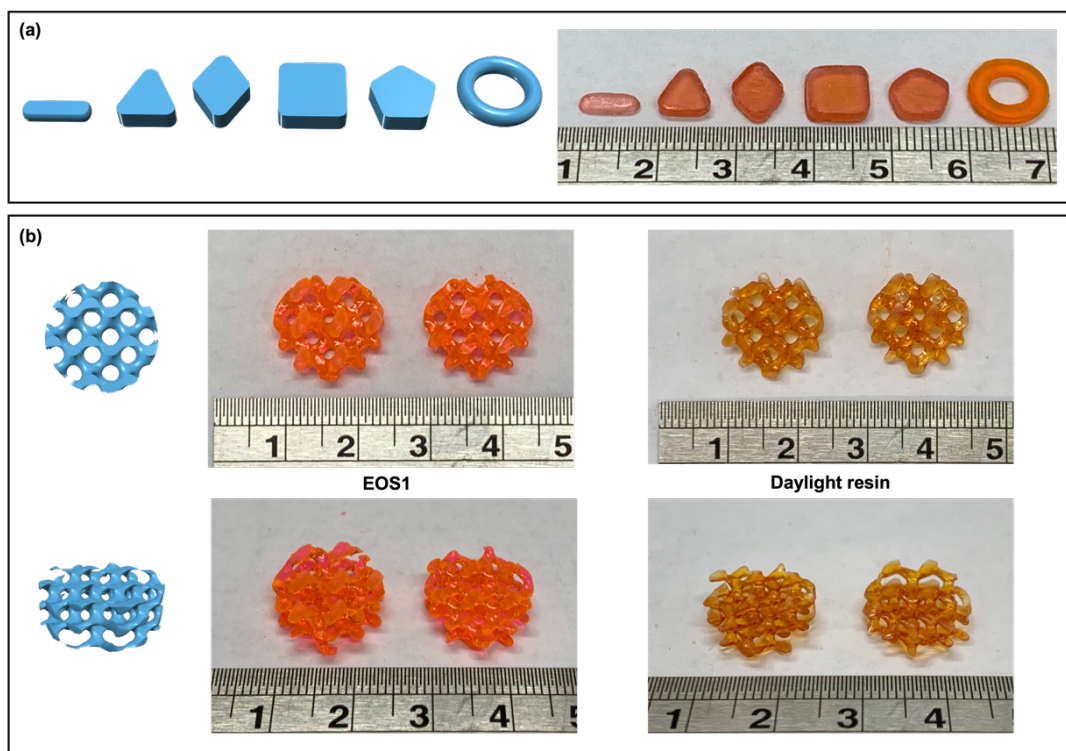
Figure 5.14 3D models (left) and pictures (right) of (a) EOS1 Printlets in various geometries including (from left to right) caplet, triangle, diamond, square, pentagon, and torus; and (b) gyroid lattice Printlets prepared with EOS1 and Daylight resin. Scale shown in cm.

Drug loading of EOS2 Printlets was evaluated using HPLC (**Table 5.4**). The theoretical loading of warfarin was 5% (w/w) and all the Printlets were fabricated with drug loadings similar to that value. By varying the diameter of the 3D design, the Printlets were fabricated to incorporate various warfarin dose of 7.54 mg, 14.30 mg, and 29.25 mg for size-8, size-11, and size-16 Printlets, respectively, highlighting the capability of this 3D printing platform in enabling flexible dosing to suit the needs of individual dose requirement.

5.6.1.2 Physical characterisation

XRPD and DSC analyses were performed to investigate the physical state of warfarin sodium in the EOS2 Printlets (**Figure 5.15**). The XRPD data (**Figure 5.15a**) showed characteristic peaks of warfarin sodium at 8.1° and 19.2° 2θ, which were not visible in the EOS2 Printlets. The results suggest that the drug is present in an amorphous phase in the printed formulations. Likewise, the DSC thermogram (**Figure 5.15b**) displayed a broad endothermic peak at 190 °C for warfarin sodium, indicating that the drug was in crystalline state and could be detected by DSC (Vuddanda et al., 2018). No melting peak was observed in the EOS2 Printlet, again suggesting the drug was in the amorphous form in the Printlet.
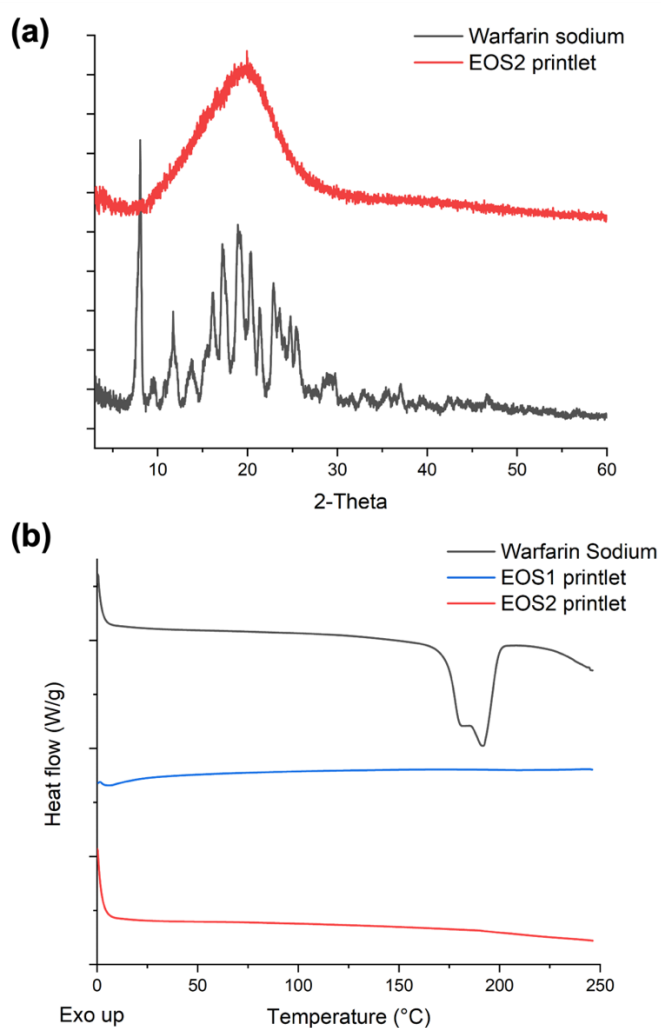
Figure 5.15 (a) X-ray powder diffractograms and (b) DSC thermograms of warfarin sodium, EOS1 Printlet, and EOS2 Printlet.

ATR-FTIR spectra (**Figure 5.16**) were obtained to investigate the possible drug-photopolymer interactions before and after 3D printing, which has been reported previously during the preparation of oral dosage forms (Xu et al., 2020). The spectrum of water was included as reference as the photoinitiator Eosin Y was prepared in 1% w/v aqueous solution. Typical bands of warfarin sodium (wavenumber highlighted in black) are seen at 2850-2950 cm^{-1} (asymmetric CH_2 stretching), 1720 cm^{-1} and 1668 cm^{-1} (C=O stretching), 1451 cm^{-1} (asymmetric bending vibrations of CH_3), and 704 cm^{-1} and 758 cm^{-1} (out-of-plane bending vibrations of C-H of phenyl rings) (Parfenyuk and Dolinina, 2017; Vuddanda et al., 2018; Yang and Song, 2015). The characteristic bands were present in the FTIR spectra of EOS2 resin formulation and EOS2 Printlet, indicating no drug-photopolymer interactions. As expected, these distinctive peaks were not observed in the blank formulation (EOS1 Printlet). Before the DLP 3D printing process, PEGDA and EOS2 resin formulation showed typical acrylate peaks at 1722 cm^{-1} (C=O stretching), 1633 cm^{-1} (C=C stretching), 1408 cm^{-1} and 810 cm^{-1} (CH_2=CH) (Kadry et al., 2019; Krkobabić et al., 2019), which disappeared after in the Printlets (EOS1 and EOS2 Printlets) contributed to the conversion of C=C bonds to C-C bonds.
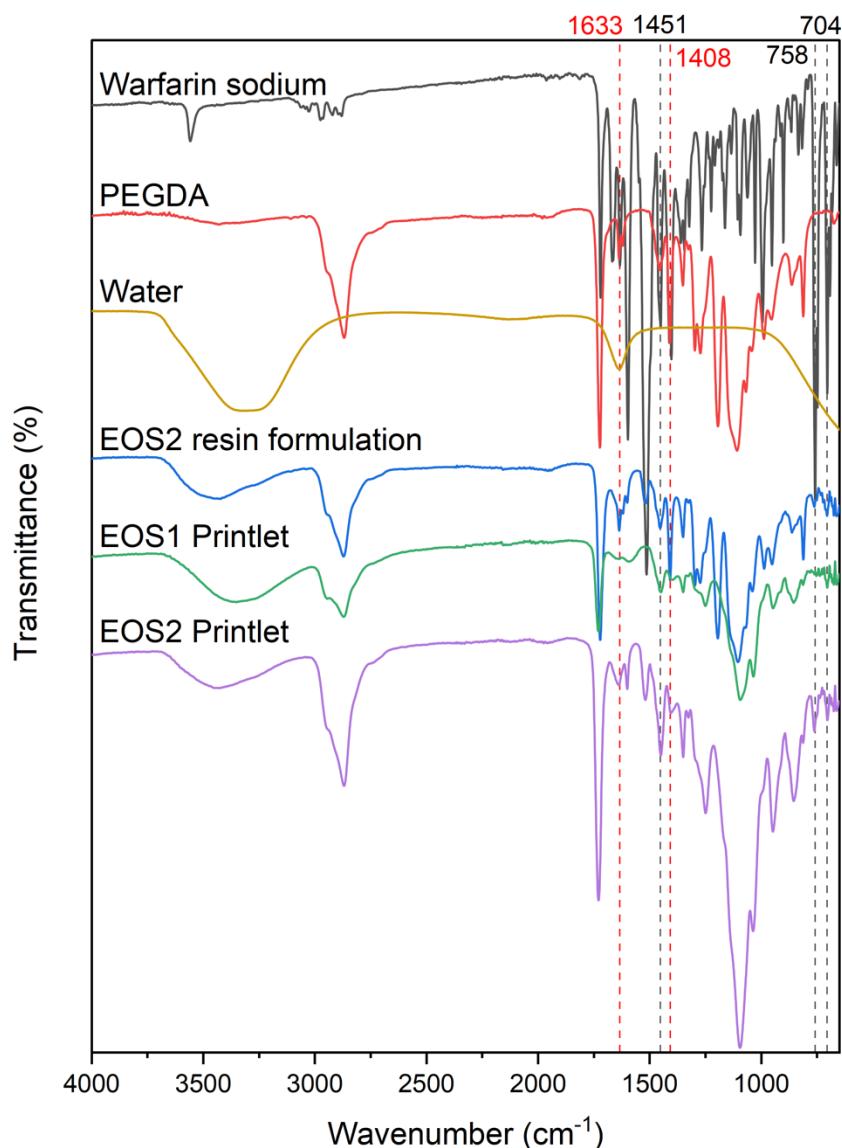
Figure 5.16 FTIR spectra of warfarin, PEGDA, water, EOS2 resin formulation, EOS1 Printlet (blank), and EOS2 Printlet.

5.6.1.3 *In vitro* drug release

The Printlets were then tested in a dynamic dissolution *in vitro* model, which mimics the gastric and intestinal conditions of the gastrointestinal tract (**Figure 5.17).** The release of warfarin commenced slowly in the gastric phase during the first 2 h. This is because warfarin sodium is a weak acid (pKa 5.05) and exhibits a pH-dependent solubility profile (Nguyenpho et al., 2015). After 2 h, the drug release rates from all Printlets increased in the intestinal phase and continued throughout the remaining 22 h. All the Printlets displayed sustained

warfarin release, reaching a release of 79.2%, 71.6%, and 76.1% from the size-8, size-11, and size-16 Printlets after 24 h, respectively.
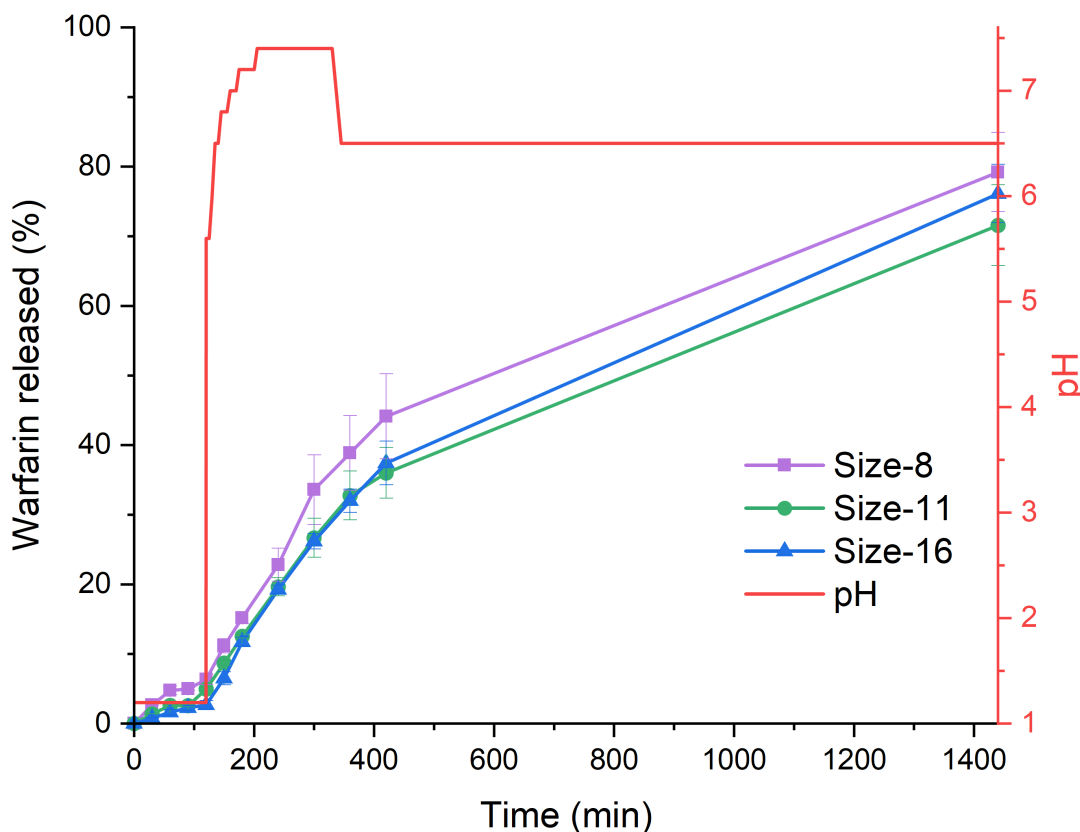
Figure 5.17 Cumulative release profiles of warfarin sodium from EOS2 size-8, size-11, and size-16 Printlets. Data values represent mean ± SD (n=3).

To better understand the release kinetics of the Printlets, various kinetic models were fitted with the *in vitro* drug release data. As shown in **Table 5.5**, all the Printlets were found best fitted with the first-order kinetic model with highest R^2 values of 0.981, 0.983 and 0.990.

In a previous study, Printlets with higher surface area to volume ratio demonstrated faster dissolution rates (Goyanes et al., 2015b). Although Printlets displayed different SA/V ratios (1.32 for size-8, 1.16 for size-11, and 1.05 for size-16), they unexpectedly showed similar release profiles and the same first-order release constant. This may be a result of the cracks present on the surface of the Printlets, which were observed after the dissolution study (**Figure 5.18**). The cause of cracking should be further investigated for future

studies. To explore the release pattern, Korsmeyer-Peppas model was used to characterise the transport mechanism based on the n values (Bruschi, 2015). All n values were higher than 0.89 (for cylinders), meaning releases from all the Printlets were characterised by the Super Case II model.

Table 5.5 Release kinetic data of the EOS2 size-8, size-11, and size-16 Printlets containing warfarin sodium.

Release kinetics model	Parameters	Size-8	Size-11	Size-16
Zero-order	R^2	0.880	0.908	0.919
	k_0 (min^{-1})	0.057	0.052	0.056
First-order	R^2	0.981	0.983	0.990
	k_1 (min^{-1})	0.001	0.001	0.001
Higuchi	R^2	0.933	0.934	0.923
	k_H ($min^{-0.5}$)	2.380	2.135	2.272
Korsmeyer-Peppas	R^2	0.948	0.956	0.955
	k (min^{-n})	0.038	0.009	0.002
	n	1.158	1.376	1.620
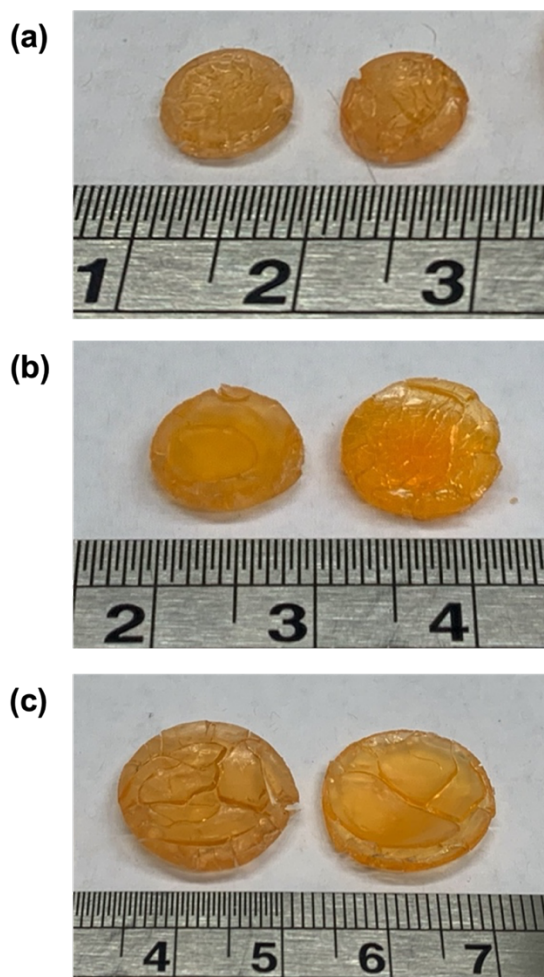
Figure 5.18 Pictures of EOS2 (a) size-8, (b) size-11, and (c) size-16 Printlets after dissolution test. Scale shown in cm.

5.6.2 Patient-specific drug delivery devices

5.6.2.1 3D printing

As everyone's anatomic features are unique and different, it is necessary to customise medical devices to adapt and fit individual patients. The use of handheld 3D scanners coupled with 3D printing has been explored, demonstrating the potential and convenience in developing a range of patient-specific drug delivery devices (Goyanes et al., 2016; Lim et al., 2021; Lim et al., 2017; Muwaffak et al., 2017; Vivero-Lopez et al., 2021b). With the advancement of mobile applications, 3D scanning smartphone apps are becoming available for acquiring 3D models. Following the successful

preparation of personalised Printlets in **Section 5.6.1**, the smartphone-enabled 3D printing system was used for the development of an all-in-one system, wherein the smartphone was used to obtain individualised 3D models and subsequently print patient-specific drug delivery devices.

As illustrated in **Figure 5.19**, personalised drug-loaded hearing aids and nose patches were successfully prepared adapting to the volunteer's own ear and nose anatomical features. Compared with the devices prepared by commercial SLA and DLP 3D printers with commercial resins, the phone printed devices demonstrated comparable resolutions and smooth external surface finish, highlighting the high precision of this system.
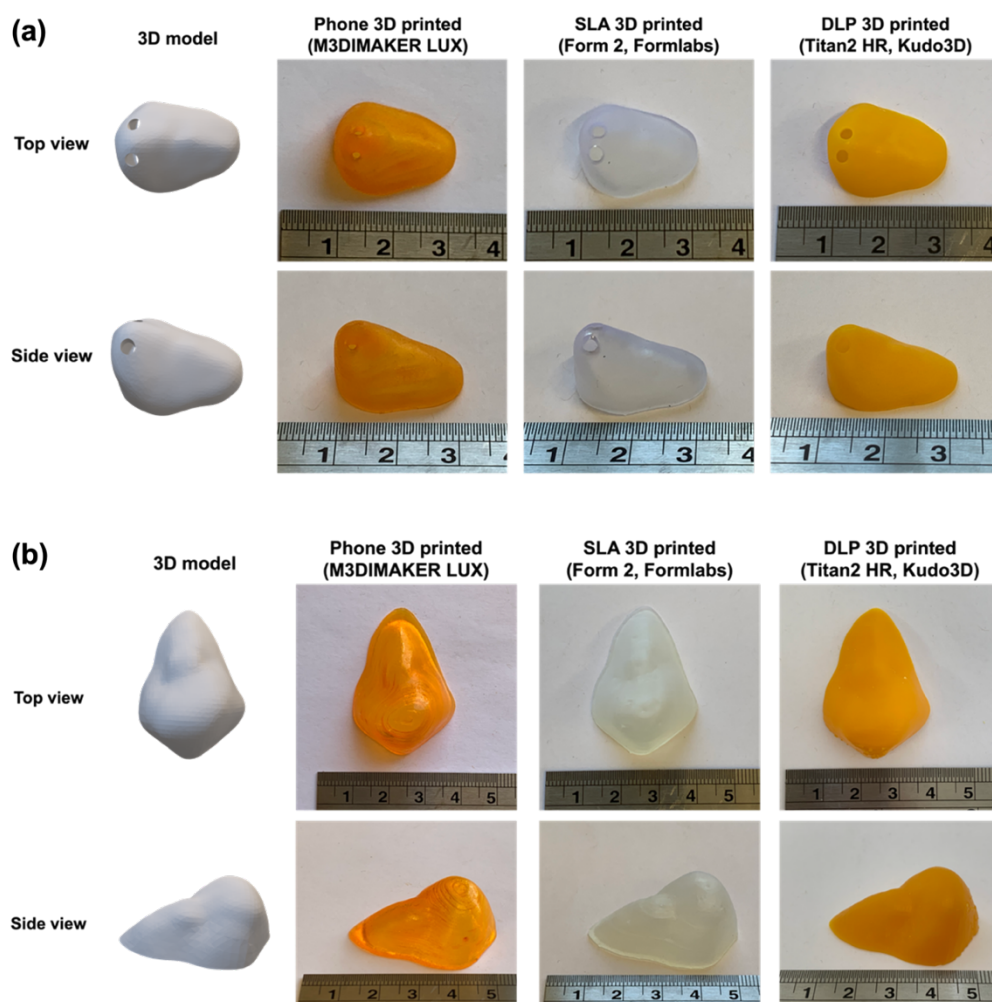
Figure 5.19 Pictures showing the 3Dmodel and 3D printed patient-specific (a) hearing aids and (b) nose patch from the smartphone-enabled 3D printer, the commercial SLA 3D printer and DLP 3D printer. Scale in cm.

In order to estimate the dimensional accuracy of the phone printed devices, the dimensions of the devices in X, Y, and Z axes were measured and compared with the dimensions of the 3D models. **Table 5.5** shows that the dimensions of the printed device are uniform and similar as the scanned 3D models.

Table 5.6 Dimensions of the 3D models and the phone printed nose patches and hearing aids.

	Nose patch		Hearing aid	
	3D model	Phone printed	3D model	Phone printed
X (mm)	29.0	29.2 ± 0.04	22.1	22.5 ± 0.04
Y (mm)	42.3	42.1 ± 0.06	17.1	17.8 ± 0.06
Z (mm)	16.2	16.2 ± 0.08	10.5	11.0 ± 0.03

5.6.2.2 Physical characterisation

XRPD was used to evaluate the physical states of both model drugs in the printed devices, salicylic acid, and ciprofloxacin hydrochloride (**Figure 5.20**). Characteristics peaks of salicylic acid at 10.9°, 17.2°, and 25.1° 2θ were not visible in the XRPD pattern of phone printed FSA2 formulation, indicating the drug has been fully dissolved in the resin formulation prior to printing and present in the amorphous phase within the printed formulation. Similarly, typical peaks of ciprofloxacin hydrochloride at 8.0°, 8.8°, 19.1°, and 26.3° 2θ were not observed in the pattern of phone printed FCH2 formulations, which suggests that the physical form of the drug is amorphous.
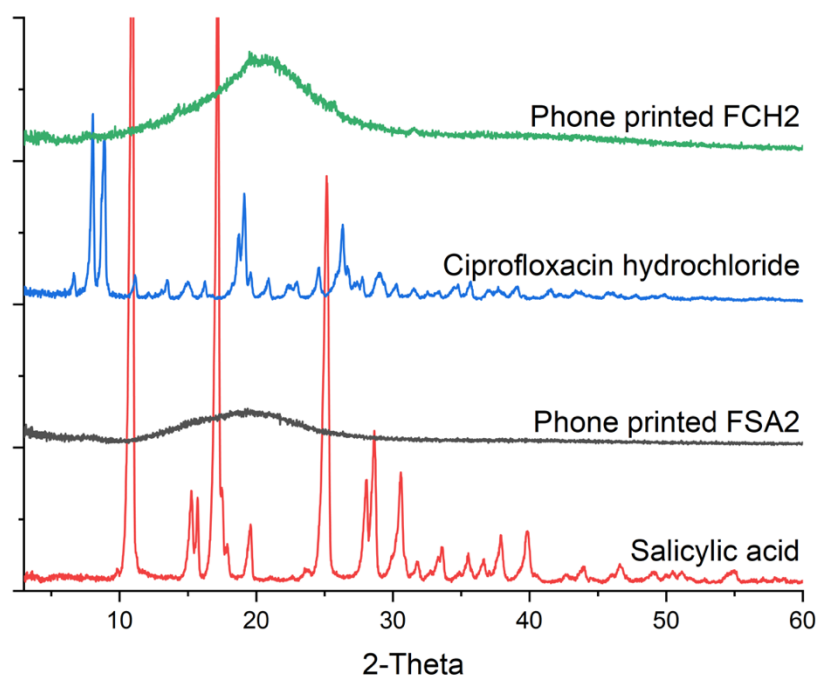
Figure 5.20 X-ray powder diffractograms of the model drugs (salicylic acid and ciprofloxacin hydrochloride) and phone printed formulations.

The DSC thermograms (**Figure 5.21**) show a sharp endothermic peak of salicylic acid at 159.8 °C and a broad endotherm of ciprofloxacin hydrochloride at 156.1°C in as reported by the literature (Goyanes et al., 2016; Vivero-Lopez et al., 2021b), implying the drug powders were in the crystalline form. In good agreement with the XRPD results, no melting events were observed in the phone printed formulations, revealing that both drugs were completely dissolved in the resin formulation before printing.
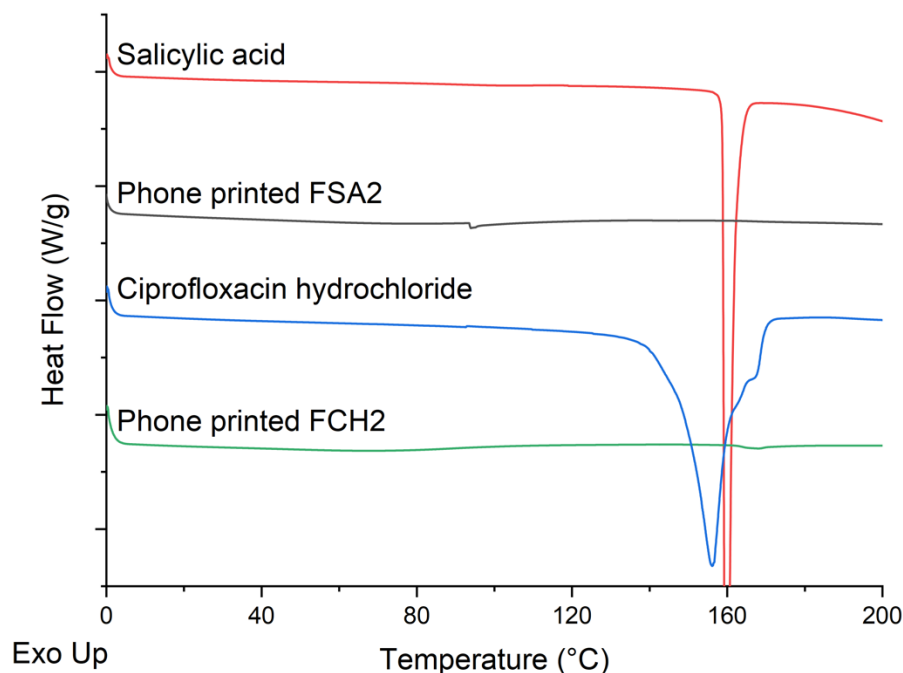
Figure 5.21 DSC thermograms of the model drugs (salicylic acid and ciprofloxacin hydrochloride) and phone printed formulations.

FTIR spectroscopy (**Figure 5.22**) was used for evaluating any possible interactions between the model drugs and the photopolymer (PEGDA) before and after phone printing of devices (Xu et al., 2020). The spectrum of PEGDA was obtained as the reference, showing its distinctive acrylate peaks at 1722 cm^{-1} (C=O stretching) and 1633 cm^{-1} (C=C stretching) (Rodríguez-Pombo et al., 2022). Specifically, the peak at 1633 cm^{-1} (wavenumber highlighted in black) was difficult to identify in the phone printed FSA2 and FCH2 spectra due to the conversion of C=C to C-C bonds during photopolymerisation process. It can be seen that salicylic acid presented its characteristic vibrational peaks at 3232 cm^{-1} (O-H stretching), 2998-2852 cm^{-1} (C-H stretching), 1650 cm^{-1} (C=O (COO$^-$) stretching), 1324 cm^{-1} (O-H (phenolic) bending), and 1291cm^{-1} (C-O (COO$^-$) stretching) (Trivedi et al., 2015) (**Figure 5.22**). Although some of them were masked by the broad signal from water (EOS 1% w/v solution), other bands (wavenumbers highlighted in red) were visible in the resin formulation and the phone printed FSA2 spectra, suggesting there were no drug-photopolymer interactions. Likewise, characteristic bands of ciprofloxacin hydrochloride could be assigned to 3528 cm^{-1} (O-H stretching), 2689-2463 cm^{-1} (N-H

stretching), and 1267 cm^{-1} (C-F stretching) (Kowalczuk, 2020), which were clearly observed (wavenumbers highlighted in blue) in the resin formulation and phone printed FCH2 spectra, indicating no detectable drug-photopolymer interactions.
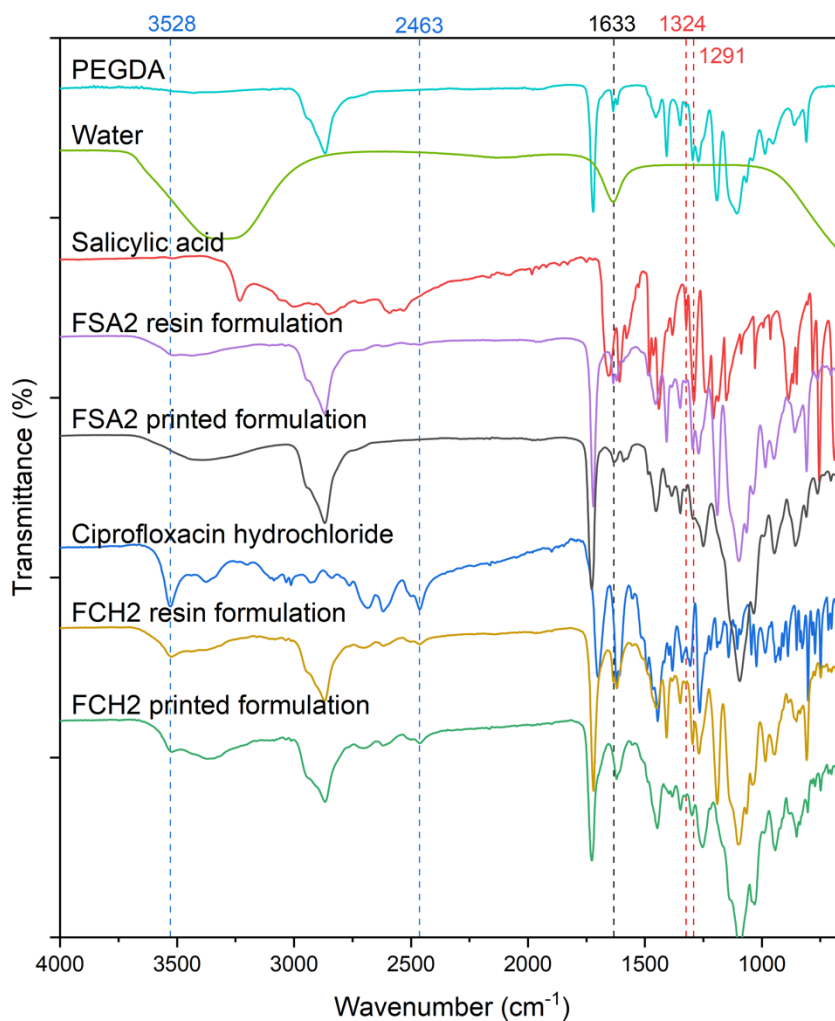
Figure 5.22 FTIR spectra of PEGDA, salicylic acid, ciprofloxacin hydrochloride, and FSA2 and FCH2 resin formulation and phone printed formulation.

5.6.2.3 *In vitro* drug release

Since both devices were intended to be used for topical drug delivery, it is important to evaluate the *in vitro* drug diffusion through synthetic membranes using Franz cells. Phone printed drug-loaded discs were prepared for

conducting the diffusion study over a period of 24 h. The results (**Figure 5.23**) show the diffusion rate of salicylic acid from the phone printed discs was much faster than that obtained from ciprofloxacin hydrochloride-loaded discs. Cumulative salicylic acid diffused was 230 and 670 $\mu g/cm^2$ at 60 and 180 min whereas cumulative ciprofloxacin hydrochloride diffused was only 10 and 36 $\mu g/cm^2$ at 60 and 180 min, respectively. Both drugs display linear diffusion rates within the first 6 h with approximately 210 $\mu g/cm^2$ of salicylic acid and 14 $\mu g/cm^2$ ciprofloxacin hydrochloride released every 1 h.
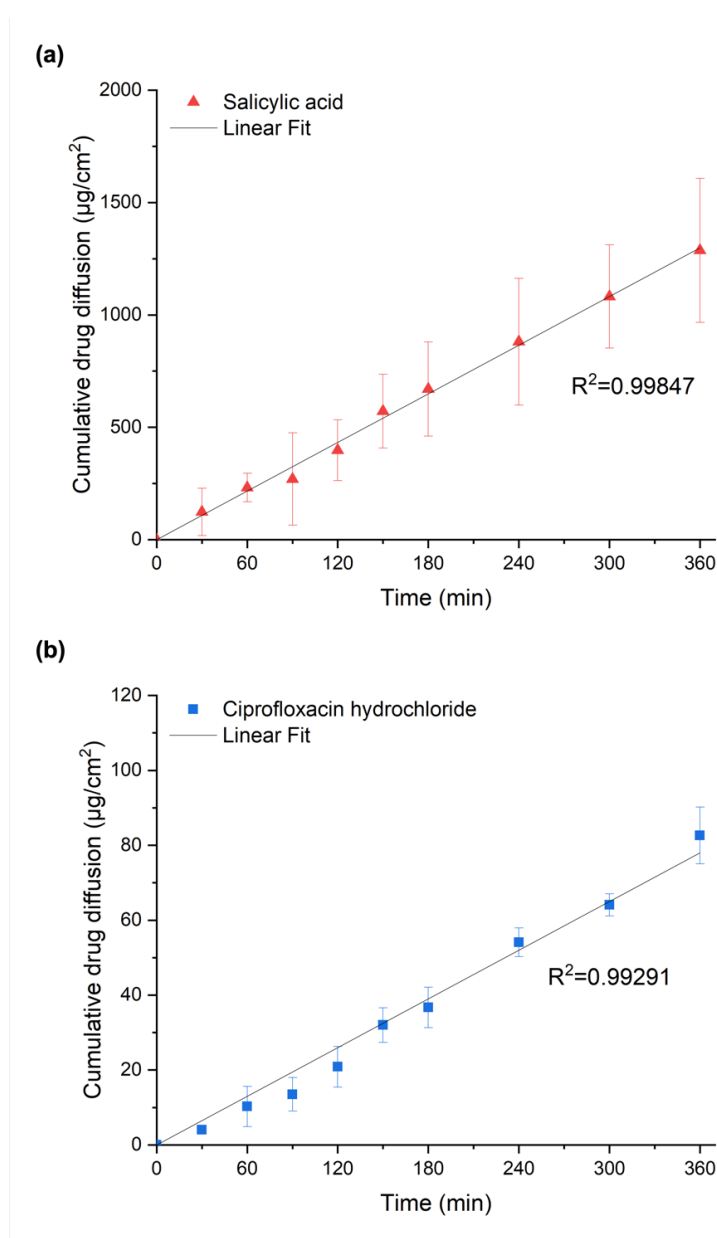
Figure 5.23 Cumulative amounts of (a) salicylic acid and (b) ciprofloxacin hydrochloride permeated from the phone printed discs. Data values represent mean ± SD (n=3).

This all-in-one smartphone-enabled 3D printing system can potentially be integrated in electronic health systems for manufacturing personalised medicines at the point-of-care (**Figure 5.24**). Nowadays, with the development of mobile sensing and health monitoring, doctors can remotely manage the patient's medication and provide adjustment of dosages according to the patient's disease condition or pain level. It can be envisioned that, in the future, patients can directly receive their daily electronic prescriptions from doctors or GP practices on their smartphone app with all the information needed including the size of the Printlet for the required doses. Patients could then simply choose the shape of oral dosage form they prefer and by clicking on the prescription, they can eventually print their own medicines overnight at home. In addition, elderly patients can benefit from this system by printing their own polypills to reduce pill burdens.
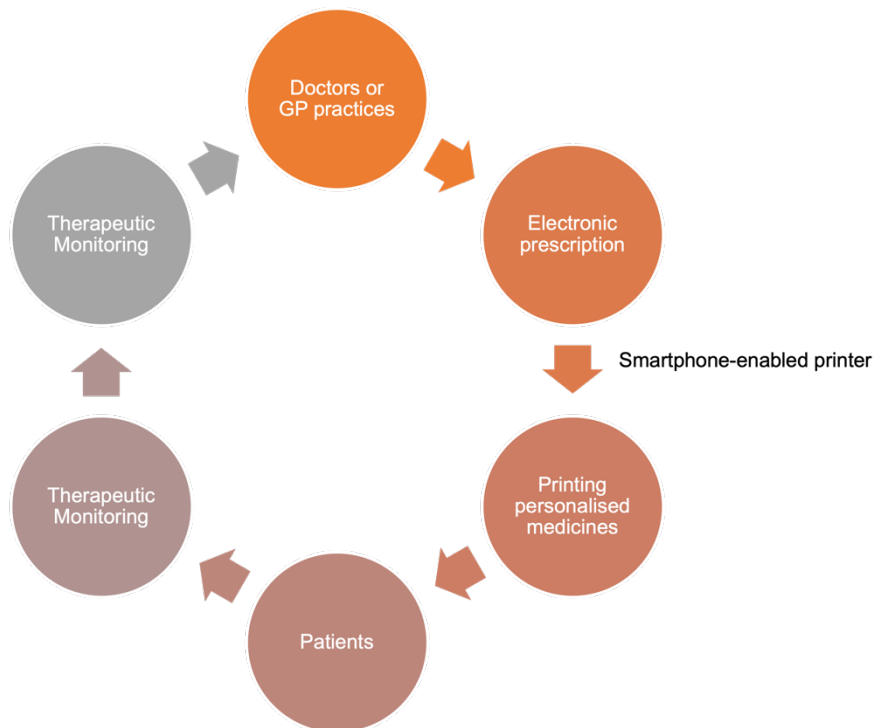
Figure 5.24 Schematic diagram of future scenario for integrated smartphone-enabled printer in the electronic healthcare system for manufacturing personalised medicines at the point-of-care.

On the other hand, one challenge could be the danger of drug abuse or misuse, potentially risking the lives of individuals. However, this can be avoided by integrating several digital health technologies that safeguard the use of medicines (Awad et al., 2021b); this could include designing a system that requires remote approval by a designated healthcare professional, integrating AI technologies to adjust printing parameters so that the final drug product meets the intended therapeutic activity (Elbadawi et al., 2021a; Elbadawi et al., 2021b), and implementing remote drug monitoring and sensing technologies to ensure that patients are adhering to their treatment plan. Additionally, a regulatory framework concerned with 3D printed drug-laden products should be developed, whereby the legislation should counterbalance the potential benefits provided to patients and the safety risks these technologies pose. It is also vital to develop quality control measures that enable the evaluation of the quality of final drug products in a quick, yet non-destructive manner. To ensure that these control measures are being met and implemented correctly, a dedicated hub should oversee the workflow of these individual production sites. While research in the field of 3D printing pharmaceuticals is still nascent, with the correct measures in place and proper framework built, its true potential can be realised sooner rather than later.

5.7   Conclusion

In this chapter, a compact smartphone-based 3D printer and a customised printing app were used for the preparation of Printlets and drug delivery devices. The light from the screen of a smartphone enabled the direct preparation of personalised medications. Warfarin sodium, a narrow-therapeutic-index drug, was used as the model compound to manufacture oral Printlets with various doses, sizes, and shapes with high accuracy. Moreover, patient-specific salicylic acid-loaded nose patches and ciprofloxacin-loaded hearing aids were also prepared by this system using the smartphone directly to obtain volunteer's unique anatomical features. The dimensions of the printed devices were measured and compared with devices printed with commercial SLA and DLP printers, showing comparable resolution and

accuracy. Finally, *in vitro* drug release was assessed from phone printed Printlets in various sizes over 24 h and diffusion study was conducted to evaluate the drug diffuse rates from the phone printed devices using Franz cells. This 3D printing platform has the potential to be integrated in digital healthcare for point-of-care manufacturing of personalised medicines at a patient's home, in emergency, or resource-limited settings. In the future, this type of system may also possess great significance for achieving a new milestone for affordable and accessible mobile-health technologies.

Chapter 6
Conclusions and future work

6   Conclusions and future work

6.1   Conclusions

3D printing has become a disruptive technology due to its capability of rapid manufacturing of bespoke objects with boundless applications emerging from various industries. Within pharmaceutical and healthcare, 3D printing has caused a paradigm shift in the way medicines are prepared, enabling the transition from 'one-size-fits-all' approach towards personalised medicines. Different 3D printing technologies such as FDM, SLS, and SSE have attracted increasing attentions for fabricating customised drug delivery systems where the dosages, shapes, sizes, and release characteristics can be tailored to suit individual patient's need. This also include vat photopolymerisation 3D printing thanks to its high accuracy and the excellent level of details and surface finish that it could provide. Additionally, its room temperature working environment is suitable for thermal-labile APIs over other technologies. In the past few years, the research carried out in the pharmaceutical field using vat photopolymerisation 3D printing has been focused on the development of oral dosage forms for controlled release whereas the exploration of its feasibility in fabricating drug delivery devices has not been widely studied yet.

In this thesis, the use of different vat photopolymerisation 3D printing technologies for the preparation of controlled drug delivery devices has been demonstrated. Chapter 1 provided an overview of 3D printing and discussed its unique advantages in preparing personalised medicines followed by a detailed introduction of vat photopolymerisation 3D printing and its recent applications in the fields of drug delivery.

In Chapter 2, SLA 3D printing was presented as a novel platform for the development of intravesical devices for extended drug delivery in the bladder. The devices were designed to be elongated in a straight tube shape and administered using a urethral catheter, which will be remained in the bladder for localised and prolonged drug delivery. This could be beneficial over the instillation treatment where repeated catheterisation is often required,

improving patient compliance. Using elastomers and different drug loadings of lidocaine hydrochloride, two types of intravesical devices (hollow and solid) have been prepared. *In vitro* drug release study has shown that the hollow intravesical devices enabled a complete release of lidocaine within 4 days while release was sustained for up to 14 days from the solid devices. The drug release results demonstrated in this work were comparable to other retentive devices found in the literature, yet the manufacturing process using SLA 3D printing is simpler and more cost-effective.

Chapter 3 described the use of DLP 3D printing as a single-step approach to create punctal plugs for the treatment of dry eye disease. Topical administration such as eye drops are common treatment, however, the ocular bioavailability is usually poor because of a number of physiological and anatomical constraints. Punctal plugs are commonly used as non-invasive medical devices for the mitigation of dry eye syndrome. Here, DLP 3D printing was effectively used for direct fabrication of drug-loaded punctal plugs. Initially, dumbbell-shaped punctal plugs were prepared using paracetamol as a model compound and a Flexible resin to investigate the feasibility of this approach. To further maximise the flexibility of this technology, punctal plugs were then prepared with a more clinically relevant drug, dexamethasone for treating dry eye using PEGDA and PEG 400, showing good resolution and uniformity in size. *In vitro* drug release study was conducted using an in-house flow rig model that mimics the front of the eye. Results demonstrated release of dexamethasone from the D20 punctal plugs was sustained for up to 21 days.

3D printing is well suited to produce multi-drug formulations due to its design freedom and the capability of accurate distribution of multiple materials, which could be useful in improving medication adherence for patients on polypharmacy treatment regimes. Chapter 4 showed the potential of SLA 3D printing in preparing oral polypills incorporating four antihypertensive drugs (atenolol, hydrochlorothiazide, irbesartan, and amlodipine) from different classes. Although successful in its fabrication, a chemical reaction between the photopolymer (PEGDA) and one of the drugs (amlodipine) was observed.

Later, FTIR and NMR spectroscopy confirmed the occurrence of a Michael addition reaction between the diacrylate group of the PEGDA and the primary amine of amlodipine. The results from this chapter have highlighted the importance of careful evaluation of compatibility between photopolymers and model drugs prior manufacture of drug-loaded dosage forms via vat photopolymerisation 3D printing.

Finally, Chapter 5 investigated the feasibility of a smartphone-enabled DLP 3D printing system for the preparation of personalised medications including oral Printlets and drug delivery devices. Different from the other chapters where commercial 3D printers were employed for preparing different drug delivery devices, the last chapter utilised a compact 3D printer where the light emitted from the screen of a smartphone was directly used as the illumination source and a custom mobile app was used to control the printer. Warfarin Printlets in various geometries were successfully prepared to incorporate different dose strengths. By using the smartphone's camera and scanning mobile apps, volunteer's unique anatomical features were captured and used to develop patient-specific drug delivery devices including anti-acne nose patches and anti-biofilm hearing aids. Compared with other large-scale 3D printers that are designed to be used with large volume of materials, such a portable platform demonstrated in this chapter could be particularly advantageous to allow manufacturing of personalised medications at the point-of-care.

6.2   Future work

The findings of this thesis emphasised the potential and suitability of vat photopolymerisation 3D printing as a simple and cost-effective platform for the development of controlled drug delivery devices. However, the resins used for the fabrication of intravesical devices in chapter 2 and punctal plugs in chapter 3 were not degradable, meaning a retrieval procedure is required after the treatment and it is not ideal for the patients. Future work could explore the use of biodegradable photopolymers for preparing these devices and investigate how the degradation time would affect the drug release rates. Additionally,

smart materials that are responsive to external stimuli such as pH and temperature could be employed to allow targeted drug delivery.

So far, the exploration of vat photopolymerisation 3D printing in the pharmaceutical field is mainly based on the use of small molecules. Since the operating conditions is relatively mild and the technology allows the production of hydrogels, it could be a suitable platform for printing with biologics such as peptides, antibodies, and bacteria. Recently, laccase has been immobilised in PEGDA hydrogels using SLA 3D printing for removal of drugs in water (Xu et al., 2022). Also, bacteria have been printed within hydrogel architectures for adsorption and sensing applications (Dubbin et al., 2021). Both studies introduce the opportunities of vat photopolymerisation 3D printing to be extended to incorporate biological compounds for drug delivery purposes.

On the other hand, an observed limitation of vat photopolymerisation 3D printing for preparing drug-loaded dosage forms has been demonstration in chapter 4 and it highlighted the need of photopolymer screening prior the printing process. This is crucial because undesired reactions taken place between the photoreactive monomers and the API could degrade or change the drug molecule, consequently, depleting the therapeutic effects. Therefore, future work could be carried out to confirm if this drug-photopolymer interaction also takes place with other drug molecules with similar chemical structures or containing the same functional groups. It is also worth exploring what alternative photoreactive monomers could be used to replace acrylate-based monomers for preparing pharmaceutical oral dosage forms. Furthermore, machine learning as an emerging technology has been recently applied in the pharmaceutical field to predict printability (Castro et al., 2021) and drug release characteristics (Madzarevic et al., 2019), reshaping the formulation development process. With large enough datasets in the future, machine learning could be a useful tool to quickly predict the drug-photopolymer compatibility before the 3D printing process. Such datasets could include data from FTIR or NMR spectroscopy to capture chemical properties of APIs and photopolymers and label the possible interactions (e.g., Michael addition).

The smartphone-enabled DLP 3D printing system has established a proof of concept for a portable platform to fabricate personalised medications. Since the light intensity from the smartphone is relatively weak, which leads to long printing hours. Other visible light-sensitive photoinitiators with better absorbance within the phone emitted region shall be explored or the use of safe and biocompatible photosensitisers can be considered to promote photoinitiating efficiency, hence improving printing speed. To fully integrate this system within the digital health loop, a simple and non-destructive method could be developed with the use of smartphone's camera as a machine vision device, ensuring the quality control and safety of the fabricated drug products.

Finally, despite the advantages of vat photopolymerisation 3D printing in the development of controlled drug delivery devices, the most important and unresolved issue is the cytotoxicity of the unreacted monomers or photoinitiators that present after the 3D printing. None of these photoreactive materials are on the Generally-Recognised-as-Safe (GRAS) list yet. Recently, a large range of biocompatible resins are becoming commercially available on the market, but they are only approved for manufacturing dental and medical applications, which means the biocompatibility is not guaranteed with the addition of APIs (Guttridge et al., 2021). The most straightforward strategy is to conduct post-processing steps that involve post-washing and post-curing under light irradiation. However, whether these steps would impact the drug release profiles and to what extent (choice of solvent for post-washing, time and temperature required for post-curing) these steps should be carried out to guarantee sufficient cytocompatibility are worth exploring in the future. Another strategy is to investigate the degree of conversion of monomers after printing and how it affects the cytotoxicity. There are many techniques that have been previously reported for the quantification of the extent of conversion for dental applications, for sample, FTIR, DSC, HPLC, NIR, and Raman spectroscopy (Alarcon et al., 2018; Moldovan et al., 2019; Stansbury and Dickens, 2001). Ideally, these techniques can be combined with 3D printing for manufacturing personalised medicines and in-line quantification determination of conversion rates to ensure safety of the printed drug delivery devices.

Publications

Publications from this thesis:

Xu, X., Seijo-Rabina, A., Awad, A., Rial, C., Gaisford, S., Basit, A.W. and Goyanes, A. *Smartphone-enabled 3D printing of medicines.* International Journal of Pharmaceutics. 609 (2021): 121199.

Xu, X., Awwad, S., Diaz-Gomez, L., Alvarez-Lorenzo, C., Brocchini, S., Gaisford, S., Goyanes, A., Basit, A. W. *3D Printed Punctal Plugs for Controlled Ocular Drug Delivery*. Pharmaceutics. 13(9) (2021):1421.

Xu, X., Awad, A., Robles-Martinez, P., Gaisford, S., Goyanes, A., Basit, A.W. *Vat photopolymerization 3D printing for advanced drug delivery and medical device applications*. Journal of Controlled Release. 329 (2021): 743-757.

Xu, X., Goyanes, A., Trenfield, S.J., Diaz-Gomez, L., Alvarez-Lorenzo, C., Gaisford, S., Basit, A.W. *Stereolithography (SLA) 3D printing of a bladder device for intravesical drug delivery*. Materials Science and Engineering: C. 120 (2021): 111773.

Xu, X., Robles-Martinez, P., Madla, C. M., Joubert, F., Goyanes, A., Basit, A.W., Gaisford, S. *Stereolithography (SLA) 3D printing of an antihypertensive polyprintlet: Case study of an unexpected photopolymer-drug reaction*. Additive Manufacturing. 33 (2020): 101071.

Other publications:

Rodríguez-Pombo, L., **Xu, X.**, Seijo-Rabina, A., Ong, J.J., Alvarez-Lorenzo, C., Rial, C., Nieto, D., Gaisford, S., Basit, A.W., Goyanes, A. *Volumetric 3D printing for rapid production of medicines*. Additive Manufacturing. 52 (2022): 102673.

Xu, X., Pose-Boirazian, T., Eibes, G., McCoubrey, L.E., Martínez-Costas, J., Gaisford, S., Goyanes, A. and Basit, A.W. *A customizable 3D printed device for enzymatic removal of drugs in water.* Water Research. 208 (2022): 117861.

Januskaite, P., **Xu, X.**, Ranmal, S.R., Gaisford, S., Basit, A.W., Tuleu, C., Goyanes, A. *I spy with my little eye: a paediatric visual preferences survey of 3D printed tablets*. Pharmaceutics. 12(11) (2020): 1100.

Vivero-Lopez, M., **Xu, X.**, Muras, A., Otero, A., Concheiro, A., Gaisford, S., Basit, A.W., Alvarez-Lorenzo, C., Goyanes, A. *Anti-biofilm multi drug-loaded 3D printed hearing aids*. Materials Science and Engineering: C. 119 (2020): 111606.

Robles-Martinez, P., **Xu, X.**, Trenfield, S.J., Awad, A., Goyanes, A., Telford, R., Basit, A.W., Gaisford, S. *3D printing of a multi-layered polypill containing six drugs using a novel stereolithographic method*. Pharmaceutics, 11(6) (2019): 274.

Weng, J., Wong, S.N., **Xu, X.**, Xuan, B., Wang, C., Chen, R., Sun, C.C., Lakerveld R., Kwok, P.C.L., Chow, S.F. *Cocrystal engineering of itraconazole with suberic acid via rotary evaporation and spray drying.* Cocrystal Growth & Design. 19(5) (2019): 2736-2745.

Wong, S.N., Hu, S., Ng, W.W., **Xu, X.**, Lai, K.L., Lee, T., Chow, A., Chow, S.F. *Cocrystallization of curcumin with benzenediols and benzenetriols via rapid solvent removal.* Cocrystal Growth & Design. 18(9) (2018): 5534-5546.

References

Ahmad, I., Iqbal, K., Sheraz, M.A., Ahmed, S., Mirza, T., Kazi, S.H., Aminuddin, M., 2013. Photoinitiated polymerization of 2-hydroxyethyl methacrylate by riboflavin/triethanolamine in aqueous solution: a kinetic study. *ISRN pharmaceutics* 2013.

Ahn, D., Stevens, L.M., Zhou, K., Page, Z.A., 2020. Rapid high-resolution visible light 3D printing. *ACS Central Science* 6, 1555-1563.

Akyol, E., Tatliyuz, M., Demir Duman, F., Guven, M.N., Acar, H.Y., Avci, D., 2018. Phosphonate‑functionalized poly (β‑amino ester) macromers as potential biomaterials. *Journal of Biomedical Materials Research Part A* 106, 1390-1399.

Al Rashid, A., Ahmed, W., Khalid, M.Y., Koc, M., 2021. Vat photopolymerization of polymers and polymer composites: Processes and applications. *Additive Manufacturing* 47, 102279.

Alarcon, R.T., Gaglieri, C., de Oliveira, A.R., Bannach, G., 2018. Use of DSC in degree of conversion of dimethacrylate polymers: easier and faster than MIR technique. *Journal of Thermal Analysis and Calorimetry* 132, 1423-1427.

Alfa Aesar, 2022. Lidocaine hydrochloride monohydrate.https://www.alfa.com/en/catalog/J63035/, (accessed 11th March, 2023).

Allahham, N., Fina, F., Marcuta, C., Kraschew, L., Mohr, W., Gaisford, S., Basit, A.W., Goyanes, A., 2020. Selective laser sintering 3D printing of orally disintegrating printlets containing ondansetron. *Pharmaceutics* 12, 110.

Alvarez-Lorenzo, C., Anguiano-Igea, S., Varela-García, A., Vivero-Lopez, M., Concheiro, A., 2019. Bioinspired hydrogels for drug-eluting contact lenses. *Acta Biomaterialia* 84, 49-62.

Anderson, D.G., Tweedie, C.A., Hossain, N., Navarro, S.M., Brey, D.M., Van Vliet, K.J., Langer, R., Burdick, J.A., 2006. A combinatorial library of photocrosslinkable and degradable materials. *Advanced Materials* 18, 2614-2618.

Andreu, A., Su, P.-C., Kim, J.-H., Ng, C.S., Kim, S., Kim, I., Lee, J., Noh, J., Subramanian, A.S., Yoon, Y.-J., 2021. 4D printing materials for vat photopolymerization. *Additive Manufacturing* 44, 102024.

Angkawinitwong, U., Awwad, S., Khaw, P.T., Brocchini, S., Williams, G.R., 2017. Electrospun formulations of bevacizumab for sustained release in the eye. *Acta Biomaterialia* 64, 126-136.

Aran, K., Chooljian, M., Paredes, J., Rafi, M., Lee, K., Kim, A.Y., An, J., Yau, J.F., Chum, H., Conboy, I., 2017. An oral microjet vaccination system elicits antibody production in rabbits. *Science Translational Medicine* 9, eaaf6413.

Arden, N.S., Fisher, A.C., Tyner, K., Lawrence, X.Y., Lee, S.L., Kopcha, M., 2021. Industry 4.0 for Pharmaceutical Manufacturing: Preparing for the Smart Factories of the Future. *International Journal of Pharmaceutics*, 120554.

Arif, T., 2015. Salicylic acid as a peeling agent: a comprehensive review. *Clinical, Cosmetic and Investigational Dermatology* 8, 455.

Asikainen, S., van Bochove, B., Seppälä, J.V., 2019. Drug-releasing biopolymeric structures manufactured via stereolithography. *Biomedical Physics & Engineering Express* 5, 025008.

ASTM ISO, 2022a. ASTM52900-15 Standard Terminology for Additive Manufacturing—General Principles—Terminology.https://www.astm.org/f3177-15.html, (accessed 20th October, 2022).

ASTM ISO, 2022b. ASTM D638-14, Standard Test Method for Tensile Properties of Plastics.https://www.astm.org/d0638-14.html, (accessed 20th October, 2022).

Awad, A., Fina, F., Goyanes, A., Gaisford, S., Basit, A.W., 2021a. Advances in powder bed fusion 3D printing in drug delivery and healthcare. *Advanced Drug Delivery Reviews* 174, 406-424.

Awad, A., Fina, F., Trenfield, S.J., Patel, P., Goyanes, A., Gaisford, S., Basit, A.W., 2019. 3D Printed Pellets (Miniprintlets): A Novel, Multi-Drug, Controlled Release Platform Technology. *Pharmaceutics* 11.

Awad, A., Trenfield, S.J., Gaisford, S., Basit, A.W., 2018a. 3D printed medicines: A new branch of digital healthcare. *International Journal of Pharmaceutics* 548, 586-596.

Awad, A., Trenfield, S.J., Goyanes, A., Gaisford, S., Basit, A.W., 2018b. Reshaping drug development using 3D printing. *Drug Discovery Today* 23, 1547-1555.

Awad, A., Trenfield, S.J., Pollard, T.D., Ong, J.J., Elbadawi, M., McCoubrey, L.E., Goyanes, A., Gaisford, S., Basit, A.W., 2021b. Connected healthcare: Improving patient care using digital health technologies. *Advanced Drug Delivery Reviews* 178, 113958.

Awad, A., Yao, A., Trenfield, S.J., Goyanes, A., Gaisford, S., Basit, A.W., 2020. 3D Printed Tablets (Printlets) with Braille and Moon Patterns for Visually Impaired Patients. *Pharmaceutics* 12, 172.

Awwad, S., Day, R.M., Khaw, P.T., Brocchini, S., Fadda, H.M., 2017a. Sustained release ophthalmic dexamethasone: In vitro in vivo correlations derived from the PK-Eye. *International Journal of Pharmaceutics* 522, 119-127.

Awwad, S., Lockwood, A., Brocchini, S., Khaw, P.T., 2015. The PK-Eye: a novel in vitro ocular flow model for use in preclinical drug development. *Journal of Pharmaceutical Sciences* 104, 3330-3342.

Awwad, S., Mohamed Ahmed, A.H.A., Sharma, G., Heng, J.S., Khaw, P.T., Brocchini, S., Lockwood, A., 2017b. Principles of pharmacology in the eye. *British Journal of Pharmacology* 174, 4205-4223.

Azad, M.A., Olawuni, D., Kimbell, G., Badruddoza, A.Z.M., Hossain, M., Sultana, T., 2020. Polymers for extrusion-based 3D printing of pharmaceuticals: A holistic materials–process perspective. *Pharmaceutics* 12, 124.

Bagheri, A., Jin, J., 2019. Photopolymerization in 3D Printing. *ACS Applied Polymer Materials* 1, 593-611.

Bahney, C., Lujan, T., Hsu, C., Bottlang, M., West, J., Johnstone, B., 2011. Visible light photoinitiation of mesenchymal stem cell-laden bioresponsive hydrogels. *European cells & materials* 22, 43.

Banks, J., 2013. Adding value in additive manufacturing: researchers in the United Kingdom and Europe look to 3D printing for customization. *IEEE pulse* 4, 22-26.

Bártolo, P.J., 2011. Stereolithography: materials, processes and applications. Springer Science & Business Media.

Bashi, Y.H.D., Murphy, D.J., McCoy, C.F., Boyd, P., Brown, L., Kihara, M., Martin, F., McMullen, N., Kleinbeck, K., Dangi, B., 2021. Silicone elastomer formulations for improved performance of a multipurpose vaginal ring releasing dapivirine and levonorgestrel. *International Journal of Pharmaceutics: X* 3, 100091.

Basit, A.W., Gaisford, S., 2018. 3D Printing of Pharmaceuticals. Springer.

Beg, S., Almalki, W.H., Malik, A., Farhan, M., Aatif, M., Rahman, Z., Alruwaili, N.K., Alrobaian, M., Tarique, M., Rahman, M., 2020. 3D printing for drug delivery and biomedical applications. *Drug Discovery Today* 25, 1668-1681.

Bellinger, A.M., Jafari, M., Grant, T.M., Zhang, S., Slater, H.C., Wenger, E.A., Mo, S., Lee, Y.-A.L., Mazdiyasni, H., Kogan, L., 2016. Oral, ultra–long-lasting drug delivery: application toward malaria elimination goals. *Science Translational Medicine* 8, 365ra157-365ra157.

Bennett, J., 2017. Measuring UV curing parameters of commercial photopolymers used in additive manufacturing. *Additive Manufacturing* 18, 203-212.

Bernal, P.N., Delrot, P., Loterie, D., Li, Y., Malda, J., Moser, C., Levato, R., 2019. Volumetric bioprinting of complex living‐tissue constructs within seconds. *Advanced Materials* 31, 1904209.

Bertolotti, S., Previtali, C., Rufs, A., Encinas, M., 1999. Riboflavin/triethanolamine as photoinitiator system of vinyl polymerization. A mechanistic study by laser flash photolysis. *Macromolecules* 32, 2920-2924.

Blanchette, C.D., Knipe, J.M., Stolaroff, J.K., DeOtte, J.R., Oakdale, J.S., Maiti, A., Lenhardt, J.M., Sirajuddin, S., Rosenzweig, A.C., Baker, S.E., 2016. Printable enzyme-embedded materials for methane to methanol conversion. *Nature Communications* 7, 1-9.

Bloomquist, C.J., Mecham, M.B., Paradzinsky, M.D., Janusziewicz, R., Warner, S.B., Luft, J.C., Mecham, S.J., Wang, A.Z., DeSimone, J.M., 2018. Controlling release from 3D printed medical devices using CLIP and drug-loaded liquid resins. *Journal of Controlled Release* 278, 9-23.

BNF, 2021. Warfarin sodium

Bozuyuk, U., Yasa, O., Yasa, I.C., Ceylan, H., Kizilel, S., Sitti, M., 2018. Light-triggered drug release from 3D-printed magnetic chitosan microswimmers. *ACS Nano* 12, 9617-9625.

Branciforti, D.S., Lazzaroni, S., Milanese, C., Castiglioni, M., Auricchio, F., Pasini, D., Dondi, D., 2019. Visible light 3D printing with epoxidized vegetable oils. *Additive Manufacturing* 25, 317-324.

Breloy, L., Ouarabi, C.A., Brosseau, A., Dubot, P., Brezova, V., Abbad Andaloussi, S., Malval, J.-P., Versace, D.-L., 2019. β-Carotene/limonene derivatives/eugenol: Green synthesis of antibacterial coatings under visible-light exposure. *ACS Sustainable Chemistry & Engineering* 7, 19591-19604.

Bruschi, M.L., 2015. Mathematical models of drug release. Woodhead Publishing Cambridge, UK, pp. 63-86.

Bryant, S.J., Nuttelman, C.R., Anseth, K.S., 2000. Cytocompatibility of UV and visible light photoinitiating systems on cultured NIH/3T3 fibroblasts in vitro. *Journal of Biomaterials Science, Polymer Edition* 11, 439-457.

Castro, B.M., Elbadawi, M., Ong, J.J., Pollard, T., Song, Z., Gaisford, S., Pérez, G., Basit, A.W., Cabalar, P., Goyanes, A., 2021. Machine learning predicts 3D printing performance of over 900 drug delivery systems. *Journal of Controlled Release* 337, 530-545.

Caudill, C.L., Perry, J.L., Tian, S., Luft, J.C., DeSimone, J.M., 2018. Spatially controlled coating of continuous liquid interface production microneedles for transdermal protein delivery. *Journal of Controlled Release* 284, 122-132.

Charlesworth, C.J., Smit, E., Lee, D.S., Alramadhan, F., Odden, M.C., 2015. Polypharmacy among adults aged 65 years and older in the United States: 1988–2010. *Journals of Gerontology Series A: Biomedical Sciences and Medical Sciences* 70, 989-995.

Chee, S.-P., 2012. Moxifloxacin punctum plug for sustained drug delivery. *Journal of Ocular Pharmacology and Therapeutics* 28, 340-349.

Chen, K.-Y., Zeng, J.-J., Lin, G.-T., 2022. Fabrication of 5-fluorouracil-loaded tablets with hyperbranched polyester by digital light processing 3D printing technology. *European Polymer Journal*, 111190.

Chikukwa, M.T., Walker, R.B., Khamanga, S.M., 2020. Formulation and characterisation of a combination captopril and hydrochlorothiazide microparticulate dosage form. *Pharmaceutics* 12, 712.

Choi, J.-W., Kim, H.-C., Wicker, R., 2011. Multi-material stereolithography. *Journal of Materials Processing Technology* 211, 318-328.

Choong, Y.Y.C., Tan, H.W., Patel, D.C., Choong, W.T.N., Chen, C.-H., Low, H.Y., Tan, M.J., Patel, C.D., Chua, C.K., 2020. The global rise of 3D printing during the COVID-19 pandemic. *Nature Reviews Materials* 5, 637-639.

Choudhury, D., Sharma, P.K., Suryanarayana Murty, U., Banerjee, S., 2021. Stereolithography-assisted fabrication of 3D printed polymeric film for topical berberine delivery: in-vitro, ex-vivo and in-vivo investigations. *Journal of Pharmacy and Pharmacology*.

Chow, C.K., Thakkar, J., Bennett, A., Hillis, G., Burke, M., Usherwood, T., Vo, K., Rogers, K., Atkins, E., Webster, R., Chou, M., Dehbi, H.M., Salam, A., Patel, A., Neal, B., Peiris, D., Krum, H., Chalmers, J., Nelson, M., Reid, C.M., Woodward, M., Hilmer, S., Thom, S., Rodgers, A., 2017. Quarter-dose quadruple combination therapy for initial treatment of hypertension: placebo-controlled, crossover, randomised trial and systematic review. *Lancet* 389, 1035-1042.

Cima, M.J., Lee, H., Daniel, K., Tanenbaum, L.M., Mantzavinou, A., Spencer, K.C., Ong, Q., Sy, J.C., Santini Jr, J., Schoellhammer, C.M., 2014. Single compartment drug delivery. *Journal of Controlled Release* 190, 157-171.

Clark, E.A., Alexander, M.R., Irvine, D.J., Roberts, C.J., Wallace, M.J., Sharpe, S., Yoo, J., Hague, R.J., Tuck, C.J., Wildman, R.D., 2017. 3D printing of tablets using inkjet with UV photoinitiation. *International Journal of Pharmaceutics* 529, 523-530.

Coursey, T.G., Henriksson, J.T., Marcano, D.C., Shin, C.S., Isenhart, L.C., Ahmed, F., De Paiva, C.S., Pflugfelder, S.C., Acharya, G., 2015. Dexamethasone nanowafer as an effective therapy for dry eye disease. *Journal of Controlled Release* 213, 168-174.

D'hers, S., Abad Vazquez, A.N., Gurman, P., Elman, N.M., 2019. Rapid reconstitution packages (RRPs) for stable storage and delivery of glucagon. *Drug Delivery and Translational Research* 9, 631-640.

da Silva, G.R., da Silva-Cunha Jr, A., Behar-Cohen, F., Ayres, E., Orefice, R.L., 2011. Biodegradable polyurethane nanocomposites containing dexamethasone for ocular route. *Materials Science and Engineering: C* 31, 414-422.

Darwish, I.A., Darwish, H.W., Bakheit, A.H., Al-Kahtani, H.M., Alanazi, Z., 2021. Irbesartan (a comprehensive profile). *Profiles of Drug Substances, Excipients and Related Methodology* 46, 185-272.

De Beer, M.P., Van Der Laan, H.L., Cole, M.A., Whelan, R.J., Burns, M.A., Scott, T.F., 2019. Rapid, continuous additive manufacturing by volumetric polymerization inhibition patterning. *Science Advances* 5, eaau8723.

de Oliveira, R.S., Fantaus, S.S., Guillot, A.J., Melero, A., Beck, R.C.R., 2021. 3D-Printed Products for Topical Skin Applications: From Personalized Dressings to Drug Delivery. *Pharmaceutics* 13, 1946.

Detamornrat, U., McAlister, E., Hutton, A.R., Larrañeta, E., Donnelly, R.F., 2022. The Role of 3D Printing Technology in Microengineering of Microneedles. *Small* 18, 2106392.

Di, J., Yao, S., Ye, Y., Cui, Z., Yu, J., Ghosh, T.K., Zhu, Y., Gu, Z., 2015. Stretch-triggered drug delivery from wearable elastomer films containing therapeutic depots. *ACS Nano* 9, 9407-9415.

Digesu, G.A., Tailor, V., Bhide, A.A., Khullar, V., 2020. The role of bladder instillation in the treatment of bladder pain syndrome: Is intravesical treatment an effective option for patients with bladder pain as well as LUTS? *International Urogynecology Journal* 31, 1387-1392.

Do, A.-V., Worthington, K.S., Tucker, B.A., Salem, A.K., 2018. Controlled drug delivery from 3D printed two-photon polymerized poly (ethylene glycol) dimethacrylate devices. *International Journal of Pharmaceutics* 552, 217-224.

Dodziuk, H., 2016. Applications of 3D printing in healthcare. *Kardiochirurgia i torakochirurgia polska/Polish Journal of Cardiovascular Surgery* 13, 283-293.

Dolinski, N.D., Page, Z.A., Callaway, E.B., Eisenreich, F., Garcia, R.V., Chavez, R., Bothman, D.P., Hecht, S., Zok, F.W., Hawker, C.J., 2018. Solution Mask Liquid Lithography (SMaLL) for One‐Step, Multimaterial 3D Printing. *Advanced Materials* 30, 1800364.

Donnelly, R.F., Singh, T.R.R., Woolfson, A.D., 2010. Microneedle-based drug delivery systems: microfabrication, drug delivery, and safety. *Drug Delivery* 17, 187-207.

Dubbin, K., Dong, Z., Park, D.M., Alvarado, J., Su, J., Wasson, E., Robertson, C., Jackson, J., Bose, A., Moya, M.L., 2021. Projection Microstereolithographic Microbial Bioprinting for Engineered Biofilms. *Nano Letters* 21, 1352-1359.

Dumpa, N., Butreddy, A., Wang, H., Komanduri, N., Bandari, S., Repka, M.A., 2021. 3D printing in personalized drug delivery: An overview of hot-melt extrusion-based fused deposition modeling. *International Journal of Pharmaceutics* 600, 120501.

Dumur, F., 2021. Recent advances on ferrocene-based photoinitiating systems. *European Polymer Journal* 147, 110328.

Economidou, S.N., Pere, C.P.P., Reid, A., Uddin, M.J., Windmill, J.F., Lamprou, D.A., Douroumis, D., 2019. 3D printed microneedle patches using stereolithography (SLA) for intradermal insulin delivery. *Materials Science and Engineering: C* 102, 743-755.

El-Gizawy, S.A., Osman, M.A., Arafa, M.F., El Maghraby, G.M., 2015. Aerosil as a novel co-crystal co-former for improving the dissolution rate of hydrochlorothiazide. *International Journal of Pharmaceutics* 478, 773-778.

Elbadawi, M., McCoubrey, L.E., Gavins, F.K.H., Ong, J.J., Goyanes, A., Gaisford, S., Basit, A.W., 2021a. Disrupting 3D printing of medicines with machine learning. *Trends in Pharmacological Sciences* 42, 745-757.

Elbadawi, M., McCoubrey, L.E., Gavins, F.K.H., Ong, J.J., Goyanes, A., Gaisford, S., Basit, A.W., 2021b. Harnessing artificial intelligence for the next generation of 3D printed medicines. *Advanced Drug Delivery Reviews* 175, 113805.

Elbadawi, M., Ong, J.J., Pollard, T.D., Gaisford, S., Basit, A.W., 2020. Additive Manufacturable Materials for Electrochemical Biosensor Electrodes. *Advanced Functional Materials*, 2006407.

Eleftheriadis, G.K., Fatouros, D.G., 2021. Haptic evaluation of 3D-printed braille-encoded intraoral films. *European Journal of Pharmaceutical Sciences* 157, 105605.

Ervin, A.M., Law, A., Pucker, A.D., 2017. Punctal occlusion for dry eye syndrome. *Cochrane Database of Systematic Reviews*.

Fadda, H.M., Basit, A.W., 2005. Dissolution of pH responsive formulations in media resembling intestinal fluids: bicarbonate versus phosphate buffers. *Journal of Drug Delivery Science and Technology* 15, 273-279.

Fairbanks, B.D., Schwartz, M.P., Bowman, C.N., Anseth, K.S., 2009. Photoinitiated polymerization of PEG-diacrylate with lithium phenyl-2, 4, 6-trimethylbenzoylphosphinate: polymerization rate and cytocompatibility. *Biomaterials* 30, 6702-6707.

FDA, 2015. 510(k) Premarket Notification: Dentca Denture Base. 510 (k) Number K143033.https://www.accessdata.fda.gov/scripts/cdrh/cfdocs/cfpmn/pmn.cfm?ID=K143033, (accessed 13th Apr, 2020).

FDA, 2017. 510(k) Premarket Notification: NextDent Denture/E-Denture. 510 (k) Number K162572.https://www.accessdata.fda.gov/scripts/cdrh/cfdocs/cfpmn/pmn.cfm?ID=K162572, (accessed 13th Apr, 2020).

Field, J., Haycock, J.W., Boissonade, F.M., Claeyssens, F., 2021. A Tuneable, Photocurable, Poly (Caprolactone)-Based Resin for Tissue Engineering—Synthesis, Characterisation and Use in Stereolithography. *Molecules* 26, 1199.

Fina, F., Gaisford, S., Basit, A.W., 2018a. Powder bed fusion: The working process, current applications and opportunities, 3D printing of pharmaceuticals. Springer, pp. 81-105.

Fina, F., Goyanes, A., Madla, C.M., Awad, A., Trenfield, S.J., Kuek, J.M., Patel, P., Gaisford, S., Basit, A.W., 2018b. 3D printing of drug-loaded gyroid lattices using selective laser sintering. *International Journal of Pharmaceutics* 547, 44-52.

Fina, F., Goyanes, A., Rowland, M., Gaisford, S., W Basit, A., 2020. 3D Printing of Tunable Zero-Order Release Printlets. *Polymers* 12, 1769.

Fina, F., Madla, C.M., Goyanes, A., Zhang, J., Gaisford, S., Basit, A.W., 2018c. Fabricating 3D printed orally disintegrating printlets using selective laser sintering. *International Journal of Pharmaceutics* 541, 101-107.

Formlabs, 2019. Introducing Elastic Resin: A Soft, Resilient 3D Printing Material.https://formlabs.com/blog/elastic-resin-soft-resilient-3d-printing/, (accessed 2nd April, 2020).

Fouassier, J.-P., Lalevée, J., 2012. Photoinitiators for polymer synthesis: scope, reactivity, and efficiency. John Wiley & Sons.

Fouassier, J.P., Allonas, X., Lalevée, J., Dietlin, C., 2010. Photoinitiators for free radical polymerization reactions. *Photochemistry and photophysics of polymer materials. Wiley, Hoboken*, 351-419.

Foulds, W.S., 1961. Intra-canalicular gelatin implants in the treatment of kerato-conjunctivitis sicca. *The British Journal of Ophthalmology* 45, 625.

Fraser, M.O., Lavelle, J.P., Sacks, M.S., Chancellor, M.B., 2002. The future of bladder control—intravesical drug delivery, a pinch of pepper, and gene therapy. *Reviews in Urology* 4, 1.

Freire, F., Costa, A.C.B.P., Pereira, C.A., Junior, M.B., Junqueira, J.C., Jorge, A.O.C., 2014. Comparison of the effect of rose bengal-and eosin Y-mediated photodynamic inactivation on planktonic cells and biofilms of Candida albicans. *Lasers in Medical Science* 29, 949-955.

Fu, J., Yu, X., Jin, Y., 2018. 3D printing of vaginal rings with personalized shapes for controlled release of progesterone. *International Journal of Pharmaceutics* 539, 75-82.

Garcia, J., Yang, Z., Mongrain, R., Leask, R.L., Lachapelle, K., 2018. 3D printing materials and their use in medical education: a review of current technology and trends for the future. *BMJ Simulation & Technology Enhanced Learning* 4, 27.

Gattefosse, Gelucire® 48/16.https://www.gattefosse.com/pharmaceuticals-products/gelucire-4816, (accessed 7th October, 2019).

Ge, Q., Sakhaei, A.H., Lee, H., Dunn, C.K., Fang, N.X., Dunn, M.L., 2016. Multimaterial 4D printing with tailorable shape memory polymers. *Scientific Reports* 6, 1-11.

Genina, N., Holländer, J., Jukarainen, H., Mäkilä, E., Salonen, J., Sandler, N., 2016. Ethylene vinyl acetate (EVA) as a new drug carrier for 3D printed medical drug delivery devices. *European Journal of Pharmaceutical Sciences* 90, 53-63.

Gennari, C.G.M., Quaroni, G.M.G., Creton, C., Minghetti, P., Cilurzo, F., 2020. SEBS block copolymers as novel materials to design transdermal patches. *International Journal of Pharmaceutics* 575, 118975.

Ghosh, U., Ning, S., Wang, Y., Kong, Y.L., 2018. Addressing unmet clinical needs with 3D printing technologies. *Advanced Healthcare Materials* 7, 1800417.

Gioumouxouzis, C.I., Katsamenis, O.L., Bouropoulos, N., Fatouros, D.G., 2017. 3D printed oral solid dosage forms containing hydrochlorothiazide for controlled drug delivery. *Journal of Drug Delivery Science and Technology* 40, 164-171.

Gittard, S.D., Ovsianikov, A., Akar, H., Chichkov, B., Monteiro‐Riviere, N.A., Stafslien, S., Chisholm, B., Shin, C.C., Shih, C.M., Lin, S.J., 2010. Two Photon Polymerization‐Micromolding of Polyethylene Glycol‐Gentamicin Sulfate Microneedles. *Advanced Engineering Materials* 12, B77-B82.

Gnanasekaran, K., Heijmans, T., Van Bennekom, S., Woldhuis, H., Wijnia, S., De With, G., Friedrich, H., 2017. 3D printing of CNT-and graphene-based conductive

polymer nanocomposites by fused deposition modeling. *Applied Materials Today* 9, 21-28.

Goh, W.J., Tan, S.X., Pastorin, G., Ho, P.C.L., Hu, J., Lim, S.H., 2021. 3D printing of four-in-one oral polypill with multiple release profiles for personalized delivery of caffeine and vitamin B analogues. *International Journal of Pharmaceutics* 598, 120360.

Göppert‑Mayer, M., 1931. Über elementarakte mit zwei quantensprüngen. *Annalen der Physik* 401, 273-294.

Gote, V., Sikder, S., Sicotte, J., Pal, D., 2019. Ocular drug delivery: present innovations and future challenges. *Journal of Pharmacology and Experimental Therapeutics* 370, 602-624.

Goto, E., Yagi, Y., Kaido, M., Matsumoto, Y., Konomi, K., Tsubota, K., 2003. Improved functional visual acuity after punctal occlusion in dry eye patients. *American Journal of Ophthalmology* 135, 704-705.

Goyanes, A., Buanz, A.B., Basit, A.W., Gaisford, S., 2014. Fused-filament 3D printing (3DP) for fabrication of tablets. *International Journal of Pharmaceutics* 476, 88-92.

Goyanes, A., Det-Amornrat, U., Wang, J., Basit, A.W., Gaisford, S., 2016. 3D scanning and 3D printing as innovative technologies for fabricating personalized topical drug delivery systems. *Journal of Controlled Release* 234, 41-48.

Goyanes, A., Fernández-Ferreiro, A., Majeed, A., Gomez-Lado, N., Awad, A., Luaces-Rodríguez, A., Gaisford, S., Aguiar, P., Basit, A.W., 2018. PET/CT imaging of 3D printed devices in the gastrointestinal tract of rodents. *International Journal of Pharmaceutics* 536, 158-164.

Goyanes, A., Fina, F., Martorana, A., Sedough, D., Gaisford, S., Basit, A.W., 2017a. Development of modified release 3D printed tablets (printlets) with pharmaceutical excipients using additive manufacturing. *International Journal of Pharmaceutics* 527, 21-30.

Goyanes, A., Hatton, G.B., Merchant, H.A., Basit, A.W., 2015a. Gastrointestinal release behaviour of modified-release drug products: Dynamic dissolution testing of mesalazine formulations. *International Journal of Pharmaceutics* 484, 103-108.

Goyanes, A., Madla, C.M., Umerji, A., Piñeiro, G.D., Montero, J.M.G., Diaz, M.J.L., Barcia, M.G., Taherali, F., Sánchez-Pintos, P., Couce, M.-L., 2019. Automated therapy preparation of isoleucine formulations using 3D printing for the treatment of MSUD: First single-centre, prospective, crossover study in patients. *International Journal of Pharmaceutics* 567, 118497.

Goyanes, A., Robles Martinez, P., Buanz, A., Basit, A.W., Gaisford, S., 2015b. Effect of geometry on drug release from 3D printed tablets. *International Journal of Pharmaceutics* 494, 657-663.

Goyanes, A., Scarpa, M., Kamlow, M., Gaisford, S., Basit, A.W., Orlu, M., 2017b. Patient acceptability of 3D printed medicines. *International Journal of Pharmaceutics* 530, 71-78.

Goyanes, A., Wang, J., Buanz, A., Martinez-Pacheco, R., Telford, R., Gaisford, S., Basit, A.W., 2015c. 3D Printing of Medicines: Engineering Novel Oral Devices with Unique Design and Drug Release Characteristics. *Molecular Pharmaceutics* 12, 4077-4084.

Grigoryan, B., Paulsen, S.J., Corbett, D.C., Sazer, D.W., Fortin, C.L., Zaita, A.J., Greenfield, P.T., Calafat, N.J., Gounley, J.P., Ta, A.H., 2019. Multivascular networks and functional intravascular topologies within biocompatible hydrogels. *Science* 364, 458-464.

Gupta, C., Chauhan, A., 2011. Ophthalmic delivery of cyclosporine A by punctal plugs. *Journal of Controlled Release* 150, 70-76.

Guttridge, C., Shannon, A., O'Sullivan, A., O'Sullivan, K.J., O'Sullivan, L.W., 2021. Biocompatible 3D printing resins for medical applications: a review of marketed intended uses, biocompatibility certification, and post-processing guidance. *Annals of 3D Printed Medicine*, 100044.

Halloran, J.W., 2016. Ceramic stereolithography: additive manufacturing for ceramics by photopolymerization. *Annual Review of Materials Research* 46, 19-40.

Han, D., Morde, R.S., Mariani, S., La Mattina, A.A., Vignali, E., Yang, C., Barillaro, G., Lee, H., 2020. 4D printing of a bioinspired microneedle array with backward‐facing barbs for enhanced tissue adhesion. *Advanced Functional Materials* 30, 1909197.

Han, D., Yang, C., Fang, N.X., Lee, H., 2019. Rapid multi-material 3D printing with projection micro-stereolithography using dynamic fluidic control. *Additive Manufacturing* 27, 606-615.

Haring, A.P., Tong, Y., Halper, J., Johnson, B.N., 2018. Programming of multicomponent temporal release profiles in 3D printed polypills via core–shell, multilayer, and gradient concentration profiles. *Advanced Healthcare Materials* 7, 1800213.

He, R., Kyu, T., 2016. Effect of plasticization on ionic conductivity enhancement in relation to glass transition temperature of crosslinked polymer electrolyte membranes. *Macromolecules* 49, 5637-5648.

Healy, A.V., Fuenmayor, E., Doran, P., Geever, L.M., Higginbotham, C.L., Lyons, J.G., 2019. Additive Manufacturing of Personalized Pharmaceutical Dosage Forms via Stereolithography. *Pharmaceutics* 11, 645.

Herrada-Manchón, H., Rodríguez-González, D., Fernández, M.A., Suñé-Pou, M., Pérez-Lozano, P., García-Montoya, E., Aguilar, E., 2020. 3D printed gummies: Personalized drug dosage in a safe and appealing way. *International Journal of Pharmaceutics* 587, 119687.

Hirschberg, C., Edinger, M., Holmfred, E., Rantanen, J., Boetker, J., 2020. Image-Based Artificial Intelligence Methods for Product Control of Tablet Coating Quality. *Pharmaceutics* 12.

Hopmann, C., Kaltbeitzel, D., Kauth, T., Dittrich, B., Grosse, J., Huppertz, N., Schwantes, U., Neumeister, C., von Walter, M., Hemateq, A., 2015. Degradation of microcellular PLGA-PEG copolymer for use in a drug delivery system for the urinary bladder. *Plastics Engineering* 71, 60-64.

Huang, D., Chen, Y.-S., Rupenthal, I.D., 2018. Overcoming ocular drug delivery barriers through the use of physical forces. *Advanced Drug Delivery Reviews* 126, 96-112.

Hull, C.W., 1984. Apparatus for production of three-dimensional objects by stereolithography. US4575330A.

Infanger, S., Haemmerli, A., Iliev, S., Baier, A., Stoyanov, E., Quodbach, J., 2019. Powder bed 3D-printing of highly loaded drug delivery devices with hydroxypropyl cellulose as solid binder. *International Journal of Pharmaceutics* 555, 198-206.

Innoventions Ltd, PharmaSphere Intravesical Drug Delivery.https://www.innoventions-med.com/pharmasphere, (accessed 7th June, 2020).

Inzana, J.A., Olvera, D., Fuller, S.M., Kelly, J.P., Graeve, O.A., Schwarz, E.M., Kates, S.L., Awad, H.A., 2014. 3D printing of composite calcium phosphate and collagen scaffolds for bone regeneration. *Biomaterials* 35, 4026-4034.

Jacobs, P.F., 1992. Fundamentals of stereolithography, 1992 International Solid Freeform Fabrication Symposium.

Jamróz, W., Kurek, M., Łyszczarz, E., Szafraniec, J., Knapik-Kowalczuk, J., Syrek, K., Paluch, M., Jachowicz, R., 2017. 3D printed orodispersible films with Aripiprazole. *International Journal of Pharmaceutics* 533, 413-420.

Jani, J.M., Leary, M., Subic, A., Gibson, M.A., 2014. A review of shape memory alloy research, applications and opportunities. *Materials & Design (1980-2015)* 56, 1078-1113.

Januskaite, P., Xu, X., Ranmal, S.R., Gaisford, S., Basit, A.W., Tuleu, C., Goyanes, A., 2020. I spy with my little eye: A paediatric visual preferences survey of 3D printed tablets. *Pharmaceutics* 12, 1100.

Januszewicz, R., Mecham, S.J., Olson, K.R., Benhabbour, S.R., 2020. Design and Characterization of a Novel Series of Geometrically Complex Intravaginal Rings with Digital Light Synthesis. *Advanced Materials Technologies* 5, 2000261.

Jehangir, N., Bever, G., Mahmood, S.M., Moshirfar, M., 2016. Comprehensive Review of the Literature on Existing Punctal Plugs for the Management of Dry Eye Disease. *J Ophthalmol* 2016, 9312340.

Jiang, H., Yu, X., Fang, R., Xiao, Z., Jin, Y., 2019a. 3D printed mold-based capsaicin candy for the treatment of oral ulcer. *International Journal of Pharmaceutics* 568, 118517.

Jiang, T., Munguia-Lopez, J.G., Flores-Torres, S., Kort-Mascort, J., Kinsella, J.M., 2019b. Extrusion bioprinting of soft materials: An emerging technique for biological model fabrication. *Applied Physics Reviews* 6, 011310.

Johnson, A.R., Caudill, C.L., Tumbleston, J.R., Bloomquist, C.J., Moga, K.A., Ermoshkin, A., Shirvanyants, D., Mecham, S.J., Luft, J.C., DeSimone, J.M., 2016. Single-step fabrication of computationally designed microneedles by continuous liquid interface production. *PLoS One* 11.

Joshi, S.C., Sheikh, A.A., 2015. 3D printing in aerospace and its long-term sustainability. *Virtual and Physical Prototyping* 10, 175-185.

Jumelle, C., Gholizadeh, S., Annabi, N., Dana, R., 2020. Advances and limitations of drug delivery systems formulated as eye drops. *Journal of Controlled Release* 321, 1-22.

Jung, J.H., Chiang, B., Grossniklaus, H.E., Prausnitz, M.R., 2018. Ocular drug delivery targeted by iontophoresis in the suprachoroidal space using a microneedle. *Journal of Controlled Release* 277, 14-22.

Kadry, H., Wadnap, S., Xu, C., Ahsan, F., 2019. Digital light processing (DLP) 3D-printing technology and photoreactive polymers in fabrication of modified-release tablets. *European Journal of Pharmaceutical Sciences* 135, 60-67.

Kalkal, A., Kumar, S., Kumar, P., Pradhan, R., Willander, M., Packirisamy, G., Kumar, S., Malhotra, B.D., 2021. Recent advances in 3D printing technologies for wearable (bio) sensors. *Additive Manufacturing* 46, 102088.

Kanyilmaz, A., Demir, A.G., Chierici, M., Berto, F., Gardner, L., Kandukuri, S.Y., Kassabian, P., Kinoshita, T., Laurenti, A., Paoletti, I., 2021. Role of metal 3D printing to increase quality and resource-efficiency in the construction sector. *Additive Manufacturing*, 102541.

Karakurt, I., Aydoğdu, A., Çıkrıkcı, S., Orozco, J., Lin, L., 2020. Stereolithography (SLA) 3D Printing of Ascorbic Acid Loaded Hydrogels: A Controlled Release Study. *International Journal of Pharmaceutics*, 119428.

Karavasili, C., Gkaragkounis, A., Moschakis, T., Ritzoulis, C., Fatouros, D.G., 2020a. Paediatric-friendly chocolate-based dosage forms for the oral administration of both hydrophilic and lipophilic drugs fabricated with extrusion-based 3D printing. *European Journal of Pharmaceutical Sciences*, 105291.

Karavasili, C., Tsongas, K., Andreadis, I.I., Andriotis, E.G., Papachristou, E.T., Papi, R.M., Tzetzis, D., Fatouros, D.G., 2020b. Physico-mechanical and finite element analysis evaluation of 3D printable alginate-methylcellulose inks for wound healing applications. *Carbohydrate Polymers* 247, 116666.

Kasim, N.A., Whitehouse, M., Ramachandran, C., Bermejo, M., Lennernäs, H., Hussain, A.S., Junginger, H.E., Stavchansky, S.A., Midha, K.K., Shah, V.P., 2004.

Molecular properties of WHO essential drugs and provisional biopharmaceutical classification. *Molecular Pharmaceutics* 1, 85-96.

Katstra, W., Palazzolo, R., Rowe, C., Giritlioglu, B., Teung, P., Cima, M., 2000. Oral dosage forms fabricated by Three Dimensional Printing™. *Journal of Controlled Release* 66, 1-9.

Kawata, S., Sun, H.-B., Tanaka, T., Takada, K., 2001. Finer features for functional microdevices. *Nature* 412, 697-698.

Kelly, B.E., Bhattacharya, I., Heidari, H., Shusteff, M., Spadaccini, C.M., Taylor, H.K., 2019. Volumetric additive manufacturing via tomographic reconstruction. *Science* 363, 1075-1079.

Khaled, S.A., Burley, J.C., Alexander, M.R., Roberts, C.J., 2014. Desktop 3D printing of controlled release pharmaceutical bilayer tablets. *International Journal of Pharmaceutics* 461, 105-111.

Khaled, S.A., Burley, J.C., Alexander, M.R., Yang, J., Roberts, C.J., 2015a. 3D printing of five-in-one dose combination polypill with defined immediate and sustained release profiles. *Journal of Control Release* 217, 308-314.

Khaled, S.A., Burley, J.C., Alexander, M.R., Yang, J., Roberts, C.J., 2015b. 3D printing of tablets containing multiple drugs with defined release profiles. *International Journal of Pharmaceutics* 494, 643-650.

Khan, A., Iqbal, Z., Shah, Y., Ahmad, L., Ullah, Z., Ullah, A., 2015. Enhancement of dissolution rate of class II drugs (Hydrochlorothiazide); a comparative study of the two novel approaches; solid dispersion and liqui-solid techniques. *Saudi Pharmaceutical Journal* 23, 650-657.

Khorsandi, D., Fahimipour, A., Abasian, P., Saber, S.S., Seyedi, M., Ghanavati, S., Ahmad, A., De Stephanis, A.A., Taghavinezhaddilami, F., Leonova, A., 2021. 3D and 4D printing in dentistry and maxillofacial surgery: Printing techniques, materials, and applications. *Acta Biomaterialia* 122, 26-49.

Kickstarter, 2021a. ONO - The $99 Smartphone 3D Printer.https://www.kickstarter.com/projects/olo3d/olo-the-first-ever-smartphone-3d-printer/description, (accessed 23rd July, 2021).

Kickstarter, 2021b. T3D - The World's First Mobile Multifunction 3D Printer.https://www.kickstarter.com/projects/906506734/t3d-the-worlds-first-mobile-multifunction-3d-print, (accessed 23rd July, 2021).

Kim, G.-T., Go, H.-B., Yu, J.-H., Yang, S.-Y., Kim, K.-M., Choi, S.-H., Kwon, J.-S., 2022. Cytotoxicity, Colour Stability and Dimensional Accuracy of 3D Printing Resin with Three Different Photoinitiators. *Polymers* 14, 979.

Kim, S.-h., Chu, C.-C., 2009. Visible light induced dextran-methacrylate hydrogel formation using (−)-riboflavin vitamin B2 as a photoinitiator and L-arginine as a co-initiator. *Fibers and Polymers* 10, 14-20.

Kimmel, S.E., 2008. Warfarin therapy: in need of improvement after all these years. *Expert opinion on pharmacotherapy* 9, 677-686.

Kirtane, A.R., Abouzid, O., Minahan, D., Bensel, T., Hill, A.L., Selinger, C., Bershteyn, A., Craig, M., Mo, S.S., Mazdiyasni, H., 2018. Development of an oral once-weekly drug delivery system for HIV antiretroviral therapy. *Nature Communications* 9, 1-12.

Kollamaram, G., Croker, D.M., Walker, G.M., Goyanes, A., Basit, A.W., Gaisford, S., 2018. Low temperature fused deposition modeling (FDM) 3D printing of thermolabile drugs. *International Journal of Pharmaceutics* 545, 144-152.

Konasch, J., Riess, A., Mau, R., Teske, M., Rekowska, N., Eickner, T., Grabow, N., Seitz, H., 2019. A Novel Hybrid Additive Manufacturing Process for Drug Delivery Systems with Locally Incorporated Drug Depots. *Pharmaceutics* 11, 661.

Kowalczuk, D., 2020. FTIR Characterization of the Development of Antimicrobial Catheter Coatings Loaded with Fluoroquinolones. *Coatings* 10, 818.

Kowsari, K., Akbari, S., Wang, D., Fang, N.X., Ge, Q., 2018. High-efficiency high-resolution multimaterial fabrication for digital light processing-based three-dimensional printing. *3D Printing and Additive Manufacturing* 5, 185-193.

Krieger, K.J., Bertollo, N., Dangol, M., Sheridan, J.T., Lowery, M.M., O'Cearbhaill, E.D., 2019. Simple and customizable method for fabrication of high-aspect ratio microneedle molds using low-cost 3D printing. *Microsystems & Nanoengineering* 5, 1-14.

Krkobabić, M., Medarević, D., Cvijić, S., Grujić, B., Ibrić, S., 2019. Hydrophilic excipients in digital light processing (DLP) printing of sustained release tablets: Impact on internal structure and drug dissolution rate. *International Journal of Pharmaceutics* 572, 118790.

Krkobabić, M., Medarević, D., Pešić, N., Vasiljević, D., Ivković, B., Ibrić, S., 2020. Digital light processing (DLP) 3D printing of atomoxetine hydrochloride tablets using photoreactive suspensions. *Pharmaceutics* 12, 833.

Kühnemund, M., Wei, Q., Darai, E., Wang, Y., Hernández-Neuta, I., Yang, Z., Tseng, D., Ahlford, A., Mathot, L., Sjöblom, T., 2017. Targeted DNA sequencing and in situ mutation analysis using mobile phone microscopy. *Nature Communications* 8, 1-8.

Laksanasopin, T., Guo, T.W., Nayak, S., Sridhara, A.A., Xie, S., Olowookere, O.O., Cadinu, P., Meng, F., Chee, N.H., Kim, J., 2015. A smartphone dongle for diagnosis of infectious diseases at the point of care. *Science Translational Medicine* 7, 273re271-273re271.

Larush, L., Kaner, I., Fluksman, A., Tamsut, A., Pawar, A.A., Lesnovski, P., Benny, O., Magdassi, S., 2017. 3D printing of responsive hydrogels for drug-delivery systems. *Journal of 3D printing in medicine* 1, 219-229.

Law, M.R., Wald, N.J., Morris, J.K., Jordan, R.E., 2003. Value of low dose combination treatment with blood pressure lowering drugs: analysis of 354 randomised trials. *BMJ* 326, 1427.

Le Néel, T.A., Mognol, P., Hascoët, J.-Y., 2018. A review on additive manufacturing of sand molds by binder jetting and selective laser sintering. *Rapid Prototyping Journal*.

Leal, J., Luengo-Fernandez, R., Sullivan, R., Witjes, J.A., 2016. Economic burden of bladder cancer across the European Union. *European Urology* 69, 438-447.

Lee, H., Cima, M.J., 2011. An intravesical device for the sustained delivery of lidocaine to the bladder. *Journal of Controlled Release* 149, 133-139.

Lee, S.H., Choy, Y.B., 2016. Implantable Devices for Sustained, Intravesical Drug Delivery. *International Neurourology Journal* 20, 101-106.

Lewis, J.A., Ahn, B.Y., 2015. Three-dimensional printed electronics. *Nature* 518, 42-43.

Li, D., Guo, G., Fan, R., Liang, J., Deng, X., Luo, F., Qian, Z., 2013. PLA/F68/Dexamethasone implants prepared by hot-melt extrusion for controlled release of anti-inflammatory drug to implantable medical devices: I. Preparation, characterization and hydrolytic degradation study. *International Journal of Pharmaceutics* 441, 365-372.

Li, D., Hao, H., Fang, B., Wang, N., Zhou, Y., Huang, X., Wang, Z., 2018. Solubility and mixing thermodynamic properties of (2, 4, 6-trimethylbenzoyl) diphenylphosphine oxide in pure and binary solvents. *Fluid Phase Equilibria* 461, 57-69.

Li, S., Pang, J., Hong, S., Chen, X., Shao, S., Wang, H., Lao, H., Xiong, L., Wu, H., Yang, W., 2022. A novel technology for preparing the placebos of vortioxetine hydrobromide tablets using LCD 3D printing. *European Journal of Pharmaceutics and Biopharmaceutics* 178, 159-167.

Li, W., Wang, M., Mille, L.S., Robledo Lara, J.A., Huerta, V., Uribe Velázquez, T., Cheng, F., Li, H., Gong, J., Ching, T., 2021. A Smartphone‑Enabled Portable Digital Light Processing 3D Printer. *Advanced Materials* 33, 2102153.

Liang, K., Carmone, S., Brambilla, D., Leroux, J.-C., 2018. 3D printing of a wearable personalized oral delivery device: A first-in-human study. *Science Advances* 4, eaat2544.

Ligon, S.C., Husar, B., Wutzel, H., Holman, R., Liska, R., 2014. Strategies to reduce oxygen inhibition in photoinduced polymerization. *Chemical Reviews* 114, 557-589.

Lim, K.S., Schon, B.S., Mekhileri, N.V., Brown, G.C., Chia, C.M., Prabakar, S., Hooper, G.J., Woodfield, T.B., 2016. New visible-light photoinitiating system for improved print fidelity in gelatin-based bioinks. *Acs Biomaterials Science & Engineering* 2, 1752-1762.

Lim, S.H., Kathuria, H., Amir, M.H.B., Zhang, X., Duong, H.T., Ho, P.C.-L., Kang, L., 2021. High resolution photopolymer for 3D printing of personalised microneedle for transdermal delivery of anti-wrinkle small peptide. *Journal of Controlled Release* 329, 907-918.

Lim, S.H., Ng, J.Y., Kang, L., 2017. Three-dimensional printing of a microneedle array on personalized curved surfaces for dual-pronged treatment of trigger finger. *Biofabrication* 9, 015010.

Lin, H., Kai, T., Freeman, B.D., Kalakkunnath, S., Kalika, D.S., 2005. The effect of cross-linking on gas permeability in cross-linked poly (ethylene glycol diacrylate). *Macromolecules* 38, 8381-8393.

Liu, C., Qin, H., Mather, P., 2007. Review of progress in shape-memory polymers. *Journal of Materials Chemistry* 17, 1543-1558.

Lorente, J., Sabater, F., Rivas, M., Fuste, J., Risco, J., Gómez, M., 2014. Ciprofloxacin plus fluocinolone acetonide versus ciprofloxacin alone in the treatment of diffuse otitis externa. *The Journal of Laryngology & Otology* 128, 591-598.

Loterie, D., Delrot, P., Moser, C., 2020. High-resolution tomographic volumetric additive manufacturing. *Nature Communications* 11, 1-6.

Lu, J., Cong, T., Wen, X., Li, X., Du, D., He, G., Jiang, X., 2019. Salicylic acid treats acne vulgaris by suppressing AMPK/SREBP 1 pathway in sebocytes. *Experimental dermatology* 28, 786-794.

Lu, Y., Mantha, S.N., Crowder, D.C., Chinchilla, S., Shah, K.N., Yun, Y.H., Wicker, R.B., Choi, J.W., 2015. Microstereolithography and characterization of poly(propylene fumarate)-based drug-loaded microneedle arrays. *Biofabrication* 7, 045001.

Lumi Industries, 2021a. LumiBee: A unique DIY resin 3D printer for smartphones.https://www.lumindustries.com/lumibee, (accessed 20th October, 2022).

Lumi Industries, 2021b. The quest for a truly portable, high quality light-curing 3D printer.https://www.lumindustries.com/the-new-lumifold, (accessed 23rd July, 2021).

Luzuriaga, M.A., Berry, D.R., Reagan, J.C., Smaldone, R.A., Gassensmith, J.J., 2018. Biodegradable 3D printed polymer microneedles for transdermal drug delivery. *Lab on a Chip* 18, 1223-1230.

Madžarević, M., Ibrić, S., 2021. Evaluation of exposure time and visible light irradiation in LCD 3D printing of ibuprofen extended release tablets. *European Journal of Pharmaceutical Sciences* 158, 105688.

Madzarevic, M., Medarevic, D., Vulovic, A., Sustersic, T., Djuris, J., Filipovic, N., Ibric, S., 2019. Optimization and prediction of ibuprofen release from 3D DLP printlets using artificial neural networks. *Pharmaceutics* 11, 544.

Maher, R.L., Hanlon, J., Hajjar, E.R., 2014. Clinical consequences of polypharmacy in elderly. *Expert Opinion on Drug Safety* 13, 57-65.

Mahmud, A., Feely, J., 2007. Low-dose quadruple antihypertensive combination: more efficacious than individual agents--a preliminary report. *Hypertension* 49, 272-275.

Mandon, C.I.A., Blum, L.J., Marquette, C.A., 2016. Adding biomolecular recognition capability to 3D printed objects. *Analytical Chemistry* 88, 10767-10772.

Mannino, R.G., Myers, D.R., Tyburski, E.A., Caruso, C., Boudreaux, J., Leong, T., Clifford, G., Lam, W.A., 2018. Smartphone app for non-invasive detection of anemia using only patient-sourced photos. *Nature Communications* 9, 1-10.

Martinez, P.R., Goyanes, A., Basit, A.W., Gaisford, S., 2017. Fabrication of drug-loaded hydrogels with stereolithographic 3D printing. *International Journal of Pharmaceutics* 532, 313-317.

Martinez, P.R., Goyanes, A., Basit, A.W., Gaisford, S., 2018. Influence of Geometry on the Drug Release Profiles of Stereolithographic (SLA) 3D-Printed Tablets. *AAPS PharmSciTech* 19, 3355-3361.

Mather, B.D., Viswanathan, K., Miller, K.M., Long, T.E., 2006. Michael addition reactions in macromolecular design for emerging technologies. *Progress in Polymer Science* 31, 487-531.

Matin-Mann, F., Gao, Z., Schwieger, J., Ulbricht, M., Domsta, V., Senekowitsch, S., Weitschies, W., Seidlitz, A., Doll, K., Stiesch, M., 2022. Individualized, Additively Manufactured Drug-Releasing External Ear Canal Implant for Prevention of Postoperative Restenosis: Development, In Vitro Testing, and Proof of Concept in an Individual Curative Trial. *Pharmaceutics* 14, 1242.

Mazaki, T., Shiozaki, Y., Yamane, K., Yoshida, A., Nakamura, M., Yoshida, Y., Zhou, D., Kitajima, T., Tanaka, M., Ito, Y., 2014. A novel, visible light-induced, rapidly cross-linkable gelatin scaffold for osteochondral tissue engineering. *Scientific Reports* 4, 1-10.

McCoy, C.F., Apperley, D.C., Variano, B., Sussman, H., Loeven, D., Boyd, P., Malcolm, R.K., 2018. Solid state 13C NMR spectroscopy provides direct evidence for reaction between ethinyl estradiol and a silicone elastomer vaginal ring drug delivery system. *International Journal of Pharmaceutics* 548, 689-697.

Melocchi, A., Inverardi, N., Uboldi, M., Baldi, F., Maroni, A., Pandini, S., Briatico-Vangosa, F., Zema, L., Gazzaniga, A., 2019. Retentive device for intravesical drug delivery based on water-induced shape memory response of poly(vinyl alcohol): design concept and 4D printing feasibility. *International Journal of Pharmaceutics* 559, 299-311.

Melocchi, A., Uboldi, M., Cerea, M., Foppoli, A., Maroni, A., Moutaharrik, S., Palugan, L., Zema, L., Gazzaniga, A., 2020. A graphical review on the escalation of fused deposition modeling (FDM) 3D printing in the pharmaceutical field. *Journal of Pharmaceutical Sciences* 109, 2943-2957.

Mendes‑Felipe, C., Oliveira, J., Etxebarria, I., Vilas‑Vilela, J.L., Lanceros‑Mendez, S., 2019. State‑of‑the‑Art and Future Challenges of UV Curable Polymer‑Based Smart Materials for Printing Technologies. *Advanced Materials Technologies* 4, 1800618.

Merchant, H.A., Goyanes, A., Parashar, N., Basit, A.W., 2014. Predicting the gastrointestinal behaviour of modified-release products: Utility of a novel dynamic dissolution test apparatus involving the use of bicarbonate buffers. *International Journal of Pharmaceutics* 475, 585-591.

Mills, K.T., Stefanescu, A., He, J., 2020. The global epidemiology of hypertension. *Nature Reviews Nephrology* 16, 223-237.

Miri, A.K., Nieto, D., Iglesias, L., Goodarzi Hosseinabadi, H., Maharjan, S., Ruiz‑Esparza, G.U., Khoshakhlagh, P., Manbachi, A., Dokmeci, M.R., Chen, S., 2018. Microfluidics ‑ enabled multimaterial maskless stereolithographic bioprinting. *Advanced Materials* 30, 1800242.

Mirzababaei, S., Pasebani, S., 2019. A review on binder jet additive manufacturing of 316L stainless steel. *Journal of Manufacturing and Materials Processing* 3, 82.

Moldovan, M., Balazsi, R., Soanca, A., Roman, A., Sarosi, C., Prodan, D., Vlassa, M., Cojocaru, I., Saceleanu, V., Cristescu, I., 2019. Evaluation of the degree of conversion, residual monomers and mechanical properties of some light-cured dental resin composites. *Materials* 12, 2109.

Muniz Castro, B., Elbadawi, M., Ong, J.J., Pollard, T., Song, Z., Gaisford, S., Perez, G., Basit, A.W., Cabalar, P., Goyanes, A., 2021. Machine learning predicts 3D printing performance of over 900 drug delivery systems. *Journal of Controlled Release* 337, 530-545.

Muwaffak, Z., Goyanes, A., Clark, V., Basit, A.W., Hilton, S.T., Gaisford, S., 2017. Patient-specific 3D scanned and 3D printed antimicrobial polycaprolactone wound dressings. *International Journal of Pharmaceutics* 527, 161-170.

Naseri, E., Cartmell, C., Saab, M., Kerr, R.G., Ahmadi, A., 2020. Development of 3D printed drug-eluting scaffolds for preventing piercing infection. *Pharmaceutics* 12, 901.

Ng, W.L., Lee, J.M., Zhou, M., Chen, Y.-W., Lee, K.-X.A., Yeong, W.Y., Shen, Y.-F., 2020. Vat polymerization-based bioprinting—process, materials, applications and regulatory challenges. *Biofabrication* 12, 022001.

Nguyen, A.K., Gittard, S.D., Koroleva, A., Schlie, S., Gaidukeviciute, A., Chichkov, B.N., Narayan, R.J., 2013. Two-photon polymerization of polyethylene glycol diacrylate scaffolds with riboflavin and triethanolamine used as a water-soluble photoinitiator. *Regenerative Medicine* 8, 725-738.

Nguyenpho, A., Ciavarella, A.B., Siddiqui, A., Rahman, Z., Akhtar, S., Hunt, R., Korang-Yeboah, M., Khan, M.A., 2015. Evaluation of in-use stability of anticoagulant drug products: warfarin sodium. *Journal of Pharmaceutical Sciences* 104, 4232-4240.

Nickel, J.C., Jain, P., Shore, N., Anderson, J., Giesing, D., Lee, H., Kim, G., Daniel, K., White, S., Larrivee-Elkins, C., 2012. Continuous intravesical lidocaine treatment for interstitial cystitis/bladder pain syndrome: safety and efficacy of a new drug delivery device. *Science Translational Medicine* 4, 143ra100.

Nickel, J.C., Moldwin, R., Lee, S., Davis, E.L., Henry, R.A., Wyllie, M.G., 2009. Intravesical alkalinized lidocaine (PSD597) offers sustained relief from symptoms of interstitial cystitis and painful bladder syndrome. *BJU international* 103, 910-918.

Niese, S., Breitkreutz, J., Quodbach, J., 2019. Development of a dosing device for individualized dosing of orodispersible warfarin films. *International Journal of Pharmaceutics* 561, 314-323.

Öblom, H., Sjöholm, E., Rautamo, M., Sandler, N., 2019. Towards printed pediatric medicines in hospital pharmacies: Comparison of 2D and 3D-printed orodispersible warfarin films with conventional oral powders in unit dose sachets. *Pharmaceutics* 11, 334.

Oesterreicher, A., Wiener, J., Roth, M., Moser, A., Gmeiner, R., Edler, M., Pinter, G., Griesser, T., 2016. Tough and degradable photopolymers derived from alkyne monomers for 3D printing of biomedical materials. *Polymer Chemistry* 7, 5169-5180.

Okwuosa, T.C., Pereira, B.C., Arafat, B., Cieszynska, M., Isreb, A., Alhnan, M.A., 2017. Fabricating a shell-core delayed release tablet using dual FDM 3D printing for patient-centred therapy. *Pharmaceutical Research* 34, 427-437.

Olivera, M.E., Manzo, R.H., Junginger, H., Midha, K., Shah, V., Stavchansky, S., Dressman, J., Barends, D., 2011. Biowaiver monographs for immediate release solid oral dosage forms: Ciprofloxacin hydrochloride. *Journal of Pharmaceutical Sciences* 100, 22-33.

Ong, J.J., Awad, A., Martorana, A., Gaisford, S., Stoyanov, E., Basit, A.W., Goyanes, A., 2020. 3D printed opioid medicines with alcohol-resistant and abuse-deterrent properties. *International Journal of Pharmaceutics* 579, 119169.

Pagac, M., Hajnys, J., Ma, Q.-P., Jancar, L., Jansa, J., Stefek, P., Mesicek, J., 2021. A Review of Vat Photopolymerization Technology: Materials, Applications, Challenges, and Future Trends of 3D Printing. *Polymers* 13.

Palmero, E.M., Casaleiz, D., de Vicente, J., Hernández-Vicen, J., López-Vidal, S., Ramiro, E., Bollero, A., 2019. Composites based on metallic particles and tuned filling factor for 3D-printing by Fused Deposition Modeling. *Composites Part A: Applied Science and Manufacturing* 124, 105497.

Palugan, L., Cerea, M., Cirilli, M., Moutaharrik, S., Maroni, A., Zema, L., Melocchi, A., Uboldi, M., Filippin, I., Foppoli, A., 2021. Intravesical drug delivery approaches for improved therapy of urinary bladder diseases. *International Journal of Pharmaceutics: X* 3, 100100.

Parfenyuk, E.V., Dolinina, E.S., 2017. Development of novel warfarin-silica composite for controlled drug release. *Pharmaceutical Research* 34, 825-835.

Park, H.K., Shin, M., Kim, B., Park, J.W., Lee, H., 2018. A visible light-curable yet visible wavelength-transparent resin for stereolithography 3D printing. *NPG Asia Materials*, 1.

Park, S.H., Yang, D.Y., Lee, K.S., 2009. Two‑photon stereolithography for realizing ultraprecise three‑dimensional nano/microdevices. *Laser & Photonics Reviews* 3, 1-11.

Parsons, C.L., 2005. Successful downregulation of bladder sensory nerves with combination of heparin and alkalinized lidocaine in patients with interstitial cystitis. *Urology* 65, 45-48.

Patane, M.A., Cohen, A., From, S., Torkildsen, G., Welch, D., Ousler III, G.W., 2011. Ocular iontophoresis of EGP-437 (dexamethasone phosphate) in dry eye patients: results of a randomized clinical trial. *Clinical ophthalmology (Auckland, NZ)* 5, 633.

Patel, A., Cholkar, K., Agrahari, V., Mitra, A.K., 2013. Ocular drug delivery systems: An overview. *World Journal of Pharmacology* 2, 47.

Patel, J., Patel, A., Raval, M., Sheth, N., 2011. Formulation and development of a self-nanoemulsifying drug delivery system of irbesartan. *Journal of Advanced Pharmaceutical Technology & Research* 2, 9.

Paunović, N., Bao, Y., Coulter, F.B., Masania, K., Geks, A.K., Klein, K., Rafsanjani, A., Cadalbert, J., Kronen, P.W., Kleger, N., 2021. Digital light 3D printing of customized bioresorbable airway stents with elastomeric properties. *Science Advances* 7, eabe9499.

Pawar, A.A., Saada, G., Cooperstein, I., Larush, L., Jackman, J.A., Tabaei, S.R., Cho, N.-J., Magdassi, S., 2016. High-performance 3D printing of hydrogels by water-dispersible photoinitiator nanoparticles. *Science Advances* 2, e1501381.

Pere, C.P.P., Economidou, S.N., Lall, G., Ziraud, C., Boateng, J.S., Alexander, B.D., Lamprou, D.A., Douroumis, D., 2018. 3D printed microneedles for insulin skin delivery. *International Journal of Pharmaceutics* 544, 425-432.

Pereira, B.C., Isreb, A., Forbes, R.T., Dores, F., Habashy, R., Petit, J.-B., Alhnan, M.A., Oga, E.F., 2019. 'Temporary Plasticiser': A novel solution to fabricate 3D printed patient-centred cardiovascular 'Polypill'architectures. *European Journal of Pharmaceutics and Biopharmaceutics* 135, 94-103.

Pereira, B.C., Isreb, A., Isreb, M., Forbes, R.T., Oga, E.F., Alhnan, M.A., 2020. Additive manufacturing of a Point‑of‑Care "Polypill:" Fabrication of concept capsules of complex geometry with bespoke release against cardiovascular disease. *Advanced Healthcare Materials* 9, 2000236.

Pietrzak, K., Isreb, A., Alhnan, M.A., 2015. A flexible-dose dispenser for immediate and extended release 3D printed tablets. *European Journal of Pharmaceutics and Biopharmaceutics* 96, 380-387.

Pires, M.A.S., Souza dos Santos, R.A., Sinisterra, R.D., 2011. Pharmaceutical composition of hydrochlorothiazide: β-cyclo-dextrin: Preparation by three different methods, physico-chemical characterization and in vivo diuretic activity evaluation. *Molecules* 16, 4482-4499.

Placone, J.K., Engler, A.J., 2018. Recent advances in extrusion‐based 3D printing for biomedical applications. *Advanced Healthcare Materials* 7, 1701161.

Popal, M., Volk, J., Leyhausen, G., Geurtsen, W., 2018. Cytotoxic and genotoxic potential of the type I photoinitiators BAPO and TPO on human oral keratinocytes and V79 fibroblasts. *Dental Materials* 34, 1783-1796.

Prasher, A., Shrivastava, R., Dahl, D., Sharma-Huynh, P., Maturavongsadit, P., Pridgen, T., Schorzman, A., Zamboni, W., Ban, J., Blikslager, A., 2021. Steroid eluting esophageal-targeted drug delivery devices for treatment of eosinophilic esophagitis. *Polymers* 13, 557.

Prendergast, M.E., Burdick, J.A., 2020. Recent advances in enabling technologies in 3D printing for precision medicine. *Advanced Materials* 32, 1902516.

PubChem, 2023a. Acetaminophen.https://pubchem.ncbi.nlm.nih.gov/compound/Acetaminophen, (accessed 11th March, 2022).

PubChem, 2023b. Amlodipine.https://pubchem.ncbi.nlm.nih.gov/compound/Amlodipine, (accessed 11th March, 2023).

PubChem, 2023c. Atenolol.https://pubchem.ncbi.nlm.nih.gov/compound/Atenolol, (accessed 11th March, 2023).

PubChem, 2023d. Dexamethasone.https://pubchem.ncbi.nlm.nih.gov/compound/Dexamethasone, (accessed 11th March, 2023).

PubChem, 2023e. Hydrochlorothiazide.https://pubchem.ncbi.nlm.nih.gov/compound/Hydrochlorothiazide, (accessed 11th March, 2023).

PubChem, 2023f. Irbesartan.https://pubchem.ncbi.nlm.nih.gov/compound/irbesartan, (accessed 11th March, 2023).

PubChem, 2023g. Salicylic acid.https://pubchem.ncbi.nlm.nih.gov/compound/Salicylic-acid, (accessed 11th March, 2023).

Quan, H., Zhang, T., Xu, H., Luo, S., Nie, J., Zhu, X., 2020. Photo-curing 3D printing technique and its challenges. *Bioactive Materials* 5, 110-115.

Radfar, P., Bazaz, S.R., Mirakhorli, F., Warkiani, M.E., 2021. The role of 3D printing in the fight against COVID-19 outbreak. *Journal of 3D Printing in Medicine* 5, 51-60.

Ranganathan, S.I., Kohama, C., Mercurio, T., Salvatore, A., Benmassaoud, M.M., Kim, T.W.B., 2020. Effect of temperature and ultraviolet light on the bacterial kill effectiveness of antibiotic-infused 3D printed implants. *Biomedical Microdevices* 22, 1-14.

Read, E.S., Thompson, K.L., Armes, S.P., 2010. Synthesis of well-defined primary amine-based homopolymers and block copolymers and their Michael addition reactions with acrylates and acrylamides. *Polymer Chemistry* 1, 221-230.

Reynolds, K.K., Jr, R.V., Hartung, B.R., Linder, M.W., 2007. Individualizing warfarin therapy. *Personalized Medicine* 4, 11-31.

Roberts, C.W., Carniglia, P.E., Brazzo, B.G., 2007. Comparison of topical cyclosporine, punctal occlusion, and a combination for the treatment of dry eye. *Cornea* 26, 805-809.

Robles-Martinez, P., Xu, X., Trenfield, S.J., Awad, A., Goyanes, A., Telford, R., Basit, A.W., Gaisford, S., 2019. 3D Printing of a Multi-Layered Polypill Containing Six Drugs Using a Novel Stereolithographic Method. *Pharmaceutics* 11, 274.

Rodríguez-Pombo, L., Xu, X., Seijo-Rabina, A., Ong, J.J., Alvarez-Lorenzo, C., Rial, C., Nieto, D., Gaisford, S., Basit, A.W., Goyanes, A., 2022. Volumetric 3D printing for rapid production of medicines. *Additive Manufacturing* 52, 102673.

Rojas-Nastrucci, E.A., Nussbaum, J.T., Crane, N.B., Weller, T.M., 2017. Ka-band characterization of binder jetting for 3-D printing of metallic rectangular waveguide circuits and antennas. *IEEE Transactions on Microwave Theory and Techniques* 65, 3099-3108.

Rouen, P.A., White, M.L., 2018. Dry eye disease: prevalence, assessment, and management. *Home Healthcare Now* 36, 74-83.

Rowe, C., Katstra, W., Palazzolo, R., Giritlioglu, B., Teung, P., Cima, M., 2000. Multimechanism oral dosage forms fabricated by three dimensional printing™. *Journal of Controlled Release* 66, 11-17.

Rycerz, K., Stepien, K.A., Czapiewska, M., Arafat, B.T., Habashy, R., Isreb, A., Peak, M., Alhnan, M.A., 2019. Embedded 3D printing of novel bespoke soft dosage form concept for pediatrics. *Pharmaceutics* 11, 630.

Rzhevskiy, A.S., Singh, T.R.R., Donnelly, R.F., Anissimov, Y.G., 2018. Microneedles as the technique of drug delivery enhancement in diverse organs and tissues. *Journal of Controlled Release* 270, 184-202.

Sachs, E.M., Haggerty, J.S., Cima, M.J., Williams, P.A., 1993. Three-dimensional printing techniques. Google Patents.

Sadia, M., Arafat, B., Ahmed, W., Forbes, R.T., Alhnan, M.A., 2018. Channelled tablets: An innovative approach to accelerating drug release from 3D printed tablets. *Journal of Controlled Release* 269, 355-363.

Saimani, S., Kumar, A., 2008. Polyethylene glycol diacrylate and thermoplastic polymers based semi-IPNs for asymmetric membranes. *Composite Interfaces* 15, 781-797.

Salmoria, G., Vieira, F., Muenz, E., Gindri, I., Marques, M., Kanis, L., 2018. Additive Manufacturing of PE/fluorouracil/progesterone intrauterine device for endometrial and ovarian cancer treatments. *Polymer Testing* 71, 312-317.

Sampson, K.L., Deore, B., Go, A., Nayak, M.A., Orth, A., Gallerneault, M., Malenfant, P.R., Paquet, C., 2021. Multimaterial vat polymerization additive manufacturing. *ACS Applied Polymer Materials* 3, 4304-4324.

Sawant, P.D., Luu, D., Ye, R., Buchta, R., 2010. Drug release from hydroethanolic gels. Effect of drug's lipophilicity (log P), polymer–drug interactions and solvent lipophilicity. *International Journal of Pharmaceutics* 396, 45-52.

Schnabel, W., 2007. Polymers and light: fundamentals and technical applications. John Wiley & Sons.

Schwartz, J., Boydston, A.J., 2019. Multimaterial actinic spatial control 3D and 4D printing. *Nature Communications* 10, 1-10.

Seoane-Viaño, I., Januskaite, P., Alvarez-Lorenzo, C., Basit, A.W., Goyanes, A., 2021a. Semi-solid extrusion 3D printing in drug delivery and biomedicine: Personalised solutions for healthcare challenges. *Journal of Controlled Release* 332, 367-389.

Seoane-Viaño, I., Ong, J.J., Luzardo-Álvarez, A., González-Barcia, M., Basit, A.W., Otero-Espinar, F.J., Goyanes, A., 2020. 3D printed tacrolimus suppositories for the treatment of ulcerative colitis. *Asian Journal of Pharmaceutical Sciences*.

Seoane-Viaño, I., Trenfield, S.J., Basit, A.W., Goyanes, A., 2021b. Translating 3D printed pharmaceuticals: From hype to real-world clinical applications. *Advanced Drug Delivery Reviews* 174, 553-575.

Sharma, P.K., Choudhury, D., Yadav, V., Murty, U., Banerjee, S., 2022. 3D printing of nanocomposite pills through desktop vat photopolymerization (stereolithography) for drug delivery reasons. *3D Printing in Medicine* 8, 1-10.

Sherif, A.Y., Mahrous, G.M., Alanazi, F.K., 2018. Novel in-situ gel for intravesical administration of ketorolac. *Saudi Pharmaceutical Journal* 26, 845-851.

Shih, H., Lin, C.C., 2013. Visible‑light‑mediated thiol‑Ene hydrogelation using eosin‑Y as the only photoinitiator. *Macromolecular Rapid Communications* 34, 269-273.

Shirazi, S.F.S., Gharehkhani, S., Mehrali, M., Yarmand, H., Metselaar, H.S.C., Kadri, N.A., Osman, N.A.A., 2015. A review on powder-based additive manufacturing for tissue engineering: selective laser sintering and inkjet 3D printing. *Science and Technology of Advanced Materials* 16, 033502.

Shusteff, M., Browar, A.E., Kelly, B.E., Henriksson, J., Weisgraber, T.H., Panas, R.M., Fang, N.X., Spadaccini, C.M., 2017. One-step volumetric additive manufacturing of complex polymer structures. *Science Advances* 3, eaao5496.

Siepmann, J., Peppas, N.A., 2012. Modeling of drug release from delivery systems based on hydroxypropyl methylcellulose (HPMC). *Advanced Drug Delivery Reviews* 64, 163-174.

Singh, R.B., Ichhpujani, P., Thakur, S., Jindal, S., 2020. Promising therapeutic drug delivery systems for glaucoma: a comprehensive review. *Therapeutic Advances in Ophthalmology* 12, 2515841420905740.

Skowyra, J., Pietrzak, K., Alhnan, M.A., 2015. Fabrication of extended-release patient-tailored prednisolone tablets via fused deposition modelling (FDM) 3D printing. *European Journal of Pharmaceutical Sciences* 68, 11-17.

Smith, D., Kapoor, Y., Hermans, A., Nofsinger, R., Kesisoglou, F., Gustafson, T.P., Procopio, A., 2018. 3D printed capsules for quantitative regional absorption studies in the GI tract. *International Journal of Pharmaceutics* 550, 418-428.

Sokolowski, W., Metcalfe, A., Hayashi, S., Raymond, J., 2007. Medical applications of shape memory polymers. *Biomedical Materials* 2, S23.

Spoerk, M., Arbeiter, F., Koutsamanis, I., Cajner, H., Katschnig, M., Eder, S., 2021. Personalised urethra pessaries prepared by material extrusion-based additive manufacturing. *International Journal of Pharmaceutics* 608, 121112.

Stansbury, J., Dickens, S.H., 2001. Determination of double bond conversion in dental resins by near infrared spectroscopy. *Dental Materials* 17, 71-79.

Steier, A., Schmieg, B., Irtel von Brenndorff, Y., Meier, M., Nirschl, H., Franzreb, M., Lahann, J., 2020. Enzyme Scaffolds with Hierarchically Defined Properties via 3D Jet Writing. *Macromolecular Bioscience* 20, 2000154.

Sun, Y., Ruan, X., Li, H., Kathuria, H., Du, G., Kang, L., 2016. Fabrication of non-dissolving analgesic suppositories using 3D printed moulds. *International Journal of Pharmaceutics* 513, 717-724.

Sun, Y., Soh, S., 2015. Printing tablets with fully customizable release profiles for personalized medicine. *Advanced Materials* 27, 7847-7853.

Tabriz, A.G., Fullbrook, D.H.G., Vilain, L., Derrar, Y., Nandi, U., Grau, C., Morales, A., Hooper, G., Hiezl, Z., Douroumis, D., 2021. Personalised Tasted Masked Chewable 3D Printed Fruit-Chews for Paediatric Patients. *Pharmaceutics* 13, 1301.

Tagami, T., Ito, E., Kida, R., Hirose, K., Noda, T., Ozeki, T., 2021a. 3D printing of gummy drug formulations composed of gelatin and an HPMC-based hydrogel for pediatric use. *International Journal of Pharmaceutics* 594, 120118.

Tagami, T., Morimura, C., Ozeki, T., 2021b. Effective and simple prediction model of drug release from "ghost tablets" fabricated using a digital light projection-type 3D printer. *International Journal of Pharmaceutics* 604, 120721.

Tai, M.-C., Cosar, C.B., Cohen, E.J., Rapuano, C.J., Laibson, P.R., 2002. The clinical efficacy of silicone punctal plug therapy. *Cornea* 21, 135-139.

Tan, D.K., Maniruzzaman, M., Nokhodchi, A., 2018. Advanced pharmaceutical applications of hot-melt extrusion coupled with fused deposition modelling (FDM) 3D printing for personalised drug delivery. *Pharmaceutics* 10, 203.

Tan, W.S., Kelly, J.D., 2018. Intravesical device-assisted therapies for non-muscle-invasive bladder cancer. *Nature Reviews Urology* 15, 667-685.

Tan, Y.J.N., Yong, W.P., Kochhar, J.S., Khanolkar, J., Yao, X., Sun, Y., Ao, C.K., Soh, S., 2020. On-demand fully customizable drug tablets via 3D printing technology for personalized medicine. *Journal of Controlled Release* 322, 42-52.

Tao, Y., Wang, H., Li, Z., Li, P., Shi, S.Q., 2017. Development and application of wood flour-filled polylactic acid composite filament for 3D printing. *Materials* 10, 339.

Tay, Y.W.D., Panda, B., Paul, S.C., Noor Mohamed, N.A., Tan, M.J., Leong, K.F., 2017. 3D printing trends in building and construction industry: a review. *Virtual and Physical Prototyping* 12, 261-276.

Thakkar, R., Pillai, A.R., Zhang, J., Zhang, Y., Kulkarni, V., Maniruzzaman, M., 2020. Novel on-demand 3-dimensional (3-D) printed tablets using fill density as an effective release-controlling tool. *Polymers* 12, 1872.

Thakur Singh, R.R., Tekko, I., McAvoy, K., McMillan, H., Jones, D., Donnelly, R.F., 2017. Minimally invasive microneedles for ocular drug delivery. *Expert Opinion on Drug Delivery* 14, 525-537.

Than, A., Liu, C., Chang, H., Duong, P.K., Cheung, C.M.G., Xu, C., Wang, X., Chen, P., 2018. Self-implantable double-layered micro-drug-reservoirs for efficient and controlled ocular drug delivery. *Nature Communications* 9, 1-12.

Tobias, I.S., Lee, H., Engelmayr Jr, G.C., Macaya, D., Bettinger, C.J., Cima, M.J., 2010. Zero-order controlled release of ciprofloxacin-HCl from a reservoir-based, bioresorbable and elastomeric device. *Journal of Controlled Release* 146, 356-362.

Trenfield, S.J., Awad, A., Goyanes, A., Gaisford, S., Basit, A.W., 2018. 3D Printing Pharmaceuticals: Drug Development to Frontline Care. *Trends in Pharmacological Sciences* 39, 440-451.

Trenfield, S.J., Awad, A., Madla, C.M., Hatton, G.B., Firth, J., Goyanes, A., Gaisford, S., Basit, A.W., 2019a. Shaping the future: recent advances of 3D printing in drug delivery and healthcare. *Expert Opinion on Drug Delivery* 16, 1081-1094.

Trenfield, S.J., Goyanes, A., Gaisford, S., Basit, A.W., 2021. Innovations in 2D and 3D printed pharmaceuticals. *International Journal of Pharmaceutics* 605, 120839.

Trenfield, S.J., Tan, H.X., Awad, A., Buanz, A., Gaisford, S., Basit, A.W., Goyanes, A., 2019b. Track-and-trace: Novel anti-counterfeit measures for 3D printed personalized drug products using smart material inks. *International Journal of Pharmaceutics* 567, 118443.

Triacca, A., Pitzanti, G., Mathew, E., Conti, B., Dorati, R., Lamprou, D.A., 2022. Stereolithography 3D printed implants: A preliminary investigation as potential local drug delivery systems to the ear. *International Journal of Pharmaceutics* 616, 121529.

Trivedi, M., Branton, A., Trivedi, D., Shettigar, H., Bairwa, K., Jana, S., 2015. Fourier transform infrared and ultraviolet-visible spectroscopic characterization of biofield treated salicylic acid and sparfloxacin. *Natural Products Chemistry & Research* 5.

Tumbleston, J.R., Shirvanyants, D., Ermoshkin, N., Janusziewicz, R., Johnson, A.R., Kelly, D., Chen, K., Pinschmidt, R., Rolland, J.P., Ermoshkin, A., 2015. Continuous liquid interface production of 3D objects. *Science* 347, 1349-1352.

Uchino, M., Schaumberg, D.A., 2013. Dry eye disease: impact on quality of life and vision. *Current Ophthalmology Reports* 1, 51-57.

Urrios, A., Parra-Cabrera, C., Bhattacharjee, N., Gonzalez-Suarez, A.M., Rigat-Brugarolas, L.G., Nallapatti, U., Samitier, J., DeForest, C.A., Posas, F., Garcia-

Cordero, J.L., 2016. 3D-printing of transparent bio-microfluidic devices in PEG-DA. *Lab on a Chip* 16, 2287-2294.

Varvara, R.-A., Szabo, K., Vodnar, D.C., 2021. 3D food printing: Principles of obtaining digitally-designed nourishment. *Nutrients* 13, 3617.

Vaut, L., Juszczyk, J.J., Kamguyan, K., Jensen, K.E., Tosello, G., Boisen, A., 2020. 3D Printing of Reservoir Devices for Oral Drug Delivery: From Concept to Functionality through Design Improvement for Enhanced Mucoadhesion. *ACS Biomaterials Science & Engineering* 6, 2478-2486.

Vaz, V.M., Kumar, L., 2021. 3D printing as a promising tool in personalized medicine. *AAPS PharmSciTech* 22, 1-20.

Visentin, A.F., Dong, T., Poli, J., Panzer, M.J., 2014. Rapid, microwave-assisted thermal polymerization of poly (ethylene glycol) diacrylate-supported ionogels. *Journal of Materials Chemistry A* 2, 7723-7726.

Vivero-Lopez, M., Muras, A., Silva, D., Serro, A.P., Otero, A., Concheiro, A., Alvarez-Lorenzo, C., 2021a. Resveratrol-Loaded Hydrogel Contact Lenses with Antioxidant and Antibiofilm Performance. *Pharmaceutics* 13, 532.

Vivero-Lopez, M., Xu, X., Muras, A., Otero, A., Concheiro, A., Gaisford, S., Basit, A.W., Alvarez-Lorenzo, C., Goyanes, A., 2021b. Anti-biofilm multi drug-loaded 3d printed hearing aids. *Materials Science and Engineering: C* 119, 111606.

Von Walter, M., Michaelis, I., Jakse, G., Grosse, J., 2009. Trospium chloride released from Intravesically applied PLGA-based carriers decreases bladder contractility in an insolated whole pig bladder model. *European Urology Supplements* 8, 178.

Vuddanda, P.R., Alomari, M., Dodoo, C.C., Trenfield, S.J., Velaga, S., Basit, A.W., Gaisford, S., 2018. Personalisation of warfarin therapy using thermal ink-jet printing. *European Journal of Pharmaceutical Sciences* 117, 80-87.

Wald, N.J., Law, M.R., 2003. A strategy to reduce cardiovascular disease by more than 80%. *BMJ* 326, 1419.

Walker, D.A., Hedrick, J.L., Mirkin, C.A., 2019. Rapid, large-volume, thermally controlled 3D printing using a mobile liquid interface. *Science* 366, 360-364.

Wallin, T., Pikul, J., Shepherd, R., 2018. 3D printing of soft robotic systems. *Nature Reviews Materials* 3, 84-100.

Wang, C.-C., Tejwani, M.R., Roach, W.J., Kay, J.L., Yoo, J., Surprenant, H.L., Monkhouse, D.C., Pryor, T.J., 2006. Development of near zero-order release dosage forms using three-dimensional printing (3-DP™) technology. *Drug Development and Industrial Pharmacy* 32, 367-376.

Wang, J., Goyanes, A., Gaisford, S., Basit, A.W., 2016. Stereolithographic (SLA) 3D printing of oral modified-release dosage forms. *International Journal of Pharmaceutics* 503, 207-212.

Wang, J., Zhang, Y., Aghda, N.H., Pillai, A.R., Thakkar, R., Nokhodchi, A., Maniruzzaman, M., 2021a. Emerging 3D printing technologies for drug delivery devices: Current status and future perspective. *Advanced Drug Delivery Reviews* 174, 294-316.

Wang, Y., Cui, H., Esworthy, T., Mei, D., Wang, Y., Zhang, L.G., 2021b. Emerging 4D Printing Strategies for Next‐Generation Tissue Regeneration and Medical Devices. *Advanced Materials*, 2109198.

Williams, C.G., Malik, A.N., Kim, T.K., Manson, P.N., Elisseeff, J.H., 2005. Variable cytocompatibility of six cell lines with photoinitiators used for polymerizing hydrogels and cell encapsulation. *Biomaterials* 26, 1211-1218.

Wu, B.M., Borland, S.W., Giordano, R.A., Cima, L.G., Sachs, E.M., Cima, M.J., 1996. Solid free-form fabrication of drug delivery devices. *Journal of Controlled Release* 40, 77-87.

Wu, S., Serbin, J., Gu, M., 2006. Two-photon polymerisation for three-dimensional micro-fabrication. *Journal of Photochemistry and Photobiology A: Chemistry* 181, 1-11.

Xie, J., Wang, C., Ning, Q., Gao, Q., Gao, C., Gou, Z., Ye, J., 2017. A new strategy to sustained release of ocular drugs by one-step drug-loaded microcapsule manufacturing in hydrogel punctal plugs. *Graefe's Archive for Clinical and Experimental Ophthalmology* 255, 2173-2184.

Xing, J.-F., Zheng, M.-L., Duan, X.-M., 2015. Two-photon polymerization microfabrication of hydrogels: an advanced 3D printing technology for tissue engineering and drug delivery. *Chemical Society Reviews* 44, 5031-5039.

Xu, J., Xue, Y., Hu, G., Lin, T., Gou, J., Yin, T., He, H., Zhang, Y., Tang, X., 2018. A comprehensive review on contact lens for ophthalmic drug delivery. *Journal of Controlled Release* 281, 97-118.

Xu, L., Yang, Q., Qiang, W., Li, H., Zhong, W., Pan, S., Yang, G., 2021a. Hydrophilic Excipient-Independent Drug Release from SLA-Printed Pellets. *Pharmaceutics* 13, 1717.

Xu, X., Awad, A., Robles-Martinez, P., Gaisford, S., Goyanes, A., Basit, A.W., 2021b. Vat photopolymerization 3D printing for advanced drug delivery and medical device applications. *Journal of Controlled Release* 329, 743-757.

Xu, X., Pose-Boirazian, T., Eibes, G., McCoubrey, L.E., Martínez-Costas, J., Gaisford, S., Goyanes, A., Basit, A.W., 2022. A customizable 3D printed device for enzymatic removal of drugs in water. *Water Research* 208, 117861.

Xu, X., Robles-Martinez, P., Madla, C.M., Joubert, F., Goyanes, A., Basit, A.W., Gaisford, S., 2020. Stereolithography (SLA) 3D printing of an antihypertensive polyprintlet: Case study of an unexpected photopolymer-drug reaction. *Additive Manufacturing* 33, 101071.

Xu, X., Zhao, J., Wang, M., Wang, L., Yang, J., 2019. 3D Printed Polyvinyl Alcohol Tablets with Multiple Release Profiles. *Scientific Reports* 9, 1-8.

Yachia, D., Hirszowicz, E., 2001. Intravesicular balloon. US6293923B1.

Yang, M.-L., Song, Y.-M., 2015. Synthesis and investigation of water-soluble anticoagulant warfarin/ferulic acid grafted rare earth oxide nanoparticle materials. *RSC advances* 5, 17824-17833.

Yang, Y., Zhou, Y., Lin, X., Yang, Q., Yang, G., 2020. Printability of External and Internal Structures Based on Digital Light Processing 3D Printing Technique. *Pharmaceutics* 12, 207.

Yellepeddi, V.K., Sheshala, R., McMillan, H., Gujral, C., Jones, D., Raghu Raj Singh, T., 2015. Punctal plug: a medical device to treat dry eye syndrome and for sustained drug delivery to the eye. *Drug Discovery Today* 20, 884-889.

Yu, C., Schimelman, J., Wang, P., Miller, K.L., Ma, X., You, S., Guan, J., Sun, B., Zhu, W., Chen, S., 2020. Photopolymerizable biomaterials and light-based 3D printing strategies for biomedical applications. *Chemical Reviews* 120, 10695-10743.

Yuan, X., Marcano, D.C., Shin, C.S., Hua, X., Isenhart, L.C., Pflugfelder, S.C., Acharya, G., 2015. Ocular drug delivery nanowafer with enhanced therapeutic efficacy. *ACS Nano* 9, 1749-1758.

Zacchè, M.M., Srikrishna, S., Cardozo, L., 2015. Novel targeted bladder drug-delivery systems: a review. *Research and Reports in Urology* 7, 169.

Zanetti-Polzi, L., Aschi, M., Daidone, I., Amadei, A., 2017. Theoretical modeling of the absorption spectrum of aqueous riboflavin. *Chemical Physics Letters* 669, 119-124.

Zarek, M., Layani, M., Cooperstein, I., Sachyani, E., Cohn, D., Magdassi, S., 2016. 3D printing of shape memory polymers for flexible electronic devices. *Advanced Materials* 28, 4449-4454.

Zhang, F., Zhu, L., Li, Z., Wang, S., Shi, J., Tang, W., Li, N., Yang, J., 2021. The recent development of vat photopolymerization: A review. *Additive Manufacturing* 48, 102423.

Zhang, J., Xiao, P., 2018. 3D printing of photopolymers. *Polymer Chemistry* 9, 1530-1540.

Zhao, Z., Kuang, X., Yuan, C., Qi, H.J., Fang, D., 2018. Hydrophilic/hydrophobic composite shape-shifting structures. *ACS Applied Materials & Interfaces* 10, 19932-19939.

Zhao, Z., Wu, J., Mu, X., Chen, H., Qi, H.J., Fang, D., 2017. Origami by frontal photopolymerization. *Science Advances* 3, e1602326.

Zhou, B., Bentham, J., Di Cesare, M., Bixby, H., Danaei, G., Cowan, M.J., Paciorek, C.J., Singh, G., Hajifathalian, K., Bennett, J.E., 2017. Worldwide trends in blood pressure from 1975 to 2015: a pooled analysis of 1479 population-based measurement studies with 19· 1 million participants. *The Lancet* 389, 37-55.

Zhou, C., Chen, Y., Yang, Z., Khoshnevis, B., 2013. Digital material fabrication using mask‑image‑projection‑based stereolithography. *Rapid Prototyping Journal*.

Ziaee, M., Crane, N.B., 2019. Binder jetting: A review of process, materials, and methods. *Additive Manufacturing* 28, 781-801.

Zidan, G., Greene, C.A., Etxabide, A., Rupenthal, I.D., Seyfoddin, A., 2021. Gelatine-based drug-eluting bandage contact lenses: effect of PEGDA concentration and manufacturing technique. *International Journal of Pharmaceutics*, 120452.